

2021

## Measurement of the Free Surface in the Wake of a Submerged Foil

Jamie Schicho  
University of Rhode Island, jlschicho@gmail.com

Follow this and additional works at: <https://digitalcommons.uri.edu/theses>

Terms of Use

All rights reserved under copyright.

---

### Recommended Citation

Schicho, Jamie, "Measurement of the Free Surface in the Wake of a Submerged Foil" (2021). *Open Access Master's Theses*. Paper 1957.  
<https://digitalcommons.uri.edu/theses/1957>

This Thesis is brought to you by the University of Rhode Island. It has been accepted for inclusion in Open Access Master's Theses by an authorized administrator of DigitalCommons@URI. For more information, please contact [digitalcommons-group@uri.edu](mailto:digitalcommons-group@uri.edu). For permission to reuse copyrighted content, contact the author directly.

Measurement of the Free Surface in the Wake of a Submerged Foil

By

Jamie Schicho

A DISSERTATION SUBMITTED IN PARTIAL FULFILLMENT OF THE  
REQUIREMENTS FOR THE DEGREE OF  
MASTER OF SCIENCE  
IN  
OCEAN ENGINEERING

UNIVERSITY OF RHODE ISLAND

2021

MASTER OF SCIENCE IN OCEAN ENGINEERING THESIS  
OF  
JAMIE SCHICHO

APPROVED:

Thesis Committee:

Major Professor      Jason Dahl

Stephan Grilli

Annette Grilli

Kathleen Donohue

Brenton DeBoef

DEAN OF THE GRADUATE SCHOOL

UNIVERSITY OF RHODE ISLAND

2021

## Abstract

This thesis investigates measurement techniques to measure the far field free surface wake of a submerged hydrofoil in a fluid flow. There were three independent variables adjusted during testing; 2 angles of attack (5 and 10 degrees), 3 depths of the foil (1\*chord length, 5/4\*chord length, and 3/2\*chord length), and 6 flow speeds (between 0.70 m/s and 1.10 m/s). The  $Fr_d^2$  values for these experiments were between 0.115 and 0.42 which was chosen to be similar to that of the Duncan Experiments in 1981.

For the surface elevation measurements two methods were explored through this research. The first method was Digital Image Correlation (DIC). This method proved effective for determining the surface elevation for waves that formed behind the foil at low flow speeds. At higher flow speeds ( $> 0.7$  m/s) a steady state wake formed behind the foil. However at these higher speeds there was substantial turbulence at the surface which caused ray crossing in the images captured through the free surface. This meant that the DIC analysis had extremely inconsistent results at the flow speeds of interest in this research.

The second surface elevation measurement method was a side view image processing method. This proved to be a viable method to capture the surface elevation for run cases of interest in these experiments. The wave form created behind the submerged foil was steady state for most of  $Fr_d^2$  values that were tested. For the majority of the run cases the wave form behind the submerged foil matched well with a curve fit based on a sum of sinusoidal waves, as expected. These experiments were only repeated once for a single angle of attack. For these repeated cases the results were consistent however this requires more testing to confirm repeatability of the experiments. In the Froude number analysis the experimental wavelength results agreed well with the expected wavelength results based on the linear dispersion relation. The results from Duncan (1981) align very well with breaking wave cases from these experiments for both wave height and wavelength.

## **Acknowledgements**

I would like to thank first and foremost the National Institute for Undersea Vehicle Technology for the funding to make this research possible. Thank you to my advisors; Professor Jason Dahl, Professor Annette Grilli, and Professor Stephan Grilli for all of their help and guidance through this research process. Thank you to my friends and family for supporting me throughout this research and graduate school process. I couldn't have done this without the help from each and every one of you!

## Contents

Abstract	ii
Acknowledgments	iv
Contents	v
List of Figures	x
List of Tables	xxvi
<b>1 Introduction and Motivation for Work</b>	<b>1</b>
<b>2 Background Information</b>	<b>5</b>
2.1 Duncan Experiments . . . . .	5
2.2 Digital Image Correlation . . . . .	8
2.3 Surface Elevation Measurement . . . . .	10
<b>3 Experimental Matrix</b>	<b>21</b>
<b>4 Experimental Design and Force Measurements</b>	<b>24</b>
4.1 Experimental Design . . . . .	24
4.1.1 Force Sensors . . . . .	24

4.1.2	Resin Foil with Kistler Force Sensors . . . . .	28
4.1.3	Resin Foil with Extended Foil around Mounting System . . . . .	30
4.1.4	HDPE Foil with ATI Force Sensor . . . . .	33
4.1.5	HDPE Foil with Rubber Edges . . . . .	35
4.2	Conclusions and Future Work . . . . .	36
<b>5</b>	<b>Digital Image Correlation</b>	<b>38</b>
5.1	Testing in the Small Aquarium . . . . .	38
5.1.1	Preliminary Test Setup . . . . .	38
5.1.2	Horizontal Displacement Test . . . . .	39
5.1.3	Slow Motion Video Analysis with Waves . . . . .	45
5.2	Testing in the Flow Channel . . . . .	55
5.2.1	Preliminary Test Setup . . . . .	55
5.2.2	Camera Mounting Setup . . . . .	58
5.2.3	Periodic Wave Test Without the Foil . . . . .	60
5.2.4	Flow Testing with the Resin Foil . . . . .	64
5.3	Conclusions and Future Work . . . . .	67
5.3.1	Testing in the Small Aquarium . . . . .	67
5.3.2	Testing in the Flow Channel . . . . .	68
<b>6</b>	<b>Side View Image Analysis</b>	<b>70</b>
6.1	Test Setup . . . . .	70
6.2	Image Processing Method . . . . .	74
6.3	Side View Image Analysis: Results and Discussion . . . . .	78

6.3.1	HDPE Foil with; angle of attack: $10^\circ$ & depth of foil: $1 \cdot \text{chord}$ length . . . . .	81
6.3.2	HDPE Foil with; angle of attack: $10^\circ$ & depth of foil: $5/4 \cdot \text{chord}$ length . . . . .	88
6.3.3	HDPE Foil with; angle of attack: $10^\circ$ & depth of foil: $3/2 \cdot \text{chord}$ length . . . . .	94
6.3.4	HDPE Foil with; angle of attack: $5^\circ$ & depth of foil: $1 \cdot \text{chord}$ length . . . . .	97
6.3.5	Froude Number Analysis of Side View Experiments . . . . .	105
6.3.6	Direct Comparison with Duncan Results . . . . .	112
6.4	Conclusions and Future Work . . . . .	116
<b>7</b>	<b>Appendix</b>	<b>118</b>
7.1	Additional Results from the Slow Motion Video Analysis . . . . .	118
7.2	Side View Image Analysis Results for the Comparison of Experiments: 1/12/2021 and 2/11/2021 . . . . .	124
7.2.1	HDPE Foil with; angle of attack: $10^\circ$ & depth of foil: $1 \cdot \text{chord}$ length . . . . .	124
7.2.2	HDPE Foil with; angle of attack: $10^\circ$ & depth of foil: $5/4 \cdot \text{chord}$ length . . . . .	130
7.2.3	HDPE Foil with; angle of attack: $10^\circ$ & depth of foil: $3/2 \cdot \text{chord}$ length . . . . .	136
7.3	Side View Image Analysis Results for $5^\circ$ angle of attack: 2/11/2021 . . . . .	142

7.3.1	HDPE Foil with; angle of attack: $5^\circ$ & depth of foil: $1 \cdot \text{chord}$ length . . . . .	142
7.3.2	HDPE Foil with; angle of attack: $5^\circ$ & depth of foil: $5/4 \cdot \text{chord}$ length . . . . .	148
7.3.3	HDPE Foil with; angle of attack: $5^\circ$ , & depth of foil: $3/2 \cdot \text{chord}$ length . . . . .	154
7.4	Scripts for synthetic Schlieren Processing and Plotting . . . . .	160
7.4.1	Script for Processing DIC Displacements to get Free Surface Values. . . . .	160
7.4.2	Script for Processing PIV Displacements to get Free Surface Values. . . . .	163
7.4.3	Script for Plotting DIC Free Surface Values. . . . .	166
7.4.4	Script for Plotting PIV Free Surface Values. . . . .	169
7.5	Scripts for Image Processing and Plotting . . . . .	171
7.5.1	Script for converting im7 images to jpg as well as cropping and stitching images from the 2 different cameras. . . . .	171
7.5.2	Script for determining Froude values and expected wavelengths. . . . .	175
7.5.3	Function for determining expected wavelengths using linear dis- persion relation. . . . .	176
7.5.4	Script for analyzing the side view images to extract the waterline. . . . .	177
7.5.5	Script for shifting the average waterline based on the foil center as well as the still waterline. . . . .	184

7.5.6	Script for extract the wave parameters for wavelength and wave heights from peak and trough values. . . . .	190
7.5.7	Script for plotting and comparing average waterlines from different experiments. . . . .	194
<b>8</b>	<b>Bibliography</b>	<b>199</b>

## List of Figures

2.1	Definition sketch for the surface profile variables (Duncan, 1981). . . . .	5
2.2	Schematic of foil location, breaking wave geometry, and following wave train (Duncan, J. H., 1983). . . . .	6
2.3	Towing tank with hydrofoil and its towing system a) side view b) top view (Duncan, J. H., 1983). . . . .	7
2.4	a) Area of Interest (AOI) and subset in a reference image; b) schematic presentation of a reference subset before deformation and the corresponding target after subset deformation (Digital, 2016). . . . .	9
2.5	Sketch of the experimental set-up with the camera above, not at scale, $h_0/H \approx 1,000$ (Moisy et al., 2009). . . . .	11
2.6	Three-dimensional ray geometry for a horizontal interface (Moisy et al., 2009). . . . .	12
2.7	Two-dimensional view of the vertical incidence plane COM. (Moisy et al., 2009). . . . .	12
2.8	Top view of the pattern plane, showing object M and its two virtual objects M' and M'' for the flat and deformed interface, respectively. (Moisy et al., 2009). . . . .	15

2.9	Three-dimensional ray geometry for an arbitrary deformed interface where the interface CAM is now defined is no longer vertical in general, and does not contain the optical axis OC (Moisy et al., 2009). . . . .	16
2.10	Two-dimensional view of the incidence plane CAM (only the principle ray is shown for clarity) (Moisy et al., 2009). . . . .	16
2.11	Apparent displacement $\delta x$ when several intermediate materials are inserted between the interface and the pattern, assuming that the camera is far above the surface. . . . .	18
4.1	Image of the Kistler type 9602 6-axis piezoelectric force sensor (Kistler, 2016). . . . .	25
4.2	Schematic and dimensions of the Kistler type 9602 6-axis piezoelectric force sensor. All dimensions are in millimeters (Kistler, 2016). . . . .	26
4.3	Schematic for the pins of the plug for the Kistler type 9602 6-axis piezoelectric force sensor (Kistler, 2016). . . . .	27
4.4	Image of the ATI Gamma SI-65-5 6-axis force sensor (ATI, 2000). . . . .	28
4.5	Solidworks model of experimental setup for the pressure fitted system that includes the inline Kistler force sensors. . . . .	29
4.6	Mounting piece inside the edge of the resin foil without the Kistler force sensor. . . . .	31
4.7	Mounting system for the resin foil without the Kistler force sensor. . . . .	32
4.8	Mounting system and attachment for the foil with the ATI force sensor experimental setup. . . . .	34

4.9	Mounting system for the HDPE foil by itself. . . . .	36
5.1	Image of the tank lit from below so as to avoid any glare on the free surface. . . . .	39
5.2	Tank location for the displacement test, red corners, orange corners, and black corners. . . . .	40
5.3	Tank in the orange location for the displacement test. . . . .	41
5.4	This is the tank located between the black markings, chosen as the zero position. . . . .	42
5.5	Results for displacement in x (left) and displacement in y (right) of the DIC analysis without any physical displacement of the tank. All units are in inches. . . . .	42
5.6	This is the tank located between the black markings, chosen as the zero position. . . . .	43
5.7	This is the tank located between the orange markings, chosen as first position. . . . .	43
5.8	Results for displacement in x (left) and displacement in y (right) of the DIC analysis with the pattern moved 0.40625 inches. All units are in inches. . . . .	43
5.9	This is the tank located between the black markings, chosen as the zero position. . . . .	44
5.10	This is the tank located between the red markings, chosen as second position. . . . .	44

5.11	Results for displacement in x (left) and displacement in y (right) of the DIC analysis with the pattern moved 0.96875 inches. All units are in inches. . . . .	45
5.12	An example photo of the experimental setup from the Samsung phone camera with lighting from below off. . . . .	46
5.13	This is an image from the camera facing the waterline. . . . .	47
5.14	Image of the tank lit from below so as to avoid any glare on the free surface. . . . .	48
5.15	Results of the DIC analysis for frame 12070, in the top left frame is the reference image, the top middle is the current time frame image, the top right is the waterline frame from the same time step. Then the bottom left shows u displacement, the bottom middle shows v displacement, and the bottom right shows surface elevation ( $\eta$ ) (All units shown in the output figures are in inches). . . . .	50
5.16	Results of the DIC analysis for frame 12070, comparing the waterline video to the surface elevation at that location. The frame on the left is an image of the surface elevation and the figure on the right is the data closest to the tank wall on this side (All units are in inches). . .	51

5.17	Results of the DIC analysis for frame 12292, in the top left frame is the reference image, the top middle is the current time frame image, the top right is the waterline frame from the same time step. Then the bottom left shows u displacement, the bottom middle shows v displacement, and the bottom right shows surface elevation ( $\eta$ ) (All units shown in the output figures are in inches). . . . .	52
5.18	Results of the DIC analysis for frame 12292, comparing the waterline video to the surface elevation at that location. The frame on the left is an image of the surface elevation and the figure on the right is the data closest to the tank wall on this side (All units are in inches). . .	53
5.19	Results of the DIC analysis for frame 12334, in the top left frame is the reference image, the top middle is the current time frame image, the top right is the waterline frame from the same time step. Then the bottom left shows u displacement, the bottom middle shows v displacement, and the bottom right shows surface elevation ( $\eta$ ) (All units shown in the output figures are in inches). . . . .	54
5.20	Results of the DIC analysis for frame 12334, comparing the waterline video to the surface elevation at that location. The frame on the left is an image of the surface elevation and the figure on the right is the data closest to the tank wall on this side (All units are in inches). . .	55
5.21	This shows the experimental setup as a schematic with the camera over the flow channel. . . . .	57
5.22	The experimental setup of the camera over the flow channel. . . . .	58

5.23	The experimental setup camera's view from above the tank of the speckle pattern mounted underneath the flow channel. . . . .	59
5.24	Results using the DIC analysis for a periodic wave in the flow channel compared with wave gauge data at a single point. . . . .	60
5.25	Results using the PIV analysis for a periodic wave in the flow channel compared with wave gauge data at a single point. . . . .	63
5.26	Reference (top left) and current (top right) images are shown and then components of the velocity (m/s), u (bottom left), v (bottom middle) and surface elevation, h (m) (bottom right). These results were outputs from the PIV analysis for the smaller resin foil at an angle of attack of 10 degrees, a depth of $3/4$ *chord length at a speed of 0.34 m/s for time step 300. . . . .	64
5.27	Reference (top left) and current (top right) images are shown and then components of the velocity (m/s), u (bottom left), v (bottom middle) and surface elevation, h (m) (bottom right). These results were outputs from the PIV analysis for the smaller resin foil at an angle of attack of 10 degrees, a depth of $3/4$ *chord length at a speed of 0.34 m/s for time step 2500. . . . .	66
5.28	Results in time using the PIV analysis for the smaller resin foil at an angle of attack of 10 degrees, a depth of $3/4$ *chord length at a speed of 0.34 m/s over time at a point coincident with the wave gauge. . . .	67

6.1	Schematic of the flow channel showing the flow direction and the location of the wave gauges. . . . .	71
6.2	2 cameras, set up with respect to the flow channel. . . . .	72
6.3	Mounting system for the 2 cameras. . . . .	73
6.4	Calibration image from the camera closest to the foil location on 2/11/2021. . . . .	75
6.5	Images of the flow channel combined from the 2 cameras showing the location of the wave gauges. . . . .	76
6.6	Flow channel images combined from the 2 cameras (top), binarized image (middle), binarized and edges image with the waterline, peaks, troughs, and wave gauge data shown (bottom). . . . .	77
6.7	Comparison of the images from the first and second set of experiments on 1/12/2021 (top) and 2/11/2021 (bottom). . . . .	79
6.8	Results using the side view analysis for the larger HDPE foil at an angle of attack of 10 degrees, a depth of 1*chord length, and with a flow speed of 0.80 m/s averaged over the time of the experiment (50 seconds). . . . .	81
6.9	Results using the side view analysis for the larger HDPE foil at an angle of attack of 10 degrees, a depth of 1*chord length, and with a flow speed of 0.80 m/s averaged over the time of the experiment (50 seconds). . . . .	82

6.10	Results using the side view analysis for the larger HDPE foil at an angle of attack of 10 degrees, a depth of 1*chord length, and with a flow speed of 0.89 m/s averaged over the time of the experiment (50 seconds).	84
6.11	Results using the side view analysis for the larger HDPE foil at an angle of attack of 10 degrees, a depth of 1*chord length at a speed of 1.10 m/s averaged over the time of the experiment (50 seconds).	86
6.12	Results using the side view analysis for the larger HDPE foil at an angle of attack of 10 degrees, a depth of 5/4*chord length at a speed of 0.80 m/s averaged over the time of the experiment (50 seconds).	88
6.13	Results using the side view analysis for the larger HDPE foil at an angle of attack of 10 degrees, a depth of 5/4*chord length at a speed of 0.97 m/s averaged over the time of the experiment (50 seconds).	90
6.14	Results using the side view analysis for the larger HDPE foil at an angle of attack of 10 degrees, a depth of 5/4*chord length at a speed of 1.10 m/s averaged over the time of the experiment (50 seconds).	92
6.15	Results using the side view analysis for the larger HDPE foil at an angle of attack of 10 degrees, a depth of 3/2*chord length at a speed of 0.89 m/s averaged over the time of the experiment (50 seconds).	94
6.16	Results using the side view analysis for the larger HDPE foil at an angle of attack of 10 degrees, a depth of 3/2*chord length at a speed of 1.06 m/s averaged over the time of the experiment (50 seconds).	96

6.17	Results using the side view analysis for the larger HDPE foil at an angle of attack of 5 degrees, a depth of 1*chord length at a speed of 0.80 m/s averaged over the time of the experiment (50 seconds). . . .	98
6.18	Results using the side view analysis for the larger HDPE foil at an angle of attack of 10 degrees, a depth of 1*chord length, and with a flow speed of 0.80 m/s averaged over the time of the experiment (50 seconds). . . . .	98
6.19	Results using the side view analysis for the larger HDPE foil at an angle of attack of 5 degrees, a depth of 1*chord length at a speed of 1.10 m/s averaged over the time of the experiment (50 seconds). . . .	101
6.20	Results using the side view analysis for the larger HDPE foil at an angle of attack of 10 degrees, a depth of 1*chord length at a speed of 1.10 m/s averaged over the time of the experiment (50 seconds). . . .	102
6.21	The wavelength in terms of chord length as a function of the $Fr_d^2$ value from the side view analysis for all the experiments on 1/12/2021. . .	107
6.22	The wavelength in terms of chord length as a function of the $Fr_{cl}^2$ from the side view analysis for all the experiments on 1/12/2021. . . . .	108
6.23	The wavelength in terms of chord length as a function of the $Fr_d^2$ value from the side view analysis for all the experiments on 2/11/2021. . .	110
6.24	The wavelength in terms of chord length as a function of the $Fr_{cl}^2$ from the side view analysis for all the experiments on 2/11/2021. . . . .	111

6.25	Breaking wavelength as a function of $Fr_{cl}^2$ . Comparison of results from Duncan (1981) to breaking wave cases from the current set of experiments. . . . .	112
6.26	Breaking wavelength as a function of $Fr_{cl}^2$ . Comparison of results from Duncan (1981) to non-breaking wave cases from the current set of experiments. . . . .	113
6.27	Breaking wave height as a function of $Fr_{cl}^2$ . Comparison of results from Duncan (1981) to breaking wave cases from the current set of experiments. . . . .	114
6.28	Breaking wave height as a function of $Fr_{cl}^2$ . Comparison of results from Duncan (1981) to non-breaking wave cases from the current set of experiments. . . . .	115
7.1	Results of the DIC analysis for frame 12070, outputs include u displacement, v displacement and surface elevation (eta). . . . .	118
7.2	Results of the DIC analysis for frame 12070, comparing the waterline video to the surface elevation at that location. . . . .	119
7.3	Results of the DIC analysis for frame 12250, outputs include u displacement, v displacement and surface elevation (eta). . . . .	119
7.4	Results of the DIC analysis for frame 12250, comparing the waterline video to the surface elevation at that location. . . . .	120
7.5	Results of the DIC analysis for frame 12292, outputs include u displacement, v displacement and surface elevation (eta). . . . .	120

7.6	Results of the DIC analysis for frame 12292, comparing the waterline video to the surface elevation at that location. . . . .	121
7.7	Results of the DIC analysis for frame 12334, outputs include u displacement, v displacement and surface elevation ( $\eta$ ). . . . .	121
7.8	Results of the DIC analysis for frame 12334, comparing the waterline video to the surface elevation at that location. . . . .	122
7.9	Results of the DIC analysis for frame 12384, outputs include u displacement, v displacement and surface elevation ( $\eta$ ). . . . .	122
7.10	Results of the DIC analysis for frame 12384, comparing the waterline video to the surface elevation at that location. . . . .	123
7.11	Results of the DIC analysis for frame 12582, outputs include u displacement, v displacement and surface elevation ( $\eta$ ). . . . .	123
7.12	Results of the DIC analysis for frame 12582, comparing the waterline video to the surface elevation at that location. . . . .	124
7.13	Results using the side view analysis for the larger HDPE foil at an angle of attack of 10 degrees, a depth of 1*chord length, and with a flow speed of 0.80 m/s averaged over the time of the experiment (50 seconds). . . . .	124
7.14	Results using the side view analysis for the larger HDPE foil at an angle of attack of 10 degrees, a depth of 1*chord length, and with a flow speed of 0.89 m/s averaged over the time of the experiment (50 seconds). . . . .	125

7.15	Results using the side view analysis for the larger HDPE foil at an angle of attack of 10 degrees, a depth of 1*chord length at a speed of 0.97 m/s averaged over the time of the experiment (50 seconds). . . .	126
7.16	Results using the side view analysis for the larger HDPE foil at an angle of attack of 10 degrees, a depth of 1*chord length at a speed of 1.06 m/s averaged over the time of the experiment (50 seconds). . . .	127
7.17	Results using the side view analysis for the larger HDPE foil at an angle of attack of 10 degrees, a depth of 1*chord length at a speed of 1.10 m/s averaged over the time of the experiment (50 seconds). . . .	128
7.18	Results using the side view analysis for the larger HDPE foil at an angle of attack of 10 degrees, a depth of 5/4*chord length at a speed of 0.80 m/s averaged over the time of the experiment (50 seconds). . .	130
7.19	Results using the side view analysis for the larger HDPE foil at an angle of attack of 10 degrees, a depth of 5/4*chord length at a speed of 0.89 m/s averaged over the time of the experiment (50 seconds). . .	131
7.20	Results using the side view analysis for the larger HDPE foil at an angle of attack of 10 degrees, a depth of 5/4*chord length at a speed of 0.97 m/s averaged over the time of the experiment (50 seconds). . .	132
7.21	Results using the side view analysis for the larger HDPE foil at an angle of attack of 10 degrees, a depth of 5/4*chord length at a speed of 1.06 m/s averaged over the time of the experiment (50 seconds). . .	133

7.22	Results using the side view analysis for the larger HDPE foil at an angle of attack of 10 degrees, a depth of $5/4$ *chord length at a speed of 1.10 m/s averaged over the time of the experiment (50 seconds).	. . . 134
7.23	Results using the side view analysis for the larger HDPE foil at an angle of attack of 10 degrees, a depth of $3/2$ *chord length at a speed of 0.80 m/s averaged over the time of the experiment (50 seconds).	. . . 136
7.24	Results using the side view analysis for the larger HDPE foil at an angle of attack of 10 degrees, a depth of $3/2$ *chord length at a speed of 0.89 m/s averaged over the time of the experiment (50 seconds).	. . . 137
7.25	Results using the side view analysis for the larger HDPE foil at an angle of attack of 10 degrees, a depth of $3/2$ *chord length at a speed of 0.97 m/s averaged over the time of the experiment (50 seconds).	. . . 138
7.26	Results using the side view analysis for the larger HDPE foil at an angle of attack of 10 degrees, a depth of $3/2$ *chord length at a speed of 1.06 m/s averaged over the time of the experiment (50 seconds).	. . . 139
7.27	Results using the side view analysis for the larger HDPE foil at an angle of attack of 10 degrees, a depth of $3/2$ *chord length at a speed of 1.10 m/s averaged over the time of the experiment (50 seconds).	. . . 140
7.28	Results using the side view analysis for the larger HDPE foil at an angle of attack of 5 degrees, a depth of $1$ *chord length at a speed of 0.71 m/s averaged over the time of the experiment (50 seconds).	. . . . 142

7.29	Results using the side view analysis for the larger HDPE foil at an angle of attack of 5 degrees, a depth of 1*chord length at a speed of 0.80 m/s averaged over the time of the experiment (50 seconds). . . .	143
7.30	Results using the side view analysis for the larger HDPE foil at an angle of attack of 5 degrees, a depth of 1*chord length at a speed of 0.89 m/s averaged over the time of the experiment (50 seconds). . . .	144
7.31	Results using the side view analysis for the larger HDPE foil at an angle of attack of 5 degrees, a depth of 1*chord length at a speed of 0.97 m/s averaged over the time of the experiment (50 seconds). . . .	145
7.32	Results using the side view analysis for the larger HDPE foil at an angle of attack of 5 degrees, a depth of 1*chord length at a speed of 1.06 m/s averaged over the time of the experiment (50 seconds). . . .	146
7.33	Results using the side view analysis for the larger HDPE foil at an angle of attack of 5 degrees, a depth of 1*chord length at a speed of 1.10 m/s averaged over the time of the experiment (50 seconds). . . .	147
7.34	Results using the side view analysis for the larger HDPE foil at an angle of attack of 5 degrees, a depth of 5/4*chord length at a speed of 0.71 m/s averaged over the time of the experiment (50 seconds). . . .	148
7.35	Results using the side view analysis for the larger HDPE foil at an angle of attack of 5 degrees, a depth of 5/4*chord length at a speed of 0.80 m/s averaged over the time of the experiment (50 seconds). . . .	149

7.36	Results using the side view analysis for the larger HDPE foil at an angle of attack of 5 degrees, a depth of $5/4$ *chord length at a speed of 0.89 m/s averaged over the time of the experiment (50 seconds). . . .	150
7.37	Results using the side view analysis for the larger HDPE foil at an angle of attack of 5 degrees, a depth of $5/4$ *chord length at a speed of 0.97 m/s averaged over the time of the experiment (50 seconds). . . .	151
7.38	Results using the side view analysis for the larger HDPE foil at an angle of attack of 5 degrees, a depth of $5/4$ *chord length at a speed of 1.06 m/s averaged over the time of the experiment (50 seconds). . . .	152
7.39	Results using the side view analysis for the larger HDPE foil at an angle of attack of 5 degrees, a depth of $5/4$ *chord length at a speed of 1.10 m/s averaged over the time of the experiment (50 seconds). . . .	153
7.40	Results using the side view analysis for the larger HDPE foil at an angle of attack of 5 degrees, a depth of $3/2$ *chord length at a speed of 0.71 m/s averaged over the time of the experiment (50 seconds). . . .	154
7.41	Results using the side view analysis for the larger HDPE foil at an angle of attack of 5 degrees, a depth of $3/2$ *chord length at a speed of 0.80 m/s averaged over the time of the experiment (50 seconds). . . .	155
7.42	Results using the side view analysis for the larger HDPE foil at an angle of attack of 5 degrees, a depth of $3/2$ *chord length at a speed of 0.89 m/s averaged over the time of the experiment (50 seconds). . . .	156

7.43	Results using the side view analysis for the larger HDPE foil at an angle of attack of 5 degrees, a depth of $3/2$ *chord length at a speed of 0.97 m/s averaged over the time of the experiment (50 seconds). . . .	157
7.44	Results using the side view analysis for the larger HDPE foil at an angle of attack of 5 degrees, a depth of $3/2$ *chord length at a speed of 1.06 m/s averaged over the time of the experiment (50 seconds). . . .	158
7.45	Results using the side view analysis for the larger HDPE foil at an angle of attack of 5 degrees, a depth of $3/2$ *chord length at a speed of 1.10 m/s averaged over the time of the experiment (50 seconds). . . .	159

## List of Tables

3.1	Experimental Matrix; with the given flow speeds and depths of the foil there was a range of squared $Fr_d^2$ values between 0.115 and 0.42. . . .	23
6.1	Results of the variability in wave height and wavelengths from the two different experiments for the case with an angle of attack of 10 degrees, a depth of 1*chord length, and with a flow speed of 0.80 m/s. . . . .	83
6.2	Results of the variability in wave height and wavelengths from the two different experiments for the case with an angle of attack 10 degrees, a depth of 1*chord length, and with a flow speed of 0.89 m/s. . . . .	85
6.3	Results of the variability in wave height and wavelengths from the two different experiments for the case with an angle of attack 10 degrees, a depth of 1*chord length, and with a flow speed of 1.10 m/s. . . . .	87
6.4	Results of the variability in wave height and wavelengths from the two different experiments for the case with an angle of attack 10 degrees, a depth of 5/4*chord length, and with a flow speed of 0.80 m/s. . . .	89
6.5	Results of the variability in wave height and wavelengths from the two different experiments for the case with an angle of attack 10 degrees, a depth of 5/4*chord length, and with a flow speed of 0.97 m/s. . . .	91

6.6	Results of the variability in wave height and wavelengths from the two different experiments for the case with an angle of attack 10 degrees, a depth of $5/4$ *chord length, and with a flow speed of 1.10 m/s. . . .	93
6.7	Results of the variability in wave height and wavelengths from the two different experiments for the case with an angle of attack 10 degrees, a depth of $3/2$ *chord length, and with a flow speed of 0.89 m/s. . . .	95
6.8	Results of the variability in wave height and wavelengths from the two different experiments for the case with an angle of attack 10 degrees, a depth of $3/2$ *chord length, and with a flow speed of 1.06 m/s. . . .	97
6.9	Results of the individual wave heights from the average waterline for both angles of attack for the case with a depth of 1*chord length, and with a flow speed of 0.80 m/s. . . . .	99
6.10	Results of the individual wavelengths from the average waterline for both angles of attack for the case with a depth of 1*chord length, and with a flow speed of 0.80 m/s. . . . .	100
6.11	Results of the individual wave heights from the average waterline for both angles of attack for the case with a depth of 1*chord length, and with a flow speed of 1.10 m/s. . . . .	103
6.12	Results of the individual wavelengths from the average waterline for both angles of attack for the case with a depth of 1*chord length, and with a flow speed of 1.10 m/s. . . . .	104

7.1	Results of the variability in wave height and wavelengths from the two different experiments for the case with an angle of attack of 10 degrees, a depth of 1*chord length, and with a flow speed of 0.80 m/s. . . . .	125
7.2	Results of the variability in wave height and wavelengths from the two different experiments for the case with an angle of attack 10 degrees, a depth of 1*chord length, and with a flow speed of 0.89 m/s. . . . .	126
7.3	Results of the variability in wave height and wavelengths from the two different experiments for the case with an angle of attack 10 degrees, a depth of 1*chord length, and with a flow speed of 0.97 m/s. . . . .	127
7.4	Results of the variability in wave height and wavelengths from the two different experiments for the case with an angle of attack 10 degrees, a depth of 1*chord length, and with a flow speed of 1.06 m/s. . . . .	128
7.5	Results of the variability in wave height and wavelengths from the two different experiments for the case with an angle of attack 10 degrees, a depth of 1*chord length, and with a flow speed of 1.10 m/s. . . . .	129
7.6	Results of the variability in wave height and wavelengths from the two different experiments for the case with an angle of attack 10 degrees, a depth of 5/4*chord length, and with a flow speed of 0.80 m/s. . . . .	131
7.7	Results of the variability in wave height and wavelengths from the two different experiments for the case with an angle of attack 10 degrees, a depth of 5/4*chord length, and with a flow speed of 0.89 m/s. . . . .	132

7.8	Results of the variability in wave height and wavelengths from the two different experiments for the case with an angle of attack 10 degrees, a depth of $5/4$ *chord length, and with a flow speed of 0.97 m/s. . . .	133
7.9	Results of the variability in wave height and wavelengths from the two different experiments for the case with an angle of attack 10 degrees, a depth of $5/4$ *chord length, and with a flow speed of 1.06 m/s. . . .	134
7.10	Results of the variability in wave height and wavelengths from the two different experiments for the case with an angle of attack 10 degrees, a depth of $5/4$ *chord length, and with a flow speed of 1.10 m/s. . . .	135
7.11	Results of the variability in wave height and wavelengths from the two different experiments for the case with an angle of attack 10 degrees, a depth of $3/2$ *chord length, and with a flow speed of 0.80 m/s. . . .	137
7.12	Results of the variability in wave height and wavelengths from the two different experiments for the case with an angle of attack 10 degrees, a depth of $3/2$ *chord length, and with a flow speed of 0.89 m/s. . . .	138
7.13	Results of the variability in wave height and wavelengths from the two different experiments for the case with an angle of attack 10 degrees, a depth of $3/2$ *chord length, and with a flow speed of 0.97 m/s. . . .	139
7.14	Results of the variability in wave height and wavelengths from the two different experiments for the case with an angle of attack 10 degrees, a depth of $3/2$ *chord length, and with a flow speed of 1.06 m/s. . . .	140

7.15	Results of the variability in wave height and wavelengths from the two different experiments for the case with an angle of attack 10 degrees, a depth of $3/2$ *chord length, and with a flow speed of 1.10 m/s. . . .	141
7.16	Results of the variability in wave height and wavelengths for the case with an angle of attack 5 degrees, a depth of 1*chord length, and with a flow speed of 0.71 m/s. . . . .	142
7.17	Results of the variability in wave height and wavelengths for the case with an angle of attack 5 degrees, a depth of 1*chord length, and with a flow speed of 0.80 m/s. . . . .	143
7.18	Results of the variability in wave height and wavelengths for the case with an angle of attack 5 degrees, a depth of 1*chord length, and with a flow speed of 0.89 m/s. . . . .	144
7.19	Results of the variability in wave height and wavelengths for the case with an angle of attack 5 degrees, a depth of 1*chord length, and with a flow speed of 0.97 m/s. . . . .	145
7.20	Results of the variability in wave height and wavelengths for the case with an angle of attack 5 degrees, a depth of 1*chord length, and with a flow speed of 1.06 m/s. . . . .	146
7.21	Results of the variability in wave height and wavelengths for the case with an angle of attack 5 degrees, a depth of 1*chord length, and with a flow speed of 1.10 m/s. . . . .	147

7.22	Results of the variability in wave height and wavelengths for the case with an angle of attack 5 degrees, a depth of $5/4$ *chord length, and with a flow speed of 0.71 m/s. . . . .	148
7.23	Results of the variability in wave height and wavelengths for the case with an angle of attack 5 degrees, a depth of $5/4$ *chord length, and with a flow speed of 0.80 m/s. . . . .	149
7.24	Results of the variability in wave height and wavelengths for the case with an angle of attack 5 degrees, a depth of $5/4$ *chord length, and with a flow speed of 0.89 m/s. . . . .	150
7.25	Results of the variability in wave height and wavelengths for the case with an angle of attack 5 degrees, a depth of $5/4$ *chord length, and with a flow speed of 0.97 m/s. . . . .	151
7.26	Results of the variability in wave height and wavelengths for the case with an angle of attack 5 degrees, a depth of $5/4$ *chord length, and with a flow speed of 1.06 m/s. . . . .	152
7.27	Results of the variability in wave height and wavelengths for the case with an angle of attack 5 degrees, a depth of $5/4$ *chord length, and with a flow speed of 1.10 m/s. . . . .	153
7.28	Results of the variability in wave height and wavelengths for the case with an angle of attack 5 degrees, a depth of $3/2$ *chord length, and with a flow speed of 0.71 m/s. . . . .	154

7.29	Results of the variability in wave height and wavelengths for the case with an angle of attack 5 degrees, a depth of $3/2$ *chord length, and with a flow speed of 0.80 m/s. . . . .	155
7.30	Results of the variability in wave height and wavelengths for the case with an angle of attack 5 degrees, a depth of $3/2$ *chord length, and with a flow speed of 0.89 m/s. . . . .	156
7.31	Results of the variability in wave height and wavelengths for the case with an angle of attack 5 degrees, a depth of $3/2$ *chord length, and with a flow speed of 0.97 m/s. . . . .	157
7.32	Results of the variability in wave height and wavelengths for the case with an angle of attack 5 degrees, a depth of $3/2$ *chord length, and with a flow speed of 1.06 m/s. . . . .	158
7.33	Results of the variability in wave height and wavelengths for the case with an angle of attack 5 degrees, a depth of $3/2$ *chord length, and with a flow speed of 1.10 m/s. . . . .	159

## Chapter 1

### Introduction and Motivation for Work

The motivation of this thesis was to collect a set of concurrent free surface wake measurements and force measurements on a submerged foil in a fluid flow. These experiments would help to validate numerical models that aim to predict the wake behind submerged objects that are close to the free surface. The experiments in this research were focused on characterizing the far field wake behind a submerged stationary foil in a fluid flow. The experiments explored in this thesis had three independent variables; 2 angles of attack (5 and 10 degrees), 3 depths of the foil ( $1 \times \text{chord length}$ ,  $5/4 \times \text{chord length}$ , and  $3/2 \times \text{chord length}$ ), and 6 flow speeds (between 0.70 m/s and 1.10 m/s). There were similar experiments performed by Duncan (1981, 1983) in which the free surface profile behind a towed hydrofoil was measured. These experiments were focused on breaking wave characteristics. The experiments from Duncan (1981, 1983) are widely used in the validation of numerical models that incorporate free surface dynamics, however when compared with numerical models, stretching of the wavelengths from Duncan's experiments are observed, so it is thought that optical effects such as parallax and lens distortion may have had an effect on the reported measurements in Duncan, particularly far downstream from the submerged foil. Since this thesis aims to provide a validation data set that can be used for far field valida-

tion of the free surface, the conducted experiments replicate some of the experiments in Duncan with a slightly different experimental setup in order to accommodate for possible lens distortion and parallax effects in the far field measurements. The  $Fr_d^2$  values for these experiments were between 0.115 and 0.42 which were comparable to Duncan's values of  $Fr_d^2$  between 0.19 and 0.53.

There are a variety of different sensors that could be used to measure the forces on the foil in lift and drag in an experimental setup. There were two force sensors that were the basis for two different experimental setups that were attempted in this research. Two 6-axis piezoelectric Kistler 9602 force sensors were intended to be utilized in line with the foil below the surface. This experimental setup was extremely versatile and these force sensors were small and waterproof. These sensors were however uncalibrated and had a large force range more suitable to very large force measurements, which was an issue when measuring smaller forces accurately. The second experimental setup was based around the ATI Industrial Automation Gamma 65-5 6-axis force sensor. This force sensor was not waterproof and therefore the experimental setup had to pierce the free surface which was an issue for concurrent measurement of forces and free surface elevation.

There are a variety of different techniques that could be used to measure the free surface behind the foil in an experimental setup. Several of these techniques were investigated in this thesis. Measuring the surface elevation in an experimental setup is a crucial yet challenging task. For these experiments it was important to capture the surface elevation over a large field of view. There are many methods for capturing

surface elevation, each with unique benefits and drawbacks. In-situ measurement methods such as wave gauges are very accurate, however they not only disrupt the free-surface slightly but also only provide point measurements. Another method is measuring the surface elevations with a mounted GoPro to capture the intersection of the laser sheet, from Stereoscopic Particle Image Velocimetry (SPIV), and the free surface (Schock et al., 2018). This method is again very accurate and has high resolution, however it only captures a short line of the surface elevation and has a relatively narrow field of view.

In light of these options a Digital Image Correlation (DIC) method was chosen initially for the experiments conducted in this thesis. This method enables the capture of a full two-dimensional field of view over a large portion of the tank. Photos were taken from above while utilizing a speckle pattern attached to the bottom of the tank visible to the camera. Then when the surface was deformed the camera captured the distortion of the speckle pattern which can then be compared to a photo of the original speckle pattern through the undisturbed surface. This DIC method has been used for deformation of solid or flexible materials (Triantafillou, 2016) but has been proven effective for measuring surface elevation in water (Moisy et al., 2009).

After the initial testing using the DIC method, there were some issues capturing images at the flow speeds of interest. At higher speeds the flow in the tank became, particularly at the free surface, turbulent which caused issues for capturing a clear image of the distorted speckle pattern at the bottom of the tank. There was clearly substantial ray crossing of the speckle pattern through the free surface which had

small asymmetrical waves which were considered noise in these experiments. With these issues a new method for measuring surface elevation was used for the majority of the results discussed in this thesis. There were 2 cameras mounted next to the wave tank capturing the free surface elevation from the side. Since the goal was to have a uniform flow over a submerged foil the waves produced by the foil were expected to be 2-dimensional across the width of the tank. Since the wave form that was meant to be captured was 2-dimensional, the side view image processing analysis proved to work well for these experiments. This allowed for a quality image of the free surface to be captured at any speed that the flow channel could produce.

## Chapter 2

### Background Information

#### 2.1 Duncan Experiments

Longuet-Higgins (1974) made measurements of the turbulent flow field below whitecaps in order to obtain experimental data on air entrapment. Duncan (1981) was different from past studies in that it investigated the dynamics of unsteady breaking (Duncan, 1981). Using the same experimental technique as Longuet-Higgins (1974), Duncan (1981) studied the breaking waves behind a towed hydrofoil. The hydrofoil was a NACA 012 with a span of 0.61 m, maximum thickness of 0.0254m and chord length of 0.203m. The hydrofoil was moved at a constant speed, depth, and angle of attack in a tow tank (24m by 0.61m by 0.61m). By adjusting these three variables, waves of various lengths and slopes were obtained.

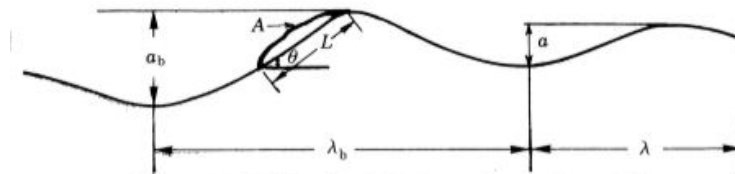


FIGURE 4. Definition sketch for the surface profile variables.

*Figure 2.1: Definition sketch for the surface profile variables (Duncan, 1981).*

Shown in Figure 2.1 is the surface profile behind the foil. Important values denoted in this sketch are the breaking wave amplitude,  $a_b$ , and breaking wavelength,  $\lambda_b$ . The

other parameters related to the breaking wave are the area of the breaking region,  $A$ , the angle of inclination of the breaking region,  $\theta$ , and the length of the breaking region,  $L$ . Free surface elevations were measured using Planar Laser Fluorescence Imaging (PLIF) with a side-viewing camera.

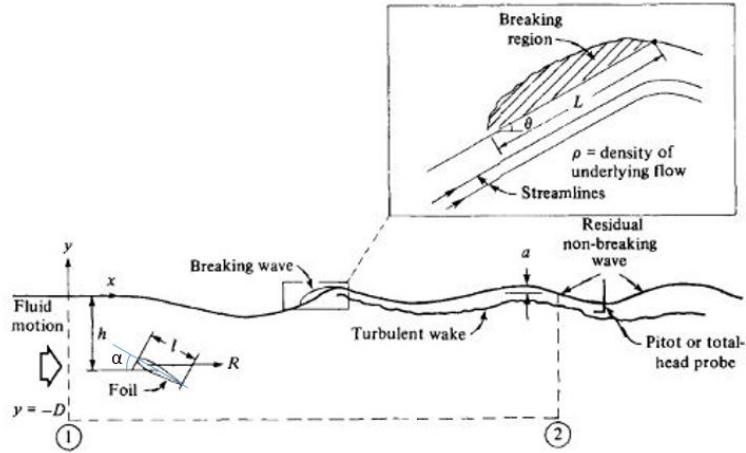


Figure 2.2: Schematic of foil location, breaking wave geometry, and following wave train (Duncan, J. H., 1983).

Shown in Figure 2.2 is a schematic of the surface height profile behind the foil. Key points in the free surface profile are noted such as the location of the breaking wave, and the residual non breaking waves or turbulent wake. The vertical thickness of the wake is the thickness of the breaking region which is denoted in Figure 2.2 as well. In these experiments the surface height profile, the vertical distribution of mean horizontal velocity in the wake, and the vertical thickness of the wake were measured and recorded. The foil was placed at either a 5 or 10 degree angle of attack ( $\alpha$ ), 4 different depths ( $h$ ), and towed at varying speeds. For these parameters, in order to calculate 2 values of theta per wave speed; 5 speeds were chosen for 2 different water

depths and a single angle of attack. There were 12 sets of experimental conditions in which surface profile measurements were recorded.

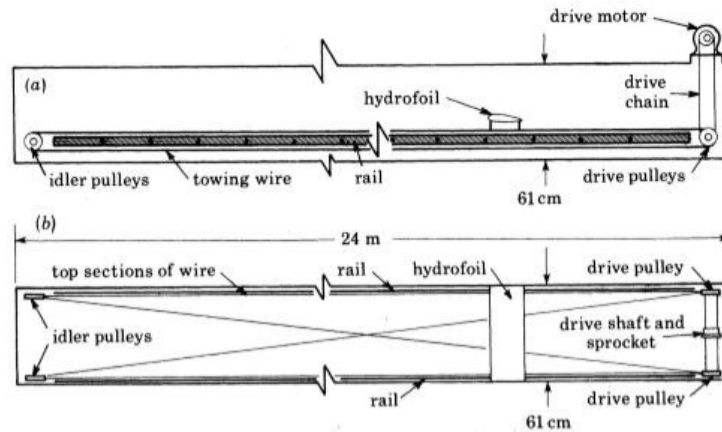


Figure 2.3: Towing tank with hydrofoil and its towing system a) side view b) top view (Duncan, J. H., 1983).

Duncan's first main finding was that the shearing force along the forward slope was equal to the component of its weight in that direction. This force produces a turbulent momentum-deficient wake similar to a towed 2D body in an infinite fluid. The momentum deficit is equal to the maximum momentum flux of a Stokes wave with the same phase speed as the breaking wave. The results from the surface profiles concluded that the independent variables are wave speed and the slope of the breaking wave's forward face. While the experiments from Duncan (1981, 1983) provide motivation for the present study, for far field numerical wave model validation and the experimental techniques used, it was determined that non-breaking waves were of more interest. Therefore, selection of the experimental parameters governing the test matrix of the present study primarily focus on parameters resulting in non-breaking wave conditions, although a few breaking conditions are observed.

## 2.2 Digital Image Correlation

Wave gauges are a common tool for capturing surface elevations however these provide point measurements of the free surface elevation in space and for many applications it is useful to obtain a spatially resolved measurement of the free surface which requires an array of wave gauges. This becomes cumbersome if measurements must be made over large spatial distances. Additionally, since wave gauges must physically penetrate the free surface, they are an intrusive measurement and when implemented as an array, can cause significant disturbance to the free surface being measured. Optical methods offer a good alternative to wave gauges since they are non-intrusive and can provide instantaneous two-dimensional measurements. Using light reflection and refraction is one way to measure free surface elevation with a fairly simple experimental setup.

In optical methods, light shining through a free surface is refracted by the free surface. If one can record how light deforms through the free surface, it is possible to reconstruct the free surface. Digital Image Correlation (DIC) is the basis for many of the methods that have been employed to do this. DIC is a method of measuring displacement over a field of view of a camera. DIC essentially compares two images before and after deformation in order to determine the displacement field. Displacements are determined by correlating the position of pixel subsets in the original and deformed image, usually this is based on contrast. This method is traditionally used to measure the deformation of a material by tracking the deformation of a non-uniform black and white speckle pattern.

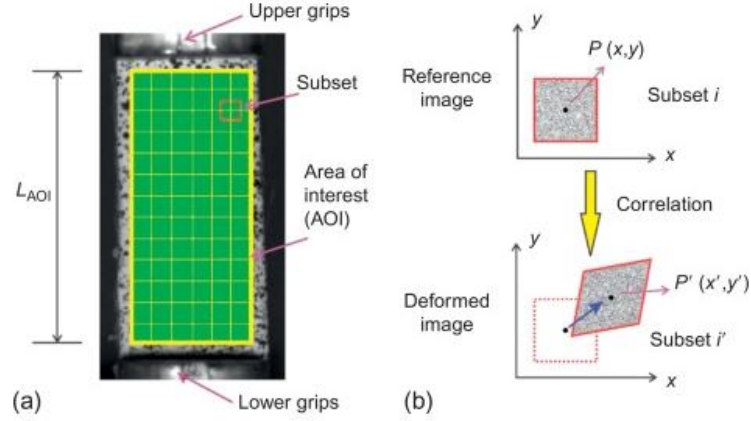


Figure 2.4: a) Area of Interest (AOI) and subset in a reference image; b) schematic presentation of a reference subset before deformation and the corresponding target after subset deformation (Digital, 2016).

The algorithm itself is based upon the calculation of a correlation coefficient that is determined from pixel intensity array subsets on multiple corresponding images and extracting the mapping function that relates the images. As shown in Figure 2.4a, the reference image of the speckle pattern is shown with the area of interest highlighted. The schematic shown in Figure 2.4b depicts how the deformation of the speckle pattern for one set of pixels is related back to the same set of pixels in the reference image in order to determine the displacement of that center point  $P'(x', y')$ . The tracking of subset is conducted using a cross-correlation function. In the present study, two different software options that applied this method were used. For preliminary testing the open source Ncorr was chosen since it used a Matlab GUI operation which made it easy to learn and use. The second software was the DaVis software from LaVision which includes the Particle Image Velocimetry package. This employs the same DIC algorithm as Ncorr however in a PIV application subsequent

images are compared in order to determine an instantaneous speed of the particles as velocity fields (Keane, R.D., 1994). Adjusting this slightly by comparing each image in a run to the reference image allows the PIV package to output displacement fields rather than velocity fields.

### **2.3 Surface Elevation Measurement**

Moisy et al. (2009) did an extensive literature review of surface elevation measurement techniques which informed the surface elevation method choice for this research. The free-surface synthetic Schlieren (FS-SS) method was based on the use of Digital Image Correlation. A displacement field from the DIC algorithm can be used to compute surface elevation.

The method utilized by Kurata et al. (1990) was originally for surface slope measurements however it was extensively applied to measurements in fluids with density variations. For stratification-induced density variations in the geophysical fluid dynamics community the method was commonly called the "synthetic Schlieren" (SS) method. However, in the aerodynamics community with reference to compressible fluids it was referred to as the "Background-Oriented Schlieren" (BOS) method. In any case, the DIC algorithm was used to determine the displacement field and a complete reconstruction of the free surface height using the step-like variation of the refraction index. This was noted by Dalziel et al. (2000) and then successfully implemented by Elwell (2004) when he obtained quantitative measurements of the surface deformation induced by vortices in a shallow water flow.

This FS-SS method from Moisy et al (2009) was a combination of the work done by Kurata et al. (1990) and the quantitative work done by Elwell (2004). The main goal was to measure the surface gradient from the displacement field given by the refracted image of a random pattern using a DIC algorithm. The displacement was then used to reconstruct the surface height by a least-square integration of the surface gradient. This reconstruction was based on a least-square inversion of the gradient operator which was first used by Roesgen et al. (1998) for the hexagonal lattice. Moisy et al. (2009) showed the formulations for a Cartesian lattice which relied on a simpler numerical scheme.

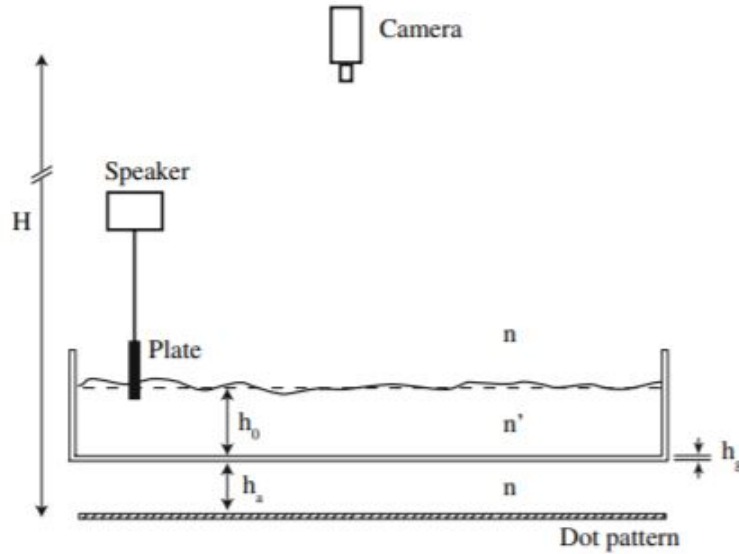


Figure 2.5: Sketch of the experimental set-up with the camera above, not at scale,  $h_0/H \approx 1,000$  (Moisy et al., 2009).

The first thing to note is the configuration of the camera in relation to the dot pattern shown in the figure above. In this configuration with the camera above the surface and the pattern on the bottom of the tank the wave crests act as magnifying

(convex) lenses and the troughs act as reducing (concave) lenses. The initial goal was to determine the optical displacement field,  $\delta\mathbf{r}(x, y)$ , induced by the refraction of the light scattered from a pattern at the bottom of the tank,  $z = 0$ , through the interface at the surface,  $z = h(x, y)$ .

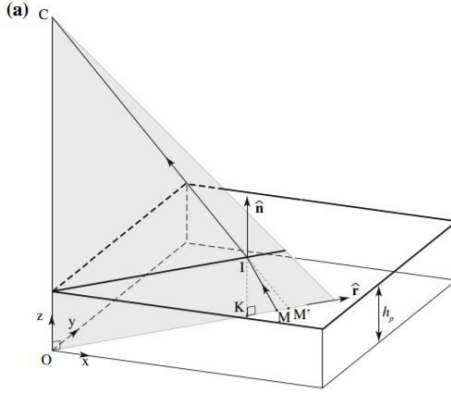


Figure 2.6: Three-dimensional ray geometry for a horizontal interface (Moisy et al., 2009).

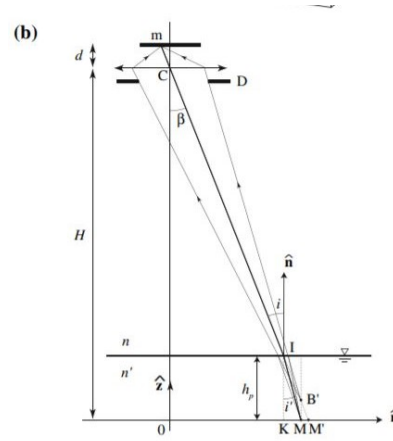


Figure 2.7: Two-dimensional view of the vertical incidence plane COM. (Moisy et al., 2009).

For a flat free surface, as shown in Figures 2.6 and 2.7, the Cartesian frame was used with the vertical optical axis  $z$  crossing the origin  $O$  and the camera  $C$ , the plane  $z=0$  corresponds to the plane in which the pattern is located. In this configuration, a ray coming from a point  $M$  on the pattern appears to come from the virtual object  $B'$  and in the pattern plane, it appears to come from the point  $M'$ . So this can be applied to every dot on the pattern to determine the virtual objects  $M'$  and  $M''$  corresponding to the flat and deformed surfaces, respectively.

For these experiments there were a few assumptions made. The first was that the

surface is assumed to be smooth enough so that the light rays reaching the camera cross the surface only once. Then three approximations were considered;

1. *Paraxial approximation* The pattern-camera distance,  $H$ , is much larger than the field size,  $L$ , yielding a maximum paraxial angle  $\beta_{max} \simeq L/(\sqrt{2}H) \ll 1$ .
2. *Weak slope approximation* The angle  $\gamma$  between the unit vector normal to the interface  $\hat{\mathbf{n}}$  and the vertical vector  $\hat{\mathbf{z}}$  is small. Therefore, the surface slope  $\theta$  measured in the incidence plane is also small.
3. *Weak amplitude approximation* Denoting  $h(x, y) = h_p + \eta(x, y)$  the surface height, the amplitude  $|\eta|$  is small compared to the mean height (still water level)  $h_p$

A linearization with respect to these three parameters was used to derive a relation between displacement,  $M'M'' = \delta\mathbf{r}$ , and the surface gradient  $\nabla h$ .

With these approximations they first consider the refracted image of the pattern through a flat interface as shown in Figures 2.6 and 2.7. In these figures,  $n$  is the refraction index of the air and  $n'$  is the refraction index of the water. The incidence and refracted angles are related by the Snell-Descartes law:

$$n \sin(i) = n' \sin(i') \tag{2.1}$$

For the flat interface the incidence angle is equal to the paraxial angle,  $\beta$ , so the paraxial approximation simplifies to;

$$MM' = \alpha h_p i \hat{\mathbf{r}} \quad (2.2)$$

Therefore, given the still water height,  $h_p$ ,  $\alpha = 1 - n/n'$ , and the location of the optical center O, the location of any point M can be determined from the position of its image M'.

The next step was to consider the refracted image of the pattern through an arbitrary deformed interface. In this case the goal was to determine the new virtual object M'' given object point M. This becomes slightly more complicated since the incidence plane is no longer vertical and does not contain the optical axis z. Now the incidence plane is defined as the plane containing M, the camera C, and the unit vector  $\hat{\mathbf{n}}$  measured at the point I, where the light ray MIC intercepts the interface, with;

$$\hat{\mathbf{n}} = \frac{\hat{\mathbf{z}} - \nabla h}{\sqrt{1 + |\nabla h|^2}} \quad (2.3)$$

Assuming weak slopes,  $|\nabla h|^2 \ll 1$ , therefore;

$$\nabla h = \hat{\mathbf{z}} - \hat{\mathbf{n}} \quad (2.4)$$

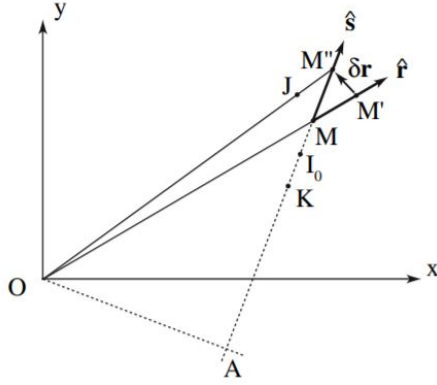


Figure 2.8: Top view of the pattern plane, showing object  $M$  and its two virtual objects  $M'$  and  $M''$  for the flat and deformed interface, respectively. (Moisy et al., 2009).

Shown in Figure 2.8, the displacement  $MM''$  occurs along the direction  $s$ , defined as the intersection of the incidence plane and the horizontal plane  $z=0$ , yielding;  $\hat{s} = \mathbf{OM}/H - \nabla h$ .  $M'M'' = \delta\mathbf{r}$  is the displacement measured by digital image correlation.



$$\nabla h = \frac{\mathbf{OM}''}{H} - i \frac{\mathbf{MM}''}{|\mathbf{MM}''|} \quad (2.6)$$

Figure 2.10 shows the oblique incidence plane CAM, the apparent displacement can then be used to derive the local height of the interface at the vertical of point I, yielding;

$$\mathbf{MM}'' = \alpha h_p i \hat{\mathbf{s}} \quad (2.7)$$

When compared with the still water surface the equation for  $\mathbf{MM}''$  is now along  $\hat{\mathbf{s}}$  rather than  $\hat{\mathbf{r}}$  for the still water case. In practice, the characteristic size of the dots on the pattern is larger than one pixel, therefore any small out of focus effect can be neglected.

Now given Equation 2.7 can be rearranged to define  $i \hat{\mathbf{s}} = \mathbf{MM}'' / \alpha h_p$ , the surface gradient becomes:

$$\nabla h = \frac{\mathbf{OM}''}{H} - i \frac{\mathbf{MM}''}{\alpha h_p} \quad (2.8)$$

Then introducing  $\mathbf{OM}'' = \mathbf{OM}' + \delta \mathbf{r}$  and  $\mathbf{MM}'' = \mathbf{MM}' + \delta \mathbf{r}$ , one can derive:

$$\nabla h = -\delta \mathbf{r} \left( \frac{1}{\alpha h_p} - \frac{1}{H} \right) + \frac{\mathbf{OM}'}{H} - \frac{\mathbf{MM}'}{\alpha h_p} \quad (2.9)$$

Lastly, the last two terms in the above equation cancel because  $\mathbf{MM}' = \alpha h_p i \hat{\mathbf{r}}$  and a simple linear relation between  $\nabla h$  and  $\delta \mathbf{r}$  is derived:

$$\nabla h = -\frac{\delta \mathbf{r}}{h_*} \quad (2.10)$$

with;

$$\frac{1}{h^*} = \left( \frac{1}{\alpha h_p} - \frac{1}{H} \right) > 0 \quad (2.11)$$

This equation shows that, to the first order in paraxial angle, surface slope and relative surface deformation, the displacement  $\delta \mathbf{r}$  is proportional to the surface gradient  $\nabla h$ .

Given that the camera is far above the imaged surface,  $H \gg \alpha h_p$  then the above equation simplifies so that  $h \simeq \alpha h_p$ .

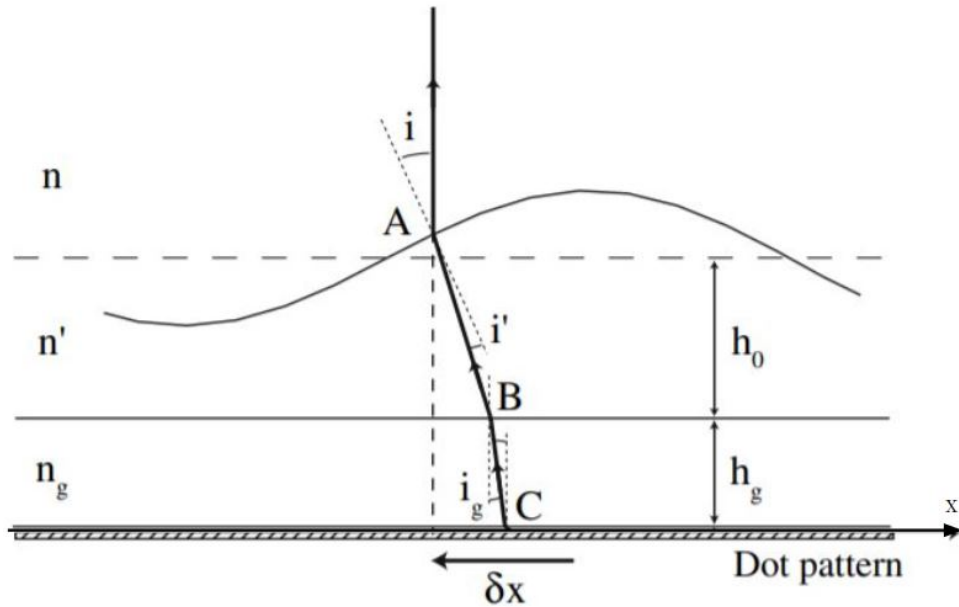


Figure 2.11: Apparent displacement  $\delta x$  when several intermediate materials are inserted between the interface and the pattern, assuming that the camera is far above the surface.

Shown in Figure 2.11 the surface-pattern distance as well as any intermediate materials of various indices, were considered in determining the expected refraction as well as the distance between the pattern and the camera. In this example there is

air above the dashed line, then the liquid between the dashed and solid lines, and a glass plate just above the dot pattern. Given  $h_0$  is the depth of the water,  $h_g$  is the thickness of the glass plate,  $n'$  is the refractive index of water at 20 degrees C,  $n_g$  is the refractive index of plate glass, and  $H$  is the distance from the camera lens to the speckle pattern.

$$h_p = h_0 + h_g \frac{n'}{n_g} \quad (2.12)$$

$$\frac{1}{h^*} = \frac{1}{\alpha h_p} - \frac{1}{H} \quad (2.13)$$

$$\xi_u(i) = u_{cur}(i) * \frac{1}{h^*} \quad (2.14)$$

$$\xi_v(i) = v_{cur}(i) * \frac{1}{h^*} \quad (2.15)$$

Given the assumption that the camera is far above the surface, only vertical light rays can be considered so that the total displacement along the respective  $\hat{\mathbf{x}}$  and  $\hat{\mathbf{y}}$  axes are the sum of the elementary displacements so;

$$\delta x = \left(-h_0 + \frac{n}{n'} h_0 + \frac{n}{n_g} h_g\right) \frac{\partial h}{\partial x} \quad (2.16)$$

$$\delta y = \left(-h_0 + \frac{n}{n'} h_0 + \frac{n}{n_g} h_g\right) \frac{\partial h}{\partial y} \quad (2.17)$$

$$\nabla h = \frac{-\delta r}{h^*} \quad (2.18)$$

This last equation is used to determine the surface elevation by doing an inverse gradient of the displacement ( $\delta r$ ) modulated by  $h^*$ . The Matlab processing scripts developed for implementing this technique to determine the surface gradient from digital image correlation and integrate to determine free surface elevation can be found in Appendices 8.4.1 and 8.4.2.

## Chapter 3

### Experimental Matrix

In the present experiments, a foil is mounted inside a recirculating flume, submerged under the free surface at an angle of attack. Unlike the experiments of Duncan (1981) where the foil was towed through a stationary fluid, the foil in the present study is stationary and experiences a current generated by the flume. One major difference between these scenarios is that the wave train generated in the flume will be largely stationary, allowing measurement of the free surface using fixed camera positions. The recirculating flow channel has dimensions; 130 cm deep, 50 cm wide, and 8 m long. A 5:1 oval cross-section foil was used with a chord length of 0.29845 m, a thickness of 0.06 m, and a span of 0.49 m. With these values the aspect ratio (span/chord length) was about 1.6 and the chord ratio (thickness/chord length) was about 1/5. These non-dimensional values are similar to the foil used by Duncan (1981), but it should be noted that Duncan used a NACA 0012 foil section, which differs from the present experiment in being a slightly thinner foil with fore-aft asymmetry. The same independent variables were changed, the angle of attack, the depth of the foil, and the speed of the flow. The measurements included force measurements, both lift and drag forces on the foil and the surface profile both close to the foil and far from it using a series of wave gauges and image processing.

The test matrix for the experiments consisted of three different depths of the foil, two different angles of attack, and six different flow speeds. The depths were 1\*chord length (0.29845 m) below the surface; 5/4\*chord length (0.3730625 m) below the surface; and 3/2\*chord length (0.447675 m) below the surface. The angles of attack were 5 degrees and 10 degrees. Lastly, the flow speeds varied between 0.71 m/s to 1.10 m/s, corresponding to a  $Fr_d^2$  range of 0.115 to 0.42. This test matrix allowed a limited number of adjustments of the experimental setup while maximizing the number of flow speeds since this was the easiest parameter to adjust. An important parameter for a submerged body near the free surface is the squared Froude number which characterizes the flow in terms of the flow speed, U, depth of the foil, d, and gravity, g.

$$Fr_d^2 = \frac{U^2}{dg} \quad (3.1)$$

A second way to define a Froude value is shown below. This value is in terms of chord length rather than depth of the foil. This will be used later on to compare more directly with results from Duncan (1981).

$$Fr_{cl}^2 = \frac{U^2}{clg} \quad (3.2)$$

In the table below the  $Froude_d^2$  values are shown under columns of  $d^*$  values which is defined below as a function of depth of foil, d and chord length, cl.

$$d^* = d/cl \quad (3.3)$$

It should be noted that this problem is defined by two non-dimensional variables and the third variable is redundant. For example, Froude number based on chord length can be obtained by multiplying the Froude number based on depth by the depth ratio. Reynolds number is an additional non-dimensional parameter for this problem. You should also report the Reynolds number here (based on chord length).

	$d^* = 1$	$d^* = 5/4$	$d^* = 3/2$
<b>current = 0.71 m/s</b>	0.172	0.138	0.115
<b>current = 0.80 m/s</b>	0.219	0.175	0.146
<b>current = 0.89 m/s</b>	0.271	0.216	0.180
<b>current = 0.97 m/s</b>	0.321	0.257	0.214
<b>current = 1.06 m/s</b>	0.384	0.307	0.256
<b>current = 1.10 m/s</b>	0.413	0.331	0.276

*Table 3.1: Experimental Matrix; with the given flow speeds and depths of the foil there was a range of squared  $Fr_d^2$  values between 0.115 and 0.42.*

The Table above shows the experimental matrix in terms of  $Fr_d^2$ . Again this range of  $Fr_d^2$  values was based on attempting to have a similar range to that in the experiments by Duncan in 1981. Duncan's range of  $Fr_d^2$  was between 0.19 and 0.53 which corresponds to the first column of data shown here under depth = cl\*1.

## Chapter 4

### Experimental Design and Force Measurements

#### 4.1 Experimental Design

##### 4.1.1 Force Sensors

There were two force sensors considered in designing an experimental setup to capture lift and drag forces of the foil in a fluid flow. The first was a 3-axis piezoelectric force sensor from Kistler. The Kistler 9602 was small and waterproof which would allow it to be directly attached in line with the foil below the free surface. This sensor was integrated with charge amplifier electronics that allow for measuring dynamic and quasistatic forces. This is a ring sensor so the sensing surface is the circular region that has a hole through it, shown in Figure 4.1. This sensing surface also needed to be preloaded for accurate measurements.



*Figure 4.1: Image of the Kistler type 9602 6-axis piezoelectric force sensor (Kistler, 2016).*

Figure 4.1 shows example configurations of the Kistler sensors used in experiments, however the one used in the present experiments had the wired connection exiting from the casing in the z-direction as noted by the casing coordinate system in the image. The plug orientation of the sensors used was perpendicular to the sensing surface where the coordinates are shown in this image. The total weight of the sensor was about 30 grams.

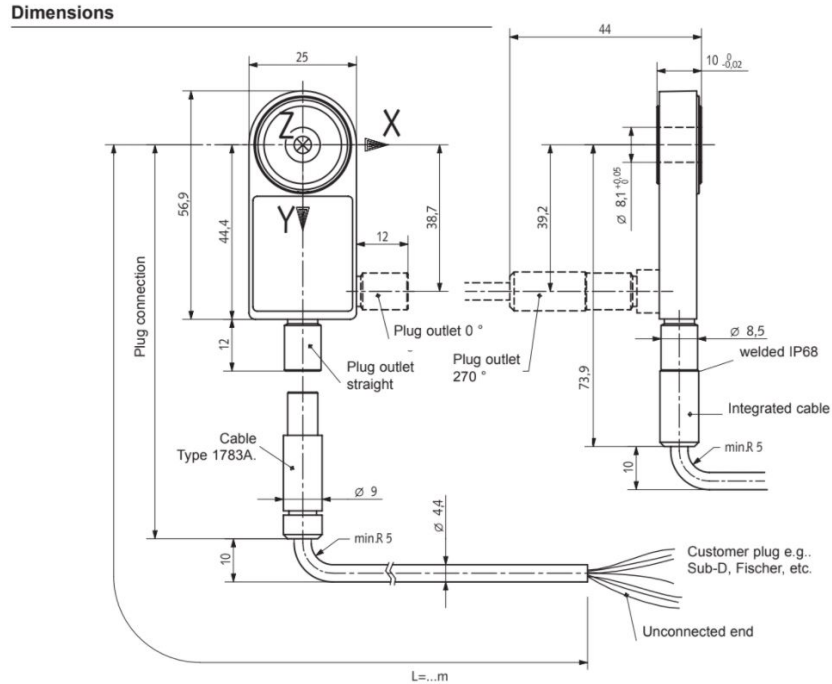


Figure 4.2: Schematic and dimensions of the Kistler type 9602 6-axis piezoelectric force sensor. All dimensions are in millimeters (Kistler, 2016).

Again in the schematic in Figure 4.2 the plug orientation is not the same as for the sensor used in experiments, however this shows the coordinate system of with respect to the sensing surface. The measuring range varied for different directional forces so forces in x and y had a range of -500 to 500 Newtons, but forces in z had a range of -1000 to 1000 Newtons. The sensitivity was also directional so for x and y the sensitivity was 10 mV/N and it was 5 mV/N for forces in the z direction.

### Sensor connector pin allocations

---

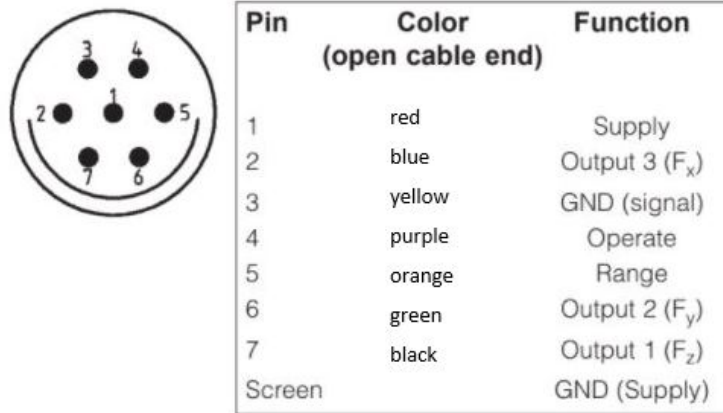


Figure 4.3: Schematic for the pins of the plug for the Kistler type 9602 6-axis piezo-electric force sensor (Kistler, 2016).

In Figure 4.3 the pins for each output and the operation wires are marked. The colors correspond to that of the Kensington Electronics connector wires that were then attached to a data acquisition board.

The second force sensor used in the present experiments was the ATI Gamma SI-65-5 6-axis force sensor. This sensor was not waterproof and therefore could not be mounted below the surface in line with the foil. There was also only one available so this would have to be considered in its attachment design. This sensor was calibrated and its ranges and resolution matched better with the expected forces for this set of experiments.

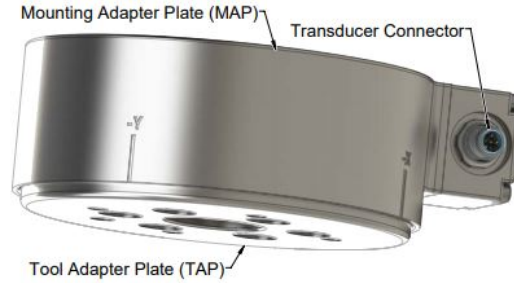


Figure 4.4: Image of the ATI Gamma SI-65-5 6-axis force sensor (ATI, 2000).

The image in Figure 4.4 shows the orientation of the x and y directions in relation to the connector location. The weight of this sensor was 0.255 kg, the diameter was 75.4 mm, and the height or thickness was 33.3 mm. The measuring range varied for different directional forces so forces in x and y had a range of -65 to 65 Newtons, but forces in z had a range of -200 to 200 Newtons. The resolution was also directional so for x and y it was 1/80 N and it was 1/40 N for forces in the z direction.

#### 4.1.2 Resin Foil with Kistler Force Sensors

The initial experimental setup was designed around the Kistler piezoelectric force sensors. These sensors were small enough to be mounted between the foil and the glass tank and were waterproof which would allow them to be submerged underwater and directly connected to the foil. The initial experimental setup was as follows. In order to mount the foil to be stationary within the tank an initial experimental design is shown below in Figure 4.5. The foil was pressure mounted between the glass tank walls with an overall length of 0.422 m. Depicted in Figure 4.5, the foil was an ellipse with a chord length of 0.156 m and a thickness of 0.026 m. The foil itself was 3D printed in resin in three parts as shown in Figure 4.5a. The foil was split into three

parts because of the bed size limitations of the resin printer. This design was meant to be adjustable so that it could expand to fit tightly between the tank walls. This system is also easily adjustable to different depths and angles of attack.

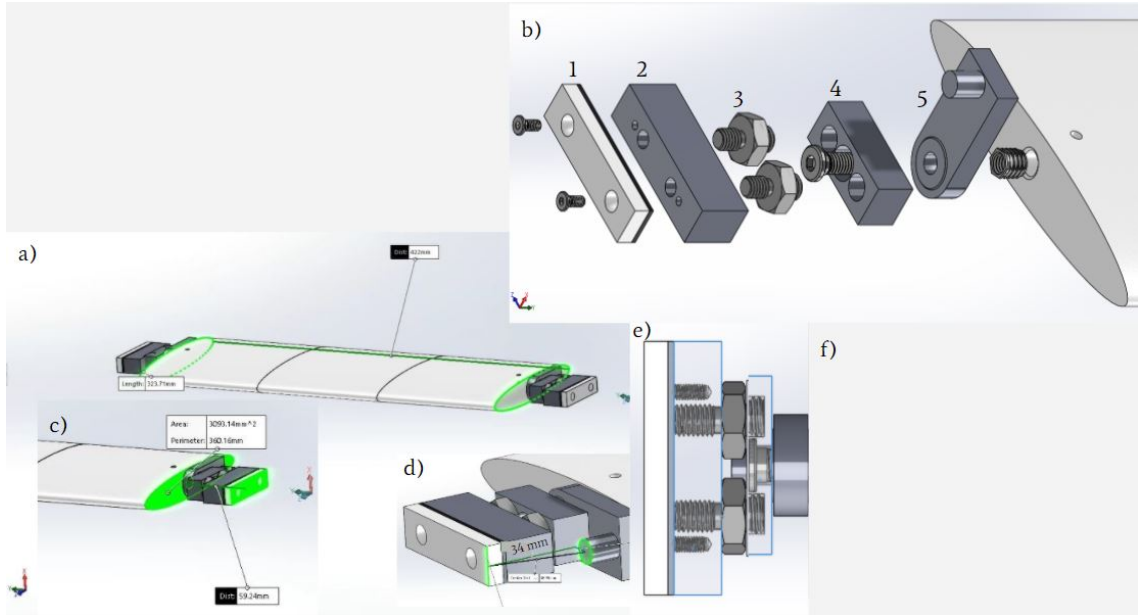


*Figure 4.5: Solidworks model of experimental setup for the pressure fitted system that includes the inline Kistler force sensors.*

In Figure 4.5b, starting from the left is shown the screws that attach the first 2 pieces together. The rectangular piece labeled as 1 on the left in Figure 4.5b was rubber with a metal mounting plate. This piece was be pressed against the glass wall of the tank to secure the system in place. The next rectangular piece labeled 2 was 3D printed in resin and had four threaded holes which can be seen more clearly in Figure 4.5e. The two outer holes were for mounting to the rubber piece and the two inner ones were for the thread adapters. Next, the thread adapters labeled as 3 in the center of Figure 4.5b were used to adjust the length of the system slightly to ensure a secure fit. The

other side of the thread adapters then fit tightly in the holes in the next rectangular piece labeled 4 in Figure 4.5b. This piece was also 3D printed in resin and had a central countersunk hole that tightly fit a screw that secures the system through the Kistler force sensor to the end of the foil. This coupler piece was carefully designed so that its' width covers the sensing surface of the force sensor entirely. The screw which fits through the force sensor in Figure 4.5b was used to tighten the rectangular piece labeled 4 against the force sensor to ensure the proper pretension on the piezoelectric sensing surface. This preloading ensured that the force sensor worked properly since the piezoelectric sensing material requires an initial pretension in order to be able to measure both positive and negative directional forces from the zero load condition. This same system was mirrored on the right side of the foil as well.

The last two important components to note in this design are that the length of the mounting system, shown in Figure 4.5c, was 59 mm and this was the minimized to limit variations along the width of the tank. The Kistler force sensor cable had needed at least 34 mm to bend without any kink in the cable, this distance is shown in Figure 4.5d. This mounting system was also made to be as close to the foil's profile as possible to again minimize the disturbances at the edge of the tank.

#### **4.1.3 Resin Foil with Extended Foil around Mounting System**

The second version of this foil system is shown in Figures 4.6 and 4.7. In this version the mounting system was encased in an extension of the foil that was hollow. This was an important adaption to decrease the disturbance at the edge of the foil, allowing the foil span to extend right up to the edge of the flume.

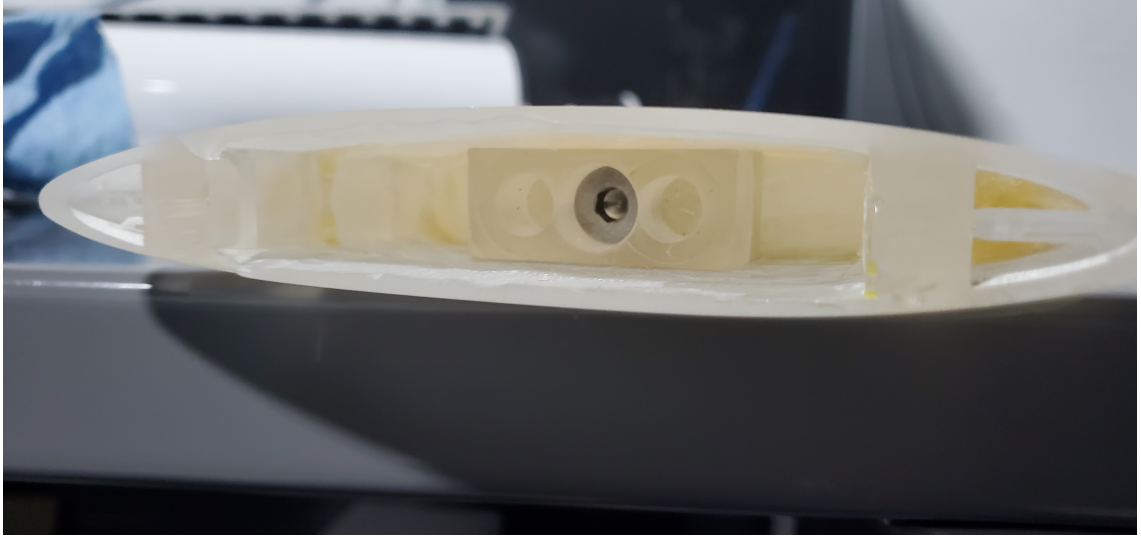


*Figure 4.6: Mounting piece inside the edge of the resin foil without the Kistler force sensor.*

After initial testing with the original design, it was found that the foil was too small to produce a measurable force by the Kistler sensor and background electrical and experimental noise was too large, overwhelming the force measurement. To alleviate this, a large foil with a shroud over the Kistler sensors was designed. After further interrogation it was determined that the force sensor was not sensitive enough to be used for this experimental setup. Essentially the sensor was meant for much larger forces than this foil would experience in the flow so the noise in the system was on the same order as the intended forces measurements. There were a few things we could have done to mitigate the noise and to stabilize the system further but since the disturbance around the edge was the first issue of concern this was addressed first. Therefore this version with the shroud was then used without the Kistler force sensors.

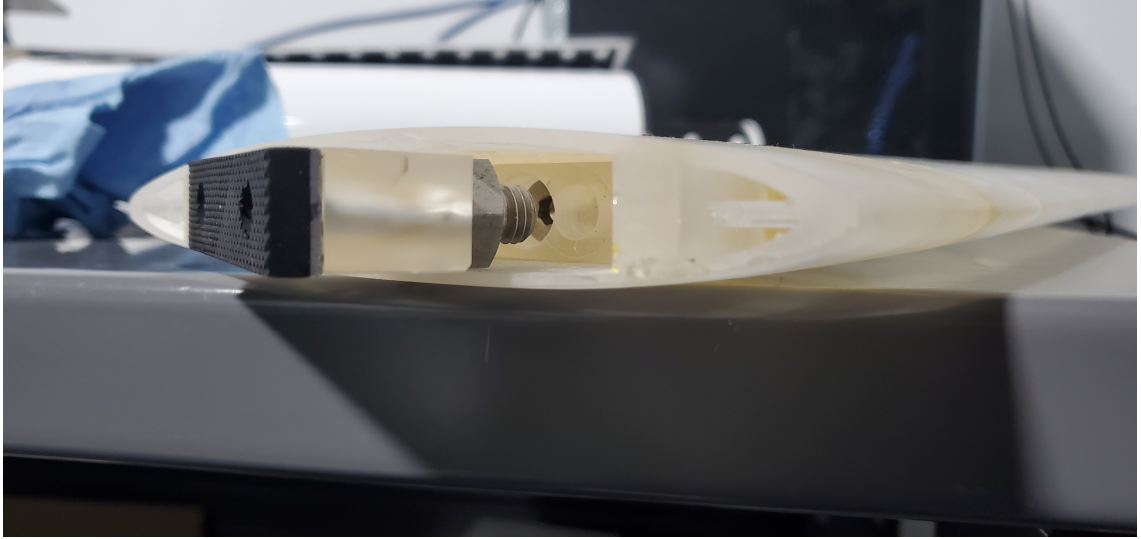


*Figure 4.7: Mounting system for the resin foil without the Kistler force sensor.*

After this change with the system, there was another issue with the fact that the foil was fairly small so the disturbance and thus the waves it would create at the free surface were small as well. The waves created were on the same order as turbulence created by the flow channel system. This issue could be solved fairly easily by increasing the size of the foil so that the free surface variation that was of interest would be substantially larger than the turbulence in the system.

The other reason behind removing the Kistler force sensors from the system was that these sensors were uncalibrated so calibration with a second force sensor was necessary. An alternative option was the ATI Gamma 65-5 6-axis force sensor. This force sensor however could not be mounted in line with the foil since it had a larger profile than the foil. The best way to mount a foil to this force sensor would be to center it above the foil and attach it rigidly with fairings on either edge of the foil. This setup was not ideal, since in order to connect the sensor to the foil, fairings

needed to pass through the free surface, which would inevitably cause an unwanted disturbance at the free surface.

#### **4.1.4 HDPE Foil with ATI Force Sensor**

One issue when increasing the size of the foil was that the resin printer could not make a foil any larger. Thus new considerations were needed to decide which material to make the foil with. The first goal was to have the foil made out of fewer pieces since smoothing the last foil was challenging and time consuming. The second consideration was weight, since the new system was going to be hanging off of the ATI force sensor. With these things in mind a High Density Poly Ethylene (HDPE) material was chosen because it could be put in a computer numerical control (CNC) router machine that would shape the foil. This material was also unique because it is neutrally buoyant which means it would minimize the force of the foil hanging on the ATI force sensor. Using the CNC router machine also poses a challenge for creating the foil shape. The best way to produce the shape was to create the top and bottom halves that could be glued and then secured with nuts and bolts.

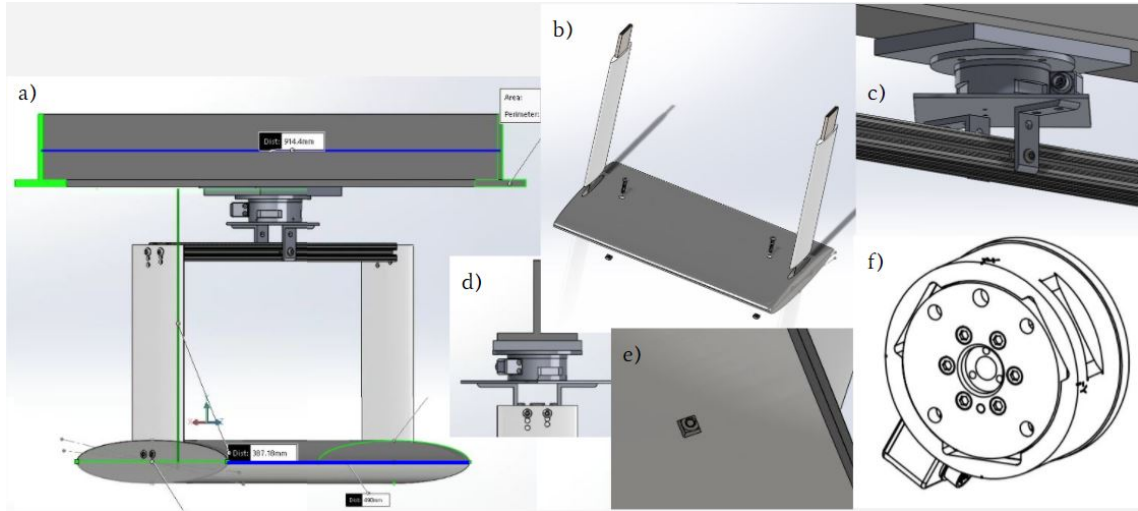


*Figure 4.8: Mounting system and attachment for the foil with the ATI force sensor experimental setup.*

In Figure 4.8a the full experimental setup is shown. The span of this foil was 0.49 m which was close to the full width of the tank to reduce any inconsistency in the flow around the edges of the foil. The chord length of the foil was about 0.3 m and the thickness was 0.06 m. The two pieces of the foil were secured with marine grade epoxy and nuts and bolts as shown in Figure 4.8b and Figure 4.8e. The fairings which are shown in Figure 4.8a and Figure 4.8b were made of HDPE as well and were also made with a gap in the middle that would fit a 304 Stainless Steel Bar that was 1/4 inch thick, 2 inches wide, and 12 inches long. This was chosen to ensure a rigid connection between the force sensor system and the foil. It was important to ensure that any forces on the foil were transferred to the force sensor which ensures that what was measured was the full lift and drag forces on the foil. The challenge with this system was creating it in a way that would allow adjustment of the foil to be a different depths and angles of attack. Changing the angle of attack was done by

placing 2 holes along that angle at the top of the fairing as shown in Figure 4.8d where the top set of holes held the foil at a 0 degrees angle of attack the next 2 down held the foil at 5 degrees angle of attack and the bottom two held the foil at 10 degrees angle of attack. The depth of the foil was adjusted by moving the entire system. The t-bar at the top of the system was mounted to the top of the tank sides. This can be moved up and down by placing spacers under the t-bar to to move the system up in the water column. The ATI force sensor was attached to the t-bar above it with a mounting plate, shown in Figure 4.8c. Then a mounting plate attached below the force sensor was attached to brackets that attach to the solid double t-slotted framing also shown in Figure 4.8c. The holes at either edge of the double t-slotted framing were tapped so that the fairings on either edge could be attached with bolts. The foil also had slots for the fairings to fit tightly into the foil to reduce any cavitation on top of the foil. This mounting system allows a low profile way of attaching the foil to the fairing by bolting through the side of the foil through the fairing and into a thread insert inside the foil.

This foil system worked well to capture force sensor data and wave gauge data was collected along side it however the surface elevation data was substantially affected by the fairings. In an attempt to capture clean surface elevation data the foil mounting system was adjusted once again.

#### **4.1.5 HDPE Foil with Rubber Edges**

With this iteration the system was simplified by removing all rigid mounting and returning to the system as a press fitted system between the tank walls. This larger

foil's span was already almost the width of the flow channel so some neoprene rubber that was 1/8 inches thick was purchased. This rubber was cut to the shape of the edges of the foil with some holes in it that would allow it to be attached to the foil in a similar manner to the fairings.



*Figure 4.9: Mounting system for the HDPE foil by itself.*

This system shown in Figure 4.9 was extremely versatile, it could be placed at any depth or angle of attack easily and stayed firmly in place during all testing. This system also allowed for an extremely clean wake behind the foil that was uniform across the width of the tank.

## **4.2 Conclusions and Future Work**

The two force sensor systems had significant issues however the both could be useful in concert. In future work the Kistler force sensor could prove to be sensitive enough for a larger foil if the expected forces were large enough. The ATI force sensor experimental setup had significant issues in interfering with the free surface however

for capturing force measurements by themselves this system worked. In future work the force measurements that were captured should be post-processed and compared to expected results from numerical models. In future work measuring the force on the fairings by themselves would also help to calibrate the force measurement system. This would be useful to calibrate the force results from the entire system to get a more accurate measurement. The HDPE material being neutrally buoyant proved very useful when being attached to the ATI force sensor as well as for ease of adjusting the experimental setup. The experimental setup which utilized the HDPE foil with rubber edges proved to be the best for cleanly capturing the free surface elevation behind the submerged foil.

## Chapter 5

### Digital Image Correlation

#### 5.1 Testing in the Small Aquarium

##### 5.1.1 Preliminary Test Setup

The following items were used in this experimental setup:

- Small fish tank
- Speckle pattern sheet
- Tripods with phone cameras: Samsung s10e–16 MP and Motorola Z4–48 MP
- Wave maker (license plate)



*Figure 5.1: Image of the tank lit from below so as to avoid any glare on the free surface.*

The experimental setup is shown above with the speckle pattern taped on the bottom of the tank with 4.25 inches of water in the tank. The bottom of the tank had a glass thickness of 0.13 inches. Lastly the camera capturing images of the speckle pattern was placed 38 inches above the speckle pattern. The refractive index of plate glass used was 1.52 and the refractive index of water at 20 degrees C was 1.33. The photo above also shows the lighting from below the speckle pattern which helped to eliminate any glare from lighting on the free surface.

### **5.1.2 Horizontal Displacement Test**

For this test the goal was just to verify an expected result from the DIC analysis. This was achieved by moving the speckle pattern a measured distance and then running those images through the DIC analysis to compare with the displacement values.



*Figure 5.2: Tank location for the displacement test, red corners, orange corners, and black corners.*

For these tests the three locations were measured by hand to then compare to the displacement results from the analysis. The distance between the orange and black marks was measured to be 0.40625 ( $13/32$ ) inches. The distance between the red and black marks was measured to be 0.96875 ( $31/32$ ) inches.



*Figure 5.3: Tank in the orange location for the displacement test.*

For this test the reference image selected was the tank at the black marked location and then this image was compared to the tank at the orange and red marked locations. This movement was expected to be shown in the positive  $u$  direction. Again, this test was meant to verify that the displacement algorithm worked as expected. For this case the small aquarium was not filled with water and the tank was simply displaced left and right a known distance and then the DIC analysis was run to compare with a known displacement value.



Figure 5.4: This is the tank located between the black markings, chosen as the zero position.

The image above was compared to itself first in order to verify that no displacement of the speckle pattern would be reflected in the results of the DIC analysis. In the following figures the results from the DIC analysis are shown all together. The figure in the top left is the displacement in  $x$ , the middle left is the displacement in  $y$ , the bottom left is the surface elevation,

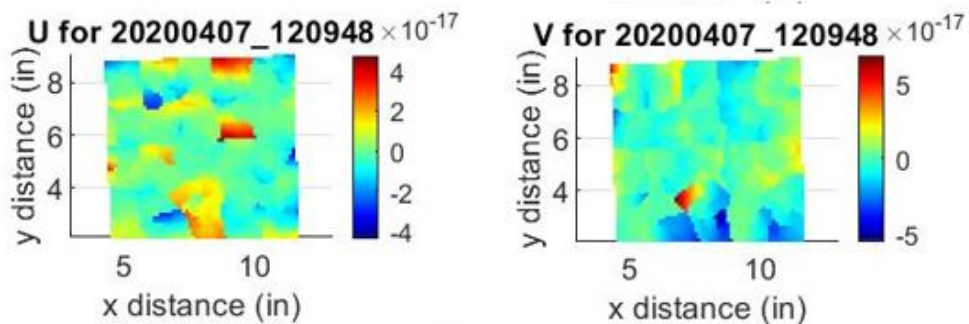


Figure 5.5: Results for displacement in  $x$  (left) and displacement in  $y$  (right) of the DIC analysis without any physical displacement of the tank. All units are in inches.

In Figure 5.5 it is clear that the displacements in x (U) and y (V) are extremely small, with the scales on both being  $10^{-17}$  inches.



Figure 5.6: This is the tank located between the black markings, chosen as the zero position.

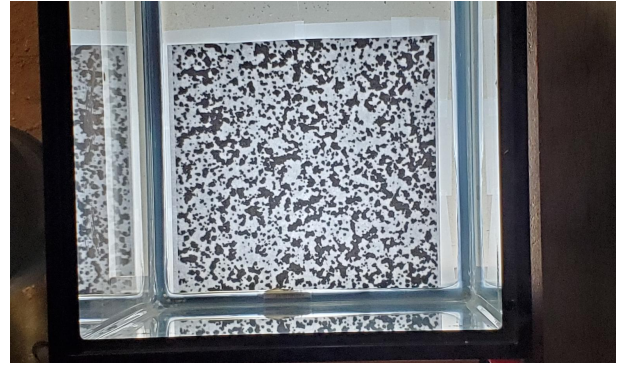


Figure 5.7: This is the tank located between the orange markings, chosen as first position.

The figures above compare the 0 position, Figure 5.6 to the first position, Figure 5.6. The second figure shows the speckle pattern displaced 0.40625 inches in the positive x direction, so this value is expected to be reflected in the DIC analysis results.

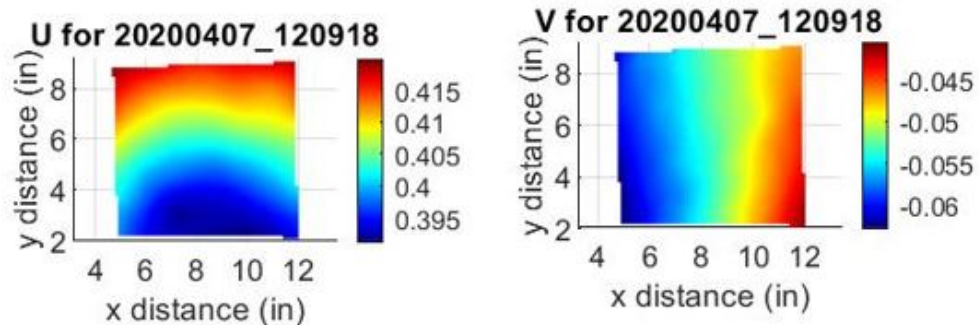


Figure 5.8: Results for displacement in x (left) and displacement in y (right) of the DIC analysis with the pattern moved 0.40625 inches. All units are in inches.

The main result of interest, shown in Figure 5.8, is the displacement in x (U) and it

is clear that over the entire area of analysis the  $u$  displacement values are between 0.395 and 0.415 inches. This corresponds well to the expected 0.40625 inches. The displacement in  $y$  ( $V$ ) values range from -0.06 to -0.045 which are fairly close to zero. The fact that the values are not exactly zero is likely due to the fact that the speckle pattern was moved by hand and it is possible it could have been shifted slightly in the  $y$  direction.



*Figure 5.9: This is the tank located between the black markings, chosen as the zero position.*



*Figure 5.10: This is the tank located between the red markings, chosen as second position.*

The figures above compare the 0 position, Figure 5.9 to the first position, Figure 5.9. The second figure shows the speck pattern displaced 0.96875 inches in the positive  $x$  direction, so this value is expected to be reflected in the DIC analysis results.

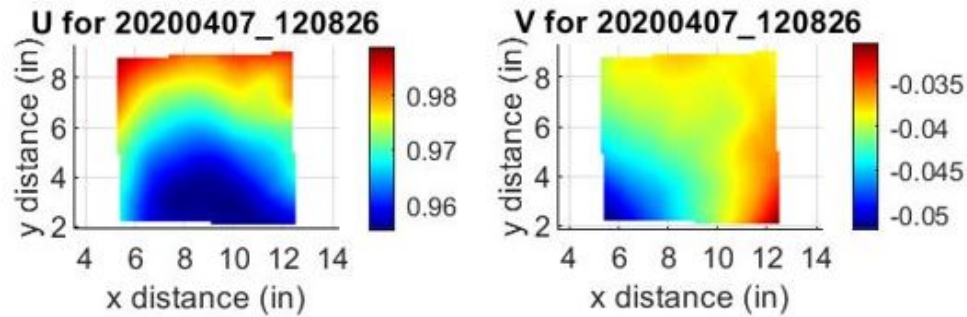


Figure 5.11: Results for displacement in  $x$  (left) and displacement in  $y$  (right) of the DIC analysis with the pattern moved 0.96875 inches. All units are in inches.

The main result again, shown in Figure 5.11, is the displacement in  $x$  ( $U$ ) and it is clear that over the entire area of analysis the  $u$  displacement values are between 0.96 and 0.98 inches. This corresponds well to the expected 0.96875 inches. The displacement in  $y$  ( $V$ ) values range from -0.05 to -0.035 which are fairly close to zero. The fact that the values are not exactly zero is again likely due to the fact that the speckle pattern was moved by hand.

### 5.1.3 Slow Motion Video Analysis with Waves

The main objective in this test was to capture images of waves in a small tank in order to perform DIC analysis on a series of images. This was done by again having a speckle pattern on the bottom of the tank now with a slow motion camera above that could capture any wave motions. A second camera was taking a slow motion video of the waterline from the side of the tank. This second video was taken to have a visualization and a way to estimate the surface elevation at the edge of the tank.

Once the videos were both rolling for a couple seconds a license plate was used as

a wave maker to create waves on the far side of the tank that traveled over the speckle pattern. The main goal here was to create small waves and avoid creating any turbulence or bubbles which are likely to affect the speckle pattern and give incorrect results. It was important to keep the camera system setup completely stationary with reference to the tank and speckle pattern for both of the videos.

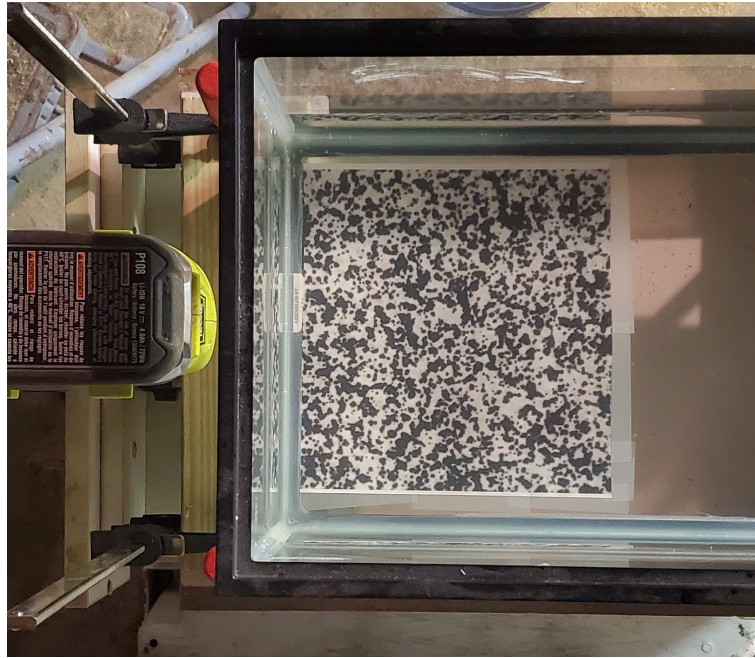


*Figure 5.12: An example photo of the experimental setup from the Samsung phone camera with lighting from below off.*

In Figure 5.12, the tank is shown from above with the speckle pattern. The gray towel at the right was used to have a uniform background for the second camera setup (not shown in this photo). The second camera setup was placed on the left side of this photo close to the tank and perpendicular to the waterline. Its view point is shown in the Figure 5.13.



*Figure 5.13: This is an image from the camera facing the waterline.*

This camera angle was intended to get an idea of the surface elevation so a ruler was taped to the side of the tank for reference. This image illuminates the waterline along the tank wall very clearly as well as the ruler taped to the side of the tank for reference. The still water level was at the 2 inch mark so the waves in this photo can be estimated from based on starting measurement.

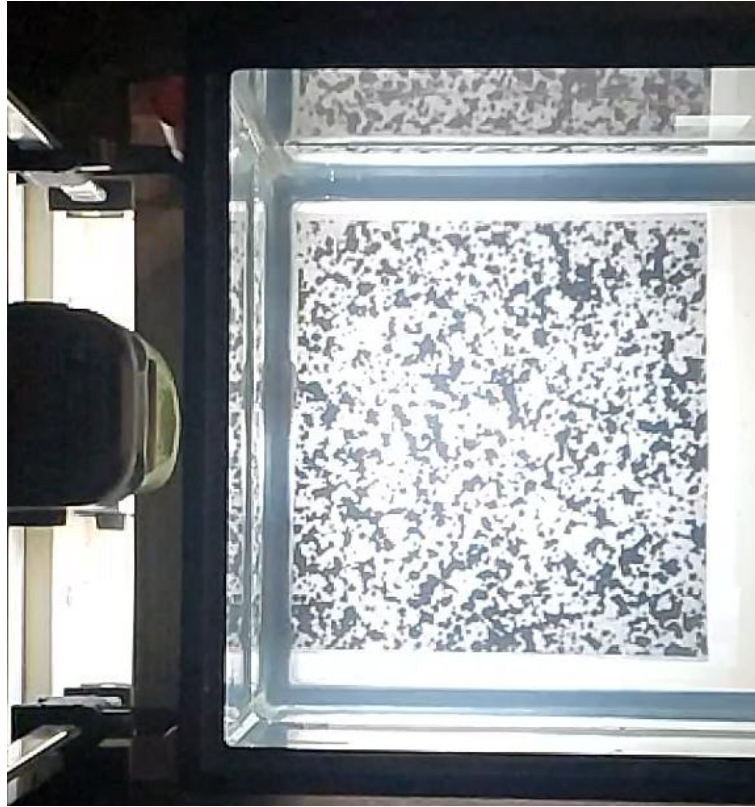


*Figure 5.14: Image of the tank lit from below so as to avoid any glare on the free surface.*

Figure 5.14 above was chosen as the reference frame after being cropped from the slow motion video taken on the camera above the tank before it was used in the DIC analysis. The other frames from the video were all compared to this frame of the speckle pattern with only still water over it.

For this analysis a slow motion video was taken from above the tank. The frames of the video with waves present were compared to frames at the beginning of the video in which the water was still. The "Original" frame is constant throughout and is the 6400th frame which was when the water was still and the "current" frame corresponds to the same time step as the waterline frame. Then the outputs from the

DIC analysis were  $U$  which is the displacement in  $x$ ,  $V$  which is the displacement in  $y$ , and  $\eta$  which is surface elevation. The orientation of the images is the same as the orientation of the output figures and the waterline image matches the bottom edge of the figures closest to  $y = 2.5$  in. There are color bars along the side of each figure that correspond to each figure with the units of inches. The other comparison that will be shown below is the waterline video with the corresponding data along that bottom edge from the surface elevation calculation field of view from the appropriate time step.

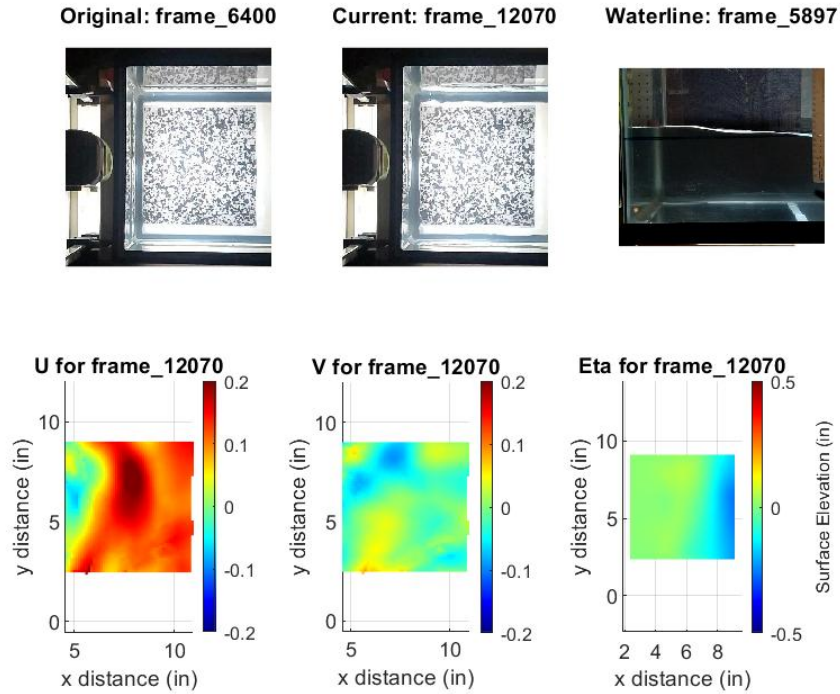
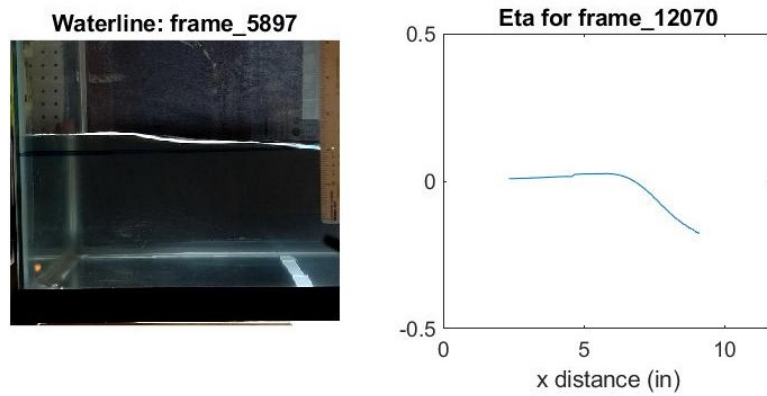


Figure 5.15: Results of the DIC analysis for frame 12070, in the top left frame is the reference image, the top middle is the current time frame image, the top right is the waterline frame from the same time step. Then the bottom left shows  $u$  displacement, the bottom middle shows  $v$  displacement, and the bottom right shows surface elevation ( $\eta$ ) (All units shown in the output figures are in inches).

In order to verify qualitatively that this analysis works a few time steps were selected for analysis. The first time step chosen is shown in Figure 5.15 there is a relatively consistent displacement in  $x$  along the right edge of the frame which seems to result in a depression of the surface elevation ( $\eta$ ) along that edge as well.



*Figure 5.16: Results of the DIC analysis for frame 12070, comparing the waterline video to the surface elevation at that location. The frame on the left is an image of the surface elevation and the figure on the right is the data closest to the tank wall on this side (All units are in inches).*

In Figure 5.16 the waterline video was compared to the corresponding data along that edge of the tank. The trend of the surface elevation follows what can be seen in this frame of the video. The dip in surface elevation at the right edge of the tank is reflected clearly in the DIC surface elevation results.

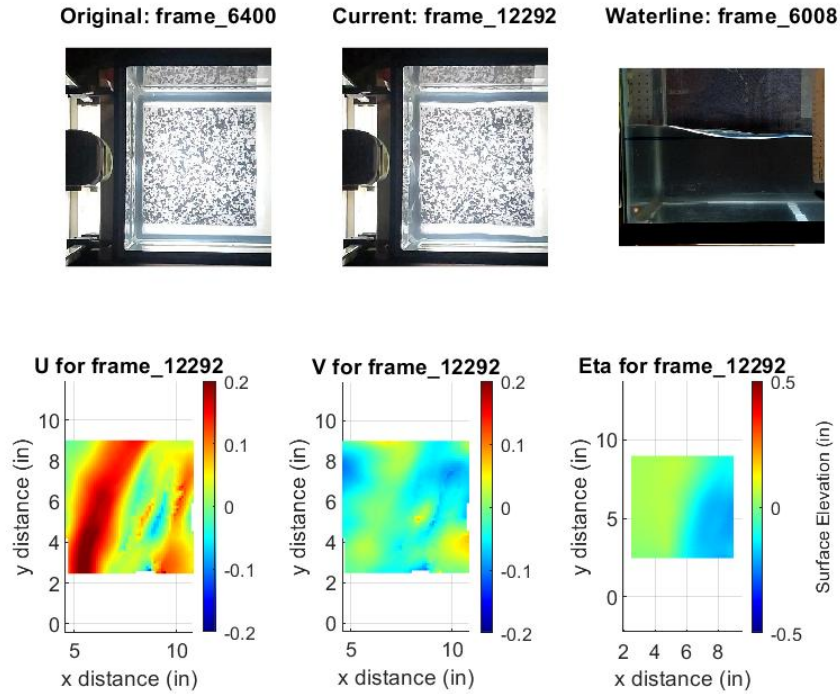
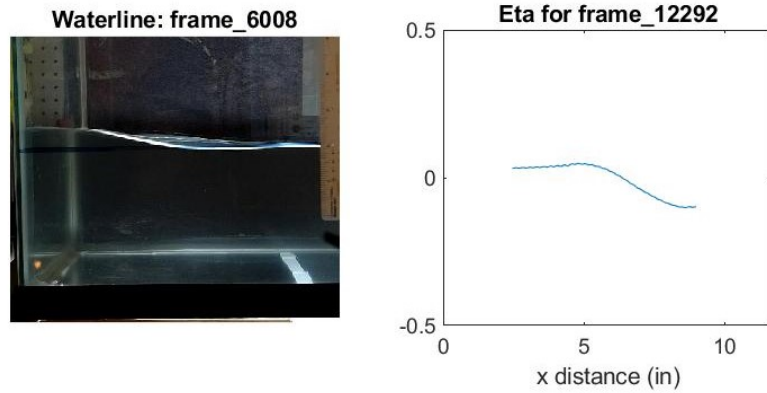


Figure 5.17: Results of the DIC analysis for frame 12292, in the top left frame is the reference image, the top middle is the current time frame image, the top right is the waterline frame from the same time step. Then the bottom left shows  $u$  displacement, the bottom middle shows  $v$  displacement, and the bottom right shows surface elevation ( $\eta$ ) (All units shown in the output figures are in inches).

The third time step chosen is shown in Figure 5.17 there is large displacement in both  $x$  and  $y$  over most of the left half of the frame which seems to result in a small surge of the surface elevation ( $\eta$ ) over that half as well. Then there is a clear dip in surface elevation at the right edge of the frame.



*Figure 5.18: Results of the DIC analysis for frame 12292, comparing the waterline video to the surface elevation at that location. The frame on the left is an image of the surface elevation and the figure on the right is the data closest to the tank wall on this side (All units are in inches).*

In Figure 5.18 the waterline video was again compared to the corresponding data along that edge of the tank. The trend of the surface elevation follows what can be seen in the video very closely. The slight increase in surface elevation over the left half of the tank followed by a clear dip is reflected clearly in the DIC results. The waterline video does seem to have a small increase again further to the right but very close to the edge of the tank was not captured by the DIC analysis since the speckle pattern does not reach all the way to the edges.

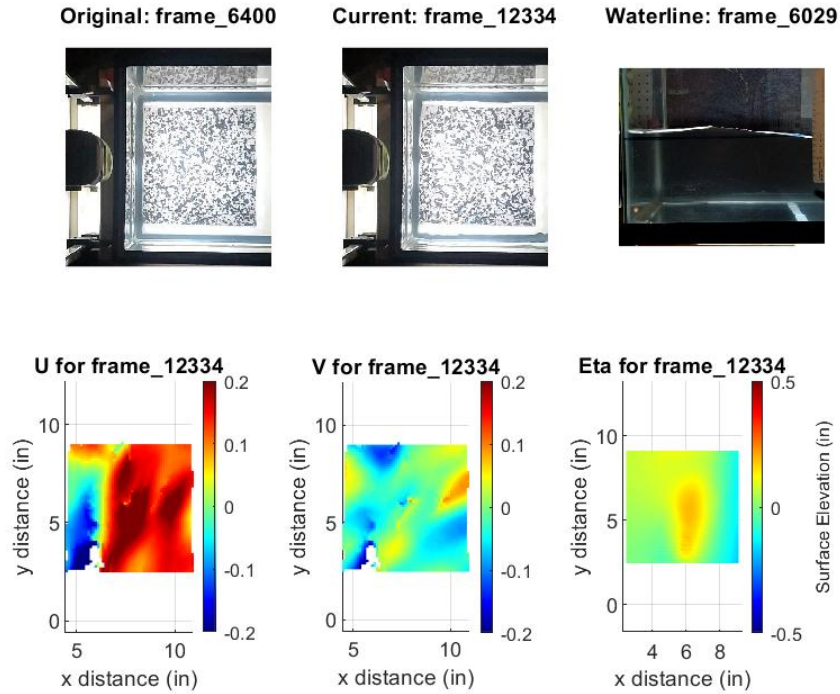


Figure 5.19: Results of the DIC analysis for frame 12334, in the top left frame is the reference image, the top middle is the current time frame image, the top right is the waterline frame from the same time step. Then the bottom left shows  $u$  displacement, the bottom middle shows  $v$  displacement, and the bottom right shows surface elevation ( $\eta$ ) (All units shown in the output figures are in inches).

The fourth time step chosen is shown in Figure 5.19 there is large displacement in  $x$  in the center of the frame which seems to result in a surge of the surface elevation ( $\eta$ ) over that area as well. Then there is a small dip in surface elevation at the right edge of the frame.

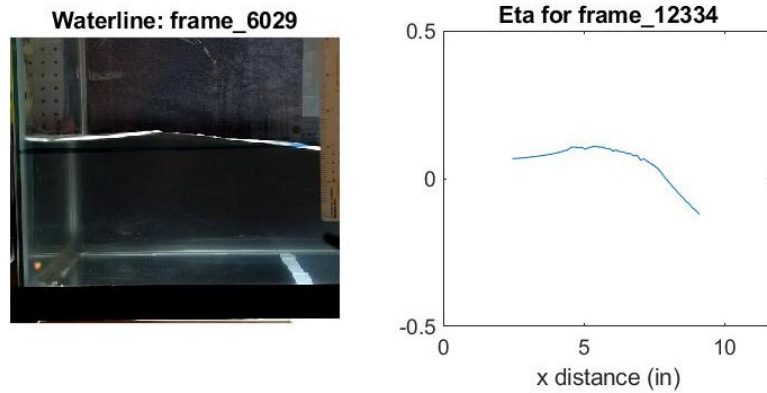


Figure 5.20: Results of the DIC analysis for frame 12334, comparing the waterline video to the surface elevation at that location. The frame on the left is an image of the surface elevation and the figure on the right is the data closest to the tank wall on this side (All units are in inches).

In Figure 5.20 the waterline video was again compared to the corresponding data along that edge of the tank. The trend of the surface elevation follows what can be seen in the video very closely. The clear increase in surface elevation in the center of the frame followed by a dip is reflected clearly in the DIC results.

## 5.2 Testing in the Flow Channel

### 5.2.1 Preliminary Test Setup

The following items were used in this experimental setup:

- Wave and Current Flume: Edinburgh Designs
  - Total length: 8 m
  - Length of experimental area: 2.44 m

- Width: 0.05 m
  - Height: 1.3 m
- Speckle pattern
  - Length: 0.91 m
  - Width: 0.3048 m
  - Diameter of Speckles: 0.01 m
- Phantom Camera: VEO-E340-L
- Edinburgh Proprietary Wave and Current software
- Edinburgh Resistance Wave Gauges: WG8USB
- Electromagnetic Current Meter
- Ncorr: Digital Image Correlation Software
- DaVis: Particle Image Velocimetry Software
- Matlab: For post-processing and plotting

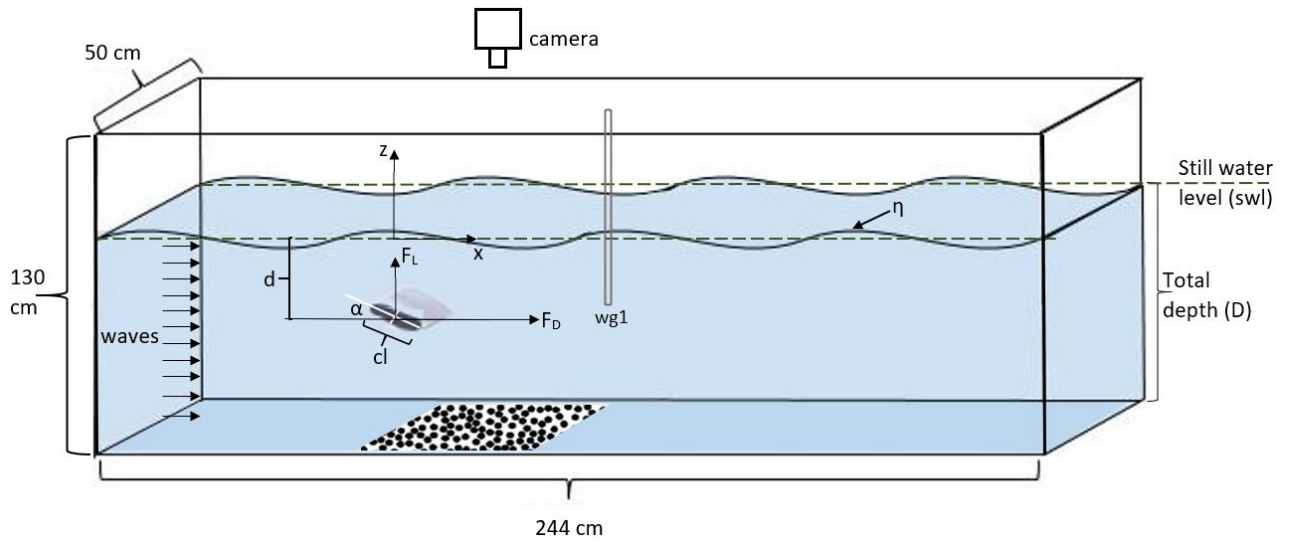


Figure 5.21: This shows the experimental setup as a schematic with the camera over the flow channel.

The schematic above in Figure 5.21 shows the orientation of the camera with respect to the wave tank. The speckle pattern shown is mounted underneath the bottom glass of the tank. The foil shown above was put in place for later testing however, for the preliminary DIC testing the foil was not placed in the tank yet. The first goal was to verify that the DIC analysis would be able to resolve a periodic wave sent down the length of the tank and then this data could be compared to wave gauge data. The wave maker parameters were set to an amplitude of 0.02 m and a frequency of 1 Hz.

### 5.2.2 Camera Mounting Setup



*Figure 5.22: The experimental setup of the camera over the flow channel.*

As show in Figure 5.22 the camera was mounted above the tank. The wave gauge was also placed just over the edge of the speckle pattern so that it could be directly related to a location on the speckle pattern. With this in mind, the DIC analysis outputs a surface elevation over the speckle pattern area. In order to compare with the wave gauge at a single spatial location over the time history, two methods were

attempted. The first extracted the surface elevation value only at the point where the wave gauge was and the second assumed a uniform wave over the width of the tank and the average value of the surface elevation over the width was used to get a single value for each time step.



*Figure 5.23: The experimental setup camera's view from above the tank of the speckle pattern mounted underneath the flow channel.*

As shown in Figure 5.23 the camera is facing down towards the speckle pattern that is mounted beneath the tank. The DIC analysis required a reference picture of the speckle pattern through the still water. This image is then used to compare with

the distorted images of the speckle pattern which were caused by the waves which create a curved free surface. The camera took a video at 60 frames per second for 50 seconds. There were a few important measurements when utilizing this test setup that were necessary to execute the DIC analysis. The first was the distance from the camera lens to the speckle pattern which was 1.67 m and then the depth of the water which was 1.016 m and the last was a known length within the speckle pattern plane. This was the width of the speckle pattern shown on the bottom of the tank which was 0.3048 m. The speckle pattern itself covered an area on the bottom of the tank of 0.6096 m by 0.3048 m and the speckles had a diameter of 0.00508 m with randomized spacing.

### 5.2.3 Periodic Wave Test Without the Foil

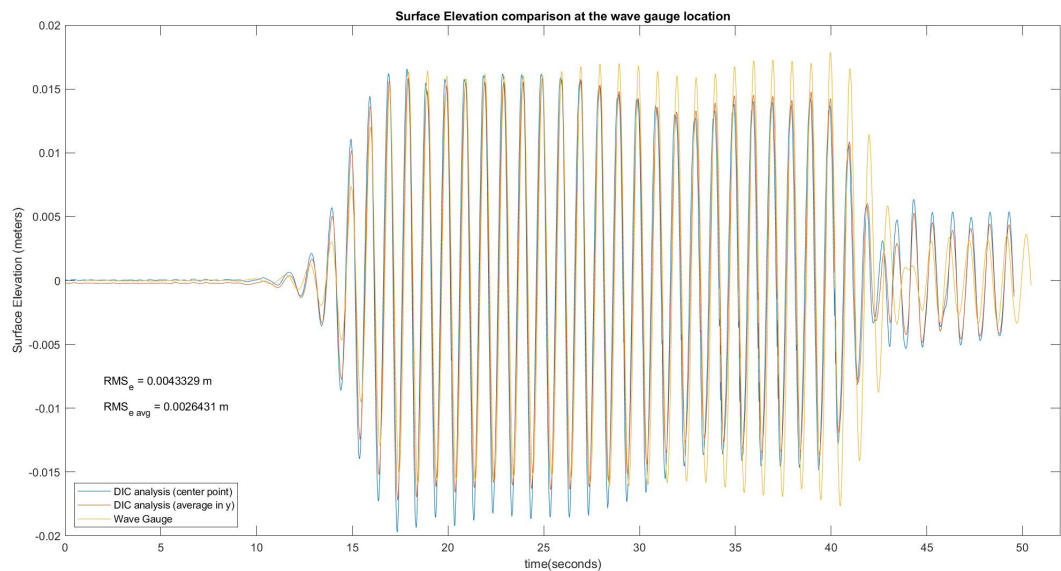


*Figure 5.24: Results using the DIC analysis for a periodic wave in the flow channel compared with wave gauge data at a single point.*

In Figure 5.24 the results from the first DIC analysis test are shown. In this test the goal was to compare DIC analysis results to wave gauge data for when a periodic wave was passed over the speckle pattern and wave gauge. The results shown here include two ways to analyze this data. The first is at the single center point of the free surface where the wave gauge was and the second was assuming a uniform free surface along the width of the tank then the values along the width of the speckle pattern could be averaged to get a single value for each time step. The first method is shown in the figure in blue, the second method is shown in the figure in red, and the wave gauge data is shown in the figure in yellow. The root mean square (RMS) error between the wave gauge data and the surface elevation measurement from the DIC analysis was computed and is displayed on Figures 5.24 and 5.25. This RMS value was calculated using the following equation.

$$RMS_{error} = \sqrt{\frac{\sum (y - y_i)^2}{n}} \quad (5.1)$$

In this equation,  $y$  is the wave gauge data and  $y_i$  is the surface elevation from the DIC analysis for each point in time. These results showed very good correlation between the DIC analysis and the wave gauge data as shown by the RMS error values displayed on the figure. The  $RMS_e$  value corresponds to comparison of the point value coincident with the wave gauge and the  $RMS_{avg}$  value corresponds to the comparison of wave gauge data with the averaged surface elevation value along the width of the tank. These two methods of extracting a point value for each time step proved to be very similar which implies that the assumption that the wave was

uniform across the width of the tank was valid. On the figure there are root mean square (RMS) errors indicated. The two RMS values correspond to the two methods of computing the surface elevation that would correspond with the location of the wave gauge. Both RMS values are relatively low when the surface elevation from the DIC analysis is compared with the wave gauge data however the averaging method appears to match better with the wave gauge data. This implies that averaging the surface elevation across the width of the tank does improve the accuracy of the surface elevation value at the location of the wave gauge.

This DIC analysis using Ncorr proved to be quite computationally expensive. The computer used for this had 20 cores for processing. This one run with 2975 frames took about 4 days to process. For each run there were 2975 frames for 50 seconds of recorded time and each frame was 2560 x 1600 pixels. For the DIC analysis the subset radius was 60 pixels. Ncorr evaluates correlation using a Discrete Fourier Transform, which is slow, but does not require specific dimensions of the discretized image. DaVis implements a Fast Fourier Transform if the image is broken into squares with pixel edges equal to multiples of 2, allowing the correlation algorithm to run much faster. This means that the DaVis algorithm was far less computationally expensive.

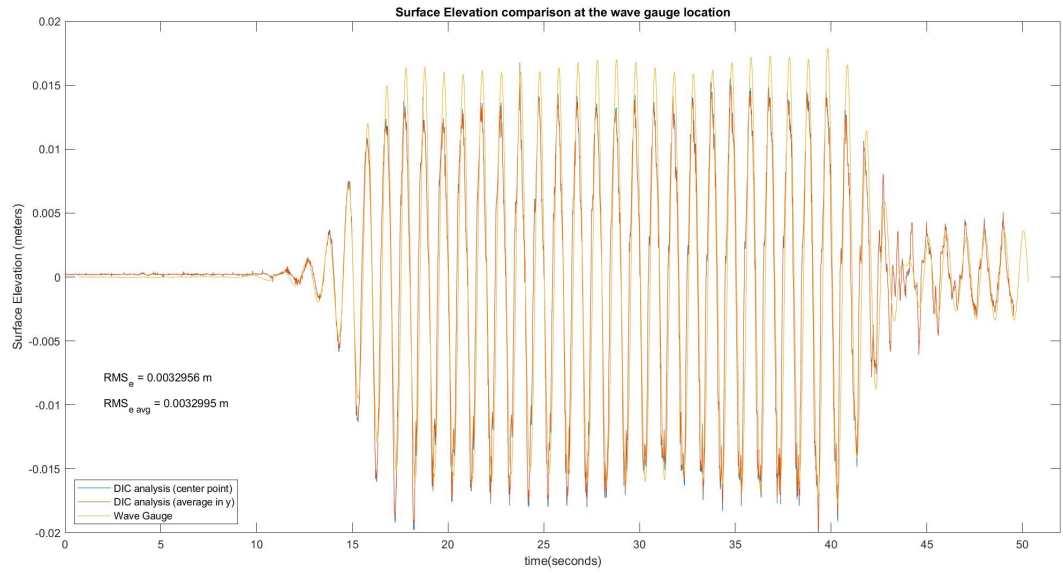


*Figure 5.25: Results using the PIV analysis for a periodic wave in the flow channel compared with wave gauge data at a single point.*

RMSE was observed to be low when using NCorr or DaVis for evaluating the displacement fields. Since there is effectively no difference in the output between these processing softwares, the significant computational time reduction from using DaVis and FFTs in evaluating cross-correlations with this method makes it a significantly better choice in applying this technique in future work.

## 5.2.4 Flow Testing with the Resin Foil

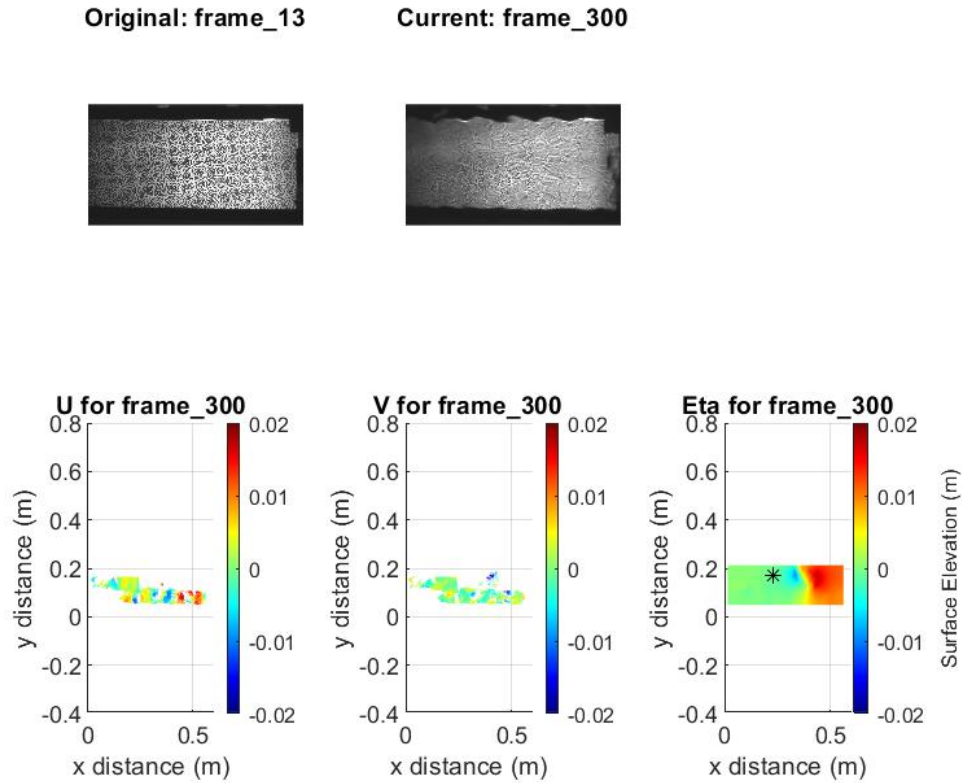


Figure 5.26: Reference (top left) and current (top right) images are shown and then components of the velocity (m/s),  $u$  (bottom left),  $v$  (bottom middle) and surface elevation,  $h$  (m) (bottom right). These results were outputs from the PIV analysis for the smaller resin foil at an angle of attack of 10 degrees, a depth of  $3/4$ \*chord length at a speed of  $0.34$  m/s for time step 300.

Figure 5.26 shows the DIC method applied to measuring the free surface in the wake of the foil with characteristics; chord length of 156 mm, thickness of 26 mm, span of 422 mm. These values give a chord ratio of  $1/6$  and an aspect ratio of 2.7. These results are promising for some time steps, where the deformation of the speckle pattern is

clear and it is possible to compute a free surface elevation in the wake of the foil. However, for other time steps as shown in Figure 5.27, the results from the DIC analysis were inconsistent, due to blurring of the speckle pattern. This problem likely occurs due to too much curvature of the free surface caused by fluctuation of the free surface at high flow speeds in the flume. This is an inherent problem in the flume that is exacerbated as the flow speed increases. The resulting blurriness of the image is a result of light ray crossing, making it impossible to distinguish individual features of the speckle pattern. It is clear from the images themselves, shown under the current frame, that the speckle pattern becomes muddled with high frequency waves and turbulence from the flow itself.

Original: frame\_13

Current: frame\_2500

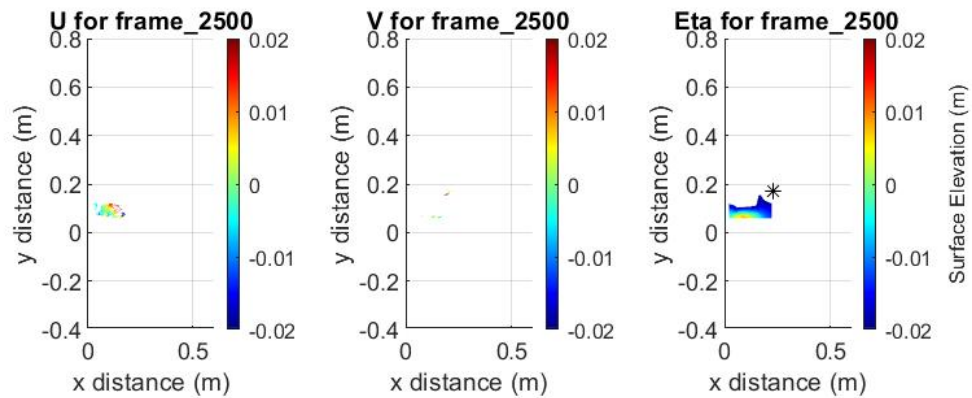
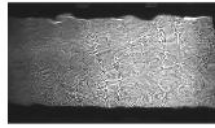
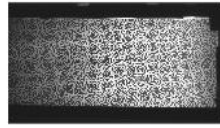


Figure 5.27: Reference (top left) and current (top right) images are shown and then components of the velocity (m/s),  $u$  (bottom left),  $v$  (bottom middle) and surface elevation,  $h$  (m) (bottom right). These results were outputs from the PIV analysis for the smaller resin foil at an angle of attack of 10 degrees, a depth of  $3/4$ \*chord length at a speed of  $0.34$  m/s for time step 2500.

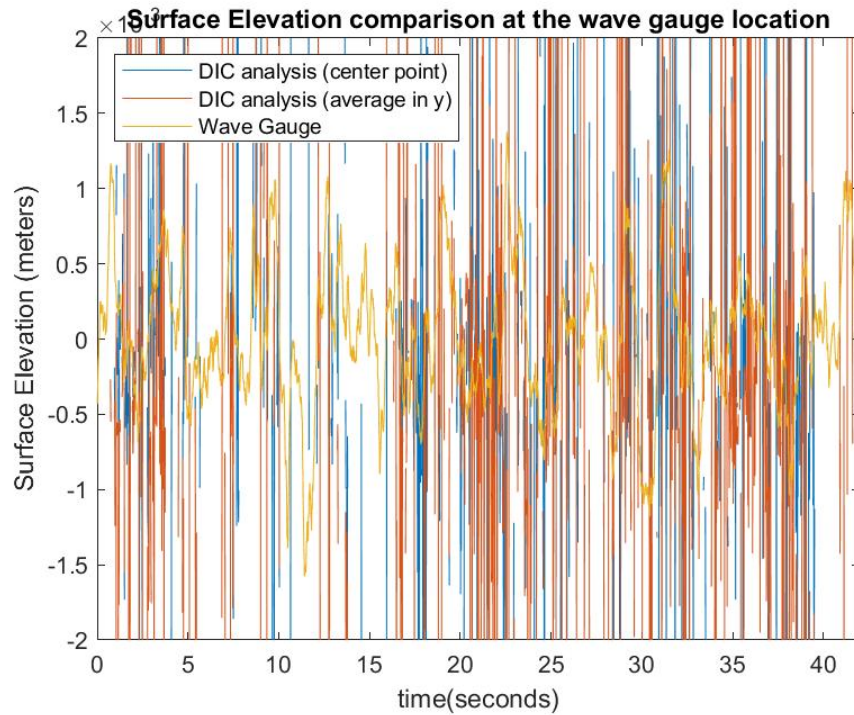


Figure 5.28: Results in time using the PIV analysis for the smaller resin foil at an angle of attack of 10 degrees, a depth of  $3/4$ \*chord length at a speed of 0.34 m/s over time at a point coincident with the wave gauge.

In Figure 5.28 the surface elevation at the same location as the wave gauge was plotted with the wave gauge data. It is clear that the surface elevation data was extremely noisy and inconsistent. As one can see from Figure 5.28, it was not possible to extract the proper free surface elevation from the blurry speckle images.

### 5.3 Conclusions and Future Work

#### 5.3.1 Testing in the Small Aquarium

The preliminary results conclusively show that the DIC analysis was reliable when comparing only displacement results to a known shift in x. The slow motion video

analysis proved qualitatively that the DIC analysis software Ncorr and the methods described by Moisy et al. work well for determining the surface elevation on a small scale. The chosen time steps were representative of larger surface elevation events which correlated well with the surface elevation results from the DIC analysis and calculations. Overall the results were promising however some further testing with quantitative results would be helpful in determining just how accurate this method is. A sensitivity analysis could also be helpful in determining what size the dots in the speckle pattern should be for a camera further from the pattern. In past work there was an optimal number of pixels per dot in the speckle pattern however it could vary widely based on the experimental setup. Optimizing the speckle pattern could improve results.

### **5.3.2 Testing in the Flow Channel**

The Digital Image Correlation method proved to have some limitations in the large flow channel. In the large flow channel the Digital Image Correlation method was accurate, when compared to wave gauge data, for long periodic waves generated by the wave maker without the foil present. Initially utilizing Ncorr and the methods described by Moisy et al. worked well for this case. However, the Da Vis Particle Image Velocimetry software was much less computationally expensive and produce comparable results for displacement as well as surface elevation utilizing the same methods from Moisy et al. for this periodic wave case. When the foil was placed in the flow channel a steady state wake formed behind it only at the higher flow speeds; 0.7 m/s and higher. When these waves were formed at higher flow speeds there was

substantial turbulence at the surface which caused ray crossing in the images captured through the free surface. At the higher flow speeds there were also issues with surface disturbance due to seams in the tank walls. This meant that the DIC analysis had extremely inconsistent results at the higher speeds. There were promising results with the DIC results at lower speeds however the  $Fr_d^2$  values of interest were at the higher flow speeds. There was a possibility that with a smaller foil the same  $Fr_d^2$  values could be achieved, however this would produce significantly lower free surface elevations that were difficult to measure. In future work a study looking into the possibility of a smaller foil with lower speeds may allow DIC to be a viable measurement method. Again a sensitivity study for the size of the speckle pattern may also prove useful in the future. since larger speckles would likely decrease ray crossing and thus make the DIC analysis a viable option for the higher flow speeds.

## Chapter 6

### Side View Image Analysis

#### 6.1 Test Setup

The following items were used in this experimental setup:

- Wave and Current Flume: Edinburgh Designs
  - Total length: 8 m
  - Length of experimental area: 2.44 m
  - Width: 0.05 m
  - Height: 1.3 m
- FLIR cameras: Blackfly S USB3
- Spinnaker Software for capturing frames from FLIR cameras
- Edinburgh Proprietary Wave and Current software
- Edinburgh Resistance Wave Gauges: WG8USB
- Electromagnetic Current Meter
- DaVis: Particle Image Velocimetry Software (used to correct for image distortion)

- Matlab: For image processing and plotting

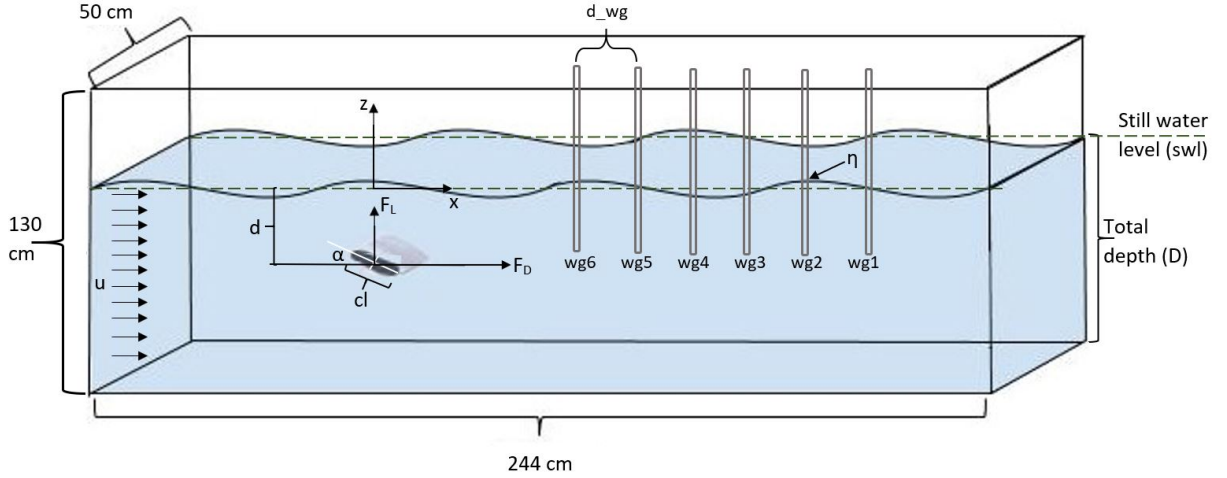


Figure 6.1: Schematic of the flow channel showing the flow direction and the location of the wave gauges.

A schematic of the experimental set up in the tank is shown in Figure 49. The elliptical foil is placed at depth  $d$  in the tank of water depth  $D$ , and at an angle of attack,  $\alpha$ . The dimension of the foil are specified by its chord length labeled  $cl$ ; the lift and drag forces are denoted here as  $F_L$  and  $F_D$  respectively. The flow speed is represented by a vector  $u$ ; in these experiments the flow was uniform with depth. The surface elevation is shown as the solid wavy line, denoted as  $\eta$ , and the still water level is represented with a dashed line; the total depth of water in the tank is labeled as  $D$  along the right edge. The still water value  $D$  was held constant over all experiments with a value of 0.71 m. Although the still water depth was not changed, due to the Bernoulli effect, as the flume speed changes, the depth of water can vary slightly in the flow channel, hence some variation of the depth can occur. All depth values in this thesis are reported relative to the still water free surface level. The

wave gauges labeled 1 to 6 are evenly spaced 0.4 m apart, denoted here as  $d_{wg}$ . The electromagnetic flow meter was used to measure the flow speed in the flume and was placed 4 m upstream from the foil setup in order to not interfere with data collection.



*Figure 6.2: 2 cameras, set up with respect to the flow channel.*

In Figure 6.2 the distance between the camera mount system and the flow channel is shown. The distance from the glass of the tank to the lenses was 2.4 meters. The lenses of the cameras were also placed at the same height as the still water line to limit distortion and parallax effects at the free surface. Although the measurements of the free surface at the intersection of the tank wall could be affected by the walls and the boundary layer on the glass, the experiments were observed to be largely two-dimensional over the width of the tank. Confirmation of this is present in measuring the variation of the observed free surface elevation from the side view, which captures deviations of the free surface if wave forms are not uniform across the width of the flume.



*Figure 6.3: Mounting system for the 2 cameras.*

The camera mounting system is shown in Figure 6.3 with the cameras mounted 1.12 meters apart, lenses center to center. The mounting system as well as the cameras were leveled in all directions.

The cameras used in this experimental setup were the FLIR Blackfly S USB3 and they were connected to the computer and images were captured through the Spinnaker software. These cameras have 6.3 megapixels, resolution of  $3072 \times 2048$ , and a frame rate of 60 frames per second. There are a few important parameters considered when optimizing the images needed for image processing. The first was brightness or aperture setting of the camera lens. These cameras record in gray-scale which was used for converting the images to binary black and white based on an appropriate threshold to capture the free surface line.

## 6.2 Image Processing Method

For each experiment, videos from the side view were taken for 50 seconds. The frames captured by both the FLIR cameras were synchronized to take images at the same time. The wave gauge data was also aligned in time by syncing the start of the camera measurements with the start of the wave gauge measurements. An auto click software was downloaded in order to do this. Auto Clicker by MurGee which had a downloadable Graphical User Interface (GUI) in which you could select multiple location on the screen to have clicked at the same time. This allowed the system to start the data acquisition of both cameras and the wave gauges at the same time. The wave gauges had their own sample rate and this data was sampled in post processing based on the camera frame rate of 10 frames per second. It is important to note that this frame rate is fairly low but was acceptable for these experiments since the measured waves were largely stationary in space.

With image processing there are two important considerations; distortion of the image and the relation between pixel and distance in space. A calibration plate was used to scale the image and correct for lens distortion and parallax effects. The calibration plate consisted of an image of equally spaced white dots on a black background as seen in Figure 6.4.

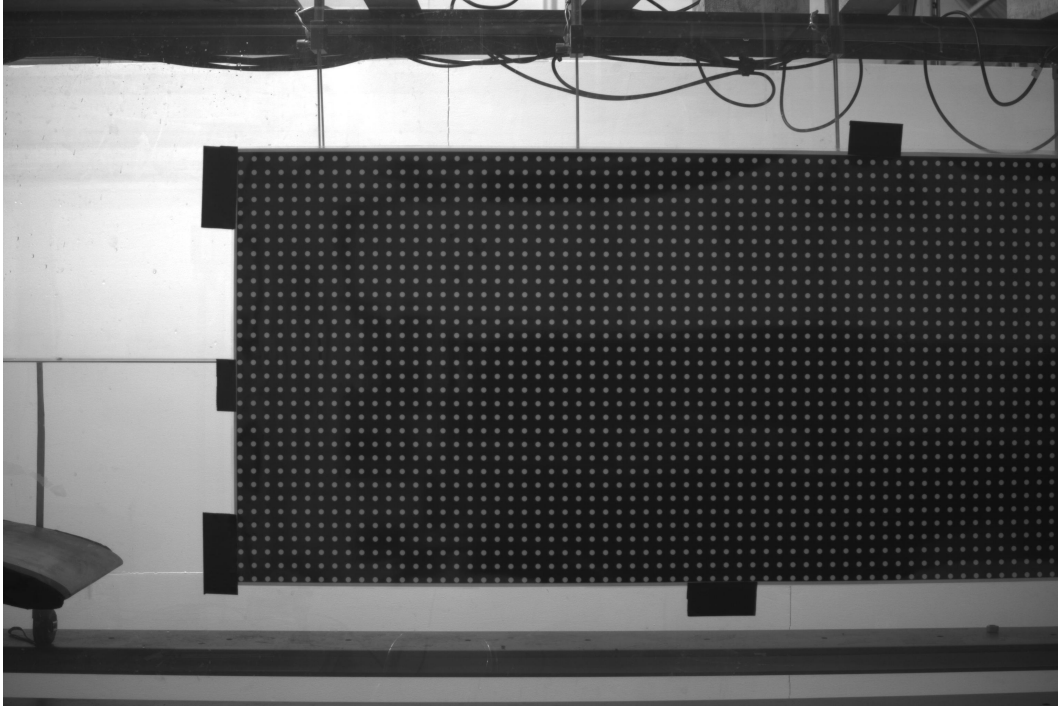


*Figure 6.4: Calibration image from the camera closest to the foil location on 2/11/2021.*

In Figure 6.4 the calibration pattern had dots with a diameter of 7.62 mm and spacing of 19.05 mm. This calibration image along with the images from each experiment were loaded into the previously mentioned PIV software, Da Vis. There was an image processing module that applies an image calibration to correct for distortion as well as give spatial parameters for the image. It is important to note here that the calibration pattern was placed against the glass wall as close as possible to the plane in space where the measurements were of interest. So here the goal was to measure the waterline at the tank wall closest to the cameras. New calibration images were collected each day that a new set of experiments were run. Each image from the two cameras were individually corrected for distortion.



*Figure 6.5: Images of the flow channel combined from the 2 cameras showing the location of the wave gauges.*

Once the images were corrected for distortion they could then be cropped and stitched together. The main goal in cropping the images was to remove any areas in the image that would make the image processing more difficult. In these experiments the goal was to have only the waterline visible but to ensure space above and below the waterline since some experiments have larger waves. Shown in the image above are the wave gauge locations are shown as well as the markers used to line up the 2 separate images from the 2 cameras. There is a divider in view of the cameras, this can be seen in center of the image on the right in Figure 6.5. The x and + markers were both 24 inches from the divider so aligning them when stitching the two images together was the best way to align the images both vertically and horizontally. This process was done for all images in the time series for each experiment.

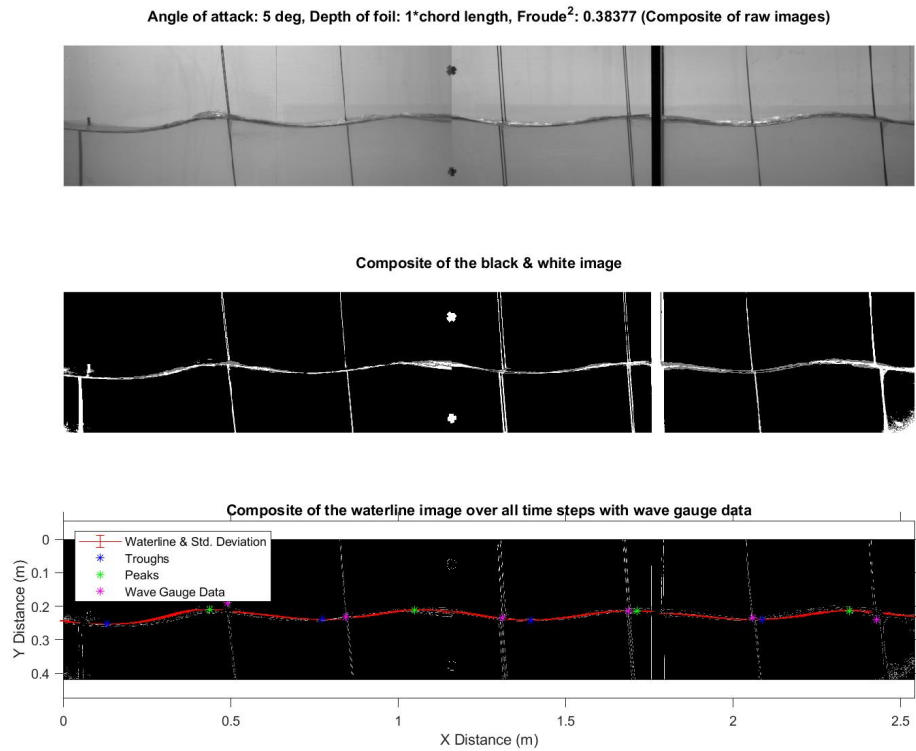


Figure 6.6: Flow channel images combined from the 2 cameras (top), binarized image (middle), binarized and edges image with the waterline, peaks, troughs, and wave gauge data shown (bottom).

As shown in Figure 6.6, once the images were stitched and cropped properly they were binarized in order to define the waterline. Once the image was binary it was then inverted so that the darkest parts of the image were shown in white (these are the ones in a binary matrix). In order to decrease the noise in the processing the edges of these dark areas were pulled from the binary image to give the third panel of Figure 6.6. This allowed the waterline to be the most defined part of the image. This step also lessened the intensity of the wave gauges and flume framing in the image, which had a similar light intensity to the free surface, allowing for better distinction

of the free surface from unwanted remnants in the binary image.

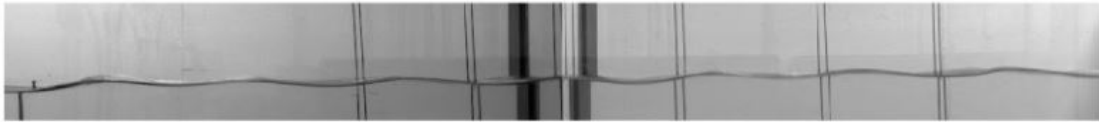
In order to define the waterline, the location of any ones at each x location was defined. The average of these locations was assumed to be the waterline at any given x location. Data was deemed unreliable and removed when the range of these values was above a certain threshold or when the average of those points was too far from the mean waterline which was defined by a separate measurement of the still water level. This process was repeated for each time step in the time series of each experiment. Then this time series of waterlines was averaged in time and statistics were evaluated for each location in x. The end result was an average waterline for each experiment with error bars for each point associated with the variance over time. From the mean free surface elevation line, the peaks and troughs of waves were determined according to the local maxima and minima of the mean curve. Wavelengths were determined by the distance between subsequent local peaks and troughs. A curve fit using a Fourier series was also applied as a reference to show the closest harmonic wave form to the measured data set.

### **6.3 Side View Image Analysis: Results and Discussion**

In the following Figures 56 through 67, the x and y axes are not equal in order to show the wave form more clearly. This means that the wave form is exaggerated in y. The x and y axes are also in terms of chord length of the foil so all values have been divided by chord length. The foil location is shown in bright blue with the center point shown and defined as the origin in x. The origin in y was chosen to be at the

free surface, this value was pulled from a separate set of calibration images of the still water level. In Figures 56 through 63 the waterline from the first set of experiments on 1/12/2021 is included and shown in yellow. The waterline from the second set of experiments on 2/11/2021 is shown in red and the fitted curves for are shown in blue. The waterlines are also shown with error bars indicating the time variance of the measurement at each point in x. For most parts of the waterline it appears to be a thick line but in areas of high variability the error bars can be seen. The peaks of the waves are shown as green asterisks, the troughs are blue asterisks, and the wave gauge data is shown as pink asterisks.

**Angle of attack: 10 deg, Depth of foil: 1\*chord length, Froude #: 0.21859 (Composite of raw images)**



**Angle of attack: 10 deg, Depth of foil: 1\*chord length, Froude<sup>2</sup>: 0.21859 (Composite of raw images)**



*Figure 6.7: Comparison of the images from the first and second set of experiments on 1/12/2021 (top) and 2/11/2021 (bottom).*

There were two sets of experiments run with slightly changed camera setups. The original set of experiments run on 1/12/2021, included tests with a 10 degree angle of attack, 3 different depths of the foil (1\*chord length, 5/4\*chord length, and 3/2\*chord length), and each for 5 different flow speeds. In Figure 6.7 the top figure shows images

from one of the experiments and in the center there was part of the tank exterior that caused some issues with the image processing. In the second experiments minimizing the profile of that frame was an important goal. The second main difference with the images themselves was to correct any lighting so that the images from the 2 different cameras would have the same lighting and lens settings. The other physical change was the addition of the x and + markers that were placed on the glass in order to align the two images at the glass which was as close to the plane of interest (where the waterline was being measured) as possible.

The root mean square between the two average waterlines was computed at every matching point in x and this gives an overall root-mean-square error which is shown for each case above the legend. Having only 2 experiments with two different camera setups causes this value to be a little unreliable. Each experiment would have to be repeated with a consistent experimental setup in order to better assess the repeatability of the experiments. The root mean square (RMS) error between the average waterline of the 2 experiments was computed and is displayed on each figure containing the comparison of the two experiments. This RMS value was calculated using the following equation.

$$RMS_{error} = \sqrt{\frac{\sum (y - y_i)^2}{n}} \quad (6.1)$$

In this equation,  $y$  and  $y_i$  are the corresponding surface elevation data for each point in x with respect to chord length. As a first look however, the root-mean-square values were all between 0.005 and 0.028 chord lengths which was a promising result

and does inspire confidence in these experiments being repeatable in the future.

The data from the first set of experiments run on 1/12/2021 for many of the cases was noisy for a few reasons. The divider that was in the middle of the field of view caused substantial noise in the image processing as did the lighting difference between the 2 cameras. The stitching of the images was also not optimized during the first set of experiments so the stitching was done by eye based on the still water level and the wave gauge that was closest to the divider. These issues caused there to be questionable waterline data near the connection between the images where the divider was so any data that strayed a good deal from the still water level was removed so as to avoid issues with the curve fit and comparison.

### 6.3.1 HDPE Foil with; angle of attack: $10^\circ$ & depth of foil: $1 \cdot \text{chord length}$

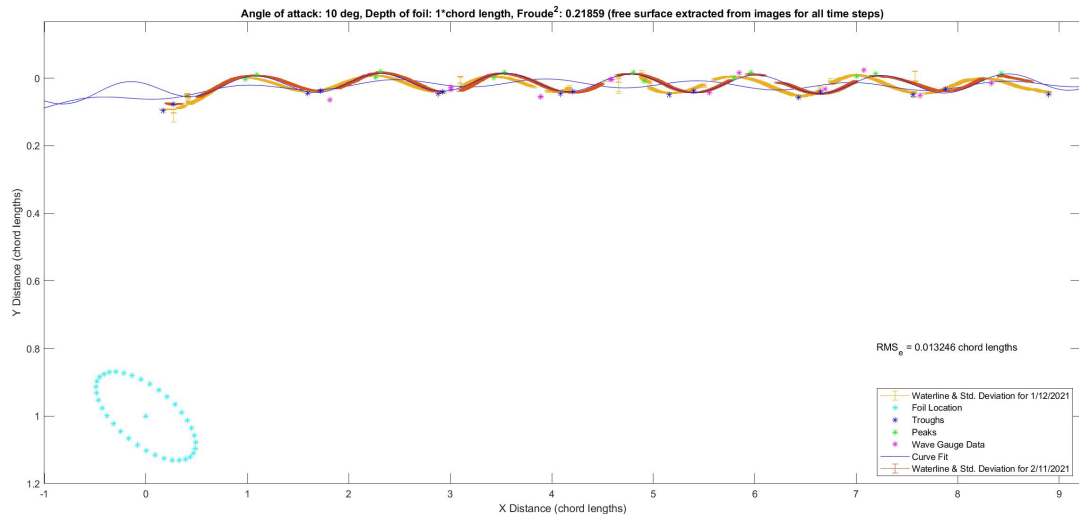
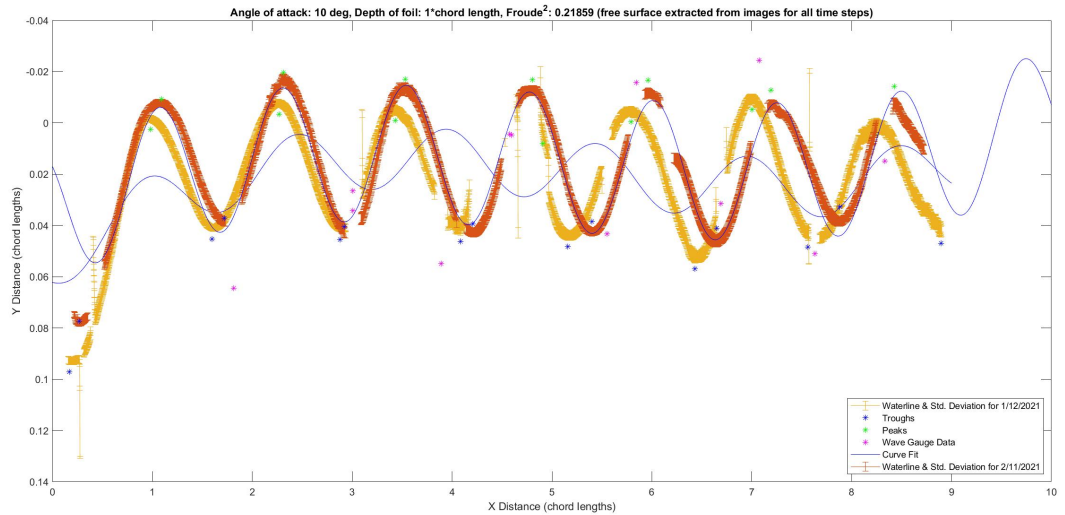


Figure 6.8: Results using the side view analysis for the larger HDPE foil at an angle of attack of 10 degrees, a depth of  $1 \cdot \text{chord length}$ , and with a flow speed of 0.80 m/s averaged over the time of the experiment (50 seconds).

In Figure 6.8 the average waterline from the two experiments are being compared. The data from the first experiment was fairly noisy as explained above. Overall there was good agreement between the two experiments for the first three wavelengths but after that it strays a bit in the far field. This is possibly due to error in calibration of the images due to the limited overlap allowed from the tank frame in between the two images. This was a common occurrence for many of the run cases. For almost all of the repeated experiments the first wave or two matched well but were not aligned in the far field.



*Figure 6.9: Results using the side view analysis for the larger HDPE foil at an angle of attack of 10 degrees, a depth of 1\*chord length, and with a flow speed of 0.80 m/s averaged over the time of the experiment (50 seconds).*

In Figure 6.9 the same waterline data is displayed without the foil location in order to see the confidence intervals more clearly.

	<b>1/12/2021</b>	<b>2/11/2021</b>
<b>Mean wave height (cl)</b>	0.0625	0.0591
<b>Range for wave height (cl)</b>	0.0561	0.0399
<b>Standard Deviation for wave height (cl)</b>	0.0194	0.0127
<b>Variance for wave height (<math>cl^2</math>)</b>	0.0004	0.0002
<b>Mean wave length (cl)</b>	1.2302	1.2455
<b>Range for wave length (cl)</b>	0.5938	0.2922
<b>Standard Deviation for wave length (cl)</b>	0.1522	0.0732
<b>Variance for wave length (<math>cl^2</math>)</b>	0.0232	0.0054

*Table 6.1: Results of the variability in wave height and wavelengths from the two different experiments for the case with an angle of attack of 10 degrees, a depth of 1\*chord length, and with a flow speed of 0.80 m/s.*

Table 2 and the subsequent tables in this section show statistics derived from the measured time-averaged wave form. Statistics are obtained by evaluating wave properties on a "per wave" basis and then computing ensemble statistics over all observed waves in the field of view. Hence, mean wave height refers to the mean value of all wave heights in the spatial history. Range refers to the difference between max and min values of the wave heights or wavelengths. Standard deviation and variance were similarly calculated for the set of wave heights and wavelengths present in the field of view. As shown in Table 6.1 the variability for both wave heights and wavelengths decrease from the experiments on 1/12/2021 to 2/11/2021 for this case. This demonstrates that the experimental setup on 1/12/2021 provided results that had higher variability and therefore these results may be less reliable than the experiments on 2/11/2021. This also implies that the changes to the camera and experimental setup

may have improved the reliability of the image processing technique and in turn improved the consistency of the results.

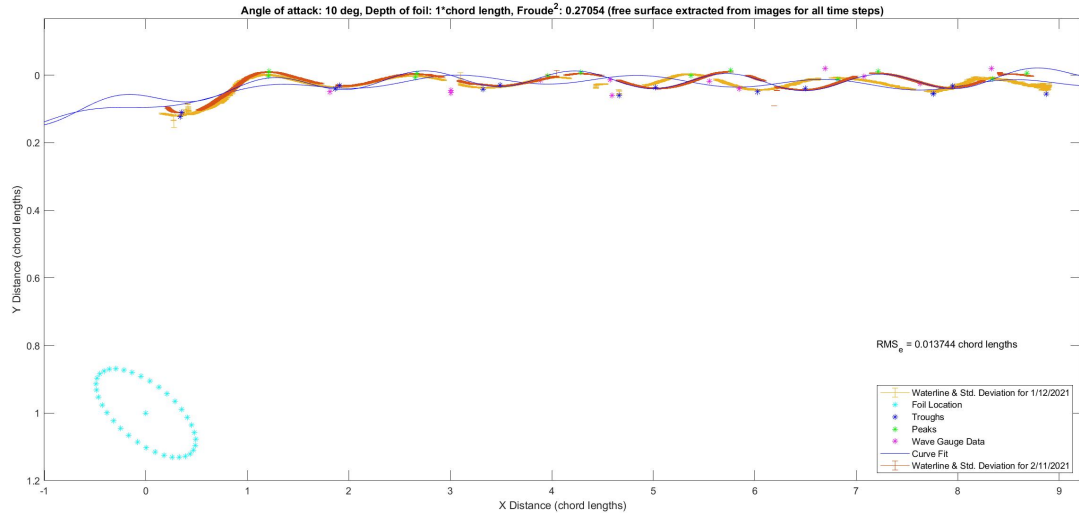


Figure 6.10: Results using the side view analysis for the larger HDPE foil at an angle of attack of 10 degrees, a depth of 1\*chord length, and with a flow speed of 0.89 m/s averaged over the time of the experiment (50 seconds).

In Figure 6.10 the average waterline from the two experiments are being compared. As in the case above, the waterlines are aligned for the first three wavelengths and then the results begin to stray. The other thing to notice in this figure is that the results are not as closely related to a sinusoidal wave form. The first wave behind the foil is becoming larger and the later waves do not have as large of an amplitude. This continues to happen at higher flow speeds when the foil is at this depth of 1\*chord length. This foil depth had the highest  $Fr_d^2$  values and in turn these higher flow speeds resulted in the first wave being a breaking wave which dissipated the energy and made the wave train smaller behind the breaking wave. This was an expected

result based on Duncan's experiments which were based around the breaking wave characteristics behind the foil at  $Fr_d^2$  values comparable to this.

	<b>1/12/2021</b>	<b>2/11/2021</b>
<b>Mean wave height (cl)</b>	0.0636	0.0553
<b>Range for wave height (cl)</b>	0.0884	0.085
<b>Standard Deviation for wave height (cl)</b>	0.0339	0.0331
<b>Variance for wave height (<math>cl^2</math>)</b>	0.0012	0.0011
<b>Mean wave length (cl)</b>	1.4242	1.5064
<b>Range for wave length (cl)</b>	0.6159	0.163
<b>Standard Deviation for wave length (cl)</b>	0.1537	0.0606
<b>Variance for wave length (<math>cl^2</math>)</b>	0.0236	0.0037

*Table 6.2: Results of the variability in wave height and wavelengths from the two different experiments for the case with an angle of attack 10 degrees, a depth of 1\*chord length, and with a flow speed of 0.89 m/s.*

Again, in Table 6.2 the variability of the experiment on 2/11/2021 was substantially less than for the experiment on 1/12/2021 for the wavelengths. The wave height variability was closer between the two experiments for this case so that shows that the amplitudes were more consistent in this case for both sets of experiments.

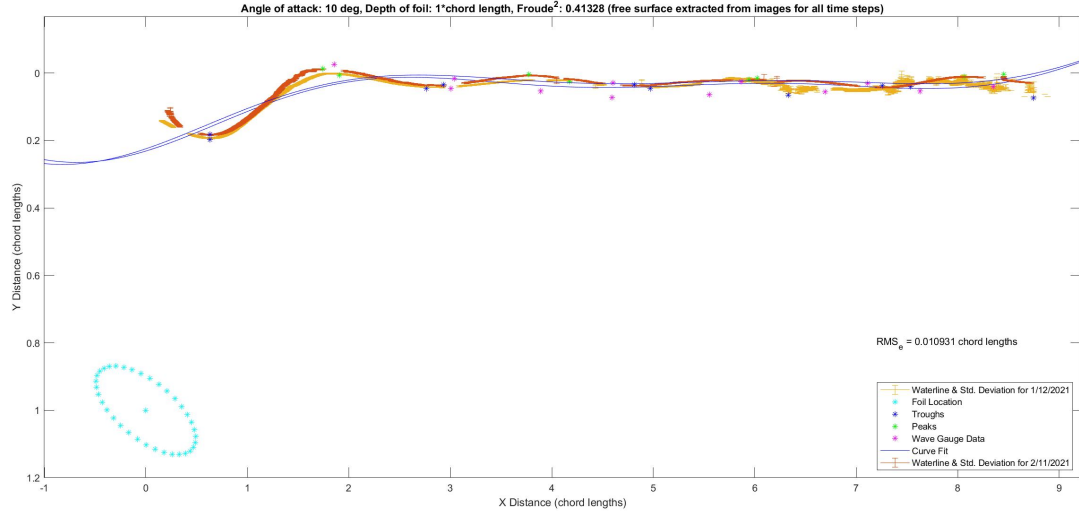


*Figure 6.11: Results using the side view analysis for the larger HDPE foil at an angle of attack of 10 degrees, a depth of 1\*chord length at a speed of 1.10 m/s averaged over the time of the experiment (50 seconds).*

Again in Figure 6.11 the average waterline from the two experiments are being compared and the results are aligned for the first three wavelengths. As in the previous cases the first wave behind the foil was larger and breaking. The later waves had smaller amplitudes and were more irregular. Again this foil depth had the highest  $Fr_d^2$  values and at the higher flow speeds the first wave was breaking and the following wave train was smaller as expected based on the results from Duncan's experiments.

	<b>1/12/2021</b>	<b>2/11/2021</b>
<b>Mean wave height (cl)</b>	0.0886	0.0698
<b>Range for wave height (cl)</b>	0.1696	0.1763
<b>Standard Deviation for wave height (cl)</b>	0.0803	0.0842
<b>Variance for wave height (<math>cl^2</math>)</b>	0.0065	0.0071
<b>Mean wave length (cl)</b>	1.7845	2.2221
<b>Range for wave length (cl)</b>	1.0593	0.5601
<b>Standard Deviation for wave length (cl)</b>	0.4619	0.2237
<b>Variance for wave length (<math>cl^2</math>)</b>	0.2133	0.0501

*Table 6.3: Results of the variability in wave height and wavelengths from the two different experiments for the case with an angle of attack 10 degrees, a depth of 1\*chord length, and with a flow speed of 1.10 m/s.*

Again, in Table 6.3 the variability of the experiment on 2/11/2021 was substantially less than for the experiment on 1/12/2021 for the wavelengths. The variability in the wave heights were again much closer between the two experiments however the variability increases for the second experiment which could be due to the irregularity in wave form after the first breaking wave.

For the higher speed cases with the foil at a depth of 1\*chord length the first wave was a larger amplitude breaking wave. It is clear that in these cases where there begins to be a hydraulic jump the curve fit based on a fourier series no longer matches well to the results.

### 6.3.2 HDPE Foil with; angle of attack: $10^\circ$ & depth of foil: $5/4$ \*chord length

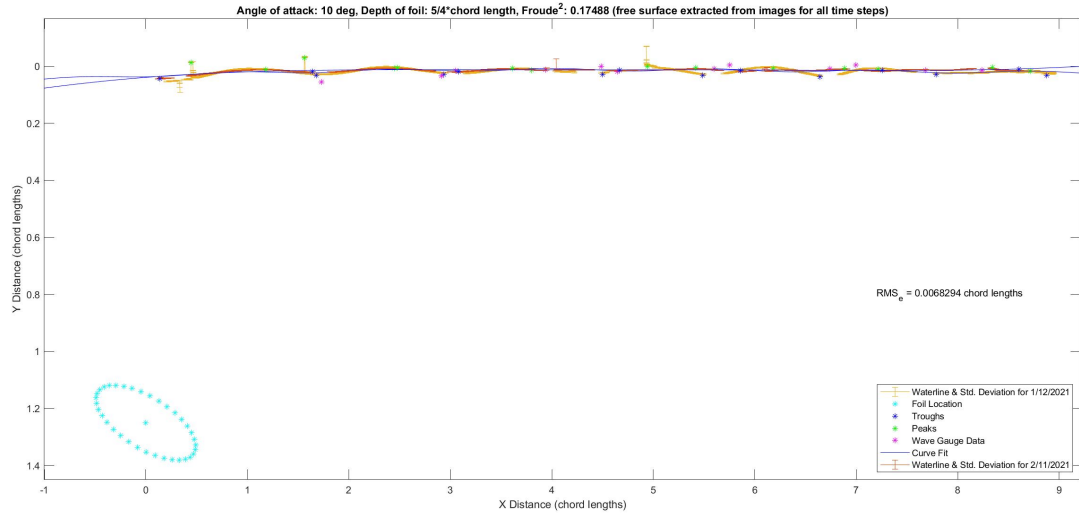


Figure 6.12: Results using the side view analysis for the larger HDPE foil at an angle of attack of 10 degrees, a depth of  $5/4$ \*chord length at a speed of 0.80 m/s averaged over the time of the experiment (50 seconds).

In Figure 6.12 the comparison between experiments is again shown however in this case the flow speed was low enough that the wave form was not in steady state yet. This happened for a few of the lower flow speeds when the foil was at a deeper depth. Therefore in these such cases the average waterline shown above was close to still water level everywhere.

	<b>1/12/2021</b>	<b>2/11/2021</b>
<b>Mean wave height (cl)</b>	0.0137	0.0141
<b>Range for wave height (cl)</b>	0.0441	0.024
<b>Standard Deviation for wave height (cl)</b>	0.0171	0.009
<b>Variance for wave height (<math>cl^2</math>)</b>	0.0003	0.0001
<b>Mean wave length (cl)</b>	1.1901	1.4204
<b>Range for wave length (cl)</b>	0.6809	0.6715
<b>Standard Deviation for wave length (cl)</b>	0.1936	0.1841
<b>Variance for wave length (<math>cl^2</math>)</b>	0.0375	0.0339

*Table 6.4: Results of the variability in wave height and wavelengths from the two different experiments for the case with an angle of attack 10 degrees, a depth of  $5/4$ \*chord length, and with a flow speed of 0.80 m/s.*

In Table 6.4 the variability of the experiment on 2/11/2021 was substantially less than for the experiment on 1/12/2021 for both wavelengths and wave heights. The variability for this case however was not very reliable since the waves were so irregular that the variability was small for both experiments because the wave form was so small. This was common for both angles of attack; 5 and 10 degrees, with the foil at the two deeper depths;  $5/4$ \*chord length and  $3/2$ \*chord length if the flow speed was below 0.85 m/s. These cases corresponded to  $Fr_d^2$  values below 0.19.

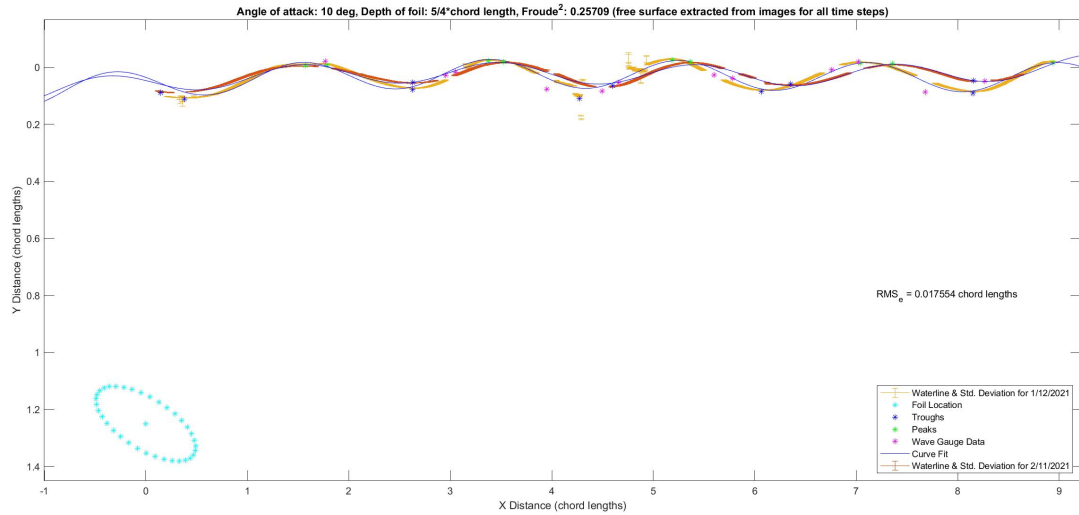


Figure 6.13: Results using the side view analysis for the larger HDPE foil at an angle of attack of 10 degrees, a depth of  $5/4$ \*chord length at a speed of 0.97 m/s averaged over the time of the experiment (50 seconds).

In Figure 6.13 the wave form was fully formed for this case. In this experiment the wave form seems to have reached steady state condition, so this average waterline was as expected. For this case the two experiments aligned very well for the first two waves after the foil but began to stray in the far field. The curve fit now matches very well with the results which indicates that the wave form has become more regular. The wavelengths for both experiments do seem to be much more consistent over the wave form.

	<b>1/12/2021</b>	<b>2/11/2021</b>
<b>Mean wave height (cl)</b>	0.1228	0.0811
<b>Range for wave height (cl)</b>	0.0368	0.0231
<b>Standard Deviation for wave height (cl)</b>	0.0166	0.0109
<b>Variance for wave height (<math>cl^2</math>)</b>	0.0003	0.0001
<b>Mean wave length (cl)</b>	1.8648	1.9697
<b>Range for wave length (cl)</b>	0.665	0.7231
<b>Standard Deviation for wave length (cl)</b>	0.219	0.2413
<b>Variance for wave length (<math>cl^2</math>)</b>	0.048	0.0582

*Table 6.5: Results of the variability in wave height and wavelengths from the two different experiments for the case with an angle of attack 10 degrees, a depth of  $5/4$ \*chord length, and with a flow speed of 0.97 m/s.*

In Table 6.5 the variability of the experiment on 2/11/2021 was substantially less than for the experiment on 1/12/2021 for the wave heights. The variability in wavelengths however was higher for the second experiment however the variability was fairly close which indicates similar results in the two experiments. These variability values for wavelengths were higher than the previous case which seems to be due to the fact that the wavelengths in the far field were larger than the wavelength of the wave closest to the foil.

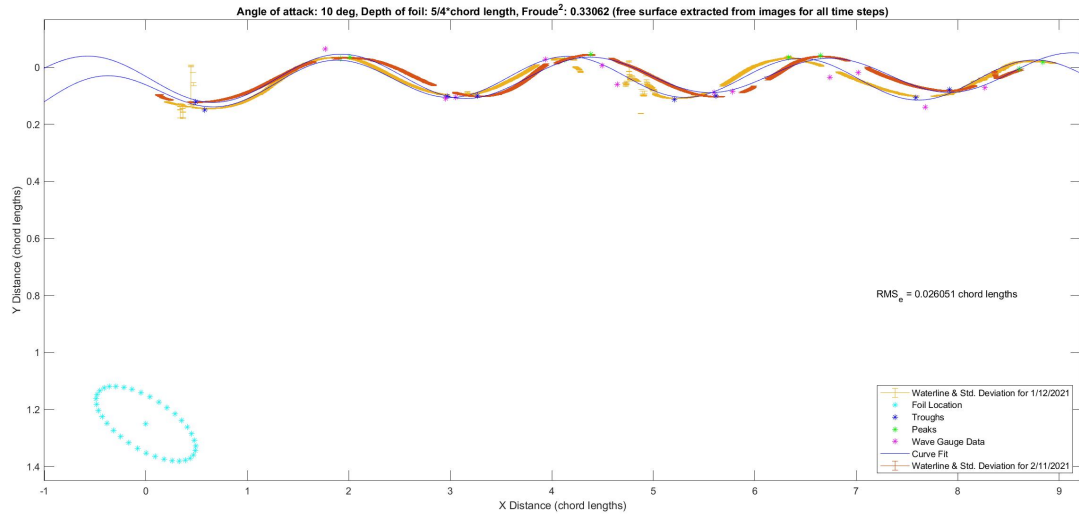


Figure 6.14: Results using the side view analysis for the larger HDPE foil at an angle of attack of 10 degrees, a depth of  $5/4$ \*chord length at a speed of 1.10 m/s averaged over the time of the experiment (50 seconds).

In Figure 6.14 the wave form was again fully formed, so this average waterline was as expected. For this case the two experiments aligned very well for the first wave after the foil but began to stray after that. The curve fit now matched very well with the results for both experiments which indicates that the wave form has become more regular. The other issue with this case was the last peak for the experiment on 2/11/2021 which seems to be cut off. Based on the curve fit the last peak should have been further from the foil however the image was cut off so a peak was placed at the edge of the data.

	<b>1/12/2021</b>	<b>2/11/2021</b>
<b>Mean wave height (cl)</b>	0.1586	0.1484
<b>Range for wave height (cl)</b>	0.0569	0.0161
<b>Standard Deviation for wave height (cl)</b>	0.0261	0.0082
<b>Variance for wave height (<math>cl^2</math>)</b>	0.0007	0.0001
<b>Mean wave length (cl)</b>	2.321	2.4124
<b>Range for wave length (cl)</b>	0.3024	0.5084
<b>Standard Deviation for wave length (cl)</b>	0.1216	0.2059
<b>Variance for wave length (<math>cl^2</math>)</b>	0.0148	0.0424

*Table 6.6: Results of the variability in wave height and wavelengths from the two different experiments for the case with an angle of attack 10 degrees, a depth of  $5/4$ \*chord length, and with a flow speed of 1.10 m/s.*

In Table 6.6 the variability of the experiment on 2/11/2021 was larger than for the experiment on 1/12/2021 for both the wave heights and wavelengths. Again the thing to note here is that there are fewer waves present in this case so there were fewer wavelengths in the computation for variability which decreases the reliability of this value.

### 6.3.3 HDPE Foil with; angle of attack: $10^\circ$ & depth of foil: $3/2$ \*chord length

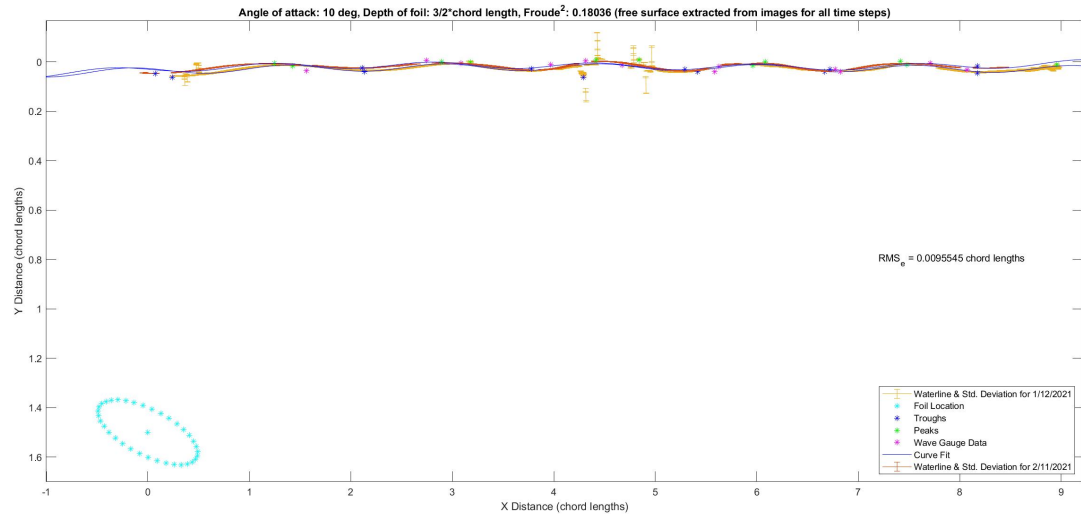


Figure 6.15: Results using the side view analysis for the larger HDPE foil at an angle of attack of 10 degrees, a depth of  $3/2$ \*chord length at a speed of 0.89 m/s averaged over the time of the experiment (50 seconds).

In Figure 6.15 the wave form was beginning to be fully formed, so this average waterline was close to what was expected still with some irregularities. For this case the two experiments aligned very well across the entire wave form. The curve fit matched well with the results for both experiments which indicates that the wave form has become more regular.

	<b>1/12/2021</b>	<b>2/11/2021</b>
<b>Mean wave height (cl)</b>	0.0495	0.0331
<b>Range for wave height (cl)</b>	0.0451	0.0172
<b>Standard Deviation for wave height (cl)</b>	0.0161	0.0066
<b>Variance for wave height (<math>cl^2</math>)</b>	0.0003	$4.355 \times 10^{-5}$
<b>Mean wave length (cl)</b>	1.5465	1.5859
<b>Range for wave length (cl)</b>	1.0339	0.7037
<b>Standard Deviation for wave length (cl)</b>	0.333	0.2048
<b>Variance for wave length (<math>cl^2</math>)</b>	0.1109	0.0419

*Table 6.7: Results of the variability in wave height and wavelengths from the two different experiments for the case with an angle of attack 10 degrees, a depth of  $3/2$ \*chord length, and with a flow speed of 0.89 m/s.*

In Table 6.7 the variability of the experiment on 2/11/2021 was lower than for the experiment on 1/12/2021 for both the wave heights and wavelengths. These values show that the experiment done on 2/11/2021 had more consistent results within the wave field.

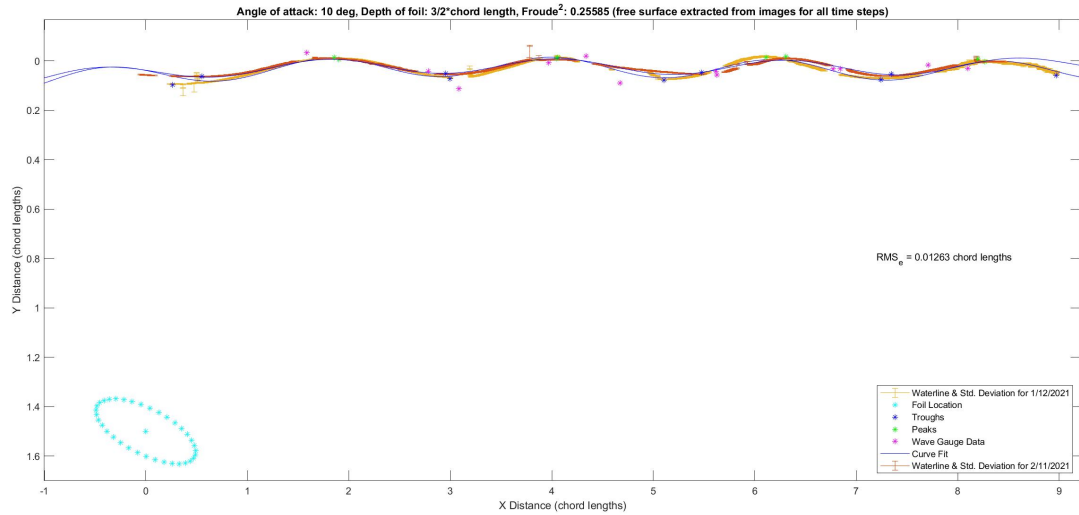


*Figure 6.16: Results using the side view analysis for the larger HDPE foil at an angle of attack of 10 degrees, a depth of  $3/2$ \*chord length at a speed of 1.06 m/s averaged over the time of the experiment (50 seconds).*

In Figure 6.16 the wave form was now fully formed, so this average waterline was as expected. For this case the two experiments aligned very well across the entire wave form. The curve fit now matched very well with the results for both experiments which indicates that the wave form had reached steady state.

	<b>1/12/2021</b>	<b>2/11/2021</b>
<b>Mean wave height (cl)</b>	0.1021	0.0666
<b>Range for wave height (cl)</b>	0.0381	0.0159
<b>Standard Deviation for wave height (cl)</b>	0.016	0.0073
<b>Variance for wave height (<math>cl^2</math>)</b>	0.0003	0.0001
<b>Mean wave length (cl)</b>	2.1527	2.1887
<b>Range for wave length (cl)</b>	1.0023	0.6505
<b>Standard Deviation for wave length (cl)</b>	0.2963	0.265
<b>Variance for wave length (<math>cl^2</math>)</b>	0.0878	0.0702

*Table 6.8: Results of the variability in wave height and wavelengths from the two different experiments for the case with an angle of attack 10 degrees, a depth of  $3/2$ \*chord length, and with a flow speed of 1.06 m/s.*

In Table 6.8 the variability of the experiment on 2/11/2021 was lower than for the experiment on 1/12/2021 for both the wave heights and wavelengths. These variability results indicate that there was more consistency across the wave field on 2/11/2021.

#### **6.3.4 HDPE Foil with; angle of attack: $5^\circ$ & depth of foil: 1\*chord length**

When compared with the results from the 10 degree angle of attack cases the results for the 5 degree angle of attack are very similar for most of the run cases however when the foil was at the most shallow depth; 1\*chord length there were some discrepancies which will be highlighted below. The complete set of these results can be found in the Appendix of this thesis.

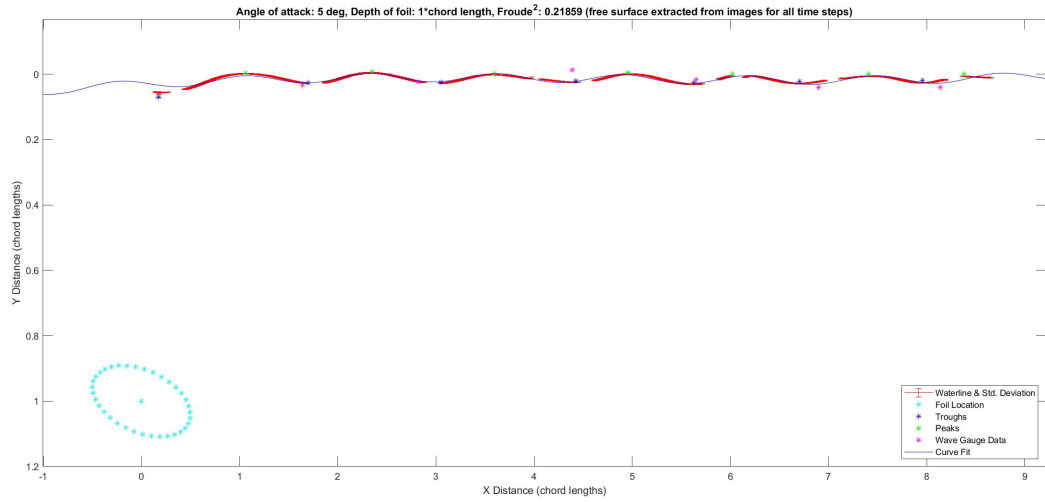


Figure 6.17: Results using the side view analysis for the larger HDPE foil at an angle of attack of 5 degrees, a depth of 1\*chord length at a speed of 0.80 m/s averaged over the time of the experiment (50 seconds).

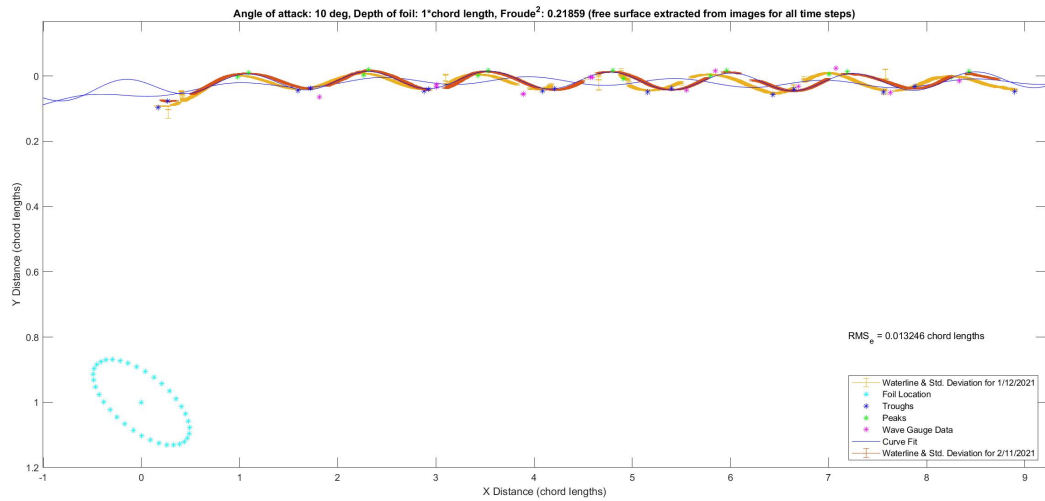


Figure 6.18: Results using the side view analysis for the larger HDPE foil at an angle of attack of 10 degrees, a depth of 1\*chord length, and with a flow speed of 0.80 m/s averaged over the time of the experiment (50 seconds).

When comparing Figure 6.17 to Figure 6.18 the wave form for both seems to be fully formed so the wave forms were as expected. The wave form in both figures includes 7 peaks over the full field of view which implies that the wavelengths of the two wave forms is almost the same. The most noticeable difference between these two cases is the wave height. The wave heights for the 10 degree angle of attack cases were larger than those in the 5 degree angle of attack case when all other parameters are held constant. This is as expected since the larger angle of attack would create a larger initial depression at the surface.

	<b>2/11/2021 5 deg</b>	<b>2/11/2021 10 deg</b>	<b>1/12/2021 10 deg</b>
<b>wave height 1 (m)</b>	0.0219	0.0259	0.031
<b>wave height 2 (m)</b>	0.0099	0.017	0.0168
<b>wave height 3 (m)</b>	0.008	0.0172	0.0158
<b>wave height 4 (m)</b>	0.0078	0.0168	0.0143
<b>wave height 5 (m)</b>	0.0077	0.0164	0.0167
<b>wave height 6 (m)</b>	0.0064	0.0161	0.0205
<b>wave height 7 (m)</b>		0.0140	0.0154
<b>Average (m)</b>	0.0103	0.0176	0.0186
<b>Variance (<math>m^2</math>)</b>	$3.356 \times 10^{-5}$	$1.443 \times 10^{-5}$	$3.362 \times 10^{-5}$

*Table 6.9: Results of the individual wave heights from the average waterline for both angles of attack for the case with a depth of 1\*chord length, and with a flow speed of 0.80 m/s.*

In Table 6.9 it is clear that the average wave height for the 5 degree angle of attack case is substantially smaller than that of the two experiments with a 10 degree angle of attack. This decrease in wave height with angle of attack is consistent for all wave

heights over the wave form. This was a common occurrence for most of the run cases when comparing the differences between 5 and 10 degrees angle of attack. This implies heavily that the amplitude of the wave is dependent on the angle of attack.

	<b>2/11/2021 5 deg</b>	<b>2/11/2021 10 deg</b>	<b>1/12/2021 10 deg</b>
<b>wavelength 1 (m)</b>	0.3839	0.3637	0.3832
<b>wavelength 2 (m)</b>	0.3729	0.3642	0.3473
<b>wavelength 3 (m)</b>	0.4061	0.3801	0.4414
<b>wavelength 4 (m)</b>	0.3165	0.3459	0.2642
<b>wavelength 5 (m)</b>	0.3873	0.3671	0.3615
<b>wavelength 6 (m)</b>	0.4543	0.3685	0.371
<b>wavelength 7 (m)</b>	0.4042	0.4331	0.4258
<b>wavelength 8 (m)</b>	0.4095	0.3589	0.3828
<b>wavelength 9 (m)</b>	0.3584	0.3839	0.3596
<b>wavelength 10 (m)</b>	0.3213	0.3555	0.3204
<b>wavelength 11 (m)</b>	0.3738	0.3724	0.3799
<b>wavelength 12 (m)</b>		0.3676	0.3374
<b>wavelength 13 (m)</b>			0.3984
<b>Average (m)</b>	0.3807	0.3717	0.3671
<b>Variance (<math>m^2</math>)</b>	0.0016	0.0005	0.0021

*Table 6.10: Results of the individual wavelengths from the average waterline for both angles of attack for the case with a depth of 1\*chord length, and with a flow speed of 0.80 m/s.*

In Table 6.10 it is clear that the average wavelengths for the 5 degree angle of attack case is not noticeably different from the two experiments with a 10 degree angle of attack. This implies that angle of attack does not have a substantial effect on the wavelength of the wave form behind the foil. This makes sense since the physics

says that flow speed and chord length are the dominant factors in determining the wavelength.

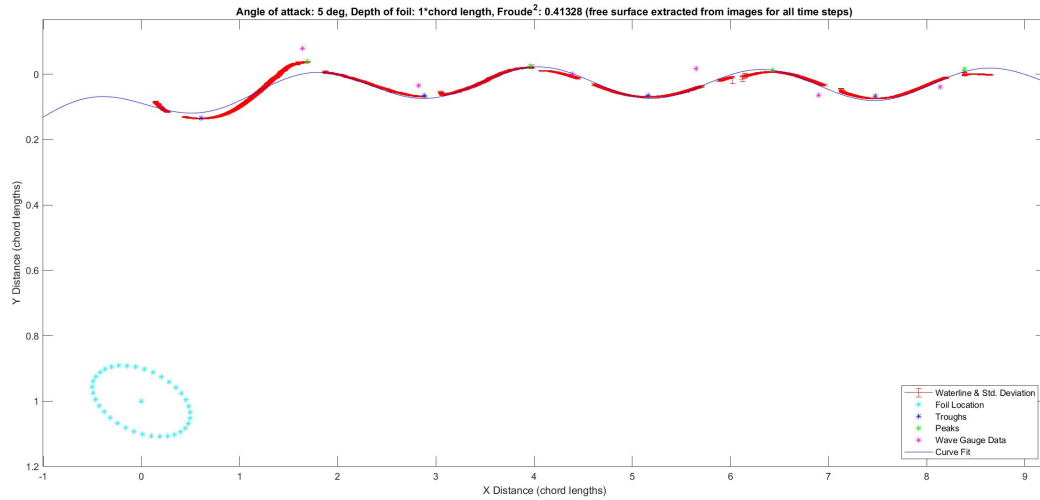


Figure 6.19: Results using the side view analysis for the larger HDPE foil at an angle of attack of 5 degrees, a depth of 1\*chord length at a speed of 1.10 m/s averaged over the time of the experiment (50 seconds).

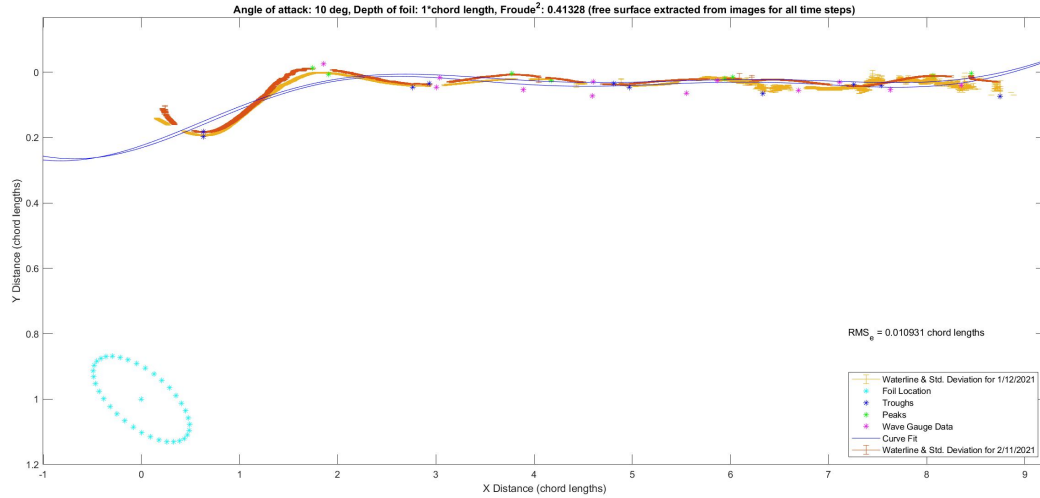


Figure 6.20: Results using the side view analysis for the larger HDPE foil at an angle of attack of 10 degrees, a depth of 1\*chord length at a speed of 1.10 m/s averaged over the time of the experiment (50 seconds).

When comparing Figures 6.19 and 6.20 there are major differences in the wave form. In Figure 6.19, the 5 degree angle of attack there is still a fairly consistent sinusoidal wave form where as in Figure 6.20, the 10 degree angle of attack case the wave form is basically just a single breaking wave behind the foil. In both cases the first wave is largest however there is a very inconsistent wave field far from the foil in the 10 degrees angle of attack case. As in the previous breaking wave cases the first wave behind the foil was breaking which dissipates energy in the rest of the wave form. The later waves had smaller amplitudes and were more irregular. Again this foil depth had the highest  $Fr_d^2$  values and at the higher flow speeds the first wave was breaking and the following wave train was smaller as expected based on the results from Duncan's experiments. The difference between the 5 and 10 degree angle of attack cases does

imply however that the larger the angle of attack the more likely there will be a hydraulic jump scenario rather than a consistent steady state sinusoidal wave form.

	2/11/2021 5 deg	2/11/2021 10 deg	1/12/2021 10 deg
<b>wave height 1 (m)</b>	0.0519	0.0585	0.0615
<b>wave height 2 (m)</b>	0.027	0.0091	0.0109
<b>wave height 3 (m)</b>	0.0233	0.0058	0.0111
<b>wave height 4 (m)</b>	0.0247	0.01	0.0222
<b>Average (m)</b>	0.0317	0.0208	0.0264
<b>Variance (<math>m^2</math>)</b>	0.0002	0.0006	0.0006

*Table 6.11: Results of the individual wave heights from the average waterline for both angles of attack for the case with a depth of 1\*chord length, and with a flow speed of 1.10 m/s.*

In Table 6.11 it is clear that the wave height for first wave for the 5 degree angle of attack case is slightly smaller than that of the two experiments with a 10 degree angle of attack. However the average wave height is actually larger than the other two cases because there are still large waves after the first breaking wave when the foil is at a smaller angle of attack. This was an interesting case for the fact that the wave form is so drastically different even though the angle of attack was the only adjustment. The wave form for the 5 degrees angle of attack is still mainly sinusoidal where as the wave form for the 10 degrees angle of attack cases has become basically just a single breaking wave with noise behind it.

	2/11/2021 5 deg	2/11/2021 10 deg	1/12/2021 10 deg
wavelength 1 (m)	0.6778	0.606	0.6767
wavelength 2 (m)	0.7366	0.6715	0.5283
wavelength 3 (m)	0.5834	0.725	0.6328
wavelength 4 (m)	0.6792	0.686	0.6375
wavelength 5 (m)	0.6807	0.5617	0.6587
wavelength 6 (m)	0.6903	0.7289	0.4045
wavelength 7 (m)			0.3606
wavelength 8 (m)			0.3615
Average (m)	0.6747	0.6632	0.5326
Variance ( $m^2$ )	0.0025	0.0045	0.019

*Table 6.12: Results of the individual wavelengths from the average waterline for both angles of attack for the case with a depth of 1\*chord length, and with a flow speed of 1.10 m/s.*

In Table 6.12 it is clear that the wavelengths for the 5 degree angle of attack case is not noticeably different from the two experiments with a 10 degree angle of attack. This implies that angle of attack does not have a substantial effect on the wavelength of the wave form behind the foil. This makes sense since the physics says that flow speed and chord length are the dominant factors in determining the wavelength. The wavelength values for the two 10 degree angle of attack cases are also less consistent for these cases due to the fact that the wave form is highly irregular. The wavelengths for the 5 degrees angle of attack are much less variable.

### 6.3.5 Froude Number Analysis of Side View Experiments

Analyzing the results of these experiments with respect to the  $Fr_d^2$  value was important for proving the validity of the experiments. With the above results, it was possible to get a series of wave heights and wavelengths from the peak and trough locations. Once these values were determined they would need to be compared to some expected values. The linear dispersion relation relates frequency of a wave to its wavelength.

$$\omega^2 = gk * \tanh(kh) \quad (6.2)$$

Wave frequency is also directly related to phase speed of a wave,  $c_p = \omega/k$  and with this the dispersion relation could also be defined as follows;

$$(c_p)^2 = g/k * \tanh(kh) \quad (6.3)$$

In these experiments, since the wave that forms behind the foil is stationary, the flow speed is equal to the phase speed of the wave,  $c_p = U$ . So now the linear dispersion relation can be redefined based on  $Fr_d^2 = U^2/dg$ .

$$Fr_d^2 * dg = g/k * \tanh(kh) \quad (6.4)$$

Which simplifies to;

$$Fr_d^2 = \frac{1}{dk} \tanh(kh) \quad (6.5)$$

With this modified linear dispersion relation the Newton-Raphson method can be used to iterate and find a solution for the expected wavelength based on linear wave theory. The basis of the Newton-Raphson method is that an original function (F), in our case linear dispersion in terms of  $Fr_d^2$ , and the derivative of that function (DF) are used as follows;

$$X_1 = X_0 - F/DF \quad (6.6)$$

Where the initial guess of  $X_0$  is used with the function and its derivative to compute a new guess,  $X_1$ . This process continues until the solution converges. This method was used to compute the expected wavelengths based on the flow speed for each of the run cases. In the following figures the actual data was shown with dashed line and error bars to show the variability in wavelength over the field of view for each run case. Then the solid lines were the expected values based on the linear dispersion relation. The y axis shows the wavelengths in terms of chord length of the foil and the x axis shows the  $Fr_d^2$  value.

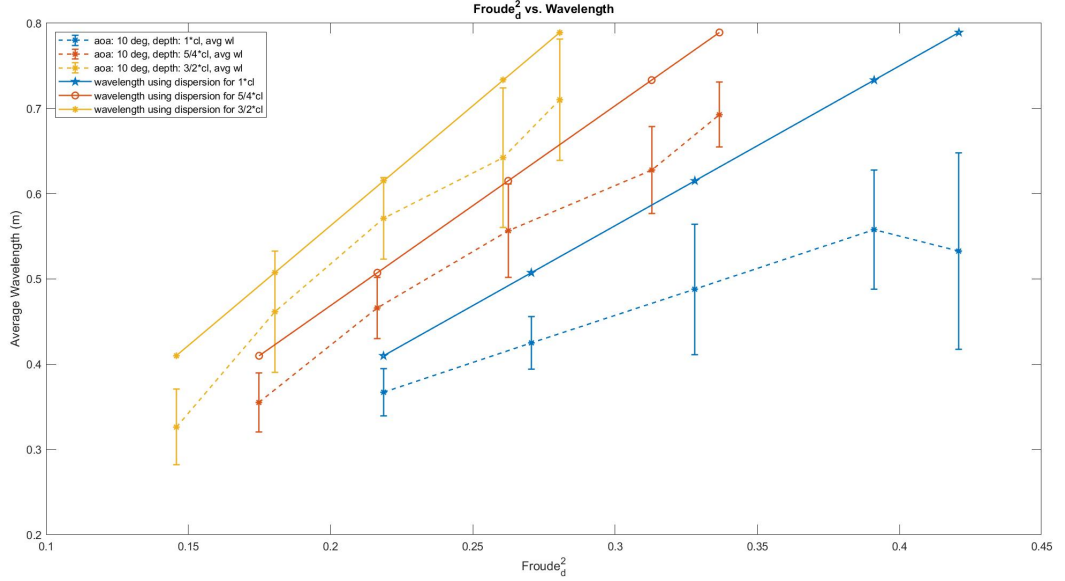


Figure 6.21: The wavelength in terms of chord length as a function of the  $Fr_d^2$  value from the side view analysis for all the experiments on 1/12/2021.

Figure 6.21 shows results from the first round of experiments which all had the foil at an angle of attack of 10 degrees. The error bars on these plots represent the 95% confidence limits of the standard deviation of wavelengths for each case. These plots show how the expected wavelength would change with the depth of the foil. The results from this experiment for depth of the foil of  $5/4$ \*chord length and  $3/2$ \*chord length, shown in red and yellow respectively, do show good agreement with the expected  $Fr_d^2$  values. Although the wavelengths are consistently smaller than the theoretical value at all  $Fr_d^2$  values. Since the dispersion relation is based on linear wave theory, it cannot account for non-linear effects which is most apparent in breaking wave cases which occur when the foil is at a depth of  $1$ \*chord length. The slopes of the red and yellow lines match accordingly with the slope of the expected values. The results for

the third depth of the foil of 1\*chord length, (blue), does not match very well with the expected values and this was likely due to the fact that in these cases the first wave began to break so the wave train was no longer sinusoidal and therefore the waves behind that breaking wave are much smaller in amplitude and more irregular in wavelength.

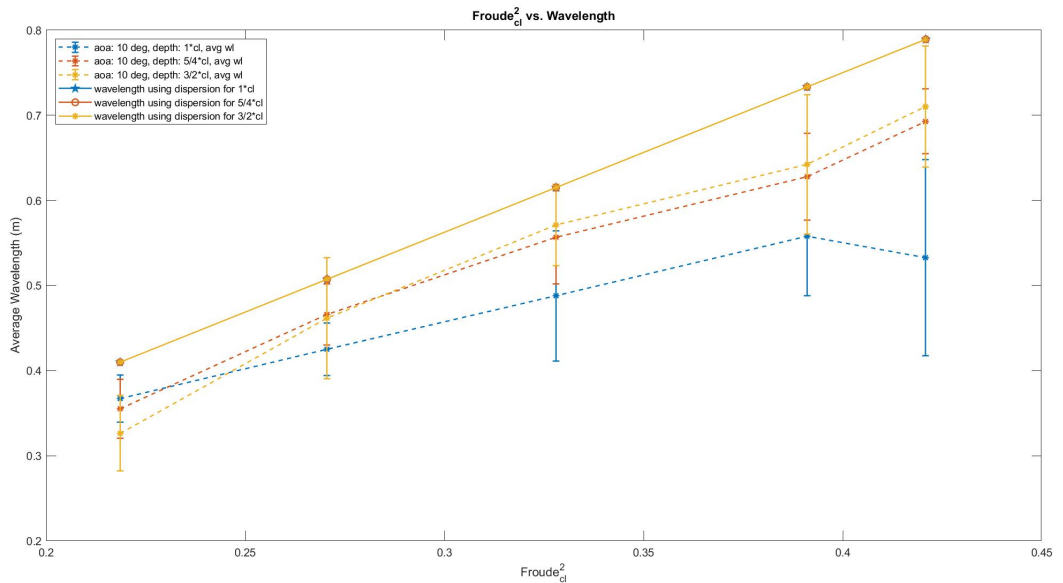


Figure 6.22: The wavelength in terms of chord length as a function of the  $Fr_d^2$  from the side view analysis for all the experiments on 1/12/2021.

In Figure 6.22 the same results from the first set of experiments are shown however the  $Fr_d^2$  values have been adjusted by depth of foil divided by chord length to get  $Fr_{cl}^2$  value which is the Froude value in terms of chord length. This adjusted Froude value removes the shift based on depth of the foil so that the results collapse to have a the same expected values for wavelength as a function of  $Fr_{cl}^2$  value. In this figure again the results for the depth of foil of  $5/4$ \*chord length and  $3/2$ \*chord length, shown in

red and yellow respectively, show good agreement with the expected results from the linear dispersion relation. However again the results from the depth of foil of 1\*chord length, shown in blue, deviate quite a bit from the expected slope. There is also still a fairly consistent offset of the results from the experiment having shorter wavelengths than the expected values. This offset is suspected to be due to an error in the flow speed measurement since the flow speed was measured about 4 m away from where the foil was placed. Further testing will have to be done to characterize the flow speed in the flume to see if it changes with location along the tank as well as with depth since the flow may not be uniform.

The following figures include the data from the second set of experiments on 2/11/2021. As previously mentioned these experiments were done with a slightly different camera setup and improvements on the lighting and image processing technique. These experiments included 2 different angles of attack (5 and 10 degrees), 3 depths of the foil (1\*chord length, 5/4\*chord length, and 3/2\*chord length), and now 6 different flow speeds. In the following figures a similar pattern was followed to display the results. The dashed lines with error bars represent the actual data from the experiments with the larger dashed lines being the results for an angle of attack of 5 degrees and the finer dashed line being the results for an angle of attack of 10 degrees. The solid lines were again the expected results based on the linear dispersion relation. It is important to note that the  $Fr_d^2$  value is not based on angle of attack.

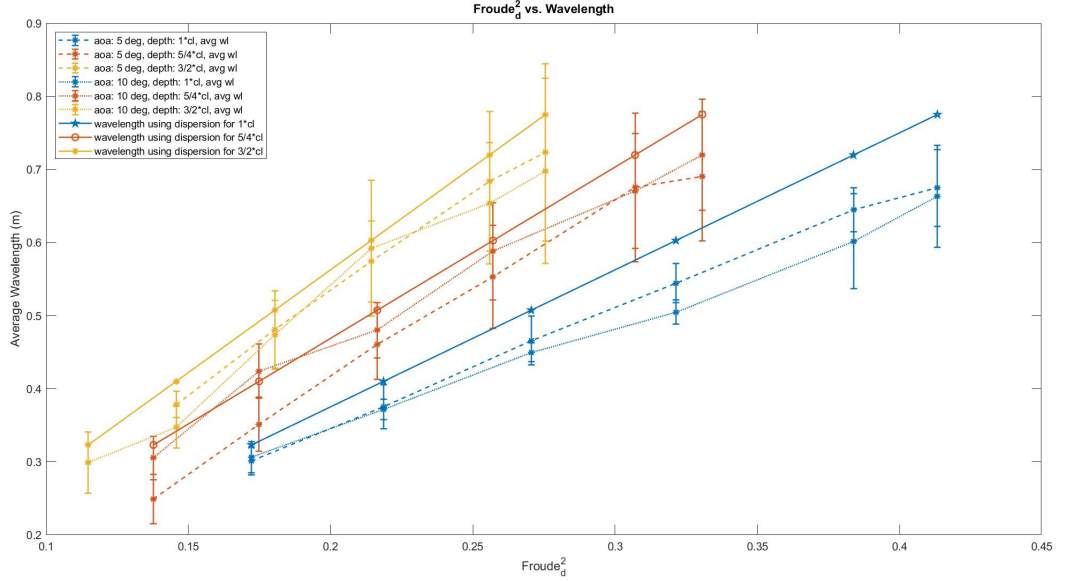


Figure 6.23: The wavelength in terms of chord length as a function of the  $Fr_d^2$  value from the side view analysis for all the experiments on 2/11/2021.

In Figure 6.23 there is very good agreement for all three depths of the foil with the expected values based on linear dispersion. There does seem to be a consistent offset between the experiments and the expected values. The expected values of wavelength are slightly higher than the data which could imply that there is some energy loss in the system whether that was in the flow or due to some wave breaking behind the foil. Likely this is due to a non-linear effect since this dispersion relation is based on linear wave theory. Non-linear effect could be breaking or just a higher order shape to the wave formation. This could also be in part due to the fact that these waves may not be linear. They may be slightly asymmetrical which would mean that the linear dispersion relation is not directly applicable and would only ever be an approximation.

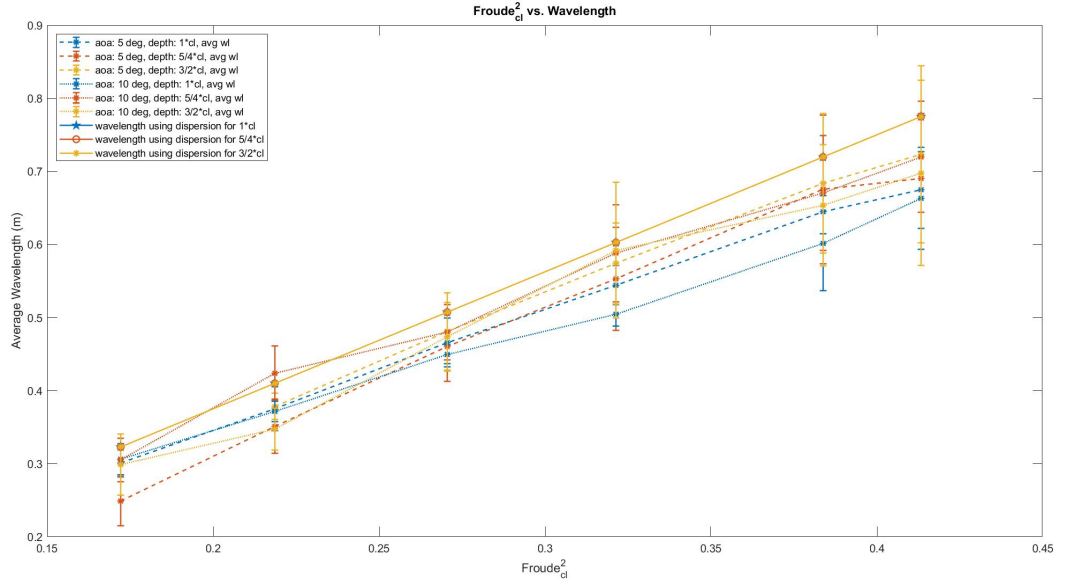


Figure 6.24: The wavelength in terms of chord length as a function of the  $Fr_{cl}^2$  from the side view analysis for all the experiments on 2/11/2021.

Again, here in Figure 6.24 the  $Fr_d^2$  values have been adjusted by depth of foil divided by chord length to get  $Fr_{cl}^2$  value which is the Froude value in terms of chord length. This again collapses the expected results to a single sloped line and the experimental data becomes very close together. This shows very good agreement between all of the experimental runs and the expected data and there is still a fairly consistent offset of the experimental data to have slightly smaller wavelengths than the expected values. It is more clear here that the data from the experimental case with an angle of attack of 5 degrees, depth of foil of  $3/2$ \*chord length, and the lowest  $Fr_{cl}^2$  value was not closely tied to the rest of the data. It is worth noting that at this depth and this lowest flow speed there was very little surface disturbance so the wave form was not very defined and therefore the image processing for this case was more difficult and

thus less reliable.

### 6.3.6 Direct Comparison with Duncan Results

In order to show good agreement with the work from Duncan a direct comparison of some of the results were explored here. In all of the following plots the blue lines correspond with the depth of the foil of  $1 \cdot \text{chord}$  length, the red lines correspond with  $5/4 \cdot \text{chord}$  length and the yellow lines correspond with  $3/2 \cdot \text{chord}$  length. The larger dashed lines correspond with the 5 degree angle of attack and the smaller dashed lines correspond with 10 degree angle of attack. Any solid lines correspond of the curve fit with Duncan's data points which are shown with black asterisks. The red curve fit is a polynomial fit where as the black solid lines are linear curve fits.

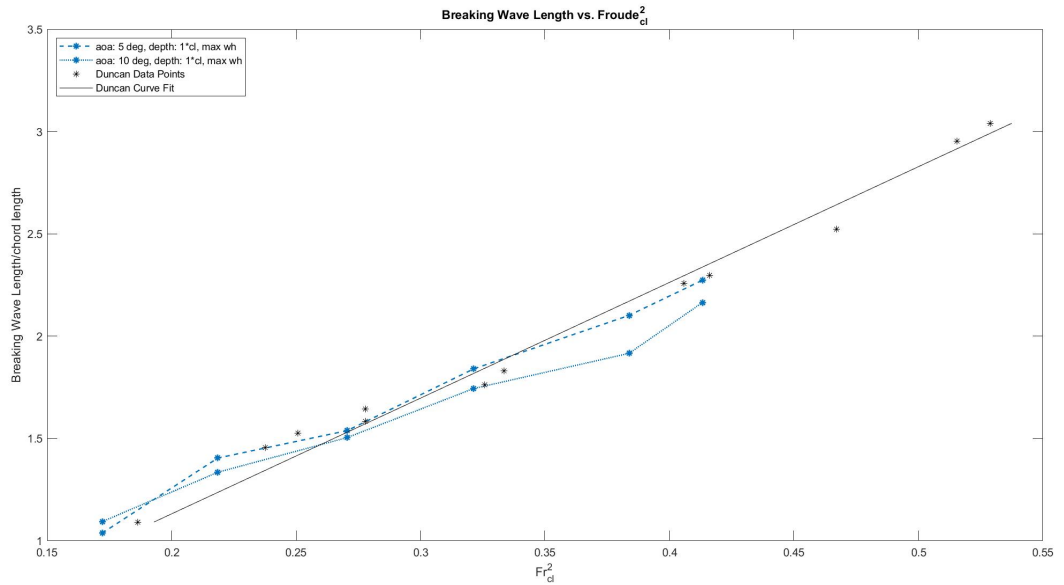


Figure 6.25: Breaking wavelength as a function of  $Fr_{cl}^2$ . Comparison of results from Duncan (1981) to breaking wave cases from the current set of experiments.

In Figure 6.25 the breaking wave length is shown as a function of  $Fr_{cl}^2$ . The cases

displayed here are only the cases with the foil at the depth of  $1 \times \text{chord}$  length which were the cases with the highest  $Fr_{cl}^2$  values and in turn were the cases with the first wave breaking most noticeably. This data does align fairly well with Duncan's data in terms of slope however more cases would always help when fitting a curve through data.

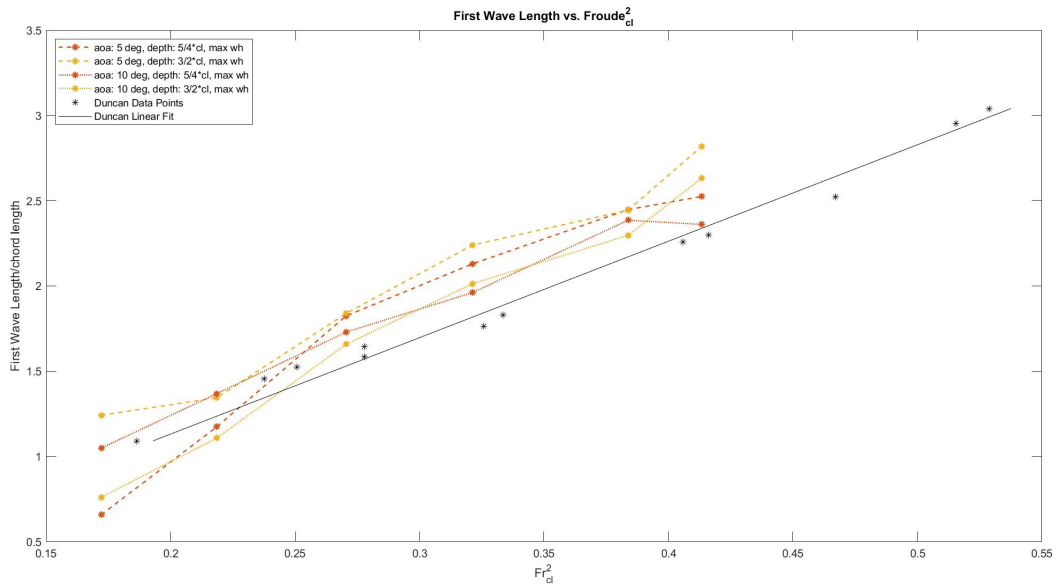


Figure 6.26: Breaking wavelength as a function of  $Fr_{cl}^2$ . Comparison of results from Duncan (1981) to non-breaking wave cases from the current set of experiments.

In Figure 6.26 the first wave length is shown as a function of  $Fr_{cl}^2$ . The cases displayed here are all of the non-breaking wave cases. This data is still close to Duncan's data however the slope of our data does not match what Duncan's linear fit is doing. This discrepancy could have to do with the fact that Duncan was focused on breaking wave cases and these are not breaking waves.

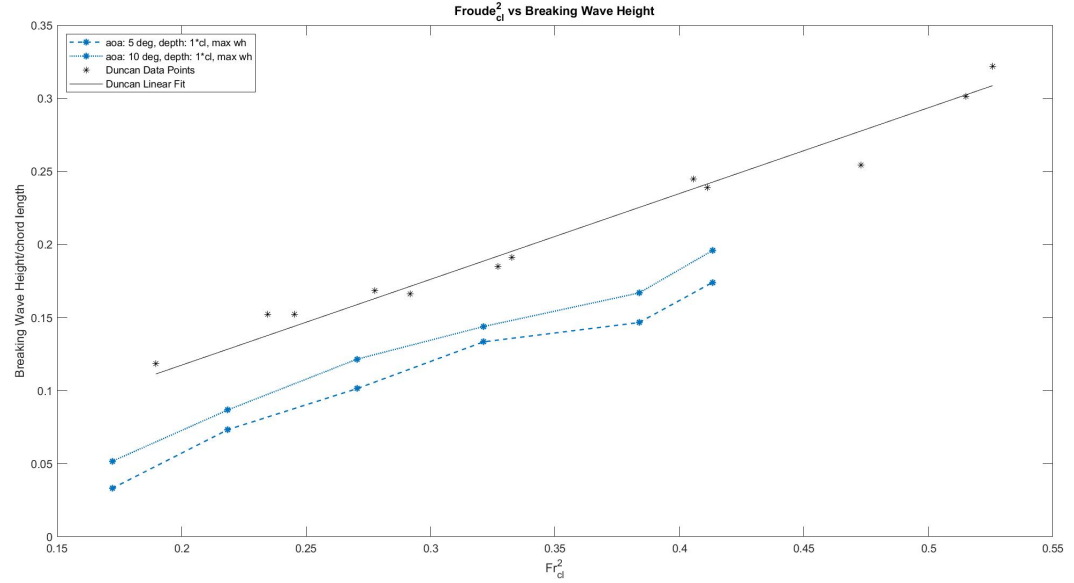


Figure 6.27: Breaking wave height as a function of  $Fr_{cl}^2$ . Comparison of results from Duncan (1981) to breaking wave cases from the current set of experiments.

In Figure 6.27 the breaking wave height is shown as a function of  $Fr_{cl}^2$ . The cases displayed here are only the cases with the foil at the depth of 1\*chord length which were the cases with the highest  $Fr_{cl}^2$  values and in turn were the cases with the first wave breaking most noticeably. This data matched the slope of Duncan’s data well. There does seem to be an offset in the data which could be due to the fact that the NACA 0012 foil that Duncan used was geometrically different from the oval foil used in these experiments. The NACA 0012 foil with a tapered edge provides more lift than an oval shape. With more lift force it is likely for wave amplitudes to be larger and thus more likely for a wave to break. It is also clear that all of the cases explored in this research were on the lower end of the  $Fr_{cl}^2$  scale which is as expected since the focus was not on breaking wave cases. The data explored here were cases where

the first wave was barely on the verge of breaking whereas Duncan’s cases were all breaking cases.

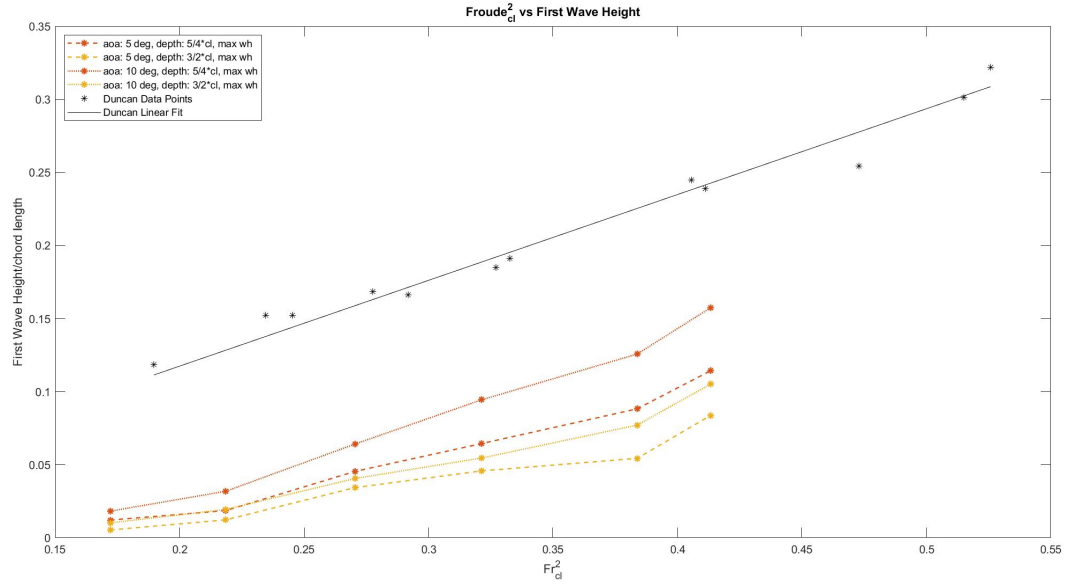


Figure 6.28: Breaking wave height as a function of  $Fr_{cl}^2$ . Comparison of results from Duncan (1981) to non-breaking wave cases from the current set of experiments.

In Figure 6.28 the breaking wave height is shown as a function of  $Fr_{cl}^2$ . The cases displayed here are only the non-breaking wave cases. Some of these cases seems to match the slope of Duncan’s data fairly well however there was again an offset. This could again be due to either the foil shape or the fact that these cases were not breaking wave cases. These non-breaking cases were also in general further from Duncan’s data which was expected since Duncan’s cases were mostly breaking wave cases. This is also apparent in the fact that all of our data is further to the left along the x axis which corresponds to a lower  $Fr_{cl}^2$  values.

## 6.4 Conclusions and Future Work

The side view image processing analysis proved to be a viable method to capture the surface elevation for these experiments. In these experiments the wave form created behind the submerged foil was steady state at the  $Fr_d^2$  values of interest. With the foil at a depth of 1\*chord length the wave form was as expected at lower  $Fr_d^2$  values but above a  $Fr_d^2$  value of about 0.3 the first wave began to break and thus the subsequent waves were smaller in amplitude due to energy dissipation in the breaking wave closest to the foil. This was more apparent for the angle of attack of 10 degrees. These experiments were only repeated once and only for the angle of attack of 10 degrees. For these repeated cases the results seem fairly consistent however the variability of wave heights and wavelengths was lower for most cases for the second set of experiments. This does seem to show that the experiments performed on 2/11/2021 were more reliable. It is difficult to definitively make this statement since the camera setup and settings did change slightly in these second experiments which could have been the cause for the improvement in results. Overall the waterline and wave parameters were as expected based on the qualitative comparison with Duncan's results. In the Froude number analysis the experimental results agreed well with the expected results based on the linear dispersion relation. A direct comparison with Duncan's experiment was not trivial since his results were based more around the breaking wave parameters. This analysis was done in order to directly compare with his results to verify that values for wave height and wave length were still comparable. There is closer agreement with Duncan's data for the cases in which breaking

did occur in the first wave however the slope of the data for both wave length and wave height aligns well with Duncan's data. In future work these experiments could be repeated with a consistent camera and experimental setup to determine if the experiments are indeed repeatable. This would be useful in assessing the variability between experiments. This would be useful to know since this experimental data is beginning to be compared with various numerical models. Further validation of these method would improve the understanding and thus the confidence in the experiments performed. With confidence in the experimental results they could effectively be used to validate numerical models like the underwater vehicle module that was recently added to Non-Hydrostatic Wave (NHWAVE) or other fully resolved Computational Fluid Dynamics (CFD) models.

## Chapter 7

### Appendix

#### 7.1 Additional Results from the Slow Motion Video Analysis

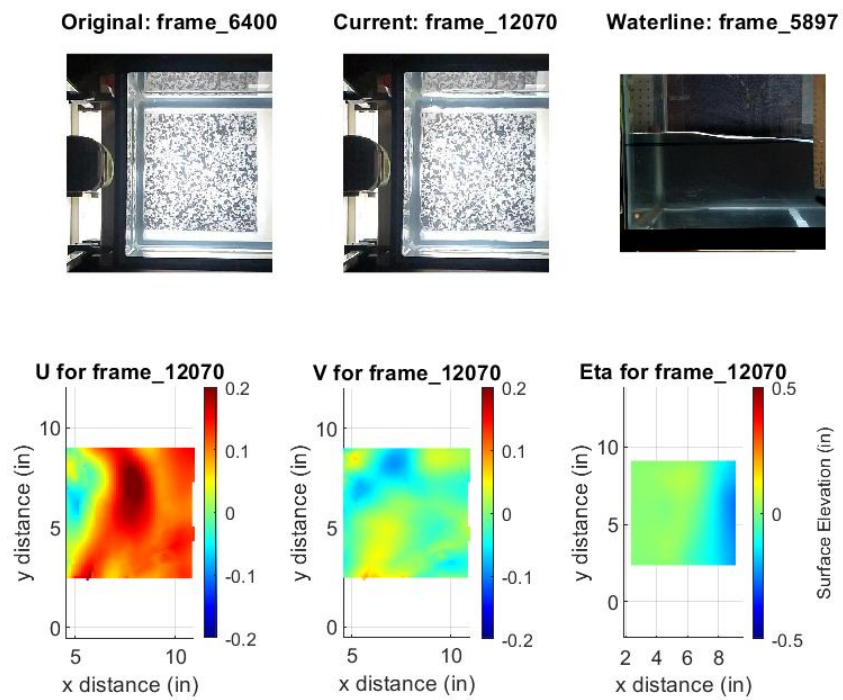


*Figure 7.1: Results of the DIC analysis for frame 12070, outputs include  $u$  displacement,  $v$  displacement and surface elevation ( $\eta$ ).*

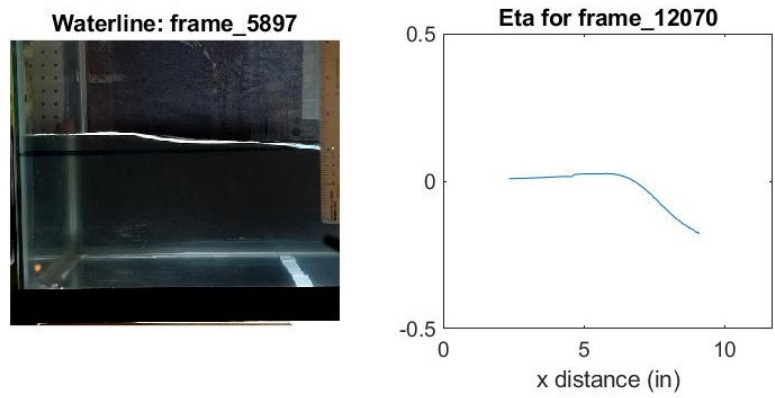


Figure 7.2: Results of the DIC analysis for frame 12070, comparing the waterline video to the surface elevation at that location.

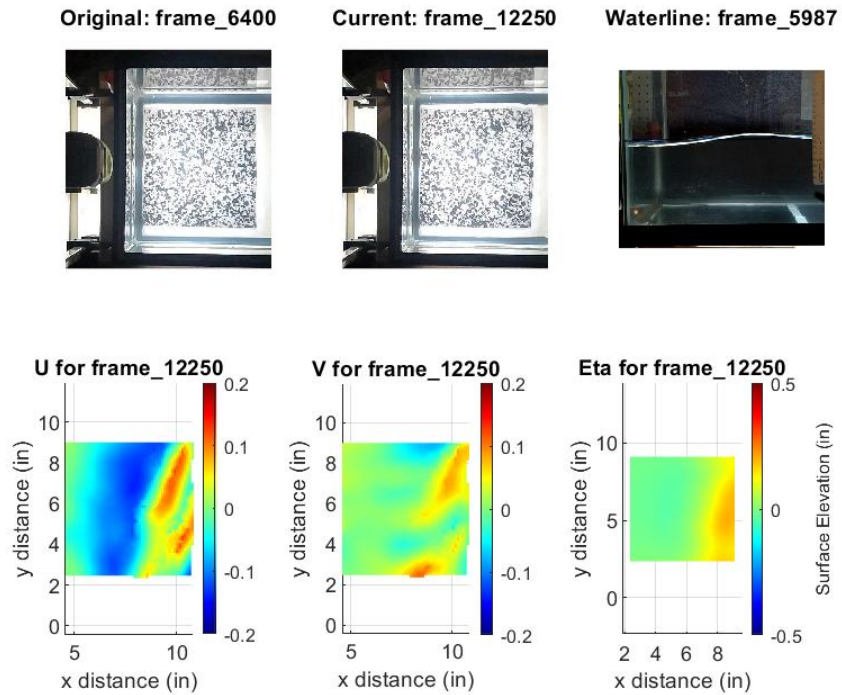


Figure 7.3: Results of the DIC analysis for frame 12250, outputs include  $u$  displacement,  $v$  displacement and surface elevation ( $\eta$ ).

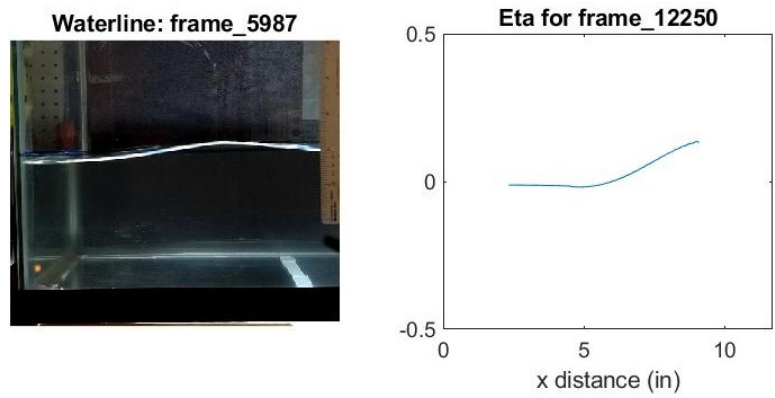


Figure 7.4: Results of the DIC analysis for frame 12250, comparing the waterline video to the surface elevation at that location.

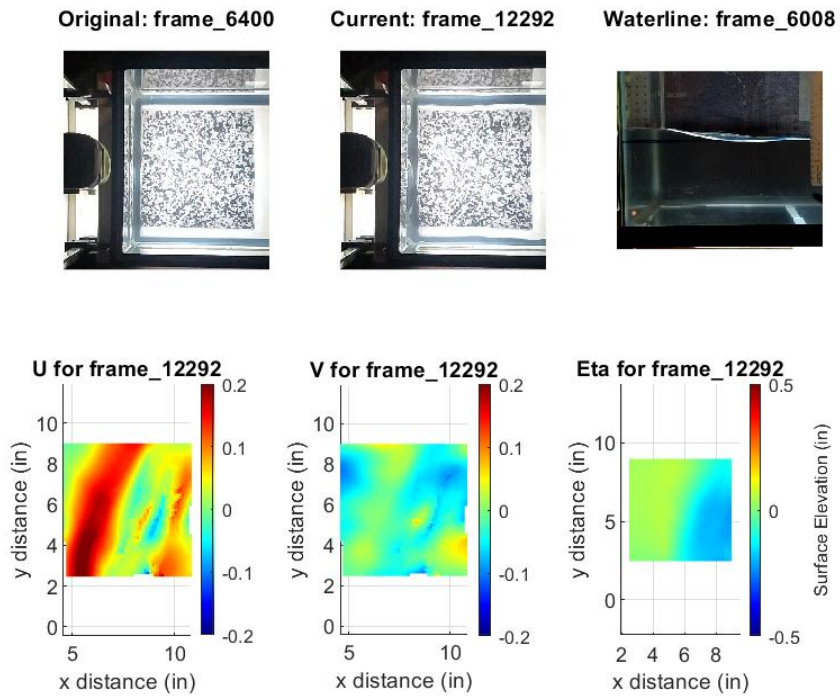


Figure 7.5: Results of the DIC analysis for frame 12292, outputs include  $u$  displacement,  $v$  displacement and surface elevation ( $\eta$ ).

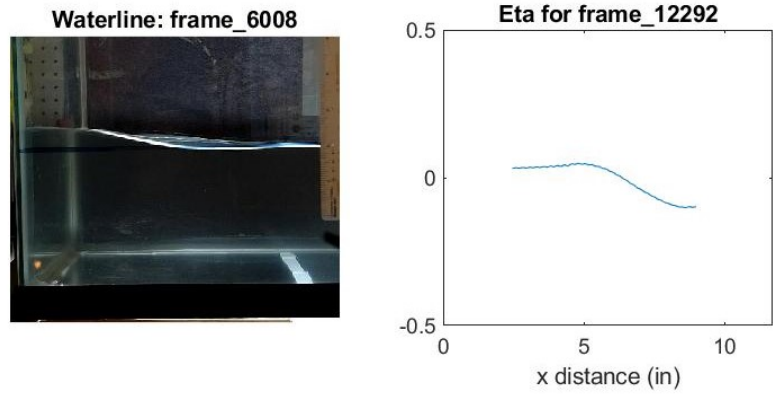


Figure 7.6: Results of the DIC analysis for frame 12292, comparing the waterline video to the surface elevation at that location.

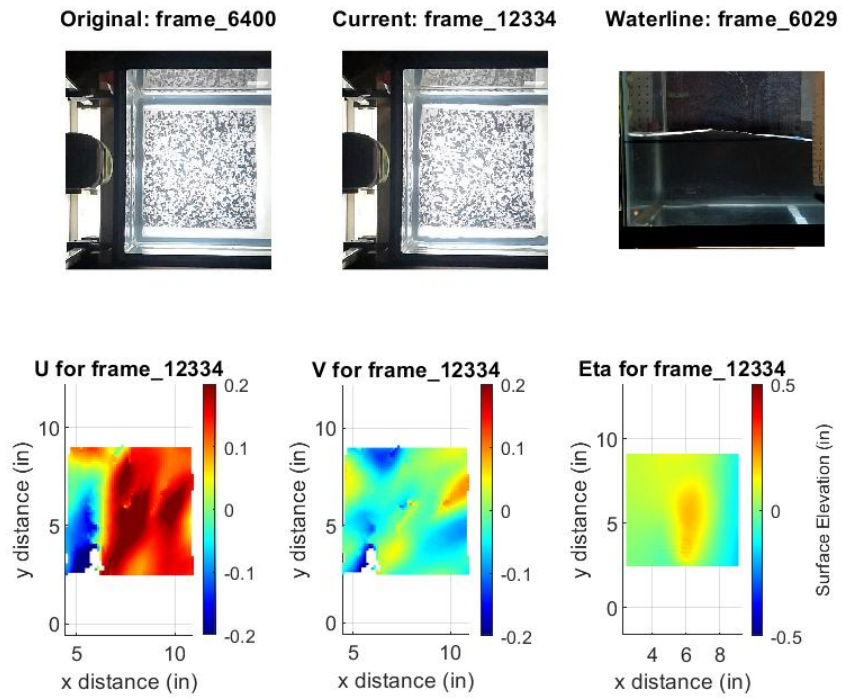


Figure 7.7: Results of the DIC analysis for frame 12334, outputs include  $u$  displacement,  $v$  displacement and surface elevation ( $\eta$ ).

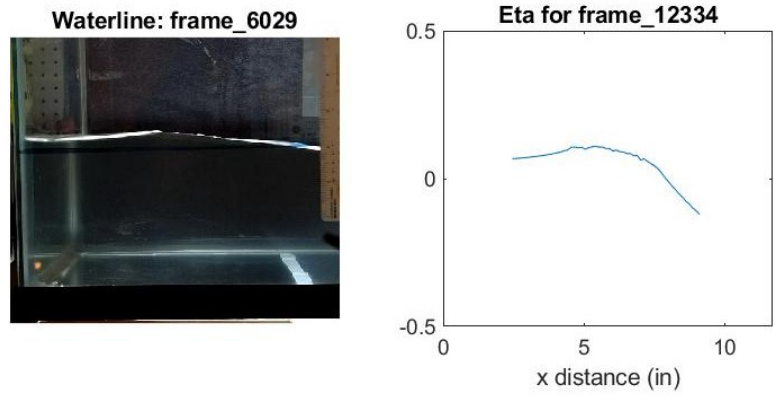


Figure 7.8: Results of the DIC analysis for frame 12334, comparing the waterline video to the surface elevation at that location.

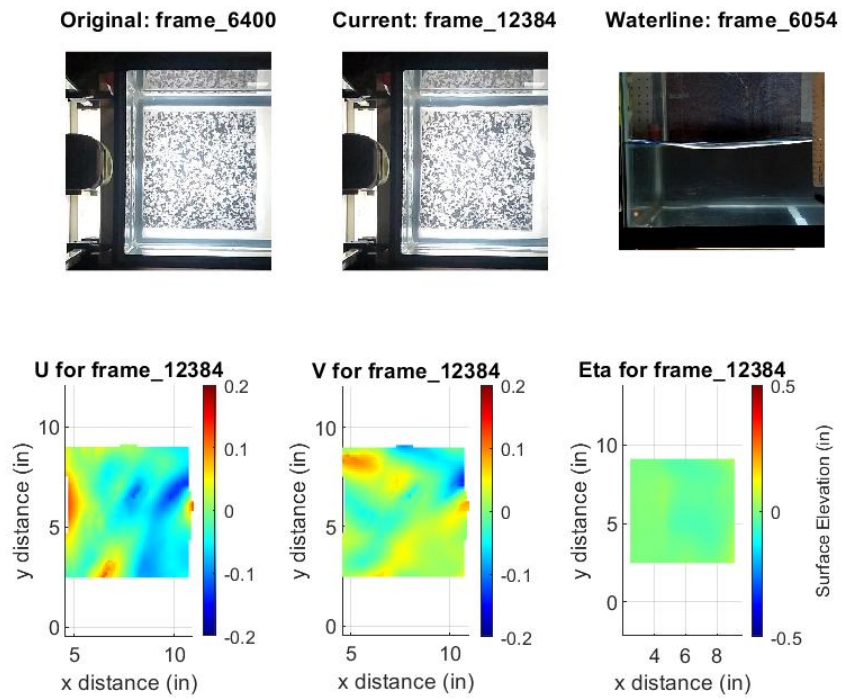


Figure 7.9: Results of the DIC analysis for frame 12384, outputs include  $u$  displacement,  $v$  displacement and surface elevation ( $\eta$ ).

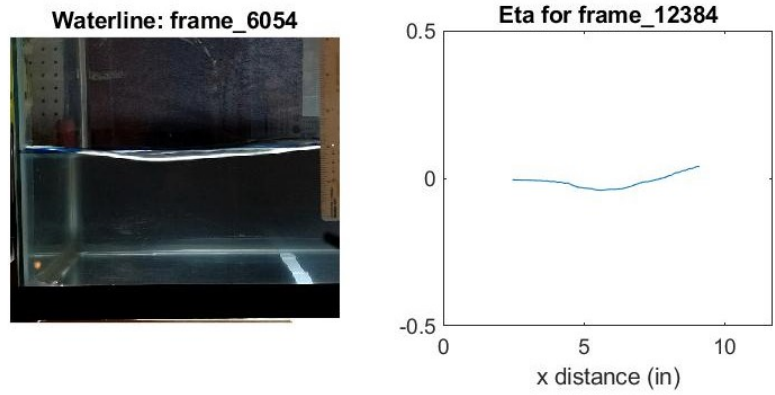


Figure 7.10: Results of the DIC analysis for frame 12384, comparing the waterline video to the surface elevation at that location.

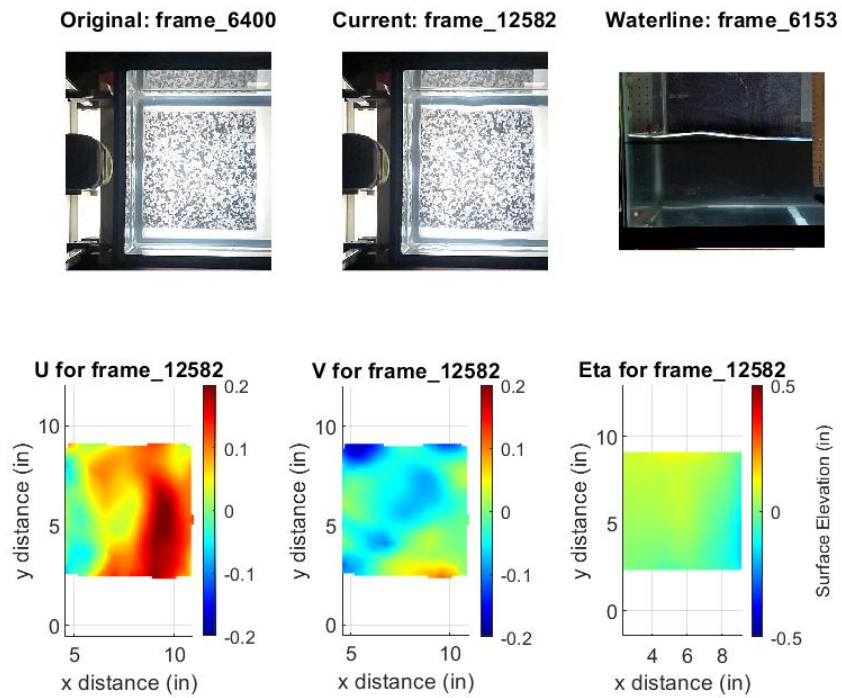


Figure 7.11: Results of the DIC analysis for frame 12582, outputs include  $u$  displacement,  $v$  displacement and surface elevation ( $\eta$ ).

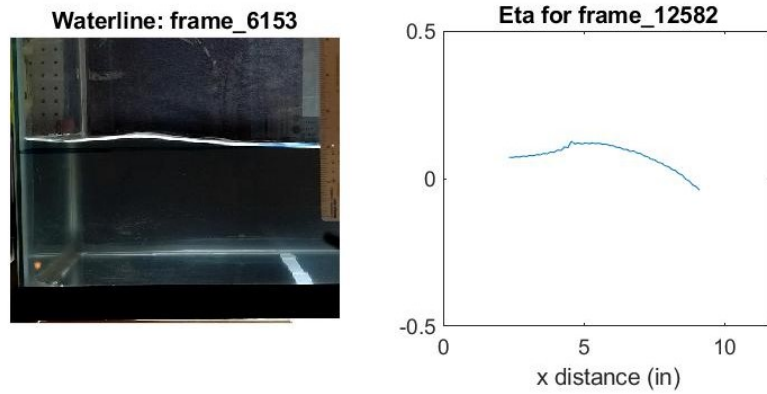


Figure 7.12: Results of the DIC analysis for frame 12582, comparing the waterline video to the surface elevation at that location.

## 7.2 Side View Image Analysis Results for the Comparison of Experiments: 1/12/2021 and 2/11/2021

### 7.2.1 HDPE Foil with; angle of attack: $10^\circ$ & depth of foil: $1 \times$ chord length

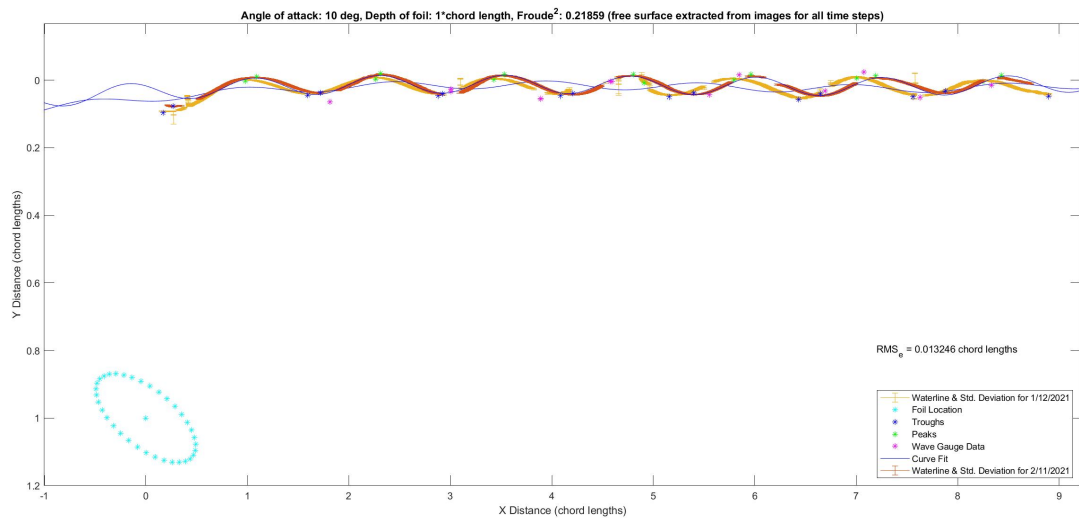


Figure 7.13: Results using the side view analysis for the larger HDPE foil at an angle of attack of 10 degrees, a depth of  $1 \times$  chord length, and with a flow speed of 0.80 m/s averaged over the time of the experiment (50 seconds).

	1/12/2021	2/11/2021
Mean wave height (cl)	0.0625	0.0591
Range for wave height (cl)	0.0561	0.0399
Standard Deviation for wave height (cl)	0.0194	0.0127
Variance for wave height ( $cl^2$ )	0.0004	0.0002
Mean wave length (cl)	1.2302	1.2455
Range for wave length (cl)	0.5938	0.2922
Standard Deviation for wave length (cl)	0.1522	0.0732
Variance for wave length ( $cl^2$ )	0.0232	0.0054

Table 7.1: Results of the variability in wave height and wavelengths from the two different experiments for the case with an angle of attack of 10 degrees, a depth of 1\*chord length, and with a flow speed of 0.80 m/s.

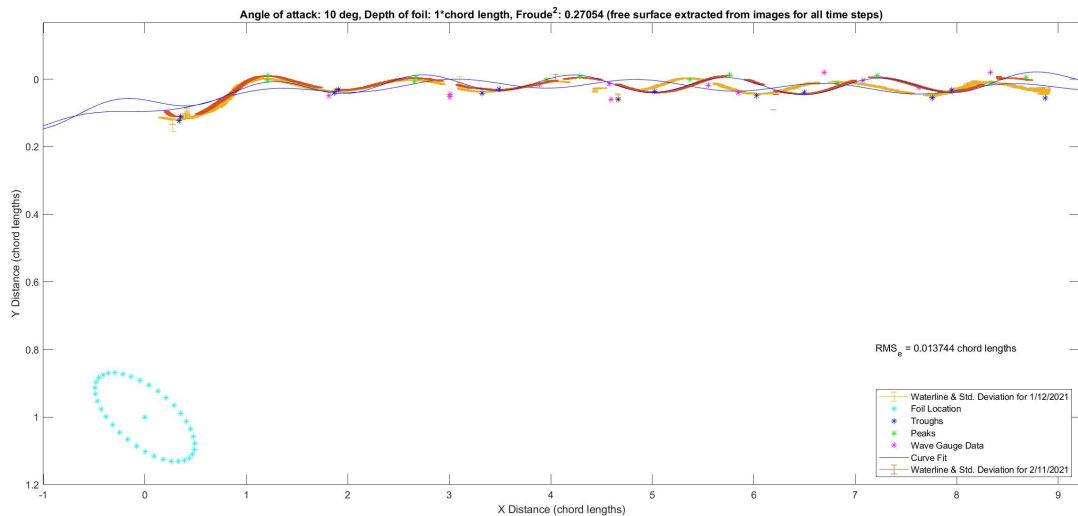


Figure 7.14: Results using the side view analysis for the larger HDPE foil at an angle of attack of 10 degrees, a depth of 1\*chord length, and with a flow speed of 0.89 m/s averaged over the time of the experiment (50 seconds).

	1/12/2021	2/11/2021
Mean wave height (cl)	0.0636	0.0553
Range for wave height (cl)	0.0884	0.085
Standard Deviation for wave height (cl)	0.0339	0.0331
Variance for wave height ( $cl^2$ )	0.0012	0.0011
Mean wave length (cl)	1.4242	1.5064
Range for wave length (cl)	0.6159	0.163
Standard Deviation for wave length (cl)	0.1537	0.0606
Variance for wave length ( $cl^2$ )	0.0236	0.0037

Table 7.2: Results of the variability in wave height and wavelengths from the two different experiments for the case with an angle of attack 10 degrees, a depth of 1\*chord length, and with a flow speed of 0.89 m/s.

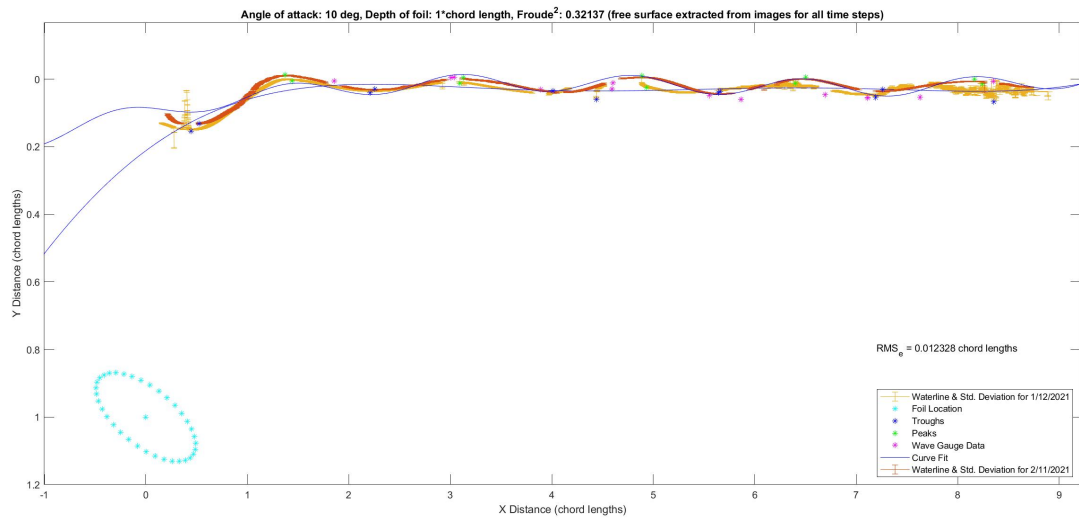


Figure 7.15: Results using the side view analysis for the larger HDPE foil at an angle of attack of 10 degrees, a depth of 1\*chord length at a speed of 0.97 m/s averaged over the time of the experiment (50 seconds).

	1/12/2021	2/11/2021
Mean wave height (cl)	0.064	0.0595
Range for wave height (cl)	0.1273	0.1137
Standard Deviation for wave height (cl)	0.0539	0.0476
Variance for wave height ( $cl^2$ )	0.0029	0.0023
Mean wave length (cl)	1.6342	1.6912
Range for wave length (cl)	1.0672	0.1404
Standard Deviation for wave length (cl)	0.3333	0.0652
Variance for wave length ( $cl^2$ )	0.1111	0.0043

Table 7.3: Results of the variability in wave height and wavelengths from the two different experiments for the case with an angle of attack 10 degrees, a depth of 1\*chord length, and with a flow speed of 0.97 m/s.

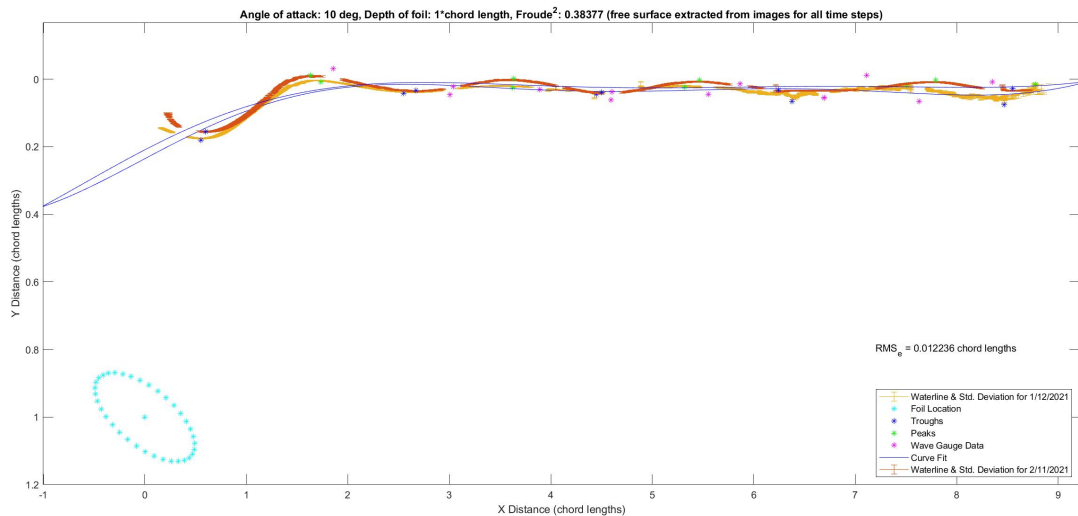


Figure 7.16: Results using the side view analysis for the larger HDPE foil at an angle of attack of 10 degrees, a depth of 1\*chord length at a speed of 1.06 m/s averaged over the time of the experiment (50 seconds).

	1/12/2021	2/11/2021
Mean wave height (cl)	0.0744	0.0667
Range for wave height (cl)	0.1552	0.1377
Standard Deviation for wave height (cl)	0.0641	0.0668
Variance for wave height ( $cl^2$ )	0.0041	0.0045
Mean wave length (cl)	1.8694	2.0162
Range for wave length (cl)	0.9089	0.5908
Standard Deviation for wave length (cl)	0.2813	0.2363
Variance for wave length ( $cl^2$ )	0.0791	0.0558

Table 7.4: Results of the variability in wave height and wavelengths from the two different experiments for the case with an angle of attack 10 degrees, a depth of 1\*chord length, and with a flow speed of 1.06 m/s.

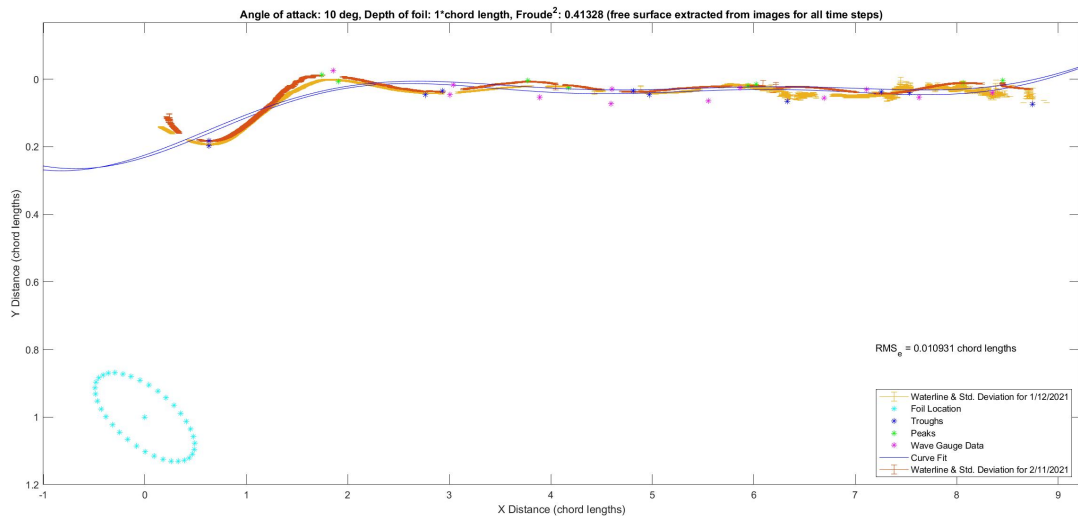


Figure 7.17: Results using the side view analysis for the larger HDPE foil at an angle of attack of 10 degrees, a depth of 1\*chord length at a speed of 1.10 m/s averaged over the time of the experiment (50 seconds).

	<b>1/12/2021</b>	<b>2/11/2021</b>
<b>Mean wave height (cl)</b>	0.0886	0.0698
<b>Range for wave height (cl)</b>	0.1696	0.1763
<b>Standard Deviation for wave height (cl)</b>	0.0803	0.0842
<b>Variance for wave height (<math>cl^2</math>)</b>	0.0065	0.0071
<b>Mean wave length (cl)</b>	1.7845	2.2221
<b>Range for wave length (cl)</b>	1.0593	0.5601
<b>Standard Deviation for wave length (cl)</b>	0.4619	0.2237
<b>Variance for wave length (<math>cl^2</math>)</b>	0.2133	0.0501

*Table 7.5: Results of the variability in wave height and wavelenghts from the two different experiments for the case with an angle of attack 10 degrees, a depth of 1\*chord length, and with a flow speed of 1.10 m/s.*

## 7.2.2 HDPE Foil with; angle of attack: $10^\circ$ & depth of foil: $5/4$ \*chord length

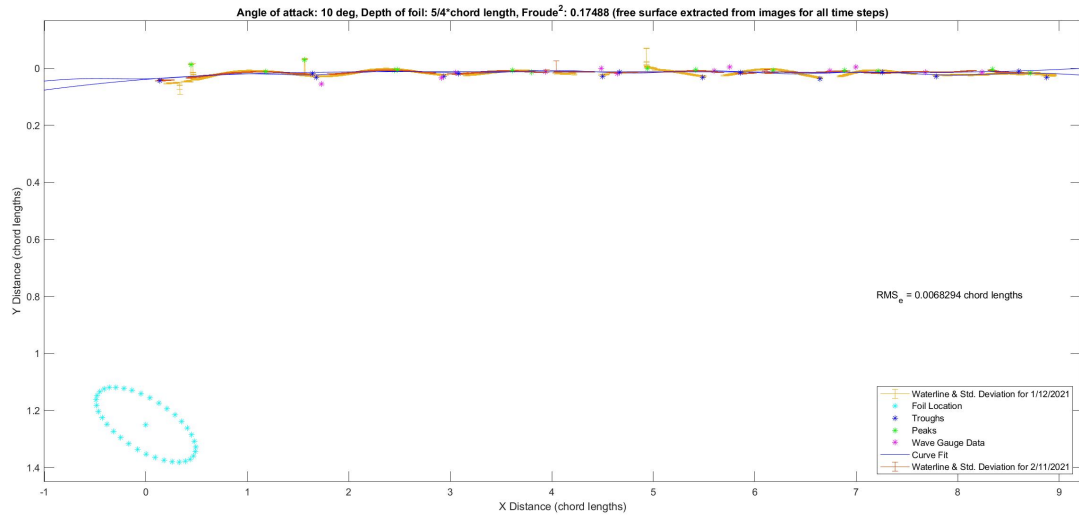


Figure 7.18: Results using the side view analysis for the larger HDPE foil at an angle of attack of 10 degrees, a depth of  $5/4$ \*chord length at a speed of 0.80 m/s averaged over the time of the experiment (50 seconds).

	1/12/2021	2/11/2021
Mean wave height (cl)	0.0137	0.0141
Range for wave height (cl)	0.0441	0.024
Standard Deviation for wave height (cl)	0.0171	0.009
Variance for wave height ( $cl^2$ )	0.0003	0.0001
Mean wave length (cl)	1.1901	1.4204
Range for wave length (cl)	0.6809	0.6715
Standard Deviation for wave length (cl)	0.1936	0.1841
Variance for wave length ( $cl^2$ )	0.0375	0.0339

Table 7.6: Results of the variability in wave height and wavelengths from the two different experiments for the case with an angle of attack 10 degrees, a depth of  $5/4$ \*chord length, and with a flow speed of 0.80 m/s.

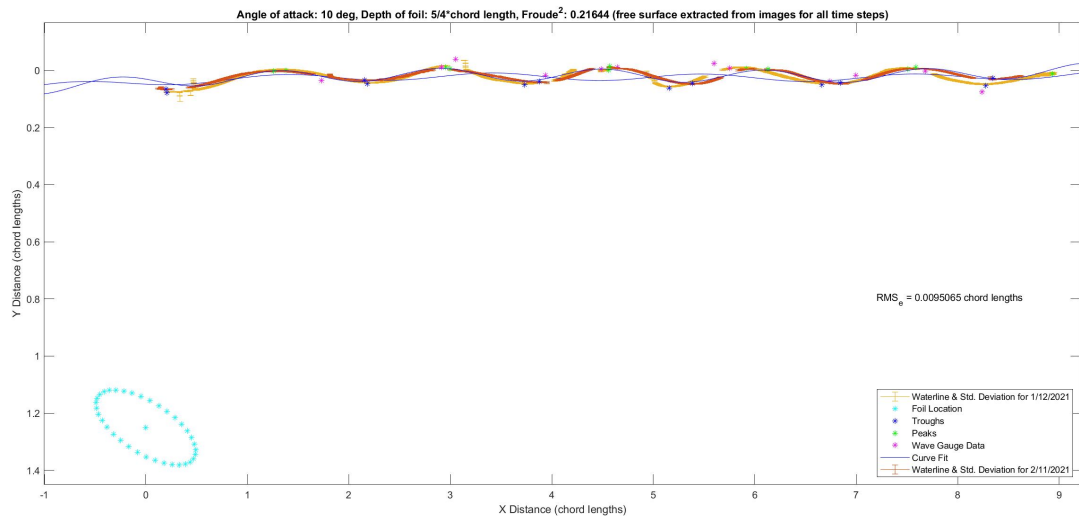


Figure 7.19: Results using the side view analysis for the larger HDPE foil at an angle of attack of 10 degrees, a depth of  $5/4$ \*chord length at a speed of 0.89 m/s averaged over the time of the experiment (50 seconds).

	1/12/2021	2/11/2021
Mean wave height (cl)	0.0683	0.0521
Range for wave height (cl)	0.0426	0.024
Standard Deviation for wave height (cl)	0.0145	0.0087
Variance for wave height ( $cl^2$ )	0.0002	0.0001
Mean wave length (cl)	1.5617	1.608
Range for wave length (cl)	0.6143	0.4988
Standard Deviation for wave length (cl)	0.1691	0.1659
Variance for wave length ( $cl^2$ )	0.0286	0.0275

Table 7.7: Results of the variability in wave height and wavelengths from the two different experiments for the case with an angle of attack 10 degrees, a depth of  $5/4$ \*chord length, and with a flow speed of 0.89 m/s.

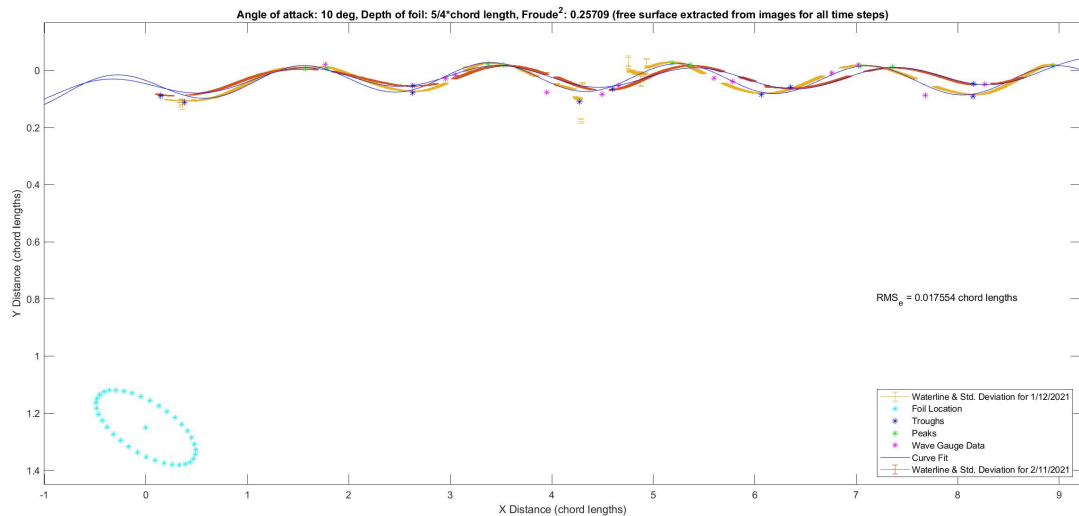


Figure 7.20: Results using the side view analysis for the larger HDPE foil at an angle of attack of 10 degrees, a depth of  $5/4$ \*chord length at a speed of 0.97 m/s averaged over the time of the experiment (50 seconds).

	1/12/2021	2/11/2021
Mean wave height (cl)	0.1228	0.0811
Range for wave height (cl)	0.0368	0.0231
Standard Deviation for wave height (cl)	0.0166	0.0109
Variance for wave height ( $cl^2$ )	0.0003	0.0001
Mean wave length (cl)	1.8648	1.9697
Range for wave length (cl)	0.665	0.7231
Standard Deviation for wave length (cl)	0.219	0.2413
Variance for wave length ( $cl^2$ )	0.048	0.0582

Table 7.8: Results of the variability in wave height and wavelengths from the two different experiments for the case with an angle of attack 10 degrees, a depth of  $5/4$ \*chord length, and with a flow speed of 0.97 m/s.

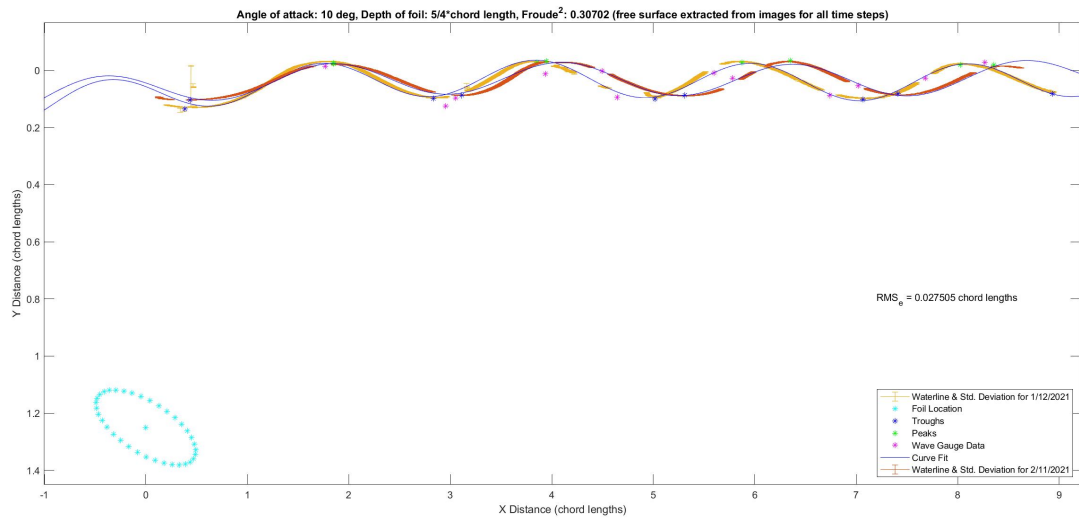


Figure 7.21: Results using the side view analysis for the larger HDPE foil at an angle of attack of 10 degrees, a depth of  $5/4$ \*chord length at a speed of 1.06 m/s averaged over the time of the experiment (50 seconds).

	1/12/2021	2/11/2021
Mean wave height (cl)	0.146	0.1167
Range for wave height (cl)	0.0438	0.0236
Standard Deviation for wave height (cl)	0.0208	0.0102
Variance for wave height ( $cl^2$ )	0.0004	0.0001
Mean wave length (cl)	2.1041	2.2468
Range for wave length (cl)	0.5843	0.6682
Standard Deviation for wave length (cl)	0.1848	0.2503
Variance for wave length ( $cl^2$ )	0.0341	0.0626

Table 7.9: Results of the variability in wave height and wavelengths from the two different experiments for the case with an angle of attack 10 degrees, a depth of  $5/4$ \*chord length, and with a flow speed of 1.06 m/s.

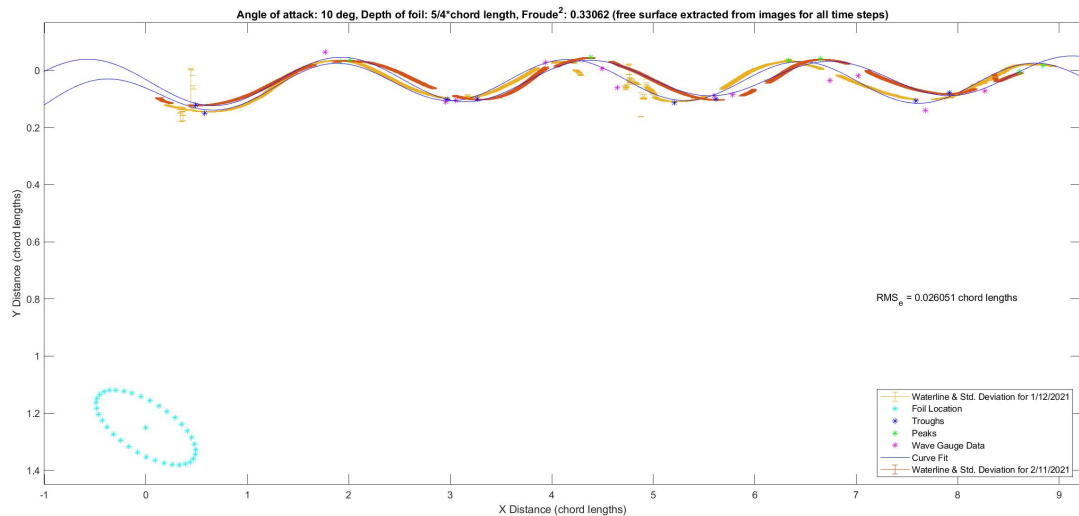


Figure 7.22: Results using the side view analysis for the larger HDPE foil at an angle of attack of 10 degrees, a depth of  $5/4$ \*chord length at a speed of 1.10 m/s averaged over the time of the experiment (50 seconds).

	<b>1/12/2021</b>	<b>2/11/2021</b>
<b>Mean wave height (cl)</b>	0.1586	0.1484
<b>Range for wave height (cl)</b>	0.0569	0.0161
<b>Standard Deviation for wave height (cl)</b>	0.0261	0.0082
<b>Variance for wave height (<math>cl^2</math>)</b>	0.0007	0.0001
<b>Mean wave length (cl)</b>	2.321	2.4124
<b>Range for wave length (cl)</b>	0.3024	0.5084
<b>Standard Deviation for wave length (cl)</b>	0.1216	0.2059
<b>Variance for wave length (<math>cl^2</math>)</b>	0.0148	0.0424

*Table 7.10: Results of the variability in wave height and wavelengths from the two different experiments for the case with an angle of attack 10 degrees, a depth of  $5/4$ \*chord length, and with a flow speed of 1.10 m/s.*

### 7.2.3 HDPE Foil with; angle of attack: $10^\circ$ & depth of foil: $3/2 \cdot \text{chord length}$ length

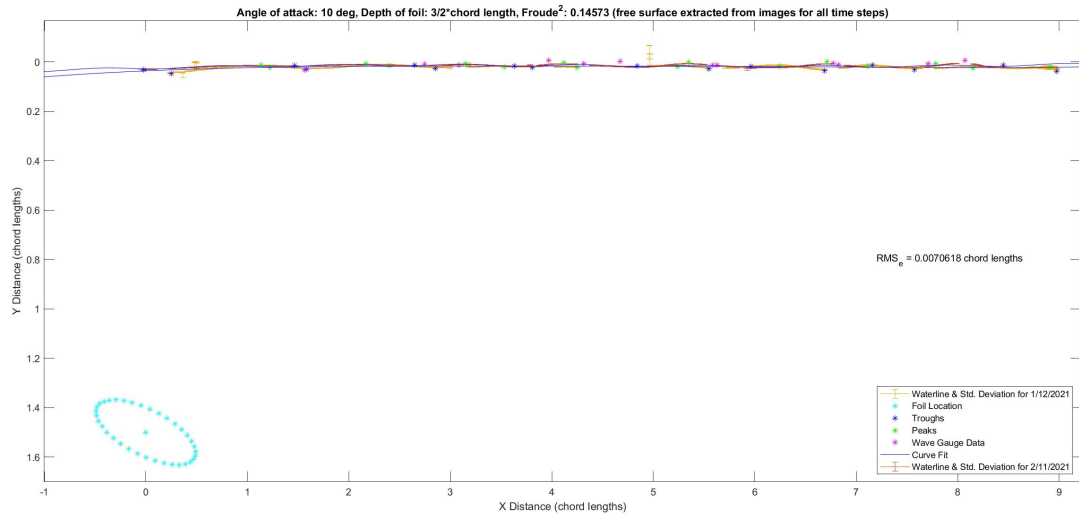


Figure 7.23: Results using the side view analysis for the larger HDPE foil at an angle of attack of 10 degrees, a depth of  $3/2 \cdot \text{chord length}$  at a speed of 0.80 m/s averaged over the time of the experiment (50 seconds).

	1/12/2021	2/11/2021
Mean wave height (cl)	0.0146	0.0125
Range for wave height (cl)	0.0299	0.0134
Standard Deviation for wave height (cl)	0.0105	0.0059
Variance for wave height ( $cl^2$ )	0.0001	$3.522 \times 10^{-5}$
Mean wave length (cl)	1.094	1.1631
Range for wave length (cl)	1.0229	0.5117
Standard Deviation for wave length (cl)	0.2671	0.1577
Variance for wave length ( $cl^2$ )	0.0713	0.0249

Table 7.11: Results of the variability in wave height and wavelengths from the two different experiments for the case with an angle of attack 10 degrees, a depth of  $3/2$ \*chord length, and with a flow speed of 0.80 m/s.

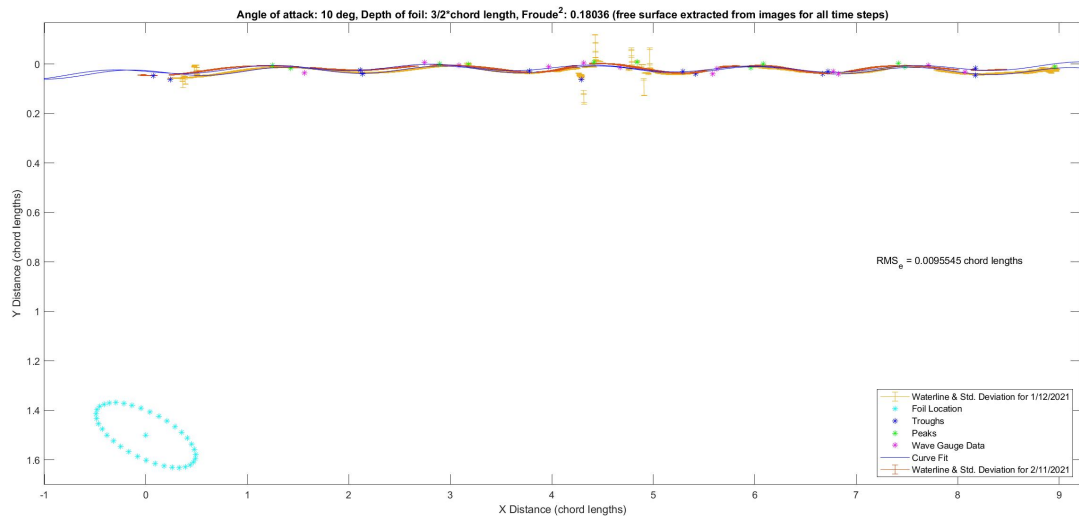


Figure 7.24: Results using the side view analysis for the larger HDPE foil at an angle of attack of 10 degrees, a depth of  $3/2$ \*chord length at a speed of 0.89 m/s averaged over the time of the experiment (50 seconds).

	1/12/2021	2/11/2021
Mean wave height (cl)	0.0495	0.0331
Range for wave height (cl)	0.0451	0.0172
Standard Deviation for wave height (cl)	0.0161	0.0066
Variance for wave height ( $cl^2$ )	0.0003	$4.355 \times 10^{-5}$
Mean wave length (cl)	1.5465	1.5859
Range for wave length (cl)	1.0339	0.7037
Standard Deviation for wave length (cl)	0.333	0.2048
Variance for wave length ( $cl^2$ )	0.1109	0.0419

Table 7.12: Results of the variability in wave height and wavelengths from the two different experiments for the case with an angle of attack 10 degrees, a depth of  $3/2$ \*chord length, and with a flow speed of 0.89 m/s.

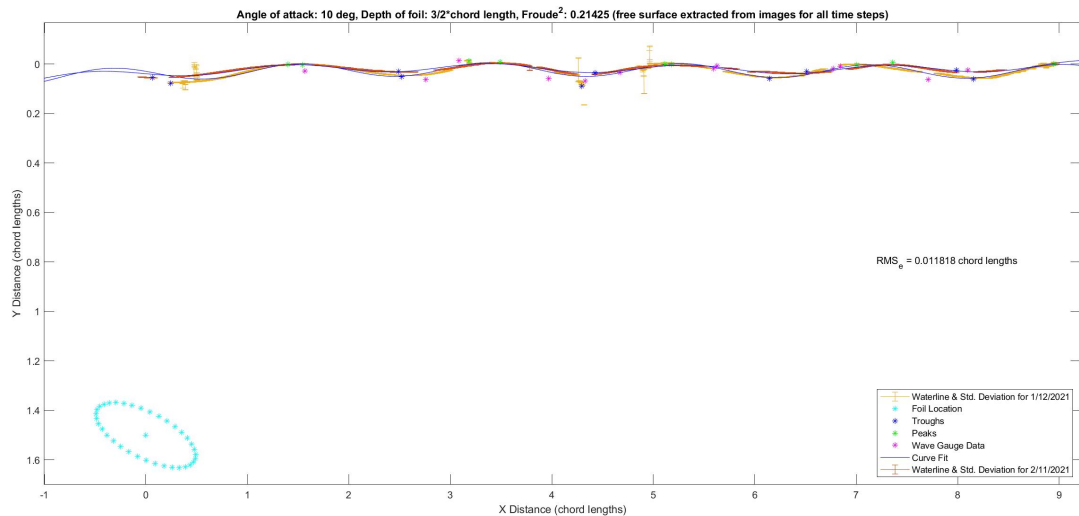


Figure 7.25: Results using the side view analysis for the larger HDPE foil at an angle of attack of 10 degrees, a depth of  $3/2$ \*chord length at a speed of 0.97 m/s averaged over the time of the experiment (50 seconds).

	1/12/2021	2/11/2021
Mean wave height (cl)	0.0788	0.0418
Range for wave height (cl)	0.0337	0.0177
Standard Deviation for wave height (cl)	0.0144	0.0086
Variance for wave height ( $cl^2$ )	0.0002	0.0001
Mean wave length (cl)	1.9139	1.984
Range for wave length (cl)	0.6381	0.9539
Standard Deviation for wave length (cl)	0.191	0.3367
Variance for wave length ( $cl^2$ )	0.0365	0.1134

Table 7.13: Results of the variability in wave height and wavelengths from the two different experiments for the case with an angle of attack 10 degrees, a depth of  $3/2$ \*chord length, and with a flow speed of 0.97 m/s.

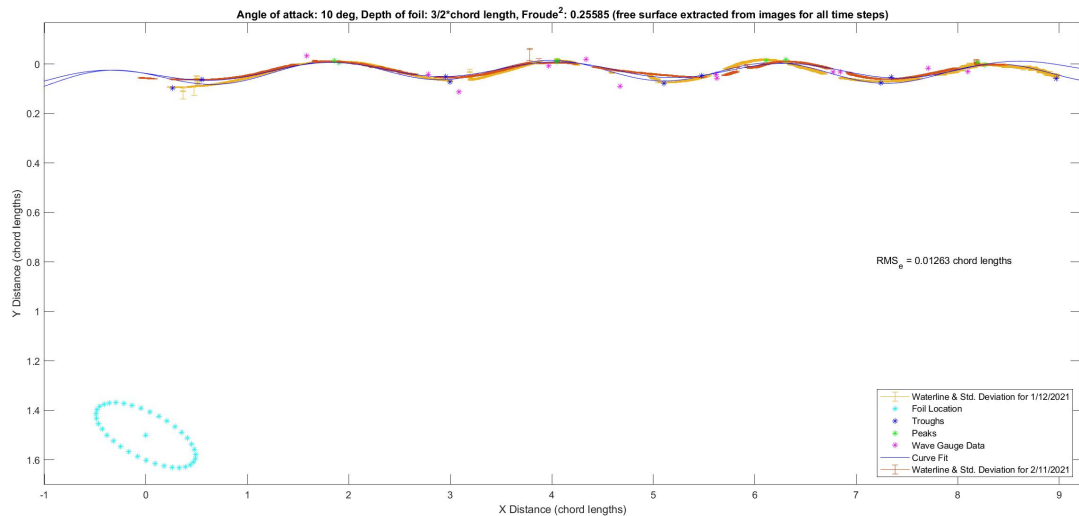


Figure 7.26: Results using the side view analysis for the larger HDPE foil at an angle of attack of 10 degrees, a depth of  $3/2$ \*chord length at a speed of 1.06 m/s averaged over the time of the experiment (50 seconds).

	1/12/2021	2/11/2021
Mean wave height (cl)	0.1021	0.0666
Range for wave height (cl)	0.0381	0.0159
Standard Deviation for wave height (cl)	0.016	0.0073
Variance for wave height ( $cl^2$ )	0.0003	0.0001
Mean wave length (cl)	2.1527	2.1887
Range for wave length (cl)	1.0023	0.6505
Standard Deviation for wave length (cl)	0.2963	0.265
Variance for wave length ( $cl^2$ )	0.0878	0.0702

Table 7.14: Results of the variability in wave height and wavelengths from the two different experiments for the case with an angle of attack 10 degrees, a depth of  $3/2$ \*chord length, and with a flow speed of 1.06 m/s.

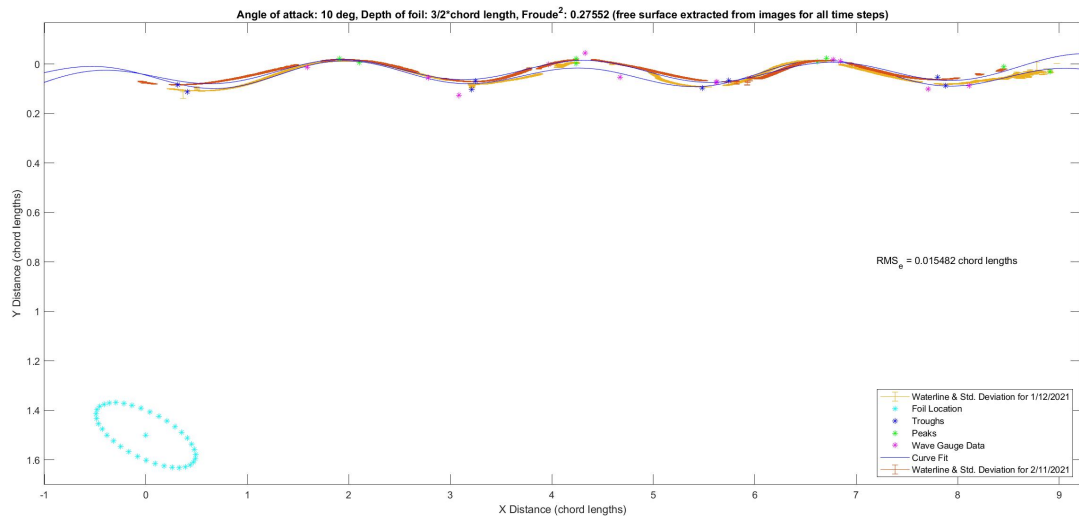


Figure 7.27: Results using the side view analysis for the larger HDPE foil at an angle of attack of 10 degrees, a depth of  $3/2$ \*chord length at a speed of 1.10 m/s averaged over the time of the experiment (50 seconds).

	<b>1/12/2021</b>	<b>2/11/2021</b>
<b>Mean wave height (cl)</b>	0.1109	0.0814
<b>Range for wave height (cl)</b>	0.0679	0.0624
<b>Standard Deviation for wave height (cl)</b>	0.029	0.0269
<b>Variance for wave height (<math>cl^2</math>)</b>	0.0008	0.0007
<b>Mean wave length (cl)</b>	2.3801	2.3386
<b>Range for wave length (cl)</b>	0.6682	1.1831
<b>Standard Deviation for wave length (cl)</b>	0.2278	0.4049
<b>Variance for wave length (<math>cl^2</math>)</b>	0.0519	0.1639

*Table 7.15: Results of the variability in wave height and wavelengths from the two different experiments for the case with an angle of attack 10 degrees, a depth of  $3/2$ \*chord length, and with a flow speed of 1.10 m/s.*

### 7.3 Side View Image Analysis Results for 5° angle of attack: 2/11/2021

#### 7.3.1 HDPE Foil with; angle of attack: 5° & depth of foil: 1\*chord length

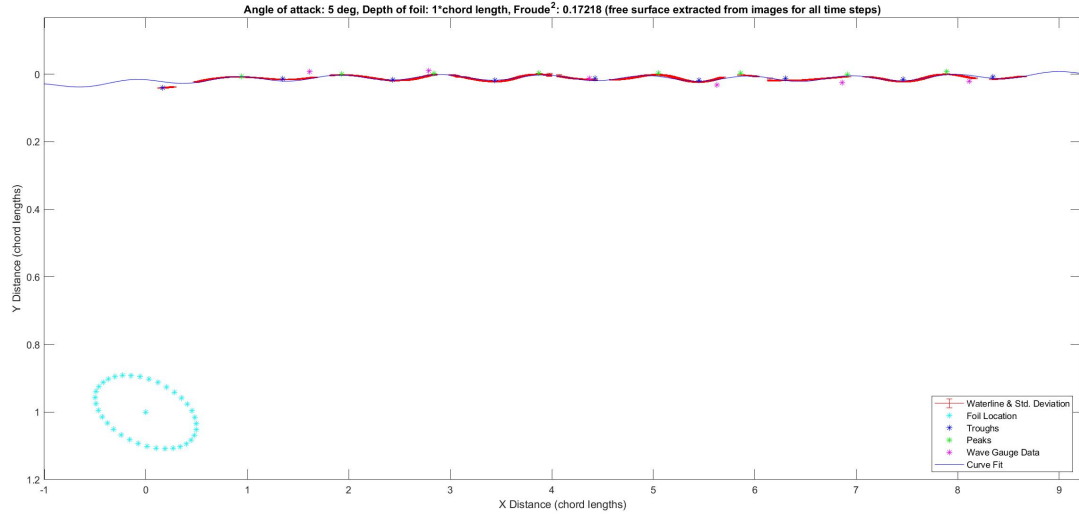


Figure 7.28: Results using the side view analysis for the larger HDPE foil at an angle of attack of 5 degrees, a depth of 1\*chord length at a speed of 0.71 m/s averaged over the time of the experiment (50 seconds).

	2/11/2021
Range for wave height (chord length)	0.020821
Standard Deviation for wave height (chord length)	0.0065761
Variance for wave height (chordlength <sup>2</sup> )	4.3245x10 <sup>-5</sup>
Range for wavelength (chord length)	0.37286
Standard Deviation for wavelength (chord length)	0.11364
Variance for wavelength (chordlength <sup>2</sup> )	0.012915

Table 7.16: Results of the variability in wave height and wavelengths for the case with an angle of attack 5 degrees, a depth of 1\*chord length, and with a flow speed of 0.71 m/s.

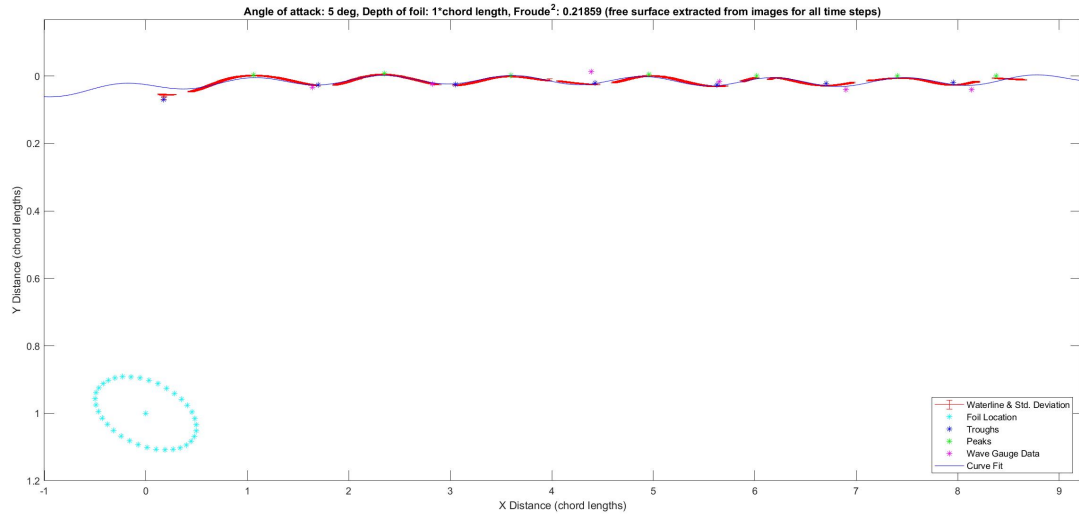


Figure 7.29: Results using the side view analysis for the larger HDPE foil at an angle of attack of 5 degrees, a depth of 1\*chord length at a speed of 0.80 m/s averaged over the time of the experiment (50 seconds).

	<b>2/11/2021</b>
<b>Range for wave height (chord length)</b>	0.052562
<b>Standard Deviation for wave height (chord length)</b>	0.018294
<b>Variance for wave height (<math>chordlength^2</math>)</b>	0.00033469
<b>Range for wavelength (chord length)</b>	0.55202
<b>Standard Deviation for wavelength (chord length)</b>	0.15911
<b>Variance for wavelength (<math>chordlength^2</math>)</b>	0.025316

Table 7.17: Results of the variability in wave height and wavelengths for the case with an angle of attack 5 degrees, a depth of 1\*chord length, and with a flow speed of 0.80 m/s.

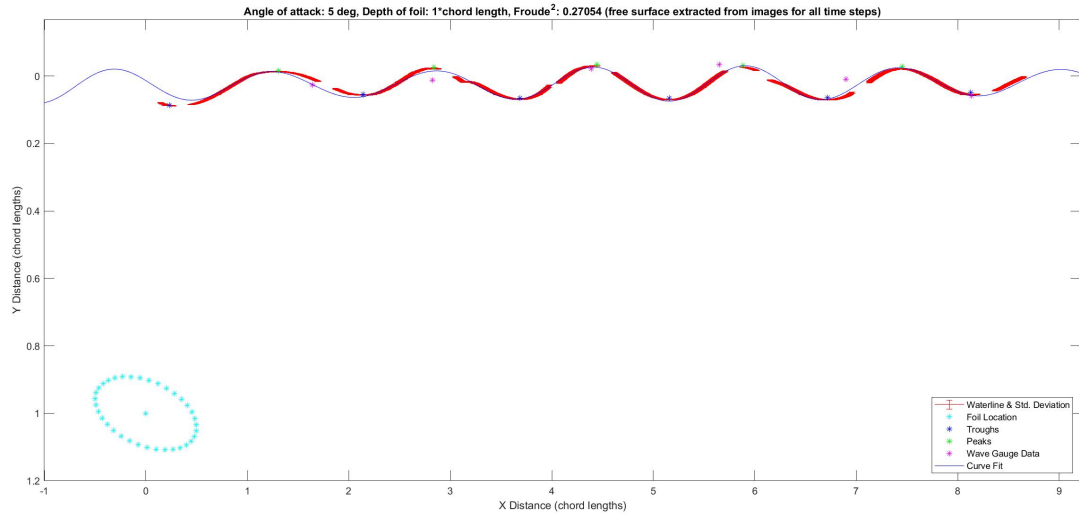


Figure 7.30: Results using the side view analysis for the larger HDPE foil at an angle of attack of 5 degrees, a depth of 1\*chord length at a speed of 0.89 m/s averaged over the time of the experiment (50 seconds).

	<b>2/11/2021</b>
<b>Range for wave height (chord length)</b>	0.021094
<b>Standard Deviation for wave height (chord length)</b>	0.0084405
<b>Variance for wave height (chordlength<sup>2</sup>)</b>	$7.1242 \times 10^{-5}$
<b>Range for wavelength (chord length)</b>	0.49553
<b>Standard Deviation for wavelength (chord length)</b>	0.14497
<b>Variance for wavelength (chordlength<sup>2</sup>)</b>	0.021016

Table 7.18: Results of the variability in wave height and wavelengths for the case with an angle of attack 5 degrees, a depth of 1\*chord length, and with a flow speed of 0.89 m/s.

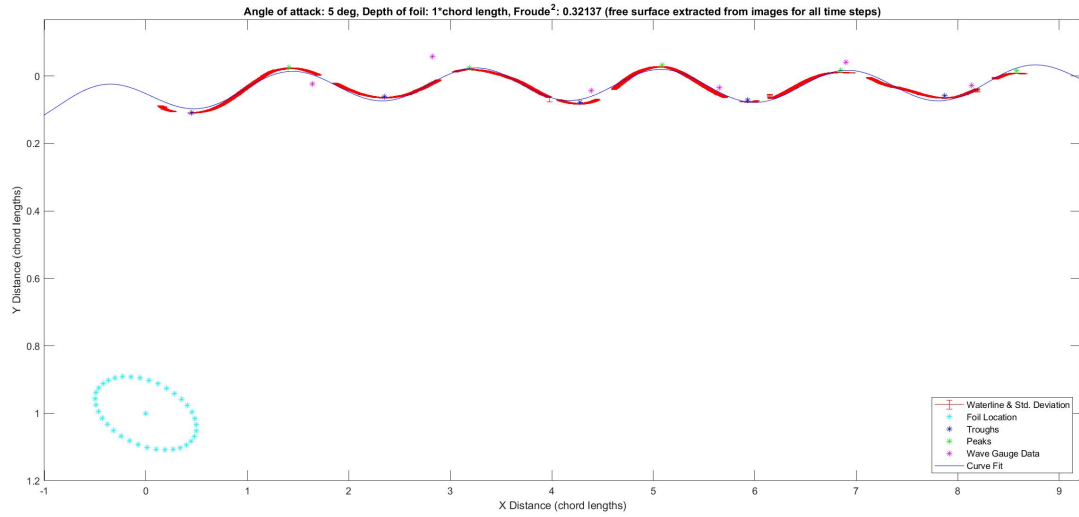


Figure 7.31: Results using the side view analysis for the larger HDPE foil at an angle of attack of 5 degrees, a depth of 1\*chord length at a speed of 0.97 m/s averaged over the time of the experiment (50 seconds).

	<b>2/11/2021</b>
<b>Range for wave height (chord length)</b>	0.059201
<b>Standard Deviation for wave height (chord length)</b>	0.023637
<b>Variance for wave height (<math>chordlength^2</math>)</b>	0.00055871
<b>Range for wavelength (chord length)</b>	0.29054
<b>Standard Deviation for wavelength (chord length)</b>	0.10675
<b>Variance for wavelength (<math>chordlength^2</math>)</b>	0.011396

Table 7.19: Results of the variability in wave height and wavelengths for the case with an angle of attack 5 degrees, a depth of 1\*chord length, and with a flow speed of 0.97 m/s.

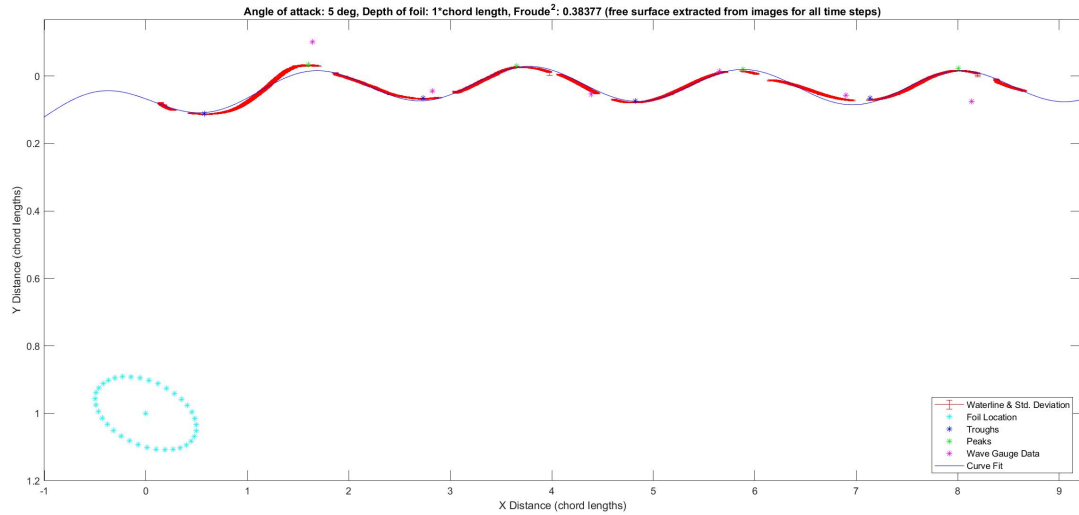


Figure 7.32: Results using the side view analysis for the larger HDPE foil at an angle of attack of 5 degrees, a depth of 1\*chord length at a speed of 1.06 m/s averaged over the time of the experiment (50 seconds).

	<b>2/11/2021</b>
<b>Range for wave height (chord length)</b>	0.057951
<b>Standard Deviation for wave height (chord length)</b>	0.027178
<b>Variance for wave height (<math>chordlength^2</math>)</b>	0.00073866
<b>Range for wavelength (chord length)</b>	0.26471
<b>Standard Deviation for wavelength (chord length)</b>	0.09707
<b>Variance for wavelength (<math>chordlength^2</math>)</b>	0.0094226

Table 7.20: Results of the variability in wave height and wavelengths for the case with an angle of attack 5 degrees, a depth of 1\*chord length, and with a flow speed of 1.06 m/s.

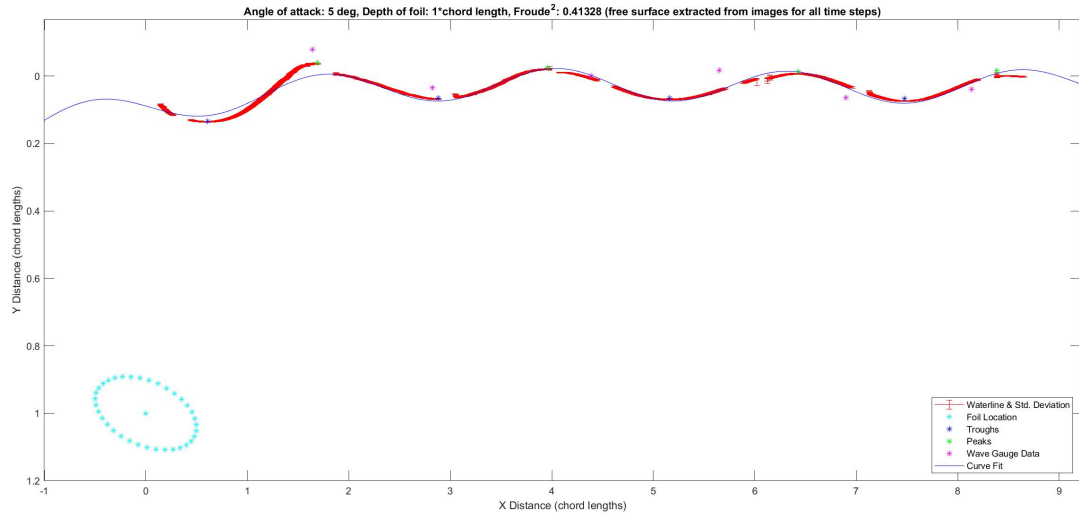


Figure 7.33: Results using the side view analysis for the larger HDPE foil at an angle of attack of 5 degrees, a depth of 1\*chord length at a speed of 1.10 m/s averaged over the time of the experiment (50 seconds).

	<b>2/11/2021</b>
<b>Range for wave height (chord length)</b>	0.096114
<b>Standard Deviation for wave height (chord length)</b>	0.045436
<b>Variance for wave height (<math>chordlength^2</math>)</b>	0.0020644
<b>Range for wavelength (chord length)</b>	0.51328
<b>Standard Deviation for wavelength (chord length)</b>	0.16738
<b>Variance for wavelength (<math>chordlength^2</math>)</b>	0.028016

Table 7.21: Results of the variability in wave height and wavelengths for the case with an angle of attack 5 degrees, a depth of 1\*chord length, and with a flow speed of 1.10 m/s.

### 7.3.2 HDPE Foil with; angle of attack: $5^\circ$ & depth of foil: $5/4$ \*chord length

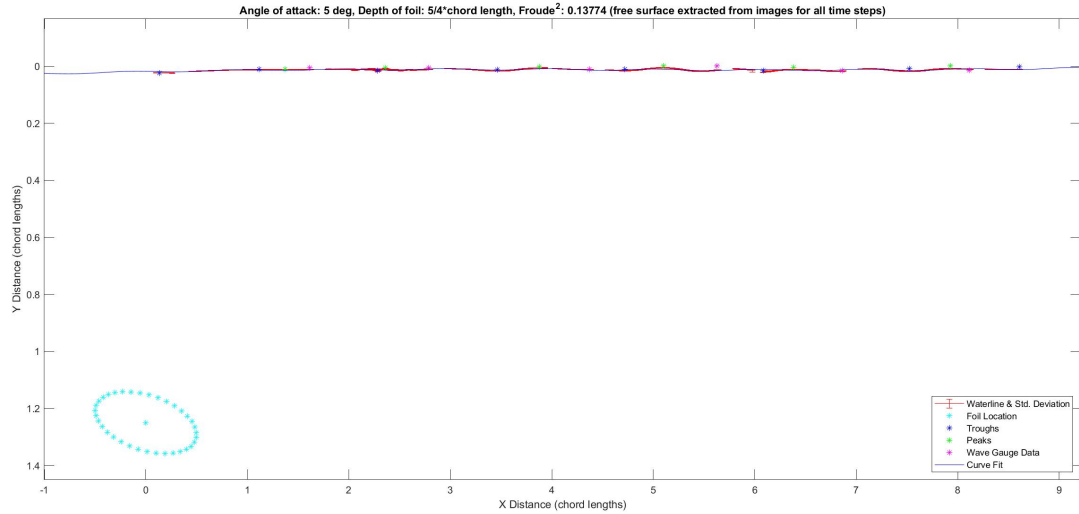


Figure 7.34: Results using the side view analysis for the larger HDPE foil at an angle of attack of 5 degrees, a depth of  $5/4$ \*chord length at a speed of 0.71 m/s averaged over the time of the experiment (50 seconds).

	2/11/2021
Range for wave height (chord length)	0.0098604
Standard Deviation for wave height (chord length)	0.0037838
Variance for wave height ( $chordlength^2$ )	$1.4317 \times 10^{-5}$
Range for wavelength (chord length)	0.71505
Standard Deviation for wavelength (chord length)	0.23638
Variance for wavelength ( $chordlength^2$ )	0.055876

Table 7.22: Results of the variability in wave height and wavelengths for the case with an angle of attack 5 degrees, a depth of  $5/4$ \*chord length, and with a flow speed of 0.71 m/s.

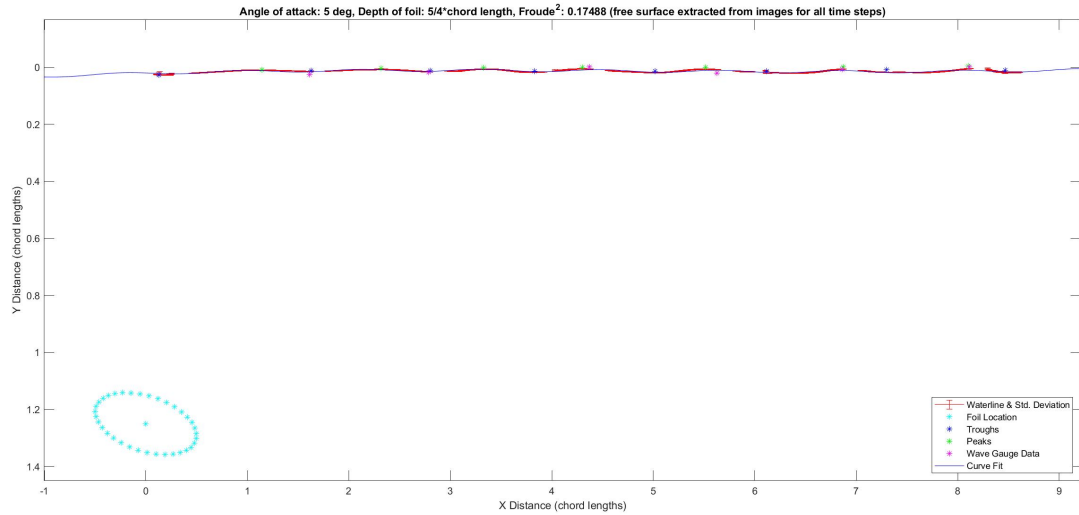


Figure 7.35: Results using the side view analysis for the larger HDPE foil at an angle of attack of 5 degrees, a depth of  $5/4$ \*chord length at a speed of 0.80 m/s averaged over the time of the experiment (50 seconds).

	<b>2/11/2021</b>
<b>Range for wave height (chord length)</b>	0.010023
<b>Standard Deviation for wave height (chord length)</b>	0.0033356
<b>Variance for wave height (chordlength<sup>2</sup>)</b>	$1.1126 \times 10^{-5}$
<b>Range for wavelength (chord length)</b>	0.7215
<b>Standard Deviation for wavelength (chord length)</b>	0.20456
<b>Variance for wavelength (chordlength<sup>2</sup>)</b>	0.041845

Table 7.23: Results of the variability in wave height and wavelengths for the case with an angle of attack 5 degrees, a depth of  $5/4$ \*chord length, and with a flow speed of 0.80 m/s.

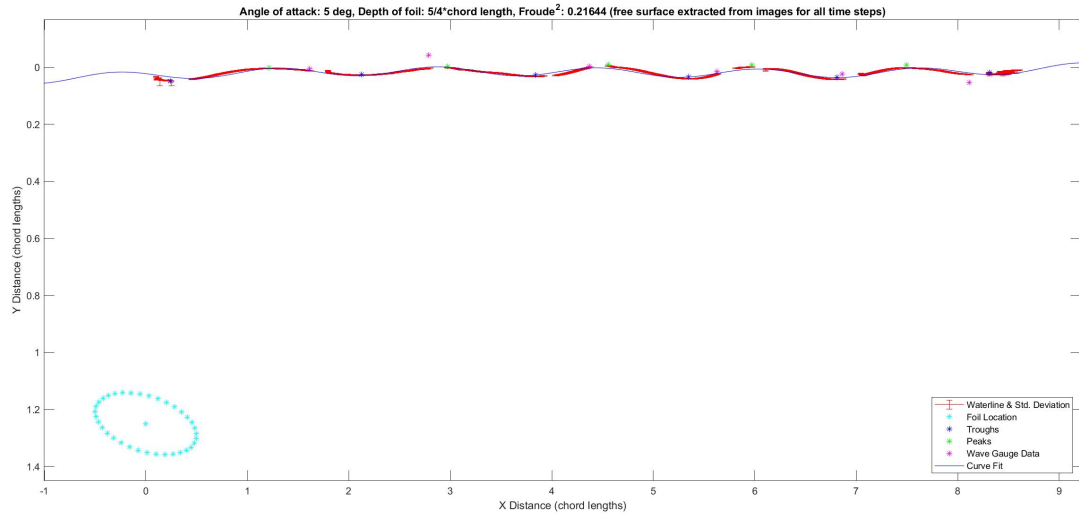


Figure 7.36: Results using the side view analysis for the larger HDPE foil at an angle of attack of 5 degrees, a depth of  $5/4$ \*chord length at a speed of 0.89 m/s averaged over the time of the experiment (50 seconds).

	<b>2/11/2021</b>
<b>Range for wave height (chord length)</b>	0.025184
<b>Standard Deviation for wave height (chord length)</b>	0.0097995
<b>Variance for wave height (chordlength<sup>2</sup>)</b>	$9.6031 \times 10^{-5}$
<b>Range for wavelength (chord length)</b>	0.82158
<b>Standard Deviation for wavelength (chord length)</b>	0.22413
<b>Variance for wavelength (chordlength<sup>2</sup>)</b>	0.050236

Table 7.24: Results of the variability in wave height and wavelengths for the case with an angle of attack 5 degrees, a depth of  $5/4$ \*chord length, and with a flow speed of 0.89 m/s.

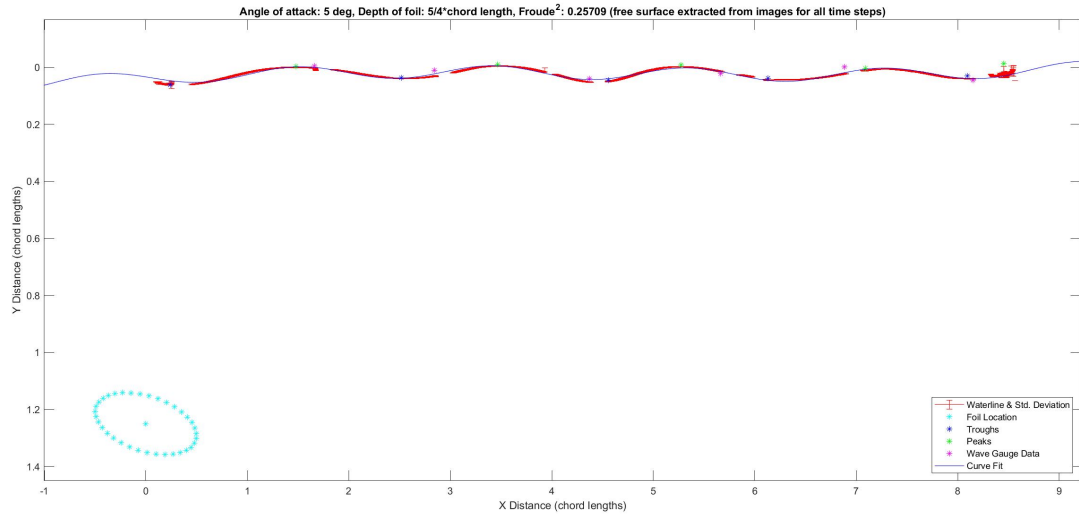


Figure 7.37: Results using the side view analysis for the larger HDPE foil at an angle of attack of 5 degrees, a depth of  $5/4$ \*chord length at a speed of 0.97 m/s averaged over the time of the experiment (50 seconds).

	<b>2/11/2021</b>
<b>Range for wave height (chord length)</b>	0.030073
<b>Standard Deviation for wave height (chord length)</b>	0.011288
<b>Variance for wave height (<math>chordlength^2</math>)</b>	0.00012742
<b>Range for wavelength (chord length)</b>	0.90874
<b>Standard Deviation for wavelength (chord length)</b>	0.28306
<b>Variance for wavelength (<math>chordlength^2</math>)</b>	0.080126

Table 7.25: Results of the variability in wave height and wavelengths for the case with an angle of attack 5 degrees, a depth of  $5/4$ \*chord length, and with a flow speed of 0.97 m/s.

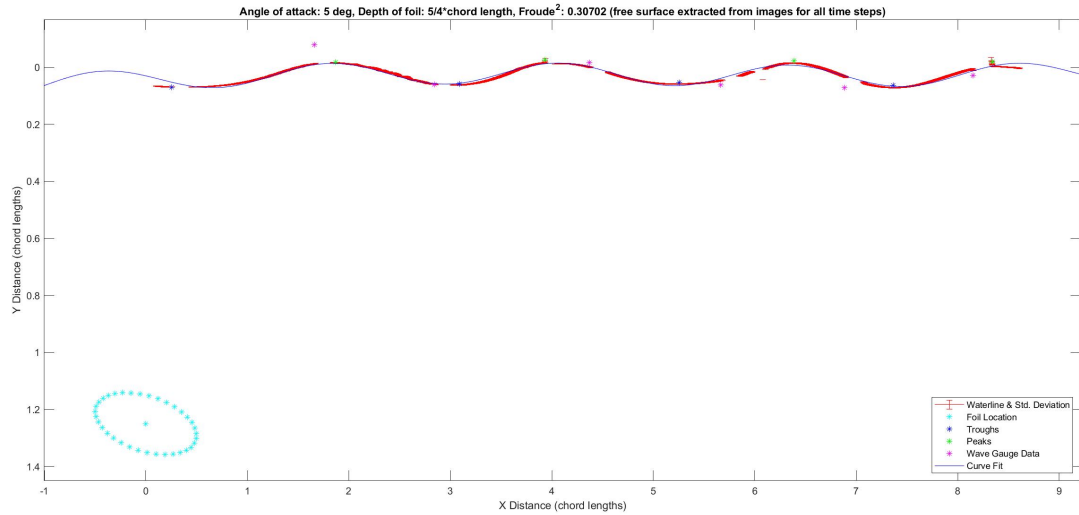


Figure 7.38: Results using the side view analysis for the larger HDPE foil at an angle of attack of 5 degrees, a depth of  $5/4$ \*chord length at a speed of 1.06 m/s averaged over the time of the experiment (50 seconds).

	<b>2/11/2021</b>
<b>Range for wave height (chord length)</b>	0.012948
<b>Standard Deviation for wave height (chord length)</b>	0.0054642
<b>Variance for wave height (chordlength<sup>2</sup>)</b>	$2.9857 \times 10^{-5}$
<b>Range for wavelength (chord length)</b>	0.87807
<b>Standard Deviation for wavelength (chord length)</b>	0.32481
<b>Variance for wavelength (chordlength<sup>2</sup>)</b>	0.1055

Table 7.26: Results of the variability in wave height and wavelengths for the case with an angle of attack 5 degrees, a depth of  $5/4$ \*chord length, and with a flow speed of 1.06 m/s.

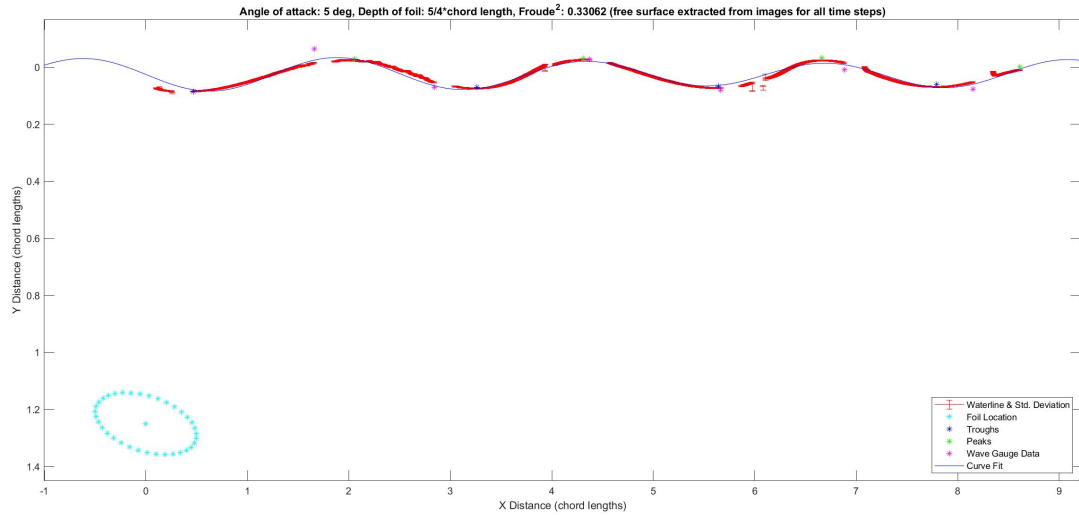


Figure 7.39: Results using the side view analysis for the larger HDPE foil at an angle of attack of 5 degrees, a depth of  $5/4$ \*chord length at a speed of 1.10 m/s averaged over the time of the experiment (50 seconds).

	<b>2/11/2021</b>
<b>Range for wave height (chord length)</b>	0.052961
<b>Standard Deviation for wave height (chord length)</b>	0.022915
<b>Variance for wave height (<math>chordlength^2</math>)</b>	0.00052512
<b>Range for wavelength (chord length)</b>	0.84579
<b>Standard Deviation for wavelength (chord length)</b>	0.28288
<b>Variance for wavelength (<math>chordlength^2</math>)</b>	0.080023

Table 7.27: Results of the variability in wave height and wavelengths for the case with an angle of attack 5 degrees, a depth of  $5/4$ \*chord length, and with a flow speed of 1.10 m/s.

### 7.3.3 HDPE Foil with; angle of attack: $5^\circ$ , & depth of foil: $3/2$ \*chord length

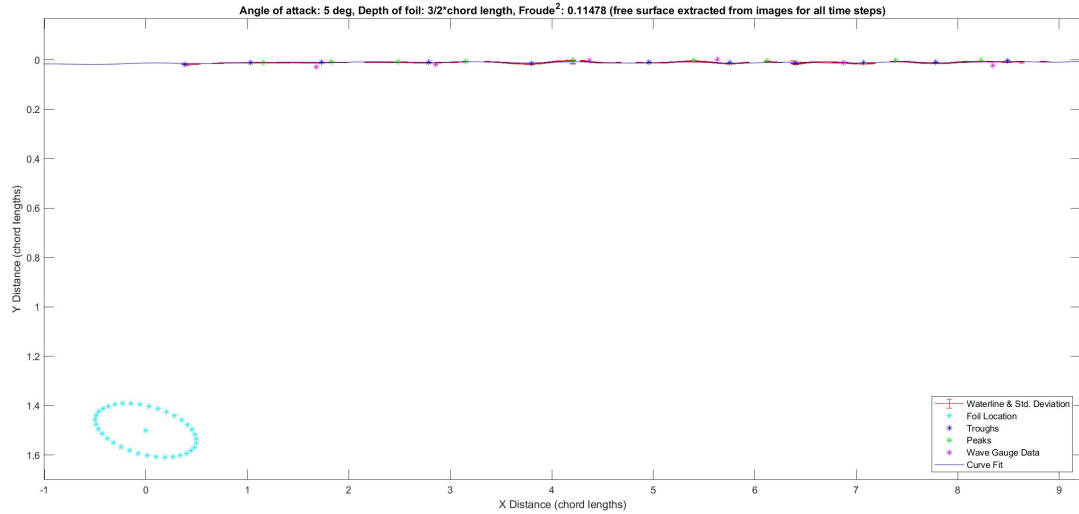


Figure 7.40: Results using the side view analysis for the larger HDPE foil at an angle of attack of 5 degrees, a depth of  $3/2$ \*chord length at a speed of 0.71 m/s averaged over the time of the experiment (50 seconds).

	<b>2/11/2021</b>
<b>Range for wave height (chord length)</b>	0.0098908
<b>Standard Deviation for wave height (chord length)</b>	0.0034438
<b>Variance for wave height (<math>chordlength^2</math>)</b>	$1.186 \times 10^{-5}$
<b>Range for wavelength (chord length)</b>	0.92972
<b>Standard Deviation for wavelength (chord length)</b>	0.32637
<b>Variance for wavelength (<math>chordlength^2</math>)</b>	0.10651

Table 7.28: Results of the variability in wave height and wavelengths for the case with an angle of attack 5 degrees, a depth of  $3/2$ \*chord length, and with a flow speed of 0.71 m/s.

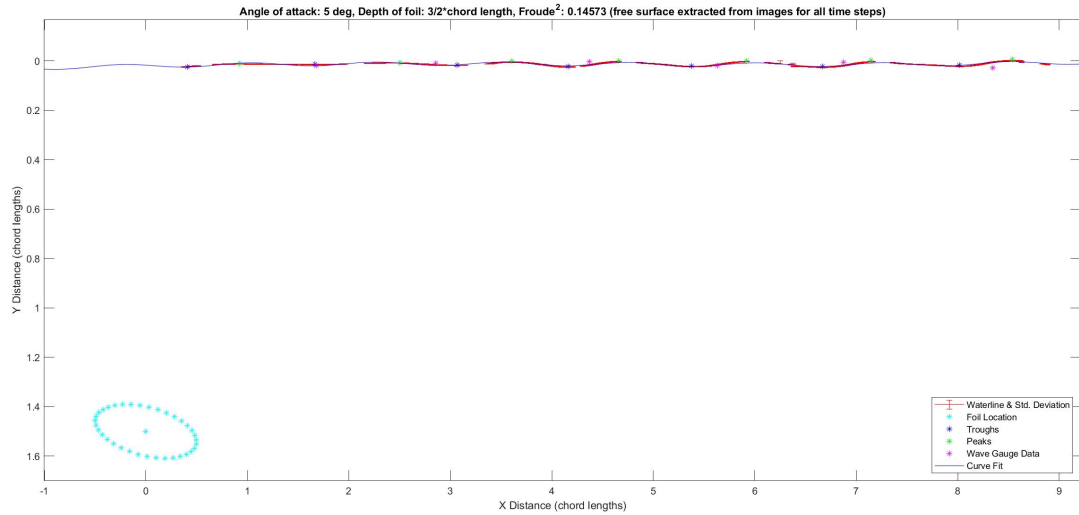


Figure 7.41: Results using the side view analysis for the larger HDPE foil at an angle of attack of 5 degrees, a depth of  $3/2$ \*chord length at a speed of 0.80 m/s averaged over the time of the experiment (50 seconds).

	<b>2/11/2021</b>
<b>Range for wave height (chord length)</b>	0.017116
<b>Standard Deviation for wave height (chord length)</b>	0.0068731
<b>Variance for wave height (chordlength<sup>2</sup>)</b>	$4.7239 \times 10^{-5}$
<b>Range for wavelength (chord length)</b>	0.29699
<b>Standard Deviation for wavelength (chord length)</b>	0.093414
<b>Variance for wavelength (chordlength<sup>2</sup>)</b>	0.0087261

Table 7.29: Results of the variability in wave height and wavelengths for the case with an angle of attack 5 degrees, a depth of  $3/2$ \*chord length, and with a flow speed of 0.80 m/s.

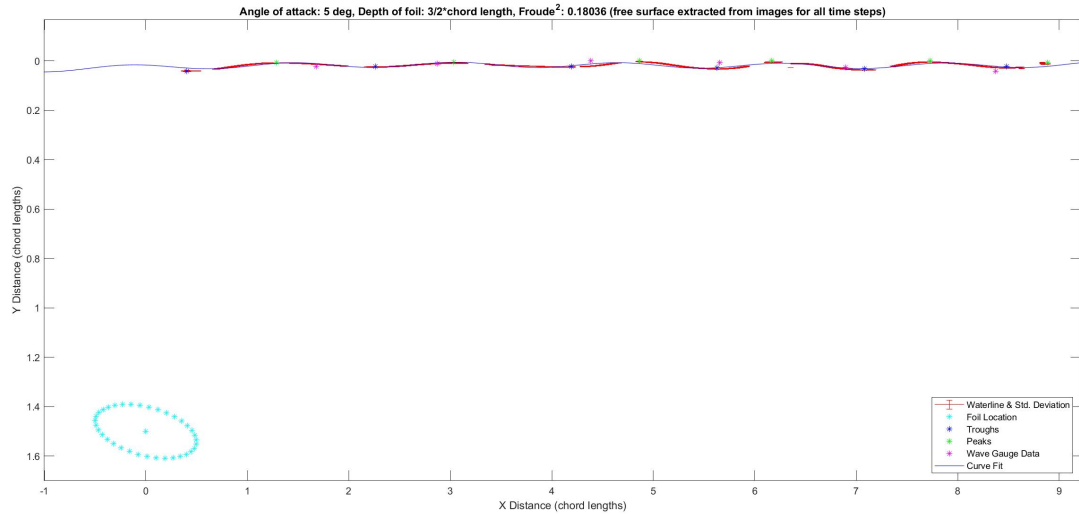


Figure 7.42: Results using the side view analysis for the larger HDPE foil at an angle of attack of 5 degrees, a depth of  $3/2$ \*chord length at a speed of 0.89 m/s averaged over the time of the experiment (50 seconds).

	<b>2/11/2021</b>
<b>Range for wave height (chord length)</b>	0.017155
<b>Standard Deviation for wave height (chord length)</b>	0.0070899
<b>Variance for wave height (chordlength<sup>2</sup>)</b>	$5.0266 \times 10^{-5}$
<b>Range for wavelength (chord length)</b>	0.62627
<b>Standard Deviation for wavelength (chord length)</b>	0.23038
<b>Variance for wavelength (chordlength<sup>2</sup>)</b>	0.053073

Table 7.30: Results of the variability in wave height and wavelengths for the case with an angle of attack 5 degrees, a depth of  $3/2$ \*chord length, and with a flow speed of 0.89 m/s.

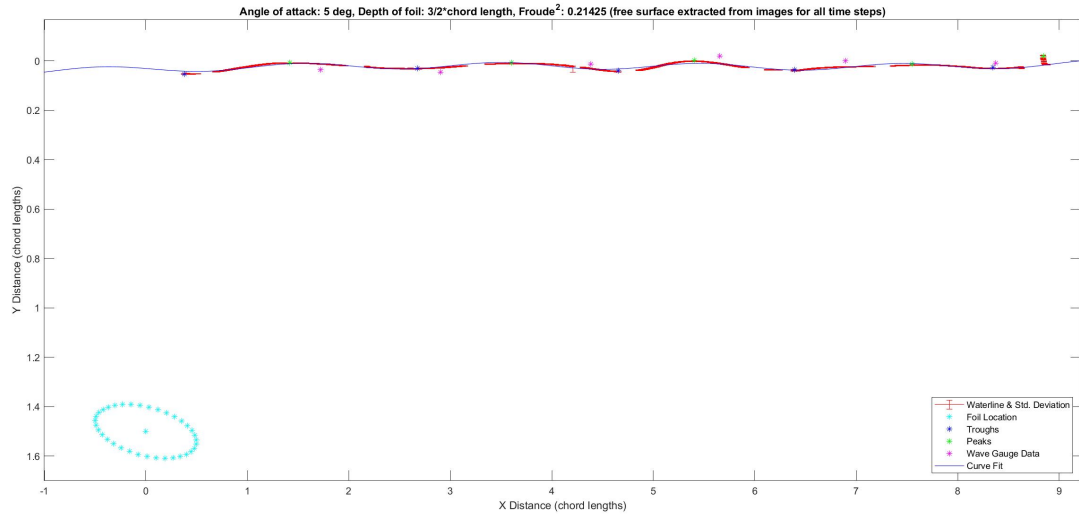


Figure 7.43: Results using the side view analysis for the larger HDPE foil at an angle of attack of 5 degrees, a depth of  $3/2$ \*chord length at a speed of 0.97 m/s averaged over the time of the experiment (50 seconds).

	<b>2/11/2021</b>
<b>Range for wave height (chord length)</b>	0.027466
<b>Standard Deviation for wave height (chord length)</b>	0.013342
<b>Variance for wave height (<math>chordlength^2</math>)</b>	0.000178
<b>Range for wavelength (chord length)</b>	0.59237
<b>Standard Deviation for wavelength (chord length)</b>	0.22207
<b>Variance for wavelength (<math>chordlength^2</math>)</b>	0.049316

Table 7.31: Results of the variability in wave height and wavelengths for the case with an angle of attack 5 degrees, a depth of  $3/2$ \*chord length, and with a flow speed of 0.97 m/s.

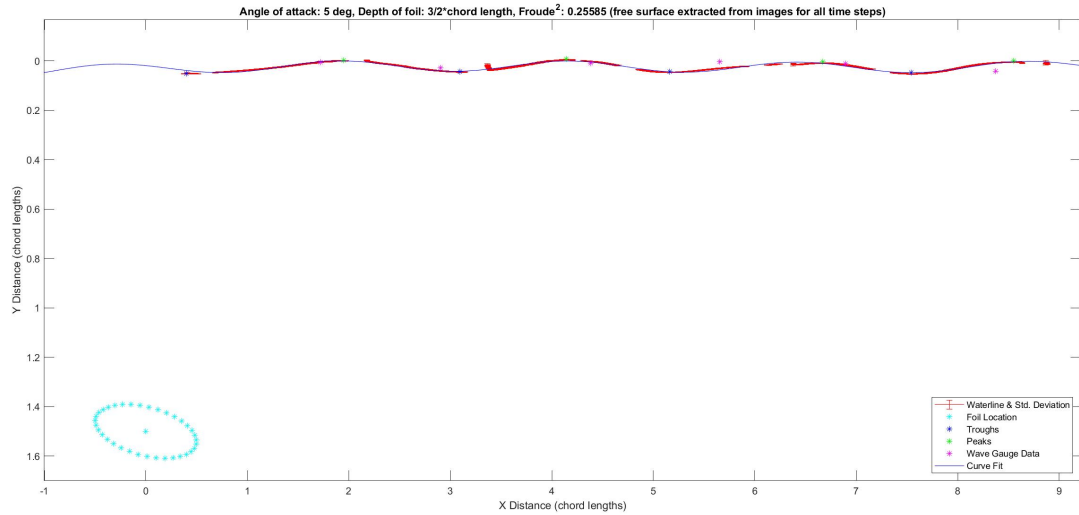


Figure 7.44: Results using the side view analysis for the larger HDPE foil at an angle of attack of 5 degrees, a depth of  $3/2$ \*chord length at a speed of 1.06 m/s averaged over the time of the experiment (50 seconds).

	<b>2/11/2021</b>
<b>Range for wave height (chord length)</b>	0.015208
<b>Standard Deviation for wave height (chord length)</b>	0.0064198
<b>Variance for wave height (chordlength<sup>2</sup>)</b>	$4.1214 \times 10^{-5}$
<b>Range for wavelength (chord length)</b>	0.81996
<b>Standard Deviation for wavelength (chord length)</b>	0.30421
<b>Variance for wavelength (chordlength<sup>2</sup>)</b>	0.092544

Table 7.32: Results of the variability in wave height and wavelengths for the case with an angle of attack 5 degrees, a depth of  $3/2$ \*chord length, and with a flow speed of 1.06 m/s.

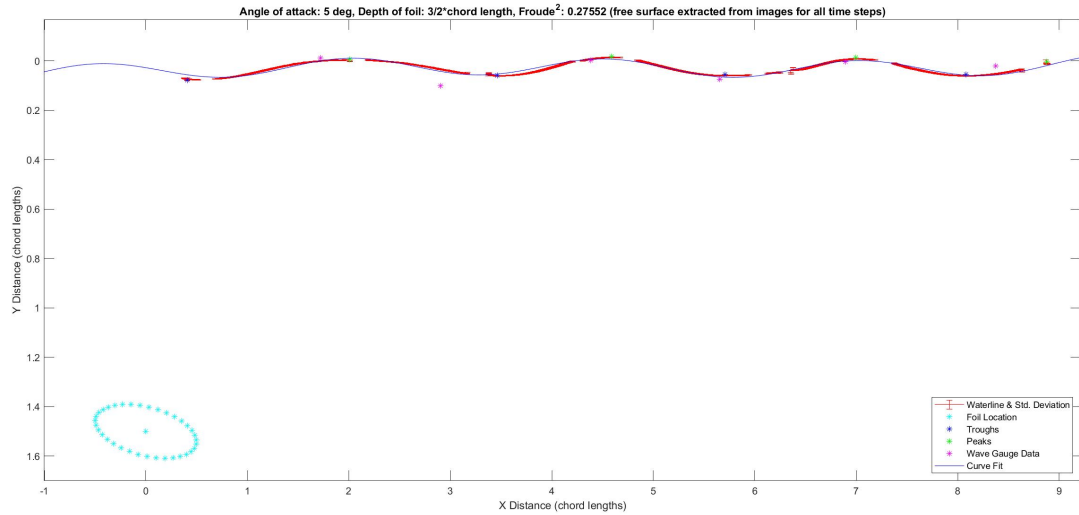


Figure 7.45: Results using the side view analysis for the larger HDPE foil at an angle of attack of 5 degrees, a depth of  $3/2$ \*chord length at a speed of 1.10 m/s averaged over the time of the experiment (50 seconds).

	<b>2/11/2021</b>
<b>Range for wave height (chord length)</b>	0.032664
<b>Standard Deviation for wave height (chord length)</b>	0.014018
<b>Variance for wave height (<math>chordlength^2</math>)</b>	0.0001965
<b>Range for wavelength (chord length)</b>	1.1734
<b>Standard Deviation for wavelength (chord length)</b>	0.38775
<b>Variance for wavelength (<math>chordlength^2</math>)</b>	0.15035

Table 7.33: Results of the variability in wave height and wavelengths for the case with an angle of attack 5 degrees, a depth of  $3/2$ \*chord length, and with a flow speed of 1.10 m/s.

## 7.4 Scripts for synthetic Schlieren Processing and Plotting

### 7.4.1 Script for Processing DIC Displacements to get Free Surface Values.

```
1 clear all;
2 %close all;
3 clc;
4
5 % all_data = load('still_water_vs_waves_in_tank_second_dic.mat'); % test 2 on 7/15/20?
6 all_data = load('still_water_vs_wave_time_sync_all.mat'); % test with comparison to wg3 (time sync test)
7 % all_data = load('foil_test_11_2_2020_0_deg_cl_4_20_percent.mat'); % foil test with large foil at 0 deg depth
   of cl/4
8 % all_data = load('foil_test_11_10_2020_10_deg_cl_2_30_percent_incomplete.mat'); % foil test with medium foil at
   10 deg depth of cl/2
9 % all_data = load('foil_test_11_12_2020_10_deg_cl_3_4_40_percent.mat'); % foil test with medium foil at 10 deg
   depth of cl*3/4
10 % all_data = load('time_sync_test_PIV.mat'); % foil test with medium foil at 10 deg depth of cl*3/4
11
12
13 num_comps = size(all_data.current_save,2);
14 pix_to_units = all_data.data_dic_save.dispinfo.pixtounits;
15 spacing = all_data.data_dic_save.dispinfo.spacing;
16 ds = spacing*pix_to_units;
17 [y_length, x_length] = size(all_data.data_dic_save.displacements(1).plot_u_cur_formatted);
18 [y_length, x_length] = size(all_data.data_dic_save.displacements.plot_u_cur_formatted{1});
19
20 x = 0:ds:ds*(x_length-1);
21 y = 0:ds:ds*(y_length-1);
22
23 h0 = 38; % depth of the water in inches
24 hg = 5/8; % thickness of the glass
25 n = 1.33; % refractive index of water at 20 deg C
26 ng = 1.52; % refractive index of plate glass
27 alpha = 0.24; % air-water interface
28 H = hg+63.75; % distance from camera lens to dot pattern
29
30 hp = h0 + hg*(n/ng);
31 one_hstar = 1/(alpha*hp)-1/H;
32
33
34 u_cur = cell(num_comps,1);
35 v_cur = cell(num_comps,1);
36
37 exx_cur = cell(num_comps,1);
38 exy_cur = cell(num_comps,1);
39 eyy_cur = cell(num_comps,1);
```

```

40
41
42 for i = 1:num_comps
43 %     u_dic = all_data.data_dic_save.displacements(i).plot_u_dic;
44 %     v_dic = all_data.data_dic_save.displacements(i).plot_v_dic;
45 %
46 %     u_ref_formatted = all_data.data_dic_save.displacements(i).plot_u_ref_formatted;
47 %     v_ref_formatted = all_data.data_dic_save.displacements(i).plot_v_ref_formatted;
48
49     u_cur_formatted = flipud(all_data.data_dic_save.displacements(i).plot_u_cur_formatted);
50     u_cur_formatted(u_cur_formatted==0)=NaN;
51     u_cur{i} = u_cur_formatted;
52     v_cur_formatted = flipud(all_data.data_dic_save.displacements(i).plot_v_cur_formatted);
53     v_cur_formatted(v_cur_formatted==0)=NaN;
54     v_cur{i} = v_cur_formatted;
55
56 %     u_cur_all_x = u_cur{i}(round(length(y)/2),:);
57 %     idx_u(i) = find(~isnan(u_cur_all_x), 1, 'first');
58 %     u_cur_wg(i) = u_cur{i}(round(length(y)/2),round(length(x)/2));
59 %
60 %     v_cur_all_x = v_cur{i}(round(length(y)/2),:);
61 %     idx_v(i) = find(~isnan(v_cur_all_x), 1, 'first');
62 %     v_cur_wg(i) = v_cur{i}(round(length(y)/2),round(length(x)/2));
63 %
64 %     if idx_u(i) == idx_v(i)
65 %         idx_wg(i) = idx_u(i);
66 %     else
67 %         end
68
69
70
71     size_u = size(u_cur{i});
72
73     for iii = 1:size_u(1)
74         if unique(isnan(u_cur{i}(iii,:))) == 1
75             all_i(iii) = iii;
76         else
77             all_i(iii) = NaN;
78         end
79     end
80
81     all_i(isnan(all_i))=[];
82
83     for jjj = 1:size_u(2)
84         if unique(isnan(u_cur{i}(:,jjj))) == 1
85             all_j(jjj) = jjj;

```

```

86     else
87         all_j(jjj) = NaN;
88     end
89 end
90
91 all_j(isnan(all_j))=[];
92
93 u_cur{i}(isnan(u_cur{i})) = 0;
94 v_cur{i}(isnan(v_cur{i})) = 0;
95
96 seta_u{i} = -u_cur{i}.*one_hstar;
97 seta_v{i} = -v_cur{i}.*one_hstar;
98
99 surface_elevation{i} = intgrad2(seta_u{i},seta_v{i},ds,ds,0);
100
101
102 surface_elevation{i}(all_i,:) = NaN;
103 surface_elevation{i}(:,all_j) = NaN;
104
105 %     surface_elevation_wg(i) = surface_elevation{i}(round(length(y)/2),idx_wg(i));
106
107 %surface_height{i} = hp+surface_elevation{i};
108
109 disp(['frame ',num2str(i)])
110
111 %     exx_cur_formatted = flipud(all_data.data_dic_save.strains(i).plot_exx_cur_formatted);
112 %     exx_cur_formatted(exx_cur_formatted==0) = NaN;
113 %     exx_cur{i} = exx_cur_formatted;
114 %     exy_cur_formatted = flipud(all_data.data_dic_save.strains(i).plot_exy_cur_formatted);
115 %     exy_cur_formatted(exy_cur_formatted==0) = NaN;
116 %     exy_cur{i} = exy_cur_formatted;
117 %     eyy_cur_formatted = flipud(all_data.data_dic_save.strains(i).plot_eyy_cur_formatted);
118 %     eyy_cur_formatted(eyy_cur_formatted==0) = NaN;
119 %     eyy_cur{i} = eyy_cur_formatted;
120
121 end
122
123 save('all_time_sync_test_PIV_dic.mat','x','y','u_cur','v_cur','surface_elevation','-v7.3');
124
125 %%
126 % clear all;
127 % close all;
128 % clc;
129 %
130 % load('all_time_sync_test_PIV_dic.mat');
131 %

```

```

132 % x_m = x.*0.0254;
133 % y_m = y.*0.0254;
134 %
135 %
136 %
137 % for i = 1:length(surface_elevation)
138 %     %%%% Converting into meters
139 %     u_cur{i}(u_cur{i}==0)=NaN;
140 %     v_cur{i}(v_cur{i}==0)=NaN;
141 %
142 %     u_cur_m{i} = u_cur{i}.*0.0254;
143 %     v_cur_m{i} = v_cur{i}.*0.0254;
144 %     surface_elevation_m{i} = surface_elevation{i}.*0.0254;
145 % end
146 %
147 %
148 % save('all_time_sync_test_PIV_dic_meters.mat','x_m','y_m','u_cur_m', 'v_cur_m', 'surface_elevation_m', '-v7.3');
149 %

```

## 7.4.2 Script for Processing PIV Displacements to get Free Surface Values.

```

1 clear all;
2 %close all;
3 clc;
4
5 % all_data = load('still_water_vs_waves_in_tank_second_dic.mat'); % test 2 on 7/15/20?
6 % all_data = load('still_water_vs_wave_time_sync_all.mat'); % test with comparison to wg3 (time sync test)
7 % all_data = load('foil_test_11_2_2020_0_deg_cl_4_20_percent.mat'); % foil test with large foil at 0 deg depth
   of cl/4
8 % all_data = load('foil_test_11_10_2020_10_deg_cl_2_30_percent_incomplete.mat'); % foil test with medium foil at
   10 deg depth of cl/2
9 % all_data = load('foil_test_11_12_2020_10_deg_cl_3_4_40_percent.mat'); % foil test with medium foil at 10 deg
   depth of cl*3/4
10 all_data = load('time_sync_test_PIV_new.mat'); % time_sync_test with PIV
11 % all_data = load('11_24_2020_10_deg_cl_2_30_percent_PIV.mat'); % foil test with medium foil at 10 deg depth of
   cl*3/4
12 % all_data = load('11_25_2020_10_deg_cl_3_4_30_percent_PIV.mat'); % foil test with medium foil at 10 deg depth
   of cl*3/4
13 % all_data = load('12_8_2020_10_deg_cl_pt34_25_percent_PIV.mat'); % foil test with medium foil at 10 deg depth
   of cl*3/4
14 % all_data = load('12_11_2020_10_deg_cl_1_65_percent_PIV.mat'); % foil test with medium foil at 10 deg depth of
   cl*3/4
15 % all_data = load('12_18_2020_10_deg_cl_5_4_120_percent_PIV.mat'); % foil test with medium foil at 10 deg depth
   of cl*3/4
16
17
18 num_comps = size(all_data.current_save,2);

```

```

19 % pix_to_units = all_data.data_dic_save.dispinfo.pixtounits;
20 % spacing = all_data.data_dic_save.dispinfo.spacing;
21 % ds = spacing*pix_to_units;
22 [y_length, x_length] = size(all_data.data_dic_save.displacements.plot_u_cur_formatted{1});
23
24 x = all_data.data_dic_save.displacements.x{1};
25 y = all_data.data_dic_save.displacements.y{1};
26
27 ds = x(2)-x(1)
28
29 h0 = 38*0.0254; % depth of the water in inches
30 hg = 5/8*0.0254; % thickness of the glass
31 n = 1.33; % refractive index of water at 20 deg C
32 ng = 1.52; % refractive index of plate glass
33 alpha = 0.24; % air-water interface
34 H = (hg+65.5)*0.0254; % distance from camera lens to dot pattern
35
36 hp = h0 + hg*(n/ng);
37 one_hstar = 1/(alpha*hp)-1/H;
38
39
40 u_cur = cell(num_comps,1);
41 v_cur = cell(num_comps,1);
42
43 exx_cur = cell(num_comps,1);
44 exy_cur = cell(num_comps,1);
45 eyy_cur = cell(num_comps,1);
46
47
48 for i = 1:num_comps
49 %     u_dic = all_data.data_dic_save.displacements(i).plot_u_dic;
50 %     v_dic = all_data.data_dic_save.displacements(i).plot_v_dic;
51 %
52 %     u_ref_formatted = all_data.data_dic_save.displacements(i).plot_u_ref_formatted;
53 %     v_ref_formatted = all_data.data_dic_save.displacements(i).plot_v_ref_formatted;
54
55     u_cur_formatted = flipud(all_data.data_dic_save.displacements.plot_u_cur_formatted{i});
56     u_cur_formatted(u_cur_formatted==0)=NaN;
57     u_cur{i} = u_cur_formatted;
58     v_cur_formatted = flipud(all_data.data_dic_save.displacements.plot_v_cur_formatted{i});
59     v_cur_formatted(v_cur_formatted==0)=NaN;
60     v_cur{i} = v_cur_formatted;
61
62 %     u_cur_all_x = u_cur{i}(round(length(y)/2),:);
63 %     idx_u(i) = find(~isnan(u_cur_all_x), 1, 'first');
64 %     u_cur_wg(i) = u_cur{i}(round(length(y)/2),round(length(x)/2));

```

```

65 %
66 %     v_cur_all_x = v_cur{i}(round(length(y)/2),:);
67 %     idx_v(i) = find(~isnan(v_cur_all_x), 1, 'first');
68 %     v_cur_wg(i) = v_cur{i}(round(length(y)/2),round(length(x)/2));
69 %
70 %     if idx_u(i) == idx_v(i)
71 %         idx_wg(i) = idx_u(i);
72 %     else
73 %         end
74
75
76
77     size_u = size(u_cur{i});
78
79     for iii = 1:size_u(1)
80         if unique(isnan(u_cur{i}(iii,:))) == 1
81             all_i(iii) = iii;
82         else
83             all_i(iii) = NaN;
84         end
85     end
86
87     all_i(isnan(all_i))=[];
88
89     for jjj = 1:size_u(2)
90         if unique(isnan(u_cur{i}(:,jjj))) == 1
91             all_j(jjj) = jjj;
92         else
93             all_j(jjj) = NaN;
94         end
95     end
96
97     all_j(isnan(all_j))=[];
98
99     u_cur{i}(isnan(u_cur{i})) = 0;
100    v_cur{i}(isnan(v_cur{i})) = 0;
101
102    seta_u{i} = -u_cur{i}.*one_hstar;
103    seta_v{i} = -v_cur{i}.*one_hstar;
104
105    surface_elevation{i} = intgrad2(seta_u{i},seta_v{i},ds,ds,0);
106
107
108    surface_elevation{i}(all_i,:) = NaN;
109    surface_elevation{i}(:,all_j) = NaN;
110

```

```

111 %     surface_elevation_wg(i) = surface_elevation{i}(round(length(y)/2),idx_wg(i));
112
113 %surface_height{i} = hp+surface_elevation{i};
114
115 disp(['frame ',num2str(i)])
116
117 %     exx_cur_formatted = flipud(all_data.data_dic_save.strains(i).plot_exx_cur_formatted);
118 %     exx_cur_formatted(exx_cur_formatted==0)= NaN;
119 %     exx_cur{i} = exx_cur_formatted;
120 %     exy_cur_formatted = flipud(all_data.data_dic_save.strains(i).plot_exy_cur_formatted);
121 %     exy_cur_formatted(exy_cur_formatted==0)= NaN;
122 %     exy_cur{i} = exy_cur_formatted;
123 %     eyy_cur_formatted = flipud(all_data.data_dic_save.strains(i).plot_eyy_cur_formatted);
124 %     eyy_cur_formatted(eyy_cur_formatted==0)= NaN;
125 %     eyy_cur{i} = eyy_cur_formatted;
126
127 end
128
129 save('all_time_sync_PIV_dic_meters.mat','x','y','u_cur', 'v_cur', 'surface_elevation', '-v7.3');
130 % save('all_foil_11_24_2020_10_deg_cl_2_30_percent_PIV.mat','x','y','u_cur', 'v_cur', 'surface_elevation', '-v7
    .3');
131 % save('all_foil_11_25_2020_10_deg_cl_3_4_30_percent_PIV.mat','x','y','u_cur', 'v_cur', 'surface_elevation', '-v7
    .3');
132 % save('all_foil_12_8_2020_10_deg_cl_pt34_25_percent_PIV.mat','x','y','u_cur', 'v_cur', 'surface_elevation', '-v7
    .3');
133 % save('all_foil_12_11_2020_10_deg_cl_1_65_percent_PIV.mat','x','y','u_cur', 'v_cur', 'surface_elevation', '-v7
    .3');
134 % save('all_foil_12_18_2020_10_deg_cl_5_4_120_percent_PIV.mat','x','y','u_cur', 'v_cur', 'surface_elevation', '-
    v7.3');

```

### 7.4.3 Script for Plotting DIC Free Surface Values.

```

1 clear all;
2 close all;
3 clc;
4
5 load('all_time_sync_output_dic_meters.mat')
6 surface_elevation = surface_elevation_m;
7 u_cur = u_cur_m;
8 v_cur = v_cur_m;
9 x = x_m;
10 y = y_m;
11
12 Directory = 'C:\Users\Jamie\Desktop\Grad Semester 5\time_sync_test_wave_gauge3\';
13 wg_filename = [Directory,'Sine Freq=1Hz Amp=0.02m ang=0rad.txt'];
14 ref_frame = '1';
15

```

```

16 %%%%%%
17
18 all_images_dic_wrong_order = dir([Directory,'frames\*.jpg']);
19
20 % images are loaded incorrectly based on file name so they need to be sorted by frame number instead
21 all_images_file_names = extractfield(all_images_dic_wrong_order,'name'); % first get file names
22 all_images_frame_num_str = strrep(all_images_file_names,'frame_',''); all_images_frame_num_str = strrep(
    all_images_frame_num_str, '.jpg',''); % then get frame number by itself
23 all_images_frame_num = cellfun(@str2num,all_images_frame_num_str); % then make it a number not a string
24 for k = 1:length(all_images_dic_wrong_order) % loop to add frame number as a field
    in the original structure
25 [all_images_dic_wrong_order(k).frame_num] = all_images_frame_num(k);
26 end
27
28 [vals,idx]=sort([all_images_dic_wrong_order.frame_num]); % now sort by frame number
29 all_images_dic = all_images_dic_wrong_order(idx);
30 num_images_dic = size(all_images_dic,1);
31
32
33
34 num_images = num_images_dic;
35 camera_fps = 60;
36
37 time_DIC = 0:1/camera_fps:(num_images-2)/camera_fps; % define a time array based on camera
    frames per second
38
39
40
41
42 %
    %%%%%%%%%%%%%%%%%%%%%%%%%%%%%%%%%%%%%%%%%%%%%%%%%%%%%%%%%%%%%%%%%%%%%%%%%
43
44
45
46 for ii = 1:length(surface_elevation)
47     u_cur_center(ii) = u_cur{ii}(round(length(x)/2),round(length(y)/2));
48     v_cur_center(ii) = v_cur{ii}(round(length(x)/2),round(length(y)/2));
49
50     eta_center(ii) = -surface_elevation{ii}(round(length(x)*(1/2)),round(length(y)/2));
51     eta_center_avg_y(ii) = -nanmean(surface_elevation{ii}(round(length(x)*(1/2)),:));
52 end
53
54 all_wg_data = readtable(wg_filename);
55 time_wg = table2array(all_wg_data(6:end,1));
56 eta_wg_3 = table2array(all_wg_data(6:end,18));

```

```

57
58 for jj = 1:length(time_wg)
59 %     t_wg(jj) = str2num(time_wg{jj});
60 %     if jj>2 && t_wg(jj)<t_wg(jj-1)
61 %         disp(['index: ',num2str(jj)])
62 %         t_wg(jj) = t_wg(jj)+60;
63 %     else
64 %     end
65
66 %     t_wg(jj) = (t_wg(jj)-str2num(time_wg{1}));
67     eta_wg(jj) = str2num(eta_wg_3{jj});
68 end
69
70 t_wg = 0:0.007814:49.563;
71
72
73 figure(3)
74 plot(time_DIC,(eta_center-nanmean(eta_center)))
75 hold on;
76 plot(time_DIC,(eta_center_avg_y-nanmean(eta_center_avg_y)))
77 % hold on;
78 % plot(time_DIC,eta_x_3_avg_y-mean(eta_x_3_avg_y))
79 % hold on;
80 plot(t_wg+0.89,eta_wg-mean(eta_wg))
81
82 tt_wg = t_wg+0.89;
83 etta_wg = eta_wg-mean(eta_wg);
84 num_t = min(length(tt_wg),length(time_DIC));
85
86 for tt = 1:num_t
87     [valst(tt),idt(tt)] = min(abs(tt_wg-time_DIC(tt)));
88 end
89
90 new_t_wg = tt_wg(idt);
91 new_time_DIC = time_DIC;
92
93 new_eta_wg = etta_wg(idt);
94 new_eta_center_y = (eta_center-nanmean(eta_center))
95 new_eta_center_avg_y = (eta_center_avg_y-nanmean(eta_center_avg_y))
96
97 delta_y = new_eta_wg-new_eta_center_y;
98 delta_y_avg = new_eta_wg-new_eta_center_avg_y;
99
100
101 rms_y = 100*sqrt(nansum(delta_y.^2)/length(delta_y));
102 rms_y_avg = 100*sqrt(nansum(delta_y_avg.^2)/length(delta_y_avg));

```

```

103
104 text(2,-0.008,['RMS = ',num2str(rms_y),'%'])
105 text(2,-0.01,['RMS_{avg} = ',num2str(rms_y_avg),'%'])
106
107 frame_h = get(handle(gcf),'JavaFrame');
108 set(frame_h,'Maximized',1);
109
110 axis([0 52 -0.02 0.02]) %t_wg(end)+1
111 xlabel('time(seconds)')
112 ylabel('Surface Elevation (meters)')
113 legend('DIC analysis (center point)','DIC analysis (average in y)','Wave Gauge','Location','southwest')
114 title('Surface Elevation comparison at the wave gauge location')
115
116 saveas(gcf,[Directory,'DIC_figures\processed_wg3_vs_surface_elevation.jpg'])

```

#### 7.4.4 Script for Plotting PIV Free Surface Values.

```

1 clear all;
2 close all;
3 clc;
4
5 load('all_time_sync_PIV_dic_meters.mat')
6 Directory = 'C:\Users\Jamie\Desktop\Grad Semester 5\time_sync_test_wave_gauge3\';
7 wg_filename = [Directory,'Sine Freq=1Hz Amp=0.02m ang=0rad.txt'];
8 ref_frame = '1';
9
10 %%%%%%%
11
12 all_images_dic_wrong_order = dir([Directory,'frames\*.jpg']);
13
14 % images are loaded incorrectly based on file name so they need to be sorted by frame number instead
15 all_images_file_names = extractfield(all_images_dic_wrong_order,'name'); % first get file names
16 all_images_frame_num_str = strrep(all_images_file_names,'frame_', ''); all_images_frame_num_str = strrep(
    all_images_frame_num_str, '.jpg', ''); % then get frame number by itself
17 all_images_frame_num = cellfun(@str2num,all_images_frame_num_str); % then make it a number not a string
18 for k = 1:length(all_images_dic_wrong_order) % loop to add frame number as a field
    in the original structure
19 [all_images_dic_wrong_order(k).frame_num] = all_images_frame_num(k);
20 end
21
22 [vals,idx]=sort([all_images_dic_wrong_order.frame_num]); % now sort by frame number
23 all_images_dic = all_images_dic_wrong_order(idx);
24 num_images_dic = size(all_images_dic,1);
25
26 num_images = num_images_dic;
27 camera_fps = 60;
28

```

```

29 time_DIC = 0:1/camera_fps:(num_images-2)/camera_fps; % define a time array based on camera
    frames per second
30
31
32
33 %
    %%%%%%%%%%%%%%%%%%%%%%%%%%%%%%%%%%%%%%%%%%%%%%%%%%%%%%%%%%%%%%%%%%%%%%%%%
34
35
36
37 for ii = 1:length(surface_elevation)
38     u_cur_center(ii) = u_cur{ii}(round(length(x)/2),round(length(y)/2));
39     v_cur_center(ii) = v_cur{ii}(round(length(x)/2),round(length(y)/2));
40
41 %     eta_x_3_avg_y(ii) = nanmean(surface_elevation{ii}(:,find(x>3,1,'first')));
42
43     eta_center(ii) = -surface_elevation{ii}(round(length(x)*(1/8)),round(length(y)/2));
44     eta_center_avg_y(ii) = -nanmean(surface_elevation{ii}(round(length(x)*(1/8)),:));
45 end
46
47 all_wg_data = readtable(wg_filename);
48 time_wg = table2array(all_wg_data(6:end,1));
49 eta_wg_3 = table2array(all_wg_data(6:end,18));
50
51 for jj = 1:length(time_wg)
52 %     t_wg(jj) = str2num(time_wg{jj});
53 %     if jj>2 && t_wg(jj)<t_wg(jj-1)
54 %         disp(['index: ',num2str(jj)])
55 %         t_wg(jj) = t_wg(jj)+60;
56 %     else
57 %     end
58
59 %     t_wg(jj) = (t_wg(jj)-str2num(time_wg{1}));
60     eta_wg(jj) = str2num(eta_wg_3{jj});
61 end
62
63 t_wg = 0:0.007814:49.563;
64
65
66 figure(3)
67 plot(time_DIC,(eta_center-nanmean(eta_center))./6)
68 hold on;
69 plot(time_DIC,(eta_center_avg_y-nanmean(eta_center_avg_y))./6)
70 % hold on;
71 % plot(time_DIC,eta_x_3_avg_y-mean(eta_x_3_avg_y))

```

```

72 % hold on;
73 plot(t_wg+0.75,eta_wg-mean(eta_wg))
74
75 tt_wg = t_wg+0.75;
76 etta_wg = eta_wg-mean(eta_wg);
77 num_t = min(length(tt_wg),length(time_DIC));
78
79 for tt = 1:num_t
80     [valst(tt),idt(tt)] = min(abs(tt_wg-time_DIC(tt)));
81 end
82
83 new_t_wg = tt_wg(idt);
84 new_time_DIC = time_DIC;
85
86 new_eta_wg = etta_wg(idt);
87 new_eta_center_y = (eta_center-nanmean(eta_center))./6
88 new_eta_center_avg_y = (eta_center_avg_y-nanmean(eta_center_avg_y))./6
89
90 delta_y = new_eta_wg-new_eta_center_y;
91 delta_y_avg = new_eta_wg-new_eta_center_avg_y;
92
93
94 rms_y = 100*sqrt(nansum(delta_y.^2)/length(delta_y));
95 rms_y_avg = 100*sqrt(nansum(delta_y_avg.^2)/length(delta_y_avg));
96
97 text(2,-0.008,['RMS = ',num2str(rms_y),'%'])
98 text(2,-0.01,['RMS_{avg} = ',num2str(rms_y_avg),'%'])
99
100 frame_h = get(handle(gcf),'JavaFrame');
101 set(frame_h,'Maximized',1);
102
103 axis([0 52 -0.02 0.02]) %t_wg(end)+1
104 xlabel('time(seconds)')
105 ylabel('Surface Elevation (meters)')
106 legend('DIC analysis (center point)','DIC analysis (average in y)','Wave Gauge','Location','southwest')
107 title('Surface Elevation comparison at the wave gauge location')
108
109 saveas(gcf,[Directory,'PIV_figures\processed_wg3_vs_surface_elevation.jpg'])

```

## 7.5 Scripts for Image Processing and Plotting

### 7.5.1 Script for converting im7 images to jpg as well as cropping and stitching images from the 2 different cameras.

```

1 clear all;
2 close all;

```

```

3  clc;
4
5  date = '1_12_2021';
6  aoa = '10';
7  depth = '3_2';
8  depth_frac = strrep(depth, '_', '/');
9  run_case = 'swl';
10
11
12  cam1_Directory = ['D:\MyProjects\Jamie_side_view_cal_', date, '_camera1\camera1_foil_', aoa, '_deg_', depth, '_',
    run_case, '\AddCameraAttributes\Correction\'];
13  cam1_files = dir([cam1_Directory, '*.im7']);
14
15  cam2_Directory = ['D:\MyProjects\Jamie_side_view_cal_', date, '_camera2\camera2_far_field_', aoa, '_deg_', depth, '_',
    run_case, '\AddCameraAttributes\Correction\'];
16  cam2_files = dir([cam2_Directory, '*.im7']);
17
18  num_files = min([length(cam1_files), length(cam2_files)]);
19
20  new_Directory = ['D:\Jamie_DIC\foil_tests\', date, '\', aoa, '_deg\depth_cl_', depth, '\', run_case, '\side_view_frames\
    '];
21
22  % rect_foil = [21.510, 879.250, 2270.980, 485.980];    %for 1/4/2021 110%
23  % rect_far_field = [540.980, 913.510, 2646.980, 485.980];
24
25  % rect_foil = [21,774,2525,590];          % for 1/8/2021 swl and 110% match x and +
26  % rect_far_field = [330,800,2770,590];
27
28  % rect_foil = [21,774,2389,590];          % for 1/8/2021 swl and 110% match x and + but get rid of the divider
29  % rect_far_field = [540,800,2500,590];
30
31  % rect_foil = [35,774,2389,590];          % for 1/11/2021 swl match x and + but get rid of the divider
32  % rect_far_field = [540,800,2500,590];
33
34  % rect_foil = [35,761,2972,590];          % for 1/12/2021 swl match x and +
35  % rect_far_field = [176,800,2500,590];
36
37  rect_foil = [35,761,2807,590];            % for 1/12/2021 swl match x and + but get rid of the divider
38  rect_far_field = [432,800,2715,590];
39
40  % rect_foil = [25,640,2405,870];          % for 2/11/2021 swl match x and + but get rid of the divider
41  % rect_far_field = [295,662,2868,870];
42
43
44
45

```

```

46 for i = 1 %:num_files
47
48     disp(['frame ',num2str(i),' of ',num2str(num_files)])
49
50     cam1_filename = cam1_files(i).name;
51     openim7([cam1_Directory, cam1_filename]);
52
53     A = im;
54     A.w = flipud(A.w');
55     A.w(A.w == 0) = NaN;
56
57     A.x = (A.x-A.x(1))./1000; % this marix is output with units mm so /1000 to get m
58     A.y = (A.y-A.y(1))./1000; % this marix is output with units mm so /1000 to get m
59
60     cam2_filename = cam2_files(i).name;
61     openim7([cam2_Directory, cam2_filename]);
62
63     B = im;
64     B.w = flipud(B.w');
65     B.w(B.w == 0) = NaN;
66
67     B.x = (B.x-B.x(1))./1000; % this marix is output with units mm so /1000 to get m
68     B.y = (B.y-B.y(1))./1000; % this marix is output with units mm so /1000 to get m
69
70     clim = [35 255];
71     figure(1)
72     subplot(2,1,1)
73     imshow(A.w, clim)
74     axis equal;
75
76 %     [im_crop1, rect_foil] = imcrop(A.w);
77     cam1_cropped = imcrop(A.w, rect_foil);
78     cam1_ds = A.x(2)-A.x(1);
79     size_crop = size(cam1_cropped);
80     cam1_x_cropped = 0:cam1_ds:(size_crop(2)-1)*cam1_ds;
81     cam1_y_cropped = 0:cam1_ds:(size_crop(1)-1)*cam1_ds;
82
83     figure(1)
84     subplot(2,1,2)
85     imshow(cam1_cropped, clim)
86     axis equal;
87
88     figure(2)
89     subplot(2,1,1)
90     imshow(B.w, clim)
91     axis equal;

```

```

92
93 % [im_crop1, rect_far_field] = imcrop(B.w);
94 cam2_cropped = imcrop(B.w,rect_far_field);
95 cam2_ds = B.x(2)-B.x(1);
96 size_crop = size(cam1_cropped);
97 cam2_x_cropped = 0:cam2_ds:(size_crop(2)-1)*cam2_ds;
98 cam2_y_cropped = 0:cam2_ds:(size_crop(1)-1)*cam2_ds;
99
100 figure(2)
101 subplot(2,1,2)
102 imshow(cam2_cropped,clims)
103 axis equal;
104
105 combImg = imfuse(cam1_cropped, cam2_cropped,'montage');
106
107 for j = 1:length(combImg)
108     if all(combImg(:,j)==0)
109         ind(j) = j;
110     else
111     end
112 end
113 ind = nonzeros(ind);
114 combImg_no_space = combImg(1:end,[1:ind(1)-1,ind(end)+1:end]);
115
116 figure(3)
117 imshow(combImg_no_space)
118 axis equal;
119
120 imwrite(combImg_no_space,[new_Directory,'frame_',sprintf('%04d.jpg', i)])
121
122 end
123
124 %%% 10_deg
125 tr_edge_x = 200-rect_foil(1); %3_2          250-rect_foil(1); %1          220-rect_foil(1); %5/4
126         selected in cam1 image
127 tr_edge_y = 2170-rect_foil(2);%3_2          1840-rect_foil(2);%1          2050-rect_foil(2);%5/4
128         selected in cam1 image          % origin for values below is top left corner of the image
129
130 % %%% 10_deg
131 % tr_edge_x = 260-rect_foil(1); %5/4          200-rect_foil(1); %1          365-rect_foil(1); %3_2
132         selected in cam1 image
133 % tr_edge_y = 2062-rect_foil(2);%5/4          1800-rect_foil(2);%1          2108-rect_foil(2);%3_2
134         selected in cam1 image          % origin for values below is top left corner of the image
135
136 % %%% 5_deg

```

```

133 % tr_edge_x = 270-rect_foil(1); %5/4      100-rect_foil(1); %3_2      243-rect_foil(1); %1
      selected in cam1 image
134 % tr_edge_y = 2020-rect_foil(2);%5/4      2090-rect_foil(2);%3_2      1765-rect_foil(2);%1
      selected in cam1 image      % origin for values below is top left corner of the image
135
136 foil_center_x = tr_edge_x*cam1_ds-(0.15*cosd(10)); % get adjacent length in m using sohcahtoa--hypotenuse is 0.15
      m (chord length/2)
137 foil_center_y = tr_edge_y*cam1_ds-(0.15*sind(10)); % get opposite length in m using sohcahtoa--hypotenuse is 0.15
      m (chord length/2)
138
139 x_dist = [[1:1:size(cam1_cropped,2)].*cam1_ds,[1:1:size(cam2_cropped,2)].*cam2_ds]; % compute the x values using
      the 2 different cam ds values
140 y_dist = [1:1:size(cam1_cropped,1)].*cam1_ds; % compute the y values using the 2 different cam ds
      values
141
142 im_data_filename = ['im_data_side_view_',date,'_',aoa,'_deg_cl_',depth,'_',run_case,'.mat'];
143
144 save(im_data_filename,'foil_center_x','foil_center_y','x_dist','y_dist','cam1_ds','cam2_ds','-v7.3');

```

## 7.5.2 Script for determining Froude values and expected wavelengths.

```

1 clear all;
2 close all;
3 clc;
4
5 % Velocity Curve values
6 percents = [0:10:120,125];
7 vel = [0, 0.09, 0.17, 0.26, 0.35, 0.44, 0.53, 0.61, 0.71, 0.80, 0.89, 0.97, 1.06, 1.10]; % velocity values with
      current meter at wave gauge 8 (slightly off-centered)
8
9 figure(1)
10 plot(percents,vel,'b*')
11 xlabel('Percentage (%)')
12 ylabel('Velocity of flow (m/s)')
13 title('Percentage vs. Velocity')
14
15 % Froude Number Calculations
16
17 chord_length_in = 11.75; % 11.75; % inches
18 chord_length_m = chord_length_in*0.0254; % 11.75*0.0254; % meters
19 g = 9.81; % m/s^2
20
21 depths = [chord_length_m*1, chord_length_m*5/4, chord_length_m*3/2];
22 % chord_lengths = [chord_length_m,chord_length_m,chord_length_m];
23 % currents = vel(3:end); % 0.1:0.1:0.7;
24
25 for i = 1:length(vel)

```

```

26     Froude(i,:) = (vel(i)./(sqrt(depths.*g)).)^2; %c^2/gl
27 end
28
29
30 VarNames={'depth = c1(1)', 'depth = c1(5/4)', 'depth = c1(3/2)'};
31 RowNames={['current =',num2str(vel(1)),' m/s'],['current =',num2str(vel(2)),' m/s'],['current =',num2str(vel(3)),
    ' m/s'],['current =',num2str(vel(4)),' m/s'],['current =',num2str(vel(5)),' m/s'],['current =',num2str(vel
    (6)),' m/s'],['current =',num2str(vel(7)),' m/s'],['current =',num2str(vel(8)),' m/s'],['current =',num2str(
    vel(9)),' m/s'],['current =',num2str(vel(10)),' m/s'],['current =',num2str(vel(11)),' m/s'],['current =',
    num2str(vel(12)),' m/s'],['current =',num2str(vel(13)),' m/s'],['current =',num2str(vel(14)),' m/s']];
32 FroudeTable = array2table(Froude,'VariableNames',VarNames,'RowNames',RowNames)
33
34 VarNames1={'depth = c1(1)', 'depth = c1(5/4)', 'depth = c1(3/2)'};
35 RowNames1={['current =',num2str(vel(9)),' m/s'],['current =',num2str(vel(10)),' m/s'],['current =',num2str(vel
    (11)),' m/s'],['current =',num2str(vel(12)),' m/s'],['current =',num2str(vel(13)),' m/s'],['current =',
    num2str(vel(14)),' m/s']];
36 FroudeTable1 = array2table(Froude(9:end,:), 'VariableNames',VarNames1,'RowNames',RowNames1)
37
38 % save('Froude_values_2_11_2021.mat','depths','percents','vel','Froude','-v7.3');
39
40 for j = 1:length(depths)
41     [L(:,j)] = Fr_ldis(Froude(:,j),depths(j),0.7112)
42 end
43
44 save('Froude_values_2_11_2021.mat','depths','percents','vel','Froude','L','-v7.3');

```

### 7.5.3 Function for determining expected wavelengths using linear dispersion relation.

```

1     function [L] = Fr_ldis(Fr,d,H)
2     %-----
3     %0 LDISF      ldis
4     %1 Purpose    ldis computes the wavelength L using the linear dispersion
5     %1              relation :  $k \tanh(k*d) = (\omega)^2 / g$  in the form
6     %1               $L = L_0 \tanh(k*h)$ , with  $L_0 = g T^2 / 2 \pi$ 
7     %2 Method     Newton-Raphson iteration method with relative error EPS
8     %2              Computations assume SI, i.e., MKS units.
9     %2              Uses :  $x = k*h$ ;  $k = 2 \pi / L$ 
10    %2               $x(n+1) = x(n) - F(x(n))/DF(x(n))$ 
11    %2               $F(x(n)) = x(n) - D/\tanh(x(n))$ 
12    %2               $DF(x(n)) = 1 + D/\sinh(x(n))^2$ 
13    %2              Number of iterations is limited to ITERM=50
14    %3 CALL arg. T : Wave period (s)
15    %3              H : Depth of the sea (m)
16    %3 RET arg. L : Wavelength (m)
17    %3 OTHERS     g : Acceleration of gravity (m/s^2)

```

```

18 %E ERRORS The number of iterations is too large
19 %9 March 00 S. Grilli, Ocean Engng. Dept., Univ. of Rhode Island
20 %L
21 %-----
22 %
23     g   = 9.81;      %m/s^2
24     EPS = 0.000001;
25     ITERM = 50;
26 %
27     D   = Fr .* d;
28     ITER = 0;
29     ERR = 1;
30 %
31 %.....Initial guess for nondimensional solution X
32 %
33     if (D >= 1)
34         X0 = D;
35     else
36         X0 = 50; %30*D
37     end
38 %
39 %.....Solution using Newton-Raphson method
40 %
41     while ((ERR > EPS) & (ITER <= ITERM))
42         F   = D.*X0 - H.*tanh(X0);
43         DF  = D - H./(cosh(X0).^2);
44         X1  = X0 - F./DF;
45         ERR = abs((X1-X0)./X0);
46         X0  = X1;
47         ITER = ITER + 1;
48     end
49 %
50     if (ITER > ITERM)
51         fprintf(1,'convergence failed\r');
52     else
53         L = 2 .* pi .*H ./ X1;
54     end

```

#### 7.5.4 Script for analyzing the side view images to extract the waterline.

```

1 clear all;
2 %close all;
3 clc;
4
5 date = '2_11_2021';
6 aoa = '5';
7 depth = '3_2';

```

```

8 percentage = '80';
9
10 wg_Directory = ['C:\Users\Jamie\Desktop\Grad Semester 5\foil_tests\' ,date, '\', aoa, '_deg\depth_cl_', depth, '\',
    percentage, '_percent\'];
11
12 wg_filename = [wg_Directory, 'all_wave_gauges_', aoa, '_deg_cl_', depth, '_', percentage, '_percent.txt'];
13
14 all_wg_data = readtable(wg_filename);
15 time_wg = table2array(all_wg_data(6:end,1));
16 all_eta_wg_tab = table2array(all_wg_data(6:end,16:21));
17 num_wg = size(all_eta_wg_tab,2);
18
19 for jj = 1:length(time_wg)
20     t_wg(jj) = str2num(time_wg{jj});
21     if jj>2 && t_wg(jj)<t_wg(jj-1)
22         disp(['index: ', num2str(jj)])
23         t_wg(jj) = t_wg(jj)+60;
24     else
25     end
26
27     t_wg(jj) = (t_wg(jj)-str2num(time_wg{1}));
28     for kk = 1:num_wg
29         all_eta_wg(jj, kk) = str2num(all_eta_wg_tab{jj, kk});
30     end
31 end
32
33 Directory = ['C:\Users\Jamie\Desktop\Grad Semester 5\foil_tests\' ,date, '\', aoa, '_deg\depth_cl_', depth, '\',
    percentage, '_percent\side_view_frames\'];
34
35 all_images = dir([Directory, '*.jpg']);
36 num_images = size(all_images,1);
37
38 swl_Dir = ['C:\Users\Jamie\Desktop\Grad Semester 5\foil_tests\' ,date, '\', aoa, '_deg\depth_cl_', depth, '\swl\
    side_view_frames\'];
39
40 load(['im_data_side_view_', date, '_', aoa, '_deg_cl_', depth, '_swl.mat']);
41
42 % ds = 5.393399894237518e-04; % 1/8/21?
43
44 ds = mean([cam1_ds, cam2_ds]); %4.725580066442489e-04; % 1/12/21
45
46 for j = 1:num_images
47     im_filename{j} = all_images(j).name;
48     im_file = imread([Directory, im_filename{j}]);
49
50     bw = im2bw(imcomplement(im_file),0.65);

```

```

51 edges = bw; %edge(bw,'canny');
52
53 RI = imref2d(size(edges));
54 RI.XWorldLimits = [0 RI.ImageExtentInWorldX*ds];
55 RI.YWorldLimits = [0 RI.ImageExtentInWorldY*ds];
56
57 swl_file = imread([swl_Dir,'frame_0001.jpg']);
58 swl_bw = im2bw(imcomplement(swl_file),0.55);
59 swl_edges = swl_bw; %edge(swl_bw,'canny');
60
61 swl_RI = imref2d(size(swl_edges));
62 swl_RI.XWorldLimits = [0 swl_RI.ImageExtentInWorldX*ds];
63 swl_RI.YWorldLimits = [0 swl_RI.ImageExtentInWorldY*ds];
64
65 if j==1
66     for i = 1:length(swl_edges)
67         swl_y_val = find(swl_edges(:,i)==1);
68         swl_x_vals(i) = i;
69         if isempty(swl_y_val) %| k<260
70             swl_y_vals(i)=NaN;
71         elseif range(swl_y_val)>=(1/100*length(swl_edges'))
72             swl_y_vals(i) = NaN; %mean(y_val);
73         else
74             swl_y_vals(i) = mean(swl_y_val);
75         end
76     end
77 else
78 end
79
80 swl_x_vals_m = swl_x_vals*ds;
81 swl_y_vals_m = swl_y_vals*ds;
82
83 % x_loc_wg1 = 2.100; % 2.100 for 110% 2.013 for 120% % for 1/4/2021
84 % x_loc_wg2 = 1.874; % 1.874 for 110% 1.735 for 120% % for 1/4/2021
85 % x_loc_wg3 = 1.555; % 1.555 for 110% 1.445 for 120% % for 1/4/2021
86 % x_loc_wg4 = 1.313; % 1.313 for 110% 1.165 for 120% % for 1/4/2021
87 % x_loc_wg5 = 1.078; % 1.078 for 110% 0.930 for 120% % for 1/4/2021
88 % x_loc_wg6 = 0.702; % 0.702 for 110% 0.605 for 120% % for 1/4/2021
89
90 % x_loc_wg1 = 2.100; % 2.100 for 110% 2.013 for 120% % for 1/8/2021
91 % x_loc_wg2 = 1.874; % 1.874 for 110% 1.735 for 120% % for 1/8/2021
92 % x_loc_wg3 = 1.555; % 1.555 for 110% 1.445 for 120% % for 1/8/2021
93 % x_loc_wg4 = 1.313; % 1.313 for 110% 1.165 for 120% % for 1/8/2021
94 % x_loc_wg5 = 1.078; % 1.078 for 110% 0.930 for 120% % for 1/8/2021
95 % x_loc_wg6 = 0.702; % 0.702 for 110% 0.605 for 120% % for 1/8/2021
96 %

```

```

97 %     x_loc_wg1 = 2.231; % for 1/12/2021
98 %     x_loc_wg2 = 1.951; % for 1/12/2021
99 %     x_loc_wg3 = 1.610; % for 1/12/2021
100 %    x_loc_wg4 = 1.341; % for 1/12/2021
101 %    x_loc_wg5 = 1.110; % for 1/12/2021
102 %    x_loc_wg6 = 0.843; % for 1/12/2021
103
104    x_loc_wg1 = 2.500; % for 2/11/2021
105    x_loc_wg2 = 2.060; % for 2/11/2021
106    x_loc_wg3 = 1.690; % for 2/11/2021
107    x_loc_wg4 = 1.312; % for 2/11/2021
108    x_loc_wg5 = 0.868; % for 2/11/2021
109    x_loc_wg6 = 0.513; % for 2/11/2021
110
111    all_xloc_wg = [x_loc_wg1,x_loc_wg2,x_loc_wg3,x_loc_wg4,x_loc_wg5,x_loc_wg6];
112
113    t_im = num_images/50*(j-1); %number of images/50 seconds to get frame rate (frames/second)
114
115    [d, ix] = min(abs(t_wg-t_im));
116    t_wg_clipped(j) = t_wg(ix);
117
118    for k = 1:num_wg
119        [val(k),ind_wg(k)] = min(abs(sw1_x_vals_m-all_xloc_wg(k)));
120        all_eta_wg_clipped(j,k) = nanmean(sw1_y_vals_m(ind_wg(k)-40:ind_wg(k)+40))-all_eta_wg(ix,k);
121    end
122
123
124
125    for i = 1:length(edges)
126        y_val = find(edges(:,i)==1);
127        x_vals(i) = i;
128        if isempty(y_val) %| k<260
129            y_vals(i)=NaN;
130        elseif i>51 && all(abs(y_val-nanmean(y_vals(i-50:i-1)))<=(1/550*length(edges'))) && nanmean(abs(y_val-
nanmean(y_vals(1:i-1))))<=(1/50*length(edges')) && range(y_val)<=(1/50*length(edges')) && nanmean(diff(y_val
))<=5
131            y_vals(i) = mean(y_val);
132 %            disp(num2str(k))
133        elseif range(y_val)>=(1/50*length(edges'))
134            y_vals(i) = NaN;
135        elseif i>2 && any(abs(y_val-nanmean(y_vals(1:i-1)))>=(1/50*length(edges')))
136            y_vals(i) = NaN;
137        elseif i>51 && any(abs(y_val-nanmean(y_vals(i-50:i-1)))>=(1/300*length(edges')))
138            y_vals(i) = NaN;
139 %            disp(num2str(k))
140        else

```

```

141         y_vals(i) = mean(y_val);
142 %         disp(num2str(k))
143     end
144 end
145
146 x_vals_m = x_vals*ds;
147 y_vals_m = y_vals*ds;
148
149 [Maxima,MaxIdx] = findpeaks(y_vals_m,'MinPeakDistance',1200);
150 Maxy = y_vals_m(MaxIdx);
151 Maxx = x_vals_m(MaxIdx);
152
153 Mins=max(y_vals_m)-y_vals_m;
154 [Minima,MinIdx] = findpeaks(Mins,'MinPeakDistance',1200);
155 Miny = y_vals_m(MinIdx);
156 Minx = x_vals_m(MinIdx);
157
158 Min_x = Minx(Minx>0.01);
159 Min_y = Miny(Miny>0.01);
160
161 Max_x = Maxx(Maxx>0.01);
162 Max_y = Maxy(Maxx>0.01);
163
164 n = 4; % expected number of peaks and troughs
165
166 Min_x(end+1:n)=nan;
167 Min_y(end+1:n)=nan;
168 Max_x(end+1:n)=nan;
169 Max_y(end+1:n)=nan;
170
171 all_min_x(:,j) = Min_x(1:n);
172 all_min_y(:,j) = Min_y(1:n);
173 all_max_x(:,j) = Max_x(1:n);
174 all_max_y(:,j) = Max_y(1:n);
175
176 water_line_x(:,j) = x_vals_m;
177 water_line_y(:,j) = y_vals_m;
178
179 Wave_lengths_m(:,j) = [diff(all_min_x(:,j));diff(all_max_x(:,j))];
180 Wave_heights_m(:,j) = [(all_max_y(1,j)-all_min_y(1,j)),(all_max_y(2,j)-all_min_y(2,j)),(all_max_y(3,j)-
    all_min_y(3,j))]; %,(all_max_y(3,j)-all_min_y(3,j)); % there were 3 peaks and troughs in 110% run but only
    2 peaks and trough in 120% run
181
182
183 % figure(1)
184 % subplot(3,1,1)

```

```

185 %   imshow(swl_file)
186 %   axis equal
187 %   title(['Raw Image of Still Water Level'])
188 %   subplot(3,1,2)
189 %   imshow(swl_bw)
190 %   axis equal
191 %   title(['Black & White Image of Still Water Level'])
192 %   subplot(3,1,3)
193 %   imshow(swl_edges,swl_RI)
194 %   hold on
195 %   axis equal
196 %   title(['Waterline from of Still Water Level'])
197 %
198 %   plot(swl_x_vals_m,swl_y_vals_m,'*r') %,'LineWidth',1.2)
199 %
200 %   frame_h = get(handle(gcf),'JavaFrame');
201 %   set(frame_h,'Maximized',1);
202 %   legend('Waterline','Location','northwest')
203 %
204 %   figure(2)
205 %   subplot(3,1,1)
206 %   imshow(im_file)
207 %   axis equal
208 %   title(['Raw Image of side view for frame: ',num2str(j)])
209 %   subplot(3,1,2)
210 %   imshow(bw)
211 %   axis equal
212 %   title(['Black & White Image of side view for frame: ',num2str(j)])
213 %   subplot(3,1,3)
214 %   imshow(edges,RI)
215 %   hold on
216 %   axis equal
217 %   title(['Waterline from image with wave gauge data for frame: ',num2str(j)])
218 %
219 %   plot(water_line_x(:,j),water_line_y(:,j),'*r') %,'LineWidth',1.2)
220 %   hold on;
221 %
222 %   plot(all_max_x(:,j),all_max_y(:,j),'b*')
223 %   hold on;
224 %   plot(all_min_x(:,j),all_min_y(:,j),'g*')
225 %   hold on;
226 %   plot(all_xloc_wg,all_eta_wg_clipped(j,:), 'm*') %
227 %   xlabel('X Distance (m)')
228 %   ylabel('Y Distance (m)')
229 %
230 %   frame_h = get(handle(gcf),'JavaFrame');

```

```

231 %     set(frame_h,'Maximized',1);
232 %     legend('Waterline','Troughs','Peaks','Wave Gauge Data','Location','northwest')
233
234 %%     saveas(gcf,[Directory,'water_line_figures\processed_waterline_',im_filename{j}])
235
236
237     disp(['frame: ',num2str(j),' of ',num2str(num_images)])
238
239 end
240
241 for k = 1:num_wg
242     all_eta_wg_avg(k) = nanmean(all_eta_wg_clipped(:,k));
243 end
244
245 avg_max_x = nanmean(all_max_x');
246 avg_max_y = nanmean(all_max_y');
247 avg_min_x = nanmean(all_min_x');
248 avg_min_y = nanmean(all_min_y');
249
250 max_y = max(all_max_y');
251 min_y = min(all_min_y');
252
253 water_line_x_avg = nanmean(water_line_x');
254 water_line_y_avg = nanmean(water_line_y');
255
256 N = size(water_line_y,2);
257 SEM = std(water_line_y','omitnan') / sqrt(N); % Standard Error Of The Mean
258 CI95 = SEM * tinvc(0.975, N-1); % 95% Confidence Intervals
259 CI95_clipped = CI95;
260 water_line_x_avg_clipped = water_line_x_avg;
261 water_line_y_avg_clipped = water_line_y_avg;
262
263 [val,ind] = find(CI95>1e-03);
264 CI95_clipped(ind) = NaN;
265 water_line_x_avg_clipped(ind) = NaN;
266 water_line_y_avg_clipped(ind) = NaN;
267
268
269 all_data_save_filename = ['all_side_view_',date,'_',aoa,'_deg_cl_',depth,'_',percentage,'_percent.mat'];
270 avg_data_save_filename = ['avg_side_view_',date,'_',aoa,'_deg_cl_',depth,'_',percentage,'_percent.mat'];
271
272 save(all_data_save_filename,'Wave_lengths_m','Wave_heights_m','water_line_x','water_line_y','all_min_x','
    all_min_y','all_max_x','all_max_y','all_xloc_wg','all_eta_wg_clipped','swl_x_vals_m','swl_y_vals_m','-v7.3')
    ;
273 save(avg_data_save_filename,'water_line_x_avg','water_line_y_avg','CI95','water_line_x_avg_clipped','
    water_line_y_avg_clipped','CI95_clipped','avg_min_x','avg_min_y','avg_max_x','avg_max_y','min_y','max_y','

```

```
all_xloc_wg','all_eta_wg_avg','swl_x_vals_m','swl_y_vals_m','-v7.3');
```

### 7.5.5 Script for shifting the average waterline based on the foil center as well as the still waterline.

```
1 clear all;
2 close all;
3 clc;
4
5 %%% tank test parameters
6 date = '1_12_2021';
7 aoa = '10';
8 depth = '1';
9 depth_frac = strrep(depth,'_','/');
10 percentage = '125';
11
12 %%% foil parameters
13 load(['im_data_side_view_',date,'_',aoa,'_deg_cl_',depth,'_swl.mat']);
14 chord_length = 11.75*0.0254; %0.29845;
15 thickness = chord_length/5;
16 depth_of_foil = str2num(depth_frac)*chord_length;
17
18
19
20 load(['Froude_values_',date,'.mat']);
21 [val_p,ind_p] = find(percents==str2num(percentage));
22 [val_d,ind_d] = find(depths==depth_of_foil);
23 speed = [num2str(vel(ind_p)),' m/s'];
24 froude = [num2str(Froude(ind_p,ind_d))];
25
26 avg_data_save_filename = ['.\',date,'\avg_side_view_',date,'_',aoa,'_deg_cl_',depth,'_',percentage,'_percent.mat'
    ];
27 load(avg_data_save_filename);
28
29 all_data_save_filename = ['.\',date,'\all_side_view_',date,'_',aoa,'_deg_cl_',depth,'_',percentage,'_percent.mat'
    ];
30 load(all_data_save_filename);
31 %
32 all_xloc_wg = [2.231,1.951,1.610,1.325,1.115,0.850];
33 %
34 % all_data_save_filename = ['all_side_view_',date,'_',aoa,'_deg_cl_',depth,'_',percentage,'_percent.mat'];
35 % avg_data_save_filename = ['avg_side_view_',date,'_',aoa,'_deg_cl_',depth,'_',percentage,'_percent.mat'];
36 %
37 % save(all_data_save_filename,'Wave_lengths_m','Wave_heights_m','water_line_x','water_line_y','all_min_x','
    all_min_y','all_max_x','all_max_y','all_max_y','all_xloc_wg','all_eta_wg_clipped','swl_x_vals_m','swl_y_vals_m','-v7.3')
    ;
```

```

38 % save(avg_data_save_filename,'water_line_x_avg','water_line_y_avg','CI95','water_line_x_avg_clipped','
    water_line_y_avg_clipped','CI95_clipped','avg_min_x','avg_min_y','avg_max_x','avg_max_y','all_xloc_wg','
    all_eta_wg_avg','swl_x_vals_m','swl_y_vals_m','-v7.3');
39
40
41 Directory = ['C:\Users\Jamie\Desktop\Grad Semester 5\foil_tests\',date,'\','_','_','_deg\depth_cl_',depth,'\','
    percentage','_percent\side_view_frames\'];
42
43 all_images = dir([Directory,'*.jpg']);
44 num_images = size(all_images,1);
45
46 % ds = 5.393399894237518e-04; % 1/8/21?
47
48 ds = mean([cam1_ds,cam2_ds]); %4.725580066442489e-04; % 1/12/21
49
50 for j = 1:2 %num_images
51
52     im_filename{j} = all_images(j).name;
53     im_file_all{j} = imread([Directory,im_filename{j}]);
54
55     bw_all{j} = im2bw(imcomplement(im_file_all{j}),0.6);
56     edges_all{j} = edge(bw_all{j},'canny');
57
58     RI_m = imref2d(size(edges_all{j}));
59     RI_m.XWorldLimits = [0 RI_m.ImageExtentInWorldX*ds];
60     RI_m.YWorldLimits = [0 RI_m.ImageExtentInWorldY*ds];
61
62
63     if j>1
64         im_file_avg = imfuse(im_file_all{j},im_file_all{j-1},'blend');
65         bw_avg = imfuse(bw_all{j},bw_all{j-1},'blend');
66         edges_avg = imfuse(edges_all{j},edges_all{j-1},'blend');
67     elseif j>2
68         im_file_avg = imfuse(im_file_all{j},im_file_avg,'blend');
69         bw_avg = imfuse(bw_all{j},bw_avg,'blend');
70         edges_avg = imfuse(edges_all{j},edges_avg,'blend');
71     else
72     end
73
74
75     disp(['frame: ',num2str(j),' of ',num2str(num_images)])
76
77 end
78
79
80

```

```

81 for i = 1:7
82     if i <7
83         x_loc = all_xloc_wg(i);
84         delta = 50;
85     elseif i == 7
86         x_loc = 0.059;
87         delta = 50;
88     end
89     [val,max_ind] = min(abs(water_line_x_avg_clipped-x_loc));
90     water_line_y_avg_clipped(max_ind-delta:max_ind+delta) = NaN;
91
92 end
93
94 [Maxima,MaxIdx] = findpeaks(water_line_y_avg_clipped,'MinPeakDistance',700);
95 Maxy = water_line_y_avg_clipped(MaxIdx);
96 Maxx = water_line_x_avg_clipped(MaxIdx);
97
98
99 Mins=max(water_line_y_avg_clipped)-water_line_y_avg_clipped;
100 [Minima,MinIdx] = findpeaks(Mins,'MinPeakDistance',700);
101 Miny = water_line_y_avg_clipped(MinIdx);
102 Minx = water_line_x_avg_clipped(MinIdx);
103
104 Min_x = Minx(Minx>0.1);
105 Min_y = Miny(Minx>0.1);
106
107 Max_x = Maxx(Maxx>0.001);
108 Max_y = Maxy(Maxx>0.001);
109
110 Wave_lengths_m_avg = [diff(Min_x),diff(Max_x)];
111 num_peaks = min(length(Min_y),length(Max_y));
112
113 for i = 1:num_peaks
114     Wave_heights_m_avg(i) = Max_y(i)-Min_y(i);
115 end
116
117 Wave_lengths_cl_avg = Wave_lengths_m_avg./chord_length;
118 Wave_heights_cl_avg =Wave_heights_m_avg./chord_length;
119
120
121
122 figure(1)
123 subplot(3,1,1)
124 imshow(im_file_avg)
125 axis equal

```

```

126 title(['Angle of attack: ',aoa,' deg, Depth of foil: ',depth_frac,'*chord length, Froude #: ',froude,' (Composite
      of raw images)'])
127 subplot(3,1,2)
128 imshow(bw_avg)
129 axis equal
130 title(['Composite of the black & white image'])
131 subplot(3,1,3)
132 imshow(edges_avg,RI_m)
133 hold on
134 axis equal
135 title(['Composite of the waterline image over all time steps with wave gauge data'])
136
137 % plot(water_line_x_avg,water_line_y_avg,'r')
138 errorbar(water_line_x_avg_clipped,water_line_y_avg_clipped, CI95_clipped,'r')
139 hold on;
140 %
141 plot(Max_x,Max_y,'b*')
142 hold on;
143 plot(Min_x,Min_y,'g*')
144 hold on;
145 plot(all_xloc_wg,all_eta_wg_avg,'m*')
146 xlabel('X Distance (m)')
147 ylabel('Y Distance (m)')
148
149 set(gcf, 'Units', 'Normalized', 'OuterPosition', [0 0 0.75 1]);
150 legend('Waterline & Std. Deviation','Troughs','Peaks','Wave Gauge Data','Location','northwest')
151
152 saveas(gcf,[Directory,'water_line_figures\processed_wl_avg_',date,'_',aoa,'_deg_cl_',depth,'_',percentage,'
      _percent.jpg'])
153 saveas(gcf,[Directory,'water_line_figures\processed_wl_avg_',date,'_',aoa,'_deg_cl_',depth,'_',percentage,'
      _percent'])
154
155 %%%%%%%%%%
156
157 c = polyfit(sw1_x_vals_m(~isnan(sw1_y_vals_m)),sw1_y_vals_m(~isnan(sw1_y_vals_m)),1);
158 y_est = polyval(c,sw1_x_vals_m);
159
160 water_line_y_avg_corrected = water_line_y_avg_clipped-(y_est-c(2));
161 for k = 1:6 %6 wave gauges
162     [vals(k),inds_eta(k)] = min(abs(water_line_x_avg-all_xloc_wg(k)));
163 end
164 all_eta_wg_avg_corrected = all_eta_wg_avg-(y_est(inds_eta)-c(2));
165 for k = 1:length(Max_x)
166     [vals(k),inds_max(k)] = min(abs(water_line_x_avg-Max_x(k)));
167 end
168 Max_y_corrected = Max_y-(y_est(inds_max)-c(2));

```

```

169 for k = 1:length(Min_x)
170     [vals(k),inds_min(k)] = min(abs(water_line_x_avg-Min_x(k)));
171 end
172 Min_y_corrected = Min_y-(y_est(inds_min)-c(2));
173
174
175 Max_y_cl = (Max_y_corrected-nanmean(sw_l_y_vals_m(1:1000)))/chord_length;
176 Max_x_cl = (Max_x-foil_center_x)/chord_length;
177
178 Min_y_cl = (Min_y_corrected-nanmean(sw_l_y_vals_m(1:1000)))/chord_length;
179 Min_x_cl = (Min_x-foil_center_x)/chord_length;
180
181
182 water_line_x_avg_cl = water_line_x_avg_clipped./chord_length;
183 water_line_y_avg_cl = (water_line_y_avg_corrected-nanmean(sw_l_y_vals_m(1:500)))/chord_length;
184 CI95_cl = CI95_clipped./chord_length;
185
186 [foil_x,foil_y] = calculateEllipse(foil_center_x, depth_of_foil, chord_length/2, thickness/2, 180-str2num(aoa));
187 foil_x_cl = [foil_x./chord_length; foil_center_x./chord_length];
188 foil_y_cl = [foil_y./chord_length; depth_of_foil./chord_length];
189
190 water_line_x_avg_cl = water_line_x_avg_cl-foil_x_cl(end);
191 all_xloc_wg_cl = all_xloc_wg./chord_length-foil_x_cl(end);
192 foil_x_cl = foil_x_cl-foil_x_cl(end);
193
194 figure(2)
195 % errorbar(water_line_x_avg_clipped./chord_length,water_line_y_avg_clipped./chord_length, CI95_clipped./
    chord_length,'g')
196 % hold on;
197 errorbar(water_line_x_avg_cl,water_line_y_avg_cl, CI95_cl,'r')
198 hold on;
199
200 plot(foil_x_cl,foil_y_cl,'c*')
201 hold on;
202 plot(Max_x_cl,Max_y_cl,'b*')
203 hold on;
204 plot(Min_x_cl,Min_y_cl,'g*')
205 hold on;
206 xlim([-0.3/chord_length 2.75/chord_length])
207 ylim([-0.05/chord_length (depth_of_foil+thickness)/chord_length])
208 % axis equal;
209 title(['Angle of attack: ',aoa,' deg, Depth of foil: ',depth_frac,'*chord length, Froude #: ',froude,' (free
    surface extracted from images for all time steps)'])
210
211
212 all_eta_wg_avg_cl = (all_eta_wg_avg_corrected-nanmean(sw_l_y_vals_m(1:500)))/chord_length;

```

```

213
214 plot(all_xloc_wg_cl,all_eta_wg_avg_cl,'m*') %
215 hold on;
216
217 idx = find(~isnan(water_line_y_avg_cl));
218 no_nan_water_line_x_avg_cl = water_line_x_avg_cl(idx) ;
219 no_nan_water_line_y_avg_cl = water_line_y_avg_cl(idx) ;
220
221 [curve_fit, goodness, output] = fit(no_nan_water_line_x_avg_cl',no_nan_water_line_y_avg_cl','sin3')
222
223 plot(curve_fit,'b')%,water_line_x_avg_cl,water_line_y_avg_cl,'r')
224 hold on;
225
226
227 % plot(sw1_x_vals_m./chord_length,y_est./chord_length,'k*')
228
229
230 xlabel('X Distance (chord lengths)')
231 ylabel('Y Distance (chord lengths)')
232
233 frame_h = get(handle(gcf),'JavaFrame');
234 set(frame_h,'Maximized',1);
235 set(gca, 'YDir','reverse')
236 set(gca,'LooseInset',get(gca,'TightInset'));
237 legend('Waterline & Std. Deviation','Foil Location','Troughs','Peaks','Wave Gauge Data','Location','southeast')
238
239 saveas(gcf,[Directory,'water_line_figures\processed_wl_with_foil_',date,'_',aoa,'_deg_cl_',depth,'_',percentage,'
    _percent.jpg'])
240 saveas(gcf,[Directory,'water_line_figures\processed_wl_with_foil_',date,'_',aoa,'_deg_cl_',depth,'_',percentage,'
    _percent'])
241
242
243 %
244 % avg_m_data_save_filename = ['.\',date,'_plotting\avg_meters_side_view_',date,'_',aoa,'_deg_cl_',depth,'_',
    percentage,'_percent_corrected.mat'];
245 % avg_cl_data_save_filename = ['.\',date,'_plotting\avg_cl_side_view_',date,'_',aoa,'_deg_cl_',depth,'_',
    percentage,'_percent_corrected.mat'];
246 %
247 % save(avg_m_data_save_filename,'chord_length','depth_of_foil','froude','aoa','im_file_avg','bw_avg','edges_avg
    ','RI_m','water_line_x_avg_clipped','water_line_y_avg_clipped','CI95_clipped','all_xloc_wg','all_eta_wg_avg
    ','-v7.3');
248 % save(avg_cl_data_save_filename,'chord_length','depth_of_foil','froude','aoa','water_line_x_avg_cl','
    water_line_y_avg_cl','CI95_cl','foil_x_cl','foil_y_cl','all_xloc_wg_cl','all_eta_wg_avg_cl','-v7.3');
249
250 % % m_data_save_filename = ['.\',date,'_plotting\avg_meters_side_view_',date,'_',aoa,'_deg_cl_',depth,'_',
    percentage,'_percent_corrected.mat'];

```

```

251 % % % save(m_data_save_filename,'chord_length','depth_of_foil','froude','aoa','im_file_avg','bw_avg','edges_avg
    ','RI_m','water_line_x_avg_clipped','water_line_y_avg_clipped','CI95_clipped','curve_fit','Max_x','Max_y','
    Min_x','Min_y','all_xloc_wg','all_eta_wg_avg','-v7.3');
252 % % %
253 % % % cl_data_save_filename = ['.\'',date,'\plotting\avg_cl_side_view_',date,'\_',aoa,'\deg_cl_',depth,'\_',
    percentage,'\percent_corrected.mat'];
254 % % % save(cl_data_save_filename,'chord_length','depth_of_foil','froude','aoa','water_line_x_avg_cl','
    water_line_y_avg_cl','CI95_cl','curve_fit','foil_x_cl','foil_y_cl','Max_x_cl','Max_y_cl','Min_x_cl','
    Min_y_cl','all_xloc_wg_cl','all_eta_wg_avg_cl','-v7.3');
255 % % %
256 % % % wh_wl_data_save_filename = ['.\'',date,'\wh_wl\avg_wh_wl_side_view_',date,'\_',aoa,'\deg_cl_',depth,'\_',
    percentage,'\percent_corrected.mat'];
257 % % % save(wh_wl_data_save_filename,'chord_length','depth_of_foil','froude','aoa','Min_x','Min_y','Max_x','Max_y
    ','Wave_heights_m_avg','Wave_lengths_m_avg','-v7.3');
258 % % %
259 % % % wh_wl_cl_data_save_filename = ['.\'',date,'\wh_wl\avg_wh_wl_cl_side_view_',date,'\_',aoa,'\deg_cl_',depth,'\_
    ',percentage,'\percent_corrected.mat'];
260 % % % save(wh_wl_cl_data_save_filename,'chord_length','depth_of_foil','froude','aoa','Min_x_cl','Min_y_cl','
    Max_x_cl','Max_y_cl','Wave_heights_cl_avg','Wave_lengths_cl_avg','-v7.3');

```

## 7.5.6 Script for extract the wave parameters for wavelength and wave heights from peak and trough values.

```

1 clear all;
2 close all;
3 clc;
4
5 %%% tank test parameters
6 date = '2_11_2021';
7 aoa = '5';
8 depth = '5_4';
9 depth_frac = strrep(depth,'\_','/');
10 percentage = '125';
11
12 %%% load data
13 load(['im_data_side_view_',date,'\_',aoa,'\deg_cl_',depth,'\swl.mat']);
14
15 avg_data_save_filename = ['.\'',date,'\avg_side_view_',date,'\_',aoa,'\deg_cl_',depth,'\_',percentage,'\percent.mat'
    ];
16 load(avg_data_save_filename);
17
18 cl_data_save_filename = ['.\'',date,'\plotting\avg_cl_side_view_',date,'\_',aoa,'\deg_cl_',depth,'\_',percentage,'\
    _percent_corrected.mat'];
19 load(cl_data_save_filename);
20
21 thickness = chord_length/5;

```

```

22
23 m_data_save_filename = ['.\'',date,'_plotting\avg_meters_side_view_',date,'_',aoa,'_deg_cl_',depth,'_',percentage,
    '_percent_corrected.mat'];
24 load(m_data_save_filename);
25
26 Directory = ['C:\Users\Jamie\Desktop\Grad Semester 5\foil_tests\'',date,'_',aoa,'_deg\depth_cl_',depth,'_',
    percentage,'_percent\side_view_frames\'];
27
28 ds = mean([cam1_ds,cam2_ds]); %4.72558006442489e-04; % 1/12/21
29
30 [Maxima,MaxIdx] = findpeaks(water_line_y_avg_clipped,'MinPeakDistance',900);
31 Maxy = water_line_y_avg_clipped(MaxIdx);
32 Maxx = water_line_x_avg_clipped(MaxIdx);
33
34
35 Mins=max(water_line_y_avg_clipped)-water_line_y_avg_clipped;
36 [Minima,MinIdx] = findpeaks(Mins,'MinPeakDistance',900);
37 Miny = water_line_y_avg_clipped(MinIdx);
38 Minx = water_line_x_avg_clipped(MinIdx);
39
40 Min_x = Minx(Minx>0.05);
41 Min_y = Miny(Minx>0.05);
42
43 Max_x = Maxx(Maxx>0.001);
44 Max_y = Maxy(Maxx>0.001);
45
46 Max_y_cl = (Max_y-nanmean(sw_l_y_vals_m(1:1000)))./chord_length;
47 Max_x_cl = (Max_x-foil_center_x)./chord_length;
48
49 Min_y_cl = (Min_y-nanmean(sw_l_y_vals_m(1:1000)))./chord_length;
50 Min_x_cl = (Min_x-foil_center_x)./chord_length;
51
52 Wave_lengths_m_avg = [diff(Min_x),diff(Max_x)];
53 num_peaks = min(length(Min_y),length(Max_y));
54
55 for i = 1:num_peaks
56     Wave_heights_m_avg(i) = Max_y(i)-Min_y(i);
57 end
58
59 Wave_lengths_cl_avg = Wave_lengths_m_avg./chord_length;
60 Wave_heights_cl_avg =Wave_heights_m_avg./chord_length;
61
62 wh_wl_data_save_filename = ['.\'',date,'_wh_wl\avg_wh_wl_side_view_',date,'_',aoa,'_deg_cl_',depth,'_',percentage,
    '_percent_corrected.mat'];
63 save(wh_wl_data_save_filename,'chord_length','depth_of_foil','froude','aoa','Min_x','Min_y','Max_x','Max_y','
    Wave_heights_m_avg','Wave_lengths_m_avg','-v7.3');

```

```

64
65 wh_wl_cl_data_save_filename = ['.\'',date,'_wh_wl\avg_wh_wl_cl_side_view_',date,'_',aoa,'_deg_cl_',depth,'_',
    percentage,'_percent_corrected.mat'];
66 save(wh_wl_cl_data_save_filename,'chord_length','depth_of_foil','froude','aoa','Min_x_cl','Min_y_cl','Max_x_cl','
    Max_y_cl','Wave_heights_cl_avg','Wave_lengths_cl_avg','-v7.3');
67
68
69
70 figure(1)
71 subplot(3,1,1)
72 imshow(im_file_avg)
73 axis equal
74 title(['Angle of attack: ',aoa,' deg, Depth of foil: ',depth_frac,'*chord length, Froude^2: ',froude,' (Composite
    of raw images)'])
75 subplot(3,1,2)
76 imshow(bw_avg)
77 axis equal
78 title(['Composite of the black & white image'])
79 subplot(3,1,3)
80 imshow(edges_avg,RI_m)
81 hold on
82 axis equal
83 title(['Composite of the waterline image over all time steps with wave gauge data'])
84
85 % plot(water_line_x_avg,water_line_y_avg,'r')
86 errorbar(water_line_x_avg_clipped,water_line_y_avg_clipped, CI95_clipped,'r')
87 hold on;
88
89 % plot(max_x,max_y,'b*')
90 % hold on;
91 % plot(min_x,min_y,'g*')
92 plot(Max_x,Max_y,'b*')
93 hold on;
94 plot(Min_x,Min_y,'g*')
95 hold on;
96 plot(all_xloc_wg,all_eta_wg_avg,'m*')
97 xlabel('X Distance (m)')
98 ylabel('Y Distance (m)')
99
100 set(gcf, 'Units', 'Normalized', 'OuterPosition', [0 0 0.75 1]);
101 legend('Waterline & Std. Deviation','Troughs','Peaks','Wave Gauge Data','Location','northwest')
102
103 % saveas(gcf,[Directory,'water_line_figures\processed_wl_avg_',date,'_',aoa,'_deg_cl_',depth,'_',percentage,'
    _percent.jpg'])
104 % saveas(gcf,[Directory,'water_line_figures\processed_wl_avg_',date,'_',aoa,'_deg_cl_',depth,'_',percentage,'
    _percent'])

```

```

105
106 %%%%%%%%%%
107 % water_line_x_avg_cl = water_line_x_avg_cl-foil_x_cl(end);
108 % foil_x_cl = foil_x_cl-foil_x_cl(end)
109 all_xloc_wg_cl = (all_xloc_wg-foil_center_x)./chord_length;
110
111
112 figure(2)
113 % errorbar(water_line_x_avg_clipped./chord_length,water_line_y_avg_clipped./chord_length, CI95_clipped./
    chord_length,'g')
114 % hold on;
115 errorbar(water_line_x_avg_cl,water_line_y_avg_cl, CI95_cl,'r')
116 hold on;
117
118 plot(foil_x_cl,foil_y_cl,'c*')
119 hold on;
120 xlim([-0.3/chord_length 2.75/chord_length])
121 ylim([-0.05/chord_length (depth_of_foil+thickness)/chord_length])
122 % axis equal;
123 title(['Angle of attack: ',aoa,' deg, Depth of foil: ',depth_frac,'*chord length, Froude^2: ',froude,' (free
    surface extracted from images for all time steps)'])
124
125 % plot(max_x_cl,max_y_cl,'b*')
126 % hold on;
127 % plot(min_x_cl,min_y_cl,'g*')
128 plot(Max_x_cl,Max_y_cl,'b*')
129 hold on;
130 plot(Min_x_cl,Min_y_cl,'g*')
131 hold on;
132 plot(all_xloc_wg_cl,all_eta_wg_avg_cl,'m*') %
133 hold on;
134
135 % idx = find(~isnan(water_line_y_avg_cl));
136 % no_nan_water_line_x_avg_cl = water_line_x_avg_cl(idx) ;
137 % no_nan_water_line_y_avg_cl = water_line_y_avg_cl(idx) ;
138 %
139 % [curve_fit, goodness, output] = fit(no_nan_water_line_x_avg_cl',no_nan_water_line_y_avg_cl', 'sin3')
140
141 plot(curve_fit,'b')%,water_line_x_avg_cl,water_line_y_avg_cl,'r')
142 hold on;
143
144 % plot(swl_x_vals_m./chord_length,y_est./chord_length,'k*')
145
146
147 xlabel('X Distance (chord lengths)')
148 ylabel('Y Distance (chord lengths)')

```

```

149
150 frame_h = get(handle(gcf),'JavaFrame');
151 set(frame_h,'Maximized',1);
152 set(gca, 'YDir','reverse')
153 set(gca,'LooseInset',get(gca,'TightInset'));
154 legend('Waterline & Std. Deviation','Foil Location','Troughs','Peaks','Wave Gauge Data','Curve Fit','Location','
    southeast')
155
156 % saveas(gcf,[Directory,'water_line_figures\processed_wl_with_foil_',date,'_',aoa,'_deg_cl_',depth,'_',percentage
    ,'_percent.jpg'])
157 % saveas(gcf,[Directory,'water_line_figures\processed_wl_with_foil_',date,'_',aoa,'_deg_cl_',depth,'_',percentage
    ,'_percent'])
158
159
160
161 m_data_save_filename = ['.\'',date,'_plotting\avg_meters_side_view_',date,'_',aoa,'_deg_cl_',depth,'_',percentage,
    '_percent_corrected.mat'];
162 save(m_data_save_filename,'chord_length','depth_of_foil','froude','aoa','im_file_avg','bw_avg','edges_avg','RI_m'
    ,'water_line_x_avg_clipped','water_line_y_avg_clipped','CI95_clipped','curve_fit','Max_x','Max_y','Min_x','
    Min_y','all_xloc_wg','all_eta_wg_avg','-v7.3');
163
164 cl_data_save_filename = ['.\'',date,'_plotting\avg_cl_side_view_',date,'_',aoa,'_deg_cl_',depth,'_',percentage,
    '_percent_corrected.mat'];
165 save(cl_data_save_filename,'chord_length','depth_of_foil','froude','aoa','water_line_x_avg_cl','
    water_line_y_avg_cl','CI95_cl','curve_fit','foil_x_cl','foil_y_cl','Max_x_cl','Max_y_cl','Min_x_cl','
    Min_y_cl','all_xloc_wg_cl','all_eta_wg_avg_cl','-v7.3');

```

### 7.5.7 Script for plotting and comparing average waterlines from different experiments.

```

1 clear all;
2 close all;
3 clc;
4
5 %%% tank test parameters
6 dates = {'1_12_2021','2_11_2021'};
7 aoa = '10';
8 depth = '3_2';
9 depth_frac = strrep(depth,'_','/');
10 percentage = '125';
11
12 Directory = ['C:\Users\Jamie\Desktop\Grad Semester 5\foil_tests\compare_waterline_figures\'];
13
14
15 for di = 1:length(dates)
16

```

```

17     date = dates{di};
18
19     if di == 1
20         color_num = '#EDB120';
21     elseif di == 2
22         color_num = '#D95319';
23     end
24
25     %% load data
26     load(['im_data_side_view_',date,'_',aoa,'_deg_cl_',depth,'_swl.mat']);
27
28     cl_data_save_filename = ['.\'',date,'_plotting\avg_cl_side_view_',date,'_',aoa,'_deg_cl_',depth,'_',percentage
29         ,'_percent_corrected.mat'];
30
31     cl_wh_wl_data_save_filename = ['.\'',date,'_wh_wl\avg_wh_wl_cl_side_view_',date,'_',aoa,'_deg_cl_',depth,'_',
32         percentage,'_percent_corrected.mat'];
33
34     both_wave_heights_cl{di} = Wave_heights_cl_avg;
35     range_wh(di) = range(Wave_heights_cl_avg);
36     std_wh(di) = std(Wave_heights_cl_avg);
37     var_wh(di) = var(Wave_heights_cl_avg);
38     both_wave_lengths_cl{di} = Wave_lengths_cl_avg;
39     range_wl(di) = range(Wave_lengths_cl_avg);
40     std_wl(di) = std(Wave_lengths_cl_avg);
41     var_wl(di) = var(Wave_lengths_cl_avg);
42
43
44     thickness = chord_length/5;
45
46     both_water_line_x_avg_cl{di} = water_line_x_avg_cl;
47     both_water_line_y_avg_cl{di} = water_line_y_avg_cl;
48
49 %     m_data_save_filename = ['.\'',date,'_plotting\avg_meters_side_view_',date,'_',aoa,'_deg_cl_',depth,'_',
50 %         percentage,'_percent_corrected.mat'];
51 %     load(m_data_save_filename);
52
53 %     figure(1)
54 %     subplot(3,1,1)
55 %     imshow(im_file_avg)
56 %     axis equal
57 %     title(['Angle of attack: ',aoa,' deg, Depth of foil: ',depth_frac,'*chord length, Froude^2: ',froude,' (
58 %         Composite of raw images)'])
59 %     subplot(3,1,2)

```

```

59 % imshow(bw_avg)
60 % axis equal
61 % title(['Composite of the black & white image'])
62 % subplot(3,1,3)
63 % imshow(edges_avg,RI_m)
64 % hold on
65 % axis equal
66 % title(['Composite of the waterline image over all time steps with wave gauge data'])
67 %
68 % plot(water_line_x_avg,water_line_y_avg,'r')
69 % errorbar(water_line_x_avg_clipped,water_line_y_avg_clipped, CI95_clipped,'r')
70 % hold on;
71 %
72 % plot(max_x,max_y,'b*')
73 % hold on;
74 % plot(min_x,min_y,'g*')
75 % plot(Max_x,Max_y,'b*')
76 % hold on;
77 % plot(Min_x,Min_y,'g*')
78 % hold on;
79 % plot(all_xloc_wg,all_eta_wg_avg,'m*')
80 % xlabel('X Distance (m)')
81 % ylabel('Y Distance (m)')
82 %
83 % set(gcf, 'Units', 'Normalized', 'OuterPosition', [0 0 0.75 1]);
84 % legend('Waterline & Std. Deviation','Troughs','Peaks','Wave Gauge Data','Location','northwest')
85 %
86 % saveas(gcf,[Directory,'water_line_figures\processed_wl_avg_',date,'_',aoa,'_deg_cl_',depth,'_',percentage,'
_percent.jpg'])
87 % saveas(gcf,[Directory,'water_line_figures\processed_wl_avg_',date,'_',aoa,'_deg_cl_',depth,'_',percentage,'
_percent'])
88
89 %%%%%%%%%
90
91 figure(2)
92 errorbar(water_line_x_avg_cl,water_line_y_avg_cl, CI95_cl,'Color',color_num)
93 hold on;
94
95 plot(foil_x_cl,foil_y_cl,'c*')
96 hold on;
97 xlim([-0.3/chord_length 2.75/chord_length])
98 ylim([-0.05/chord_length (depth_of_foil+thickness)/chord_length])
99 % axis equal;
100 title(['Angle of attack: ',aoa,' deg, Depth of foil: ',depth_frac,'*chord length, Froude^2: ',froude,' (free
surface extracted from images for all time steps)'])
101

```

```

102 plot(Max_x_cl,Max_y_cl,'b*')
103 hold on;
104 plot(Min_x_cl,Min_y_cl,'g*')
105 hold on;
106 plot(all_xloc_wg_cl,all_eta_wg_avg_cl,'m*') %
107 hold on;
108
109 plot(curve_fit,'b')
110 hold on;
111
112 xlabel('X Distance (chord lengths)')
113 ylabel('Y Distance (chord lengths)')
114
115 frame_h = get(handle(gcf),'JavaFrame');
116 set(frame_h,'Maximized',1);
117 set(gca,'YDir','reverse')
118 set(gca,'LooseInset',get(gca,'TightInset'));
119 legend('Waterline & Std. Deviation for 1/12/2021','Foil Location','Troughs','Peaks','Wave Gauge Data','Curve
Fit','Waterline & Std. Deviation for 2/11/2021','Location','southeast')
120
121 % first_wave_data_x = waterline_x_avg_cl
122
123 end
124
125 num_x = min(length(both_water_line_x_avg_cl{1}),length(both_water_line_x_avg_cl{2}));
126
127 for xx = 1:num_x
128     [vals(xx),idx(xx)] = min(abs(both_water_line_x_avg_cl{1}-both_water_line_x_avg_cl{2}(xx)));
129 end
130
131 new_avg_x_cl_exp1 = both_water_line_x_avg_cl{1}(1,idx);
132 new_avg_x_cl_exp2 = both_water_line_x_avg_cl{2};
133
134 new_avg_y_cl_exp1 = both_water_line_y_avg_cl{1}(1,idx);
135 new_avg_y_cl_exp2 = both_water_line_y_avg_cl{2};
136
137 delta_y = new_avg_y_cl_exp2-new_avg_y_cl_exp1;
138
139 rms_y = 100*sqrt(nansum(delta_y.^2)/length(delta_y))
140
141 text(7.2,0.8,['RMS = ',num2str(rms_y),'%'])
142
143 saveas(gcf,[Directory,'compare_wl_with_foil_',dates{1},'_',dates{2},'_',aoa,'_deg_cl_',depth,'_',percentage,'
_percent.jpg'])
144 saveas(gcf,[Directory,'compare_wl_with_foil_',dates{1},'_',dates{2},'_',aoa,'_deg_cl_',depth,'_',percentage,'
_percent'])

```

```

145
146 % save(m_data_save_filename,'chord_length','depth_of_foil','froude','aoa','im_file_avg','bw_avg','edges_avg','
      RI_m','water_line_x_avg_clipped','water_line_y_avg_clipped','CI95_clipped','curve_fit','Max_x','Max_y','
      Min_x','Min_y','all_xloc_wg','all_eta_wg_avg','-v7.3');
147
148 variability = [range_wh;std_wh;var_wh;range_wl;std_wl;var_wl];
149 VarNames={'1/12/2021','2/11/2021'};
150 RowNames={'Range for wave height', 'Standard Deviation for wave height', 'Variance for wave height', 'Range for
      wave length', 'Standard Deviation for wave length', 'Variance for wave length'};
151 varTable = array2table(variability,'VariableNames',VarNames,'RowNames',RowNames)
152
153 % figure(3)
154 % plot(new_avg_x_cl_exp1,new_avg_y_cl_exp1,'r')
155 % hold on;
156 % plot(new_avg_x_cl_exp2,new_avg_y_cl_exp2,'b')
157 % hold on;
158 % plot(foil_x_cl,foil_y_cl,'c*')
159 % hold on;
160 % set(gca, 'YDir','reverse')

```

## Chapter 8

### Bibliography

- [1] ATI Industrial Automation. Network Force/Torque Sensor System Document : 9620-05-NET FT, App. Engineering, 2000.
- [2] Cox C.S. (1958) Measurement of slopes of high frequency wind waves. J Mar Res 16: 199–225
- [3] Dalziel SB, et al., (2000) Whole-field density measurements by "synthetic Schlieren". Exp Fluids 28:322–335
- [4] Derakhti M., et al., 2015, NHWAVE: Model revisions and tests of wave breaking in shallow and deep water, Research Report No. CACR-15-18, Center for Applied Coastal Research, Dept. of Civil Environmental Engineering, University of Delaware.
- [5] “Digital Image Correlation.” Textile Fibre Composites in Civil Engineering, by Thanasis Triantafillou, UK, 2016.
- [6] Duncan, J. H. “An Experimental Investigation of Breaking Waves Produced by a Towed Hydrofoil.” Proceedings of the Royal Society of London. A. Mathematical and Physical Sciences, vol. 377, no. 1770, 1981, pp. 331–348., doi:10.1098/rspa.1981.0127.
- [7] Duncan, James H. “The Breaking and Non-Breaking Wave Resistance of a Two-Dimensional Hydrofoil.” Journal of Fluid Mechanics, vol. 126, 1983, pp. 507–520. doi:10.1017/s0022112083000294.

- [8] Elwell FC (2004) Flushing of embayments. PhD thesis, University of Cambridge
- [9] Fadlun, E.A., Verzicco, R., Orlandi, P., Mohd-Yusof, J., 2000. Combined immersed boundary finite-difference methods for three-dimensional complex flow simulations. *J. Comput. Phys.* 161, 35–60.
- [10] Jhne B, Schmidt M, Rocholz R (2005) Combined optical slope/ height measurements of short wind waves: principle and calibration. *Meas Sci Technol* 16:1937–1944
- [11] Keane R.D. (1994) Correlation Methods of PIV Analysis. In: Lading L., Wigley G., Buchhave P. (eds) *Optical Diagnostics for Flow Processes*. Springer, Boston, MA. [https://doi.org/10.1007/978-1-4899-1271-8\\_13](https://doi.org/10.1007/978-1-4899-1271-8_13)
- [12] Keller WC, Gotwols BL (1983) Two-dimensional optical measurement of wave slope. *Appl Opt* 22:3476–3478
- [13] Kistler Instrumente AG. Force Sensor with Integrated Electronics, Kistler Manual, 2016.
- [14] Kurata J, Grattan KTV, Uchiyama H, Tanaka T (1990) Water surface measurement in a shallow channel using the transmitted image of a grating. *Rev Sci Instrum* 61(2):736
- [15] McHugh, Michael L. The SSBN Security Program, [fas.org/nuke/guide/usa/slbm/ssbn-secure.htm](https://fas.org/nuke/guide/usa/slbm/ssbn-secure.htm).
- [16] Moisy, Frédéric, et al. “A Synthetic Schlieren Method for the Measurement of the Topography of a Liquid Interface.” *Experiments in Fluids*, vol. 46, no. 6, 2009, pp. 1021–1036., doi:10.1007/s00348-008-0608-z.

- [17] Roesgen T, Lang A, Gharib M (1998) Fluid surface imaging using microlens arrays. *Exp Fluids* 25:126
- [18] Savalsberg R, Holten A, et al. (2006) Measurement of the gradient field of a turbulent free surface. *Exp Fluids* 41:629–640
- [19] Schock J, Dahl J. Simultaneous Measurement of Free Surface Elevation and Three-Component Velocity Field Around a Translating Surface-Piercing Foil. *Journal of Offshore Mechanics and Arctic Engineering*. 2018; 140(3), 031103. doi: 10.1115/1.4038586
- [20] Zhang X (1996) An algorithm for calculating water surface elevations from surface gradient image data. *Exp Fluids* 21:43–48
- [21] Zilman, Gregory, and Touvia Miloh. “Kelvin and V-like Ship Wakes Affected by Surfactants.” *Journal of Ship Research*, vol. 45, no. 02, 2001, pp. 150–163., doi:10.5957/jsr.2001.45.2.150.